INFORMATION TO USERS

This manuscript has been reproduced from the microfilm master. UMI films the text directly from the original or copy submitted. Thus, some thesis and dissertation copies are in typewriter face, while others may be from any type of computer printer.

The quality of this reproduction is dependent upon the quality of the copy submitted. Broken or indistinct print, colored or poor quality illustrations and photographs, print bleedthrough, substandard margins, and improper alignment can adversely affect reproduction.

In the unlikely event that the author did not send UMI a complete manuscript and there are missing pages, these will be noted. Also, if unauthorized copyright material had to be removed, a note will indicate the deletion.

Oversize materials (e.g., maps, drawings, charts) are reproduced by sectioning the original, beginning at the upper left-hand corner and continuing from left to right in equal sections with small overlaps. Each original is also photographed in one exposure and is included in reduced form at the back of the book.

Photographs included in the original manuscript have been reproduced xerographically in this copy. Higher quality 6" x 9" black and white photographic prints are available for any photographs or illustrations appearing in this copy for an additional charge. Contact UMI directly to order.

U·M·I

University Microfilms International
A Bell & Howell Information Company
300 North Zeeb Road, Ann Arbor, MI 48106-1346 USA
313/761-4700 800/521-0600

Order Number 9405583

Generation of ultrashort pulses from chromium-doped forsterite laser

Seas, Antonios, Ph.D.

City University of New York, 1993

U·M·I
300 N. Zeeb Rd.
Ann Arbor, MI 48106

GENERATION OF ULTRASHORT PULSES FROM CHROMIUM DOPED FORSTERITE LASER

by

ANTONIOS SEAS

A dissertation submitted to the Graduate Faculty in Engineering in partial fulfillment of the requirements for the degree of Doctor of Philosophy, The City University of New York.

1993

This manuscript has been read and accepted for the Graduate Faculty in Engineering in satisfaction of the dissertation requirement for the degree of Doctor of Philosophy.

7/16/93
Date

Prof. Robert R. Alfano
Chair of Examining Committee

7/16/93
Date

Prof. Gerard D. Lowen
Executive Officer

Prof. Samir Ahmed

Prof. Roger Dorsinville

Prof. Ping Pei Ho

Prof. Swapan Gayen

Dr. Frank Allario

Dr. Peter Delfyett

Supervisory Committee

The City University of New York

Abstract

GENERATION OF ULTRASHORT PULSES FROM CHROMIUM-DOPED FORSTERITE LASER

by

Antonios Seas

Adviser: Robert R. Alfano, Distinguished Professor of Science and Engineering.

This thesis discusses the generation of ultrashort pulses from the chromium-doped forsterite laser, the various designs, construction and operation of forsterite laser systems capable of generating picosecond and femtosecond pulses in the near infrared. Various mode-locking techniques including synchronous optical pumping, active mode-locking, and self-mode-locking were successfully engineered and implemented.

Active and synchronously pumped mode-locking using a three mirror, astigmatically compensated cavity design and a forsterite crystal with a figure of merit of 26 (FOM=$\alpha_{1064nm}/\alpha_{1250nm}$) generated pulses with FWHM of 49 and 260 ps, respectively. The tuning range of the mode-locked forsterite laser in both cases was determined to be in the order of 100 nm limited only by the dielectric coatings of the mirrors used in the cavity. The slope efficiency was measured to be 12.5% for synchronous pumping and 9.1% for active mode-locking.

A four mirror astigmatically compensated cavity was found to be more appropriate for mode-locking. Active mode-locking using the four-mirror cavity generated pulses with FWHM of 31 ps. The pulsewidth was further reduced to 6 ps by using a forsterite crystal with a higher figure of merit (FOM=39). Pulsewidth-bandwidth

measurements indicated the presence of chirp in the output pulses. Numerical calculation of the phase characteristics of various optical materials indicated that a pair of prisms made of SF 14 optical glass can be used in the cavity in order to compensate for the chirp. The insertion of the prisms in the cavity resulted in a reduction of the pulsewidth from 6 ps down to 900 fs. Careful optimization of the laser cavity resulted in the generation of stable 90-fs pulses. Pulses as short as 60 fs were generated and self-mode-locked mode of operation using the Cr:forsterite laser was demonstrated for the first time. Pure self-mode-locking was next achieved generating 105-fs pulses tunable between 1230 - 1270 nm.

Numerical calculations of the cubic phase characteristics of the prism pair used indicated that the pair of SF 14 prisms compensated for quadratic phase but introduced a large cubic phase term. Numerical evaluation of other optical glasses indicated that a pair of SFN 64 prisms can introduce the same quadratic phase as SF 14 prisms but introduce a smaller cubic phase. When the SF 14 prisms were replaced by SFN 64 prisms the pulsewidth was reduced to 50 fs. Great improvement was also observed in the stability of the self mode-locked forsterite laser and in the ease of achieving mode-locking. Using the same experimental arrangement and a forsterite crystal with improved FOM the pulse width was reduced to 36 fs.

To my parents, Andreas and Anastasia Seas

and my wife Constantia Seas

ACKNOWLEDGMENTS

I would like to thank and gratefully acknowledge my thesis adviser Prof. Robert R. Alfano. His patience, vast knowledge of science, and willingness to spend his valuable time to listen, insight to what to do next, and teaching me how to be first were of enormous help in achieving the research goals. Most important I appreciate the fact that he trusted me with mode-locked operation of the forsterite laser and he envisioned that I can complete this line of work.

Sincere thanks to Professor Roger Dorsinville for his advice, support and valuables discussions. Special thanks for introducing me to the Ph.D. program and guiding my initial steps in the exciting world of research.

I am particularly indebted to Professor Vladimir Petricevic for his valuable theoretical and experimental instructions, collaboration, and fruitful discussions. His friendship, patience and support during my research is deeply appreciated.

I am most grateful to Dr. Bob Guenther of the Army Research Office, Dr. Frank Allario and Dr. Norman Barnes of NASA Langley Research Center who made this research possible by providing financial support. I am obliged to Professors Samir Ahmed, Ping Pei Ho, Swapan Gayen, and Dr. Peter Delfyett for serving on the doctoral committee. I would also like to take this opportunity to thank IUSL's laser engineer Mr. Yuri Budansky and secretary Mrs. Megan Gibbs for their friendly support and valuable assistance.

Last but not least I would like to thank my parents and my wife for their endless support and love. Their sacrifice and understanding shed happiness even to the worst of times.

TABLE OF CONTENTS

LIST OF TABLES

CHAPTER 2

CHAPTER 3

CHAPTER 4

CHAPTER 5

CHAPTER 6

LIST OF FIGURES

CHAPTER 1

CHAPTER 2

CHAPTER 3

CHAPTER 4

CHAPTER 5

CHAPTER 6

APPENDIX

CHAPTER 1

INTRODUCTION

1.1. Tunable Solid- State Lasers

The discovery and development of tunable solid-state lasers[1] initiated a wide field of research due to their potential use in many areas There has been considerable interest in wavelength-agile lasers due to widespread use of tunable coherent sources in scientific fields, as well as potential applications in areas such as eye-safe ranging, remote sensing, LIDAR, optical communications and various medical and biological applications. During the past 10 years tunable solid-state laser have emerged as a viable alternative to dye lasers.

Dye lasers suffer many disadvantages such as toxicity, poor long-term reliability and relatively narrow tuning range making them unsuitable for hospital, airborne, mobile or space borne use. Tunable solid-state lasers on the other hand do not posses these problems and offer many advantages over dye lasers. Some of these advantages are:

* Tunable solid state lasers cover a very wide spectrum up to 400 nm (Ti:sapphire). This makes them prime candidates as tunable sources of radiation and for the generation of ultrashort pulses.
* The laser medium is a non-toxic solid material. This makes tunable solid state lasers useful tools in places where toxicity and containment is a problem such as hospital's operating rooms, airborne operations, and space stations.

* Solid state lasers are very reliable systems with long life and require minimum maintenance.
* Solid state lasers can be build very compact since they can be pumped by semiconductor lasers.
* Solid state lasers are relatively easy to use. This makes them useful for people with no background in laser engineering.
* Long life and little maintenance makes solid state lasers very cost effective sources of radiation.

Although there are several tunable solid-state lasers that cover the spectral range from 700 - 1100 nm, there are basically only two that are at an advanced stage of development or look particularly promising. The most developed commercially available tunable solid-state laser is titanium-doped sapphire ($Ti^{3+}:Al_2O_3$) with tuning range covering 660-1100 nm.[2] Another rapidly developing laser system is chromium-doped LISAF ($Cr^{3+}:LiSrAlF_6$) with tuning range extending from 780 - 1060 nm, whose advantages over Ti:sapphire are longer emission lifetime and consequently better energy storage capabilities, and possibility of diode pumping.[3]

Unfortunately, none of the above lasers cover the near infrared range beyond 1100 nm. This void has been successfully filled by introducing a new laser ion, Cr^{4+}. The discovery and subsequent development of chromium-doped forsterite ($Cr:Mg_2SiO_4$),[4,5,6] an important tunable solid state laser which is tunable in the spectral region between 1150-1350 nm, have generated growing interest in this material as well as other crystals that may accommodate Cr^{4+} in their structure. Wide tunability in the near infrared[7,8], high gain cross section ($2x10^{-19}$ cm^{-2}) and lack of any significant excited state absorption[9] make chromium-doped forsterite a promising tunable solid state laser.

A list of some important tunable solid state lasers and their corresponding tuning ranges are shown in figure 1.1.1.

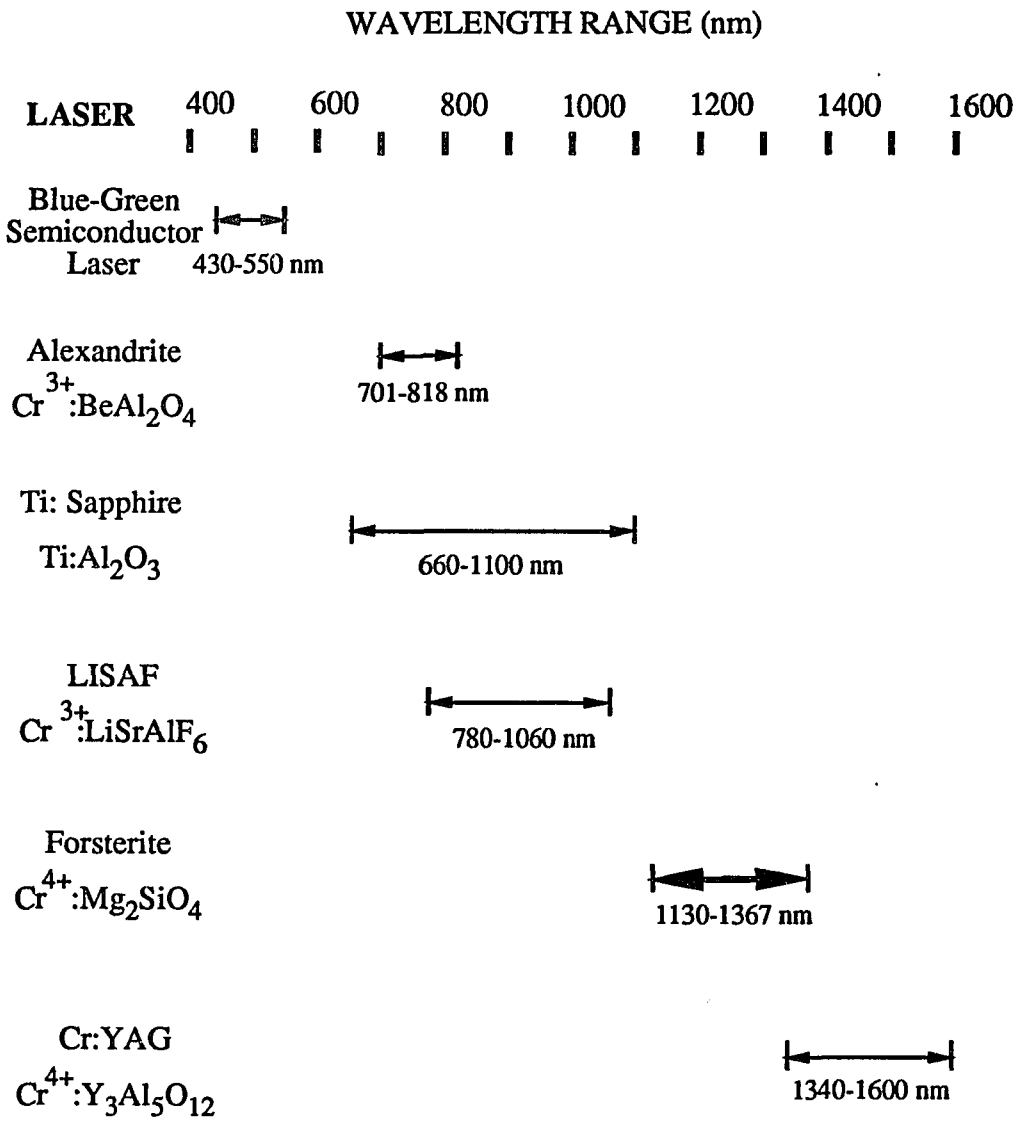

Fig. 1.1.1. Most important tunable solid state lasers and their tuning ranges.

Over the past few years, research has been concentrated on the generation of ultrashort pulses suggesting that a new ultrashort pulse laser technology can be developed for tunable solid state laser sources.[10,11,12,13] These new laser systems can achieve superior performance and reduce the cost and complexity as compared to the traditional dye laser technology. The techniques used for ultrashort pulse generation are of particular

interest because they exemplify several general concepts that can be applied to femtosecond laser engineering. In the near future these concepts suggest that it will be possible to develop a low cost, compact ultrashort pulse technology applicable to a wide range of solid state materials, towards the ultimate diode laser pumped solid state tunable fs lasers.[14]

1.2. Thesis Statement

The research described in this thesis has focused on the generation of ultrashort pulses from the chromium-doped forsterite laser. The main objective was the generation of ultrashort pulses using different methods of mode-locking and ultimately the generation of tunable femtosecond pulses in the near infrared. Different methods of mode-locking were successfully engineered and tested including synchronous optical pumping, active mode-locking, and self mode-locking. As a result of the continuous research efforts, the chromium-doped forsterite laser has been established as a reliable source of stable, tunable, sub-100-fs pulses in the near infrared.

The main accomplishments of this thesis are the following:

1. Design and engineering of a three-mirror astigmatically compensated Cr:forsterite laser and the first demonstration of mode-locking of the Cr:forsterite laser. These experiments resulted in the generation of 260 ps pulses using synchronous optical pumping and 49 ps using active mode-locking.[15,16]

2. Design and engineering of a four-mirror astigmatically compensated cavity and the generation of 6 ps pulses from an actively mode-locked forsterite laser.

3. Design of a four-mirror astigmatically compensated Cr:forsterite laser with intracavity chirp compensation and the generation of 90 fs pulses. More

significantly this was the first demonstration of self mode-locking of the forsterite laser.[17,18]

4. Design and engineering of a self-mode-locked forsterite laser with improved phase compensating characteristics and the generation of pulses with FWHM of 36 fs .[19,20]

1.3. Thesis Organization

This thesis is organized in six chapters including the introduction. Throughout the thesis, particular attention has been paid to accurately describe the experimental methods and techniques used that were crucial for the completion of the research goals.

Chapter 2 serves as an introduction to chromium-doped forsterite crystal. Chromium-doped forsterite is an intriguing laser crystal. The ion responsible for lasing action was identified as tetravalent chromium in tetrahedral coordination,[5,21,22,23,24] but further spectroscopic investigations indicated the presence of other non-lasing centers such as Cr^{2+} and Cr^{3+} in octahedral coordination, which degrade the lasing performance of the forsterite laser.[25] Absorption and emission experiments are presented where the crystal quality was evaluated and also provided the grounds for comparison between different laser crystals used during the mode-locking experiments.

Mode-locking can be achieved using a variety of techniques such as active mode-locking, synchronous optical pumping, and passive mode-locking. Chapter 3 reviews the basic concept of mode-locking and the different methods used for mode-locking of the Cr:forsterite laser. Forsterite laser is the first laser whose fundamental radiation covers the wavelength region between 1150-1350 nm, and there are no commercially available autocorrelators to measure femtosecond pulses in this region. The design of an autocorrelator capable of measuring femtosecond pulses in the near infrared is presented in the final section of chapter 3.

Laser cavities used for mode-locking are usually complex multielement optical systems where there is a need for careful design in order to eliminate perturbations due to unwanted reflections, astigmatic and heating effects. Chapter 4 presents the analysis and design criteria for a three-mirror and four-mirror z-fold astigmatically compensated cavities used in mode-locking of the Cr:forsterite laser. Numerical simulations of the two cavity designs are presented and their usefulness is determined. Tuning of the forsterite laser was accomplished using a single plate quartz birefringent filter. The theory of tuning using birefringent crystals and the design of a three stage birefringent filter suitable for the Cr:forsterite laser is presented next. Chapter 4 continues with the experimental results obtained by using the three mirror cavity in combination with synchronously pumped mode-locking and active mode-locking. The three mirror cavity and synchronously pumped mode-locking using the Cr:forsterite laser resulted in the generation of pulses with FWHM of 260 ps. The tuning range was determined to be 100 nm (1195-1295 nm) using only one set of mirrors, limited only by the dielectric coatings of the mirrors used. Slope efficiency experiments resulted in a 12.9% slope efficiency and detuning experiments indicating that the synchronously pumped forsterite laser was capable of generating pulses with FWHM of less than 300 ps for $\pm$ 5 μm of detuning from optimum mode-locking position. The three mirror cavity was also used in combination with active mode locking generating pulses with FWHM of 49 ps. Tuning and slope efficiency experiments indicated a tuning range of 70 nm and 9.1% slope efficiency. Better results were obtained using active mode-locking with the z-fold four-mirror astigmatically compensated cavity design. The pulse width of the output pulses was reduced to 31 ps and then to 6 ps by using a new forsterite crystal. Pulsewidth-bandwidth measurements indicated the presence of chirp in the output pulses.

The presence of chirp in the output pulses of the actively mode-locked Cr:forsterite laser indicated that special attention should be given to phase distortions compensation in the laser cavity. Chapter 5 starts by reviewing the theory of pulse

broadening, pulse compression and chirp compensation using a pair of prisms. Numerical evaluations of different types of glass indicated a pair of SF 14 prisms can selectively introduce positive or negative chirp in the cavity. The insertion of SF 14 prisms in the actively mode locked forsterite laser resulted in a reduction of the pulse width from 6 ps down to 900 fs. By further optimization of the laser cavity a dramatic reduction of the pulse duration from 900 fs down to 90 fs was observed. Self mode locking was realized for the first time when the RF power from the acousto-optic modulator was disconnected and the forsterite laser continued generating femtosecond pulses. The final section of chapter 5 presents the design and construction of a self-mode-locked forsterite laser.

The calculations performed up to this point did not consider the cubic phase introduced by the pair of prisms or other optical elements. Minimization of cubic phase distortions is critical for the generation of shorter pulses and improved stability of the output femtosecond pulses. Next numerical calculations were performed to determine the type of optical glass that can compensate for chirp in the forsterite laser and will introduce minimum cubic phase term. The calculations indicated that a pair of prisms made of SFN 64 glass will compensate for chirp and will introduce minimum cubic phase. When the SF 14 prisms were replaced by SFN 64 prisms the pulse width was reduced to 50 fs. The stability and the ease of achieving self-mode-locking of the forsterite laser were greatly improvement. The forsterite laser was operating in a self-mode-locked mode of operation for hours without any noticeable change in the pulse width of the output pulses. Further reduction of the pulse width down to 36 fs was achieved when the forsterite crystal was replaced by a new forsterite crystal with a higher figure of merit (FOM).

The final chapter of the thesis summarizes the achievements of research and further research to advance fs operation of the Cr:forsterite laser is recommended. Some

of the subjects presented is diode pumped operation, intracavity second harmonic generation, and the generation of higher power from the forsterite laser.

1.4. References

1. P. F. Moulton, "Tunable Paramagnetic-Ion Lasers", in: *Laser Handbook*, edited by M. Bass and M. L. Stitch, Elseviers Science Publishers B. V., (1985) and references therein.

2. P. F. Moulton, " Spectroscopic and laser characteristics of Ti:Al_2O_3", J. Opt. Soc. Am. **B3**, 125 (1986).

3. S. A. Payne, L. L. Chase, L. K. Smith, L. Kway, and H. W. Newkirk, " Laser performance of $LiSrAlF_6:Cr^{3+}$", J. Appl. Phys. **66**, 1051 (1989).

4. V. Petričević, S. K. Gayen, R. R. Alfano, K. Yamagishi, H. Anzai, and Y. Yamaguchi, "Laser action in chromium-doped forsterite", Appl. Phys. Lett. **52**, 1040 (1988).

5. V. Petričević, S. K. Gayen, and R. R. Alfano, "Laser action in Cr-activated forsterite for near infrared excitation: Is Cr^{4+} the lasing ion?", Appl. Phys. Lett. **53**, 2590 (1988).

6. R. R. Alfano and V. Petričević, "Tetravalent chromium (Cr4+) as a laser-active ion for tunable solid-state lasers", U.S. Patent# 4,987,575 (January 22, 1991).

7. V. Petričević, S. K. Gayen, and R. R. Alfano, "Near infrared tunable operation of chromium doped forsterite laser", Appl. Opt. **28**, 1609 (1989).

8. V. G. Baryshevskii, M. V. Korzhik, A. E. Kimaev, M. G. Livshitz, V. B. Pavlenko, M. L. Meil'man, and B. I. Minkov, Zh. Prikl. Spectrosk. **53**, 7 (1990).

9. V. Petričević, A. Seas, and R. R. Alfano, "Effective gain measurements in chromium-doped forsterite", *OSA Proceedings of the Advanced Solid-State Lasers Conference*, March 5-7, 1990, Salt Lake City, Utah, Vol. **6** of the OSA Proceedings Series, H. P. Jenssen and G. Dube, eds. (Optical Society of America, Washington, D.C., 1991) pp. 73-78.

10. D. E. Spence, P. N. Kean, and W. Sibbett, "60-fs pulse generation from a self-mode-locked Ti:sapphire laser", Optics Letters, Vol. **16**, 42 (1991).

11. F. Krausz, M. E. Fermann, T. Brabec, P. F. Curley, M. Hofer, M. H. Ober, C. Spielmann, E. Wintner, and A. J. Schmidt, "Femtosecond solid-state lasers" IEEE Journal of Quantum Electronics, **QE-28**, 2097 (1992).

12. H. A. Hauss, J. G. Fujimoto, and E. P. Ippen, "Analytic theory of additive pulse and Kerr lens mode-locking", IEEE Journal of Quantum Electronics, **QE-28**, 2086 (1992).

13. T. Brabec, Ch. Spielmann, P. F. Curley, and F. Krausz, "Kerr lens mode locking", Optics Letters, Vol. **17**, 1292 (1992).

14. J. G. Fujimoto, "New technologies for ultrashort pulse generation in solid-state lasers", Optics & Photonics News, pp 9, March 1991.

15. A. Seas, V. Petričević,, R. R. Alfano, " Continuous-Wave Mode-Locked Operation of Chromium-Doped Forsterite Laser", Optics Letters, Vol. **16**, pp.1668 (1991).

16. A. Seas, V. Petričević,, R. R. Alfano, "CW Mode-Locked Operation of Chromium-Doped Forsterite Laser", *Proceedings on Advanced Solid-State Lasers,* G. Dube and L. Chase, eds., Optical Society of America, Washington DC, Vol. **10**, pp. 69-71 (1991).

17. A. Seas, V. Petričević,, R. R. Alfano, "Generation of Sub-100-fs Pulses from a Continuous-Wave Mode-Locked Chromium-Doped Forsterite Laser", Optics Letters, Vol. **17**, pp. 937 (1992).

18. A. Seas, V. Petričević, R. R. Alfano, "60-fs Chromium-Doped Forsterite (Cr^{4+}:Mg_2SiO_4) Laser", Ultrafast Phenomena VIII, J. L. Martin, A. Migus, G. A. Mourou, and A. H. Zewail, eds., Springer Series in Chemical Physics, Vol. **55**, pp. 174 (1993).

19. A. Seas, V. Petričević,, R. R. Alfano, "Femtosecond Pulses Generated From a Synchronously Pumped Chromium-Doped Forsterite Laser", to be published in the Proceedings of the Topical Meeting on Advanced Solid-State Lasers, New Orleans, Louisiana, February 1-3, 1993.

20. A. Seas, V. Petričević,, R. R. Alfano, "Self-Mode-Locked Chromium-Doped Forsterite Laser Generates 50-fs Pulses", Optics Letters, Vol. **18**, pp. 891 (1993).

21. H. R. Verdun, L. M. Thomas, D. M. Andrauskas, T. McCollum, and A. Pinto, "Chromium-doped forsterite laser pumped by 1.06 μm radiation", Appl. Phys. Lett. **53**, 2593 (1988).

22. V. Petričević, S. K. Gayen, and R. R. Alfano, "Chromium-activated forsterite laser", in *Tunable Solid-State Lasers*, Vol. **5** of the OSA Proceeding Series, M. L. Shand and H. P. Jenssen, eds. (Optical Society of America, Washington, D.C., 1989), pp. 77-84.

23 H. R. Verdun, L. M. Thomas, and D. M. Andrauskas, "Laser performance of chromium-aluminum-doped forsterite", in *Tunable Solid-State Lasers*, Vol. **5** of the OSA Proceeding Series, M. L. Shand and H. P. Jenssen, eds. (Optical Society of America, Washington, D.C., 1989), pp. 85-92.

24. R. Moncorge, D. J. Simkin, G. Cormier, and J. A. Capobianco, "Spectroscopic properties and fluorescence dynamics in chromium-doped forsterite", in *Tunable Solid-State Lasers*, Vol. **5** of the OSA Proceeding Series, M. L. Shand and H. P. Jenssen, eds. (Optical Society of America, Washington, D.C., 1989), pp. 93-97.

25. Y. Yamaguchi, K. Yamagishi, A. Sugimoto, and Y. Nobe, " Optical properties and crystal growth atmosphere of forsterite", in *Advanced Solid-State Lasers*, Vol. **10** of

the OSA Proceeding Series, G. Dube and L. Chase, eds. (Optical Society of America, Washington, D.C., 1991), pp. 52-56.

CHAPTER 2

CHROMIUM-DOPED FORSTERITE CRYSTAL

2.1. Introduction

The discovery and subsequent development of chromium-doped forsterite laser ($Cr:Mg_2SiO_4$) fills the void in the spectral region between 1150-1350 nm. This laser has generated growing interest in this material as well as other crystals that may accommodate Cr^{4+} in their structure. Pulsed[1,2,3] and continuous-wave[4] laser action was obtained and tunability over the 1130-1367 nm was demonstrated for both laser and flashlamp pumping.[5,6,7] The maximum slope efficiency of 38% was achieved, and the extrapolated limiting slope efficiency in the absence of passive losses was estimated to be 65%.[8] Mode-locked operation of chromium-doped forsterite laser was achieved using several methods including synchronous optical pumping and active mode-locking to generate 260-ps and 31-ps pulses, respectively.[9] Actively mode-locked Cr:forsterite laser with intracavity chirp compensation produced pulses as short as 60 fs.[10] Pulses with FWHM of 150 fs were generated at 77 K using additive pulse mode-locking technique.[11] Recently 50-fs pulses were generated using self mode-locking and prisms that compensate for the quadratic phase distortions and introduce minimum cubic phase term. The 50-fs pulses were reduced to 36 fs by using a forsterite crystal with higher figure of merit (FOM).[12]

The unique spectroscopic property of chromium-doped forsterite is that in this crystal the lasing center is tetravalent chromium (Cr^{4+}) substituting for tetrahedrally coordinated Si^{4+}.[2,13] Chromium-doped forsterite has shown that the Cr^{4+} ion in a

suitable host crystal can make an attractive laser source for the near infrared spectral range. These novel tunable solid state lasers are expected to operate in the technologically important near infrared spectral region between 1 - 2 μm. Conventional chromium-doped lasers are based on Cr^{3+} as an active ion and their tuning range rarely goes beyond 1 μm.

In this chapter spectroscopic properties of the chromium-doped forsterite crystals used in this study are presented. In section 2.2.1 the most common features of the absorption spectra are presented. Section 2.2.2 deals with the emission spectrum of the forsterite crystal, and section 2.2.3 presents a simplified energy level and the most important spectroscopic and laser properties of Cr:forsterite laser.

2.2. Basic Spectroscopic Properties of Chromium-Doped Forsterite Crystal

Forsterite (Mg_2SiO_4) is a member of the olivine family of crystals and is a naturally occurring gem called peridot. Single crystals of chromium-doped forsterite have been grown successfully using the Czochralski method,[14,15] as well as the laser-heated-pedestal-growth (LHPG) technique.[16] A unit cell of forsterite has four formula units in an orthorhombic structure of the space group Pbnm.[17,18] The unit cell dimensions are a =4.76 Å, b =10.22 Å and c =5.99 Å.

Early spectroscopic work on chromium-doped forsterite was based on the assumption that only trivalent chromium (Cr^{3+}) substitutes for the octahedrally coordinated Mg^{2+} ions in Mg_2SiO_4. Later work indicated that tetravalent chromium (Cr^{4+}) substitutes for tetrahedrally coordinated Si^{4+}. Divalent chromium (Cr^{2+}) can substitute for the octahedrally coordinated Mg^{2+} ions.[19] The relative concentration of Cr^{2+}, Cr^{3+} and Cr^{4+} ions in Mg_2SiO_4 depends on the growth atmosphere and annealing of the crystals. By growing the crystal in a reducing atmosphere (less oxygen) the relative concentration of Cr^{4+} ions can be reduced and that of Cr^{3+} increased. By annealing the forsterite crystals in oxygen, it was shown that the concentration of divalent chromium ions decreases and the concentration of tetravalent chromium ions in Si site increases.[19]

The characteristics of the forsterite crystals used in this study are listed in Table 2.2.1. Column 1 numbers the crystals and in parenthesis the source of the crystal is indicated. The forsterite crystals were supplied from the following three crystal growers:

Japan - Mitsui Mining and Smelting Co., Ltd., Japan

Belarus - Dr. Sergey G. Bartoshevich, Republic of Belarus

China - Dr. Pan Peicong of Shangai Institute of Ceramics, Shangai, China

Column 2 indicates the physical dimensions of the laser crystals. Column 3 list the absorption coefficient at 1064 nm (α_{1064nm}), and Column 4 list the figure of merit (FOM). FOM is defined as the absorption coefficient at the pump wavelength (1064 nm) over the absorption coefficient at the lasing wavelength (1250 nm),

$$FOM \equiv \frac{\alpha_{1064nm}}{\alpha_{1250nm}} \qquad (2.2.1)$$

Table 2.2.1. Chromium-doped forsterite crystals used in the mode-locking experiments.

1	2	3	4
Sample Number	Dimensions	α_{1064nm} (cm^{-1})	Figure of Merit
Crystal 1 (Japan)	8x8x10 mm	0.5304	26
Crystal 2 (Japan)	4x4x10 mm	0.7224	39
Crystal 3 (Belarus)	4x4x12 mm	0.6162	47
Crystal 4 (China)	5x5x14.4 mm	1.1610	58

2.2.1. Absorption Spectrum

The absorption spectra of Cr:Mg_2SiO_4 were taken with a Perkin-Elmer Lambda-9 spectrophotometer coupled with a personal computer. Figure 2.2.1 shows the polarized absorption spectrum recorded for E parallel to the three crystallographic axis of Cr:forsterite. The absorption spectrum is characterized by broad absorption bands spanning the near ultraviolet to near infrared spectral regions and depend strongly on the polarization of the incident radiation with respect to the crystallographic axes of the host. In particular, the peak position of the strongest band in the red-green spectral region shifts considerably with the polarization. Smaller shift has been observed in the near infrared region as well.

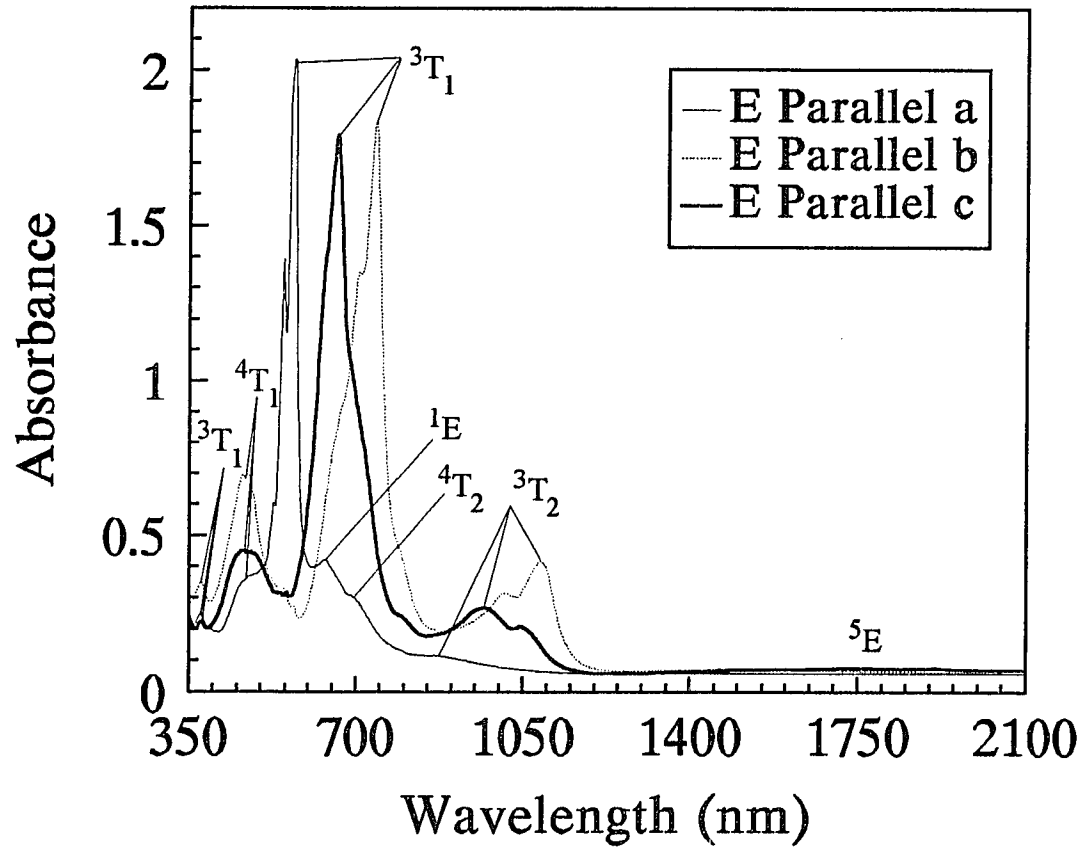

Fig. 2.2.1. Room temperature absorption spectrum of Cr:Mg_2SiO_4 for all three crystal orientations. Absorbance A or optical density OD is defined as $A=\log_{10}(I/I_o)$, where I_o is light intensity incident on the sample and I is the intensity of the transmitted radiation.

The polarization dependence of the absorption spectra had been extensively studied by V. Petričević et al[13] using the Tanabe-Sugano formalism. The absorption due to Cr^{3+} and Cr^{4+} overlap in the visible and near ultraviolet spectral regions. The Cr^{3+} was taken to occupy octahedrally coordinated sides and Cr^{4+} to be in tetrahedrally coordinated sides. The Tanabe-Sugano diagrams for Cr^{3+} and Cr^{4+}, with transitions indicated are shown in figure 2.2.2. The energy levels for the two ions are summarized in tables 2.2.2 and 2.2.3.[13]

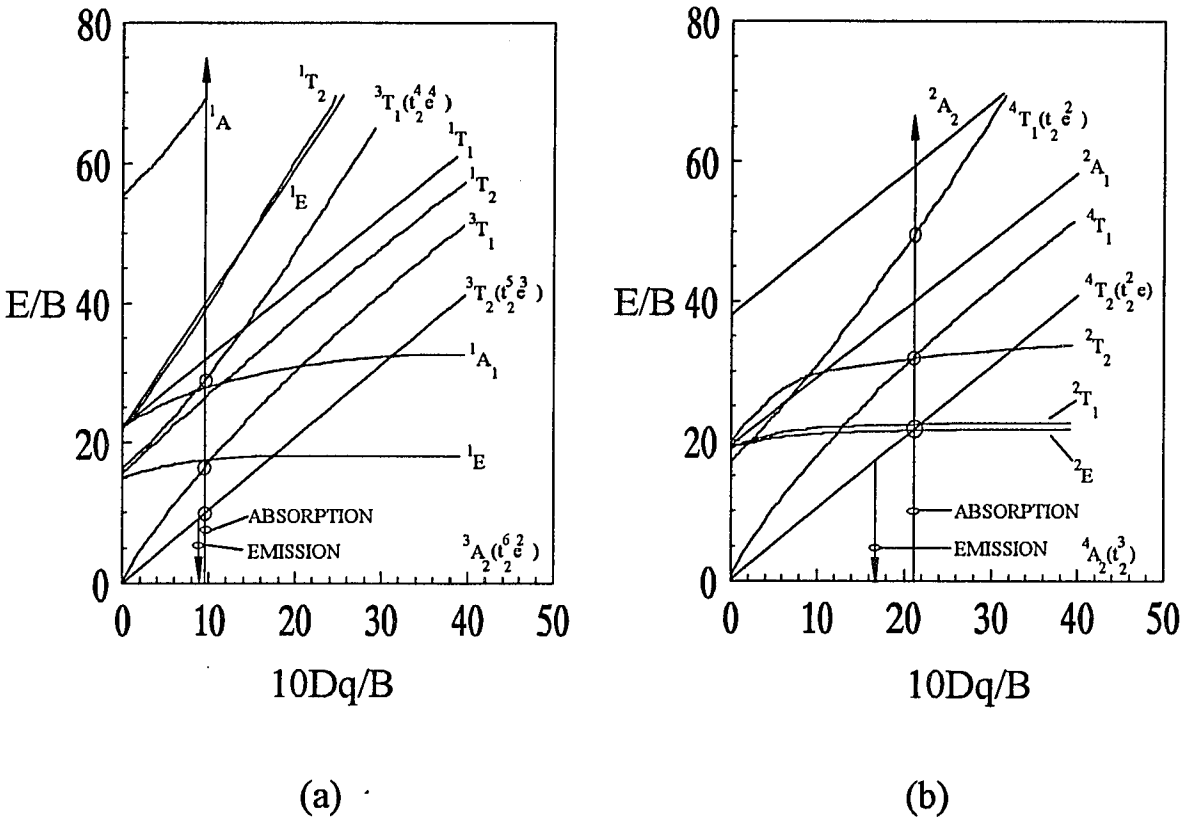

Fig. 2.2.2. Tanabe-Sugano diagram for (a) Cr^{4+} in tetrahedral coordination and (b) Cr^{3+} in octahedral coordination.

Table 2.2.2. Energy Levels of Cr^{4+}:Mg_2SiO_4.

Transition	Energy (cm^{-1})
$^3A_2$ -> $^3T_2$	9150
$^3A_2$ -> $^3T_1$	15430
$^3A_2$ -> ^1E	15875
$^3A_2$ -> $^3T_1$	26810
$^3A_2$ -> $^1T_2$	28735
$^3T_2$ -> $^3A_2$	8750

Table 2.2.3. Energy Levels of Cr^{3+}:Mg_2SiO_4.

Transition	Energy (cm^{-1})
$^4A_2$ -> $^4T_2$	15100
$^4A_2$ -> ^2E	14450
$^4A_2$ -> $^2T_1$	15380
$^4A_2$ -> $^2T_2$	21050
$^4A_2$ -> $^4T_{1a}$	21500
$^4A_2$ -> $^4T_{1b}$	33780
$^4T_2$ -> $^4A_2$	11100
^2E -> $^4A_2$	14437

The study of the Tanabe-Sugano diagram predicted that some absorption bands are due to tetrahedrally coordinated Cr^{4+} and correspond to transitions between the ground level $^3A_2$ and higher lying energy levels $^3T_2$, ^1E, and $^3T_1$. The rest of the absorption features in the visible and near ultraviolet are due to octahedrally coordinated Cr^{3+} and correspond to transitions between the $^4A_2$ and the $^4T_2$ and $^4T_1$ energy levels. The weak absorption band labeled ^5E, center at about 1800 nm was attributed to Cr^{2+} in octahedral coordination.[19]

The quality of the forsterite crystals used during this research was partially evaluated using the absorption properties of the different crystal. The absorption coefficient was evaluated using the following procedure.

a) The polarized transmission for E parallel to the b crystallographic axis was recorded using the Perkin-Elmer Lambda-9 spectrophotometer.

b) The transmission was corrected for the Fresnel losses and then the fraction of the radiation absorbed by the forsterite crystal was estimated by using the relation

$$T_M = 1 - L_F - L_I \tag{2.2.2}$$

where: T_M - measured transmission

L_F - Fresnel losses. Loss due to the forsterite crystal surfaces

L_I - loss due to absorption in the forsterite crystal

The Fresnel losses for an interface can be evaluated using the expressions[20]

$$1 = L + T \tag{2.2.3}$$

$$T = \frac{n_2}{n_1}\left(\frac{2n_1}{n_2 + n_1}\right)^2 \tag{2.2.4}$$

where: T - transmission of interface between air and forsterite crystal surface

L - loss due to interface between air and forsterite crystal surface ($2L = L_F$)

n_2 - index of refraction of forsterite crystal ($n_2 = 1.635$)

n_1 - index of refraction of air

The Fresnel losses of the forsterite crystal are 11.61% for polarization parallel to b axis. Combining eqs. (2.2.2)-(2.2.4) the corrected transmission of the forsterite crystal can be evaluated using

$$T_I = 0.1161 + T_M \tag{2.2.5}$$

c) The transmission is related to the absorption coefficient through the relations

$$T_I = \frac{I}{I_0} \tag{2.2.6}$$

$$I = I_0 e^{-\alpha d} \tag{2.2.7}$$

where: I - transmitted light intensity

I_0 - incident light intensity

α - absorption Coefficient

d - length of the forsterite crystal

By combining equations (2.2.6) and (2.2.7) we get

$$T_I = e^{-\alpha d} \tag{2.2.8}$$

and by taking the natural logarithm of both sides of the equation (2.2.8) we get

$$\alpha = -\frac{\ln(T_I)}{d} \tag{2.2.9}$$

Figure 2.2.3 (a) and (b) show the absorption coefficient (α) of the Cr:forsterite crystals used in the mode-locking experiments as a function of wavelength. In figure 2.2.3 (a) α is graphed using linear axis while in figure 2.2.3 (b) logarithmic axis is used to emphasize the absorption band in the 1200-1500 nm region.

Crystal 1 has the smallest α compared with the other crystals and it was used in the first mode locking experiments. The shortest pulses generated using crystal 1 had FWHM of 31 ps. When crystal 2 that has a higher α at 1064 nm replaced crystal 1 the FWHM of the output pulses was reduced to 6 ps. Crystal 2 was the first crystal to demonstrate self-mode-locked mode of operation when chirp compensation was included in the cavity, generating 90-fs pulses. Crystal 3 has a smaller α at 1064 nm as compared with crystal 2 but less absorption at 1250 nm yielding a higher FOM. When crystal 3 replaced crystal 2 in the laser cavity comparable pulse widths were generated but the stability of the self mode-locked forsterite laser was improved. Pulses with FWHM of 50 fs were generated using crystal 3 but this was the result of improved phase compensation

in the cavity. The best results were obtained using crystal 4 that has the highest α at 1064 nm and the highest FOM. The shortest pulses measured using crystal 4 were 36 fs long.

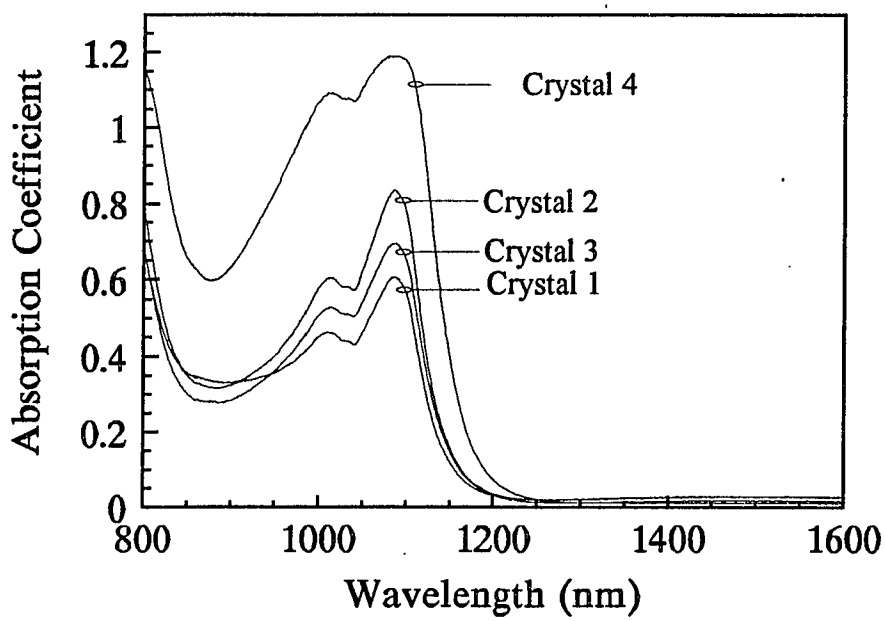

(a)

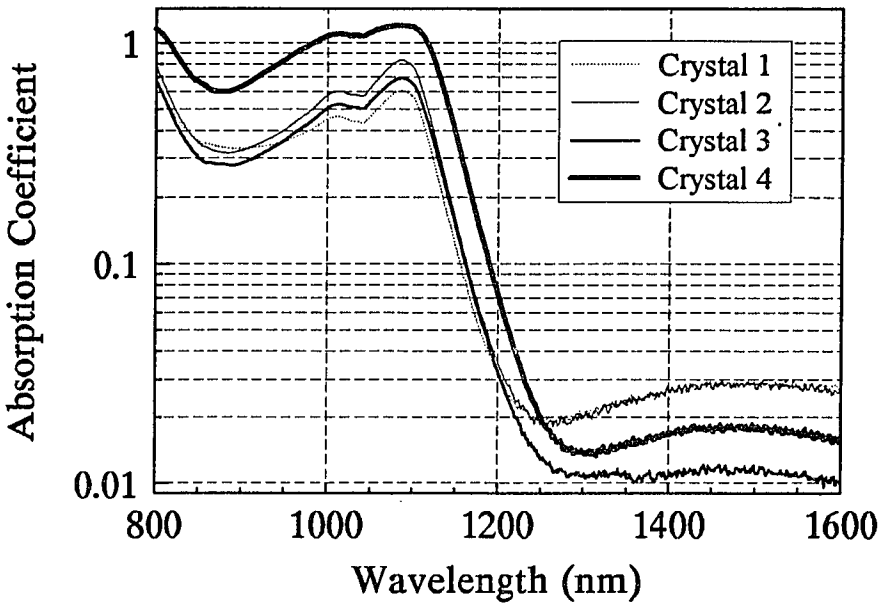

(b)

Fig. 2.2.3. Absorption coefficient of the Cr:forsterite crystals used in mode-locking experiments.

2.2.2. Emission Spectrum

The fluorescence spectra was measured by exciting the Cr:forsterite crystals by a chopped 670-nm excitation from a diode laser. The experimental arrangement for the fluorescence experiment is shown in figure 2.2.4. Fluorescence was detected by a Hamamatsu P394A uncooled PbS detector coupled to a 0.25-m SPEX monochromator and Stanford Research lock-in amplifier (SR530) controlled by a personal computer. The PbS detector was placed at the exit slit of the SPEX Minimate 0.25-m monochromator equipped with a 1000-nm blazed grating. Chopped 1064-nm radiation from a cw Nd:YAG laser was also used to selectively excite only the Cr^{4+} ions.

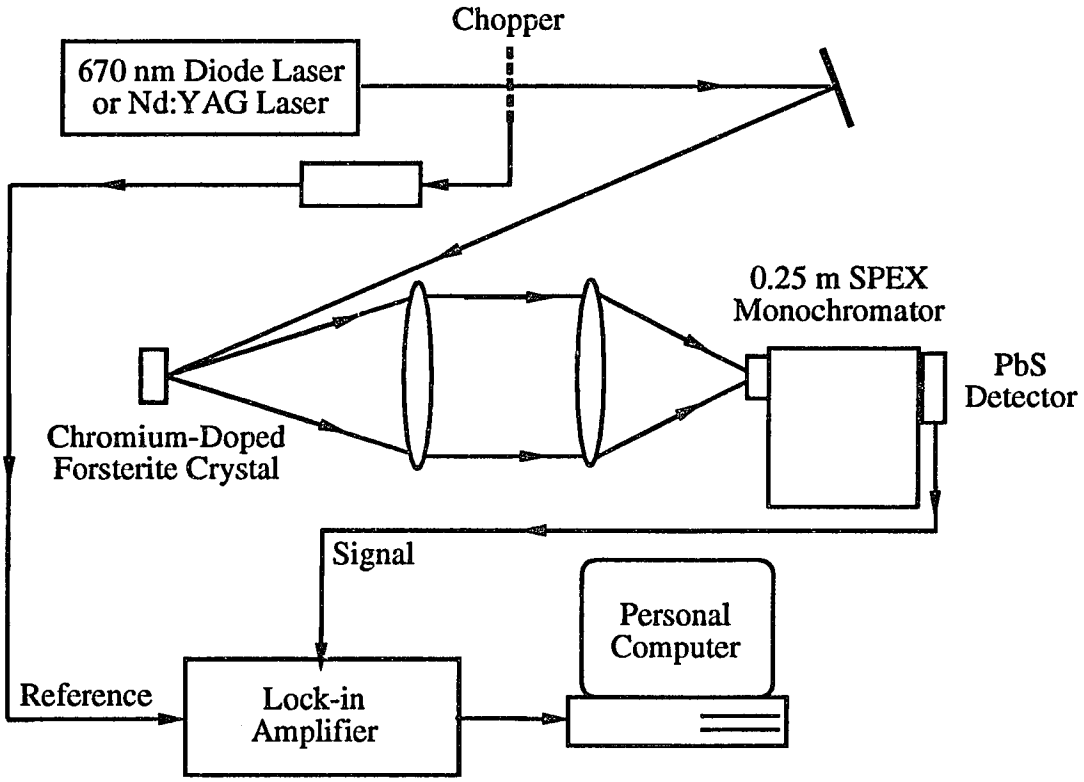

Fig. 2.2.4. Experimental setup for measurement of the fluorescence spectrum of Cr:forsterite.

The normalized fluorescence spectra at room temperature corresponding to the four Cr:forsterite crystals used in this study are shown in figures 2.2.5 -2.2.8 The

radiation from the diode laser was circularly polarized and the Cr:forsterite crystals were arranged so that the radiation was parallel to the b and c crystallographic axes. The emission spectra is characterized by two broad emission bands one due to Cr^{4+} and the other to Cr^{3+}. The emission band centered at 900 nm corresponds to Cr^{3+} ions and is due to the $^4T_2 \rightarrow {}^4A_2$ transition. The other emission band centered at 1150 nm corresponds to Cr^{4+} ions and is due to the $^3T_2 \rightarrow {}^3A_2$ transition which is the laser transition. The recorded emission spectra provide useful information of the relative concentrations of Cr^{3+} and Cr^{4+} and confirm arguments made earlier regarding the quality of the laser crystals used in the mode-locking experiments.

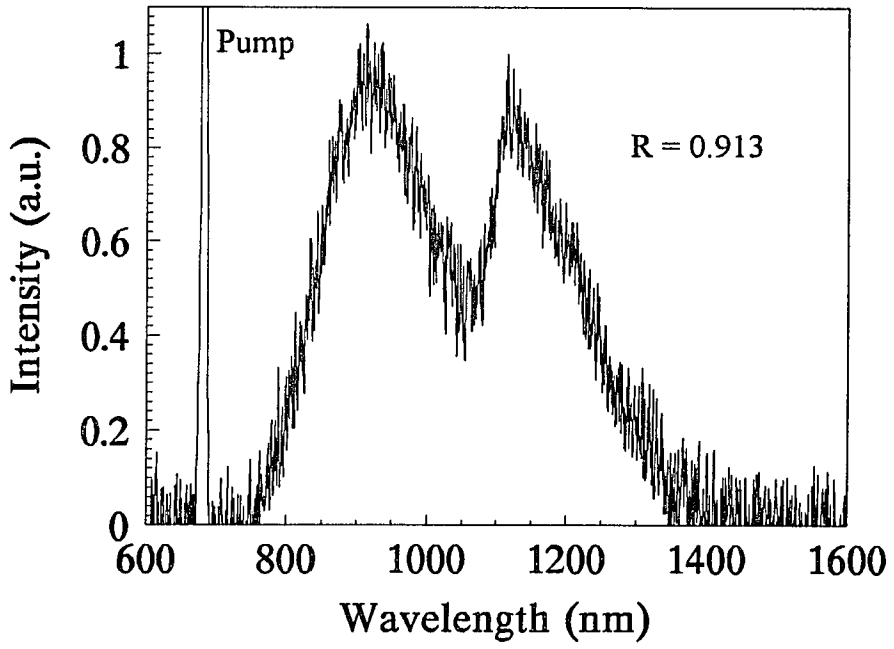

Fig. 2.2.5. Room temperature emission spectrum of Crystal 1 when excited with 670 nm radiation from a diode laser.

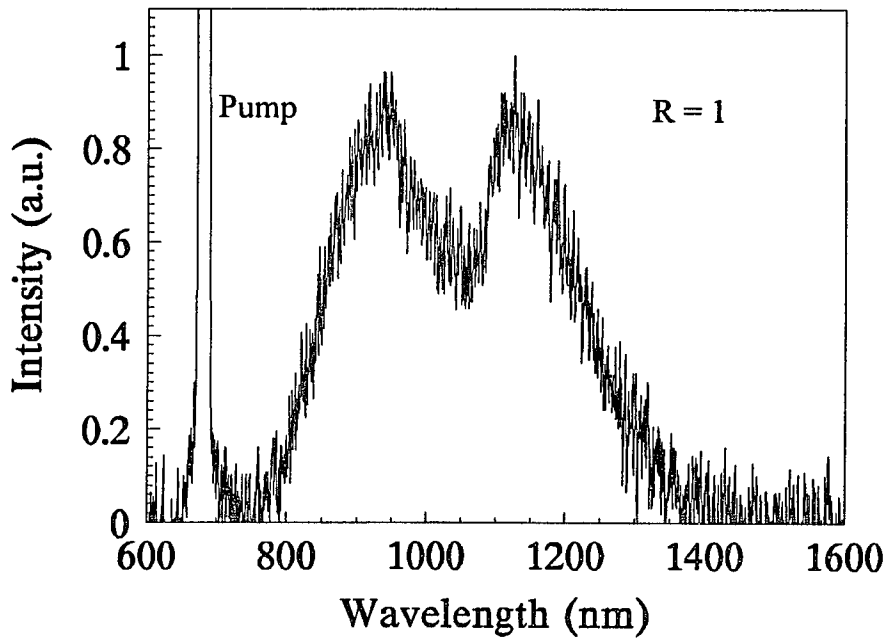

Fig. 2.2.6. Room temperature emission spectrum of Crystal 2 when excited with 670 nm radiation from a diode laser.

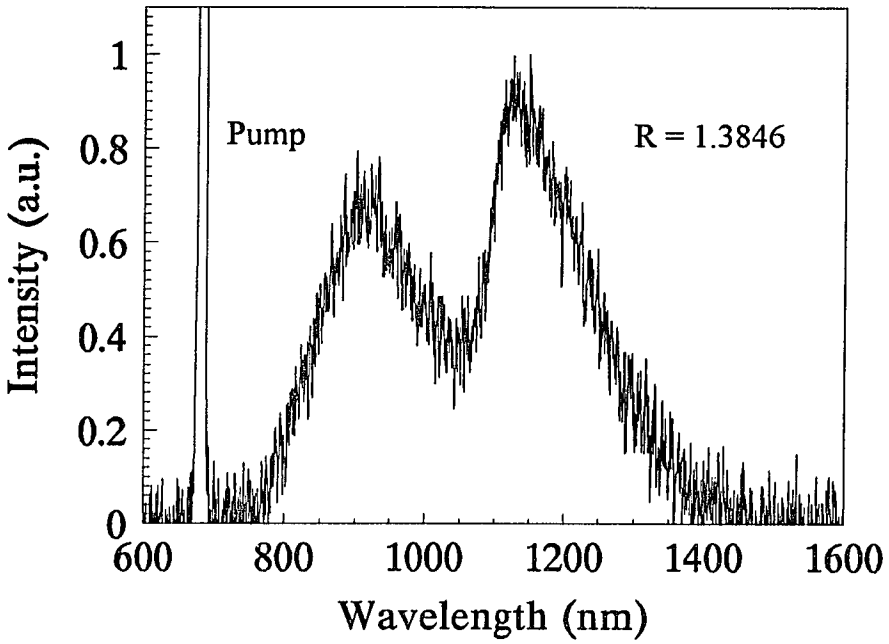

Fig. 2.2.7. Room temperature emission spectrum of Crystal 3 when excited with 670 nm radiation from a diode laser.

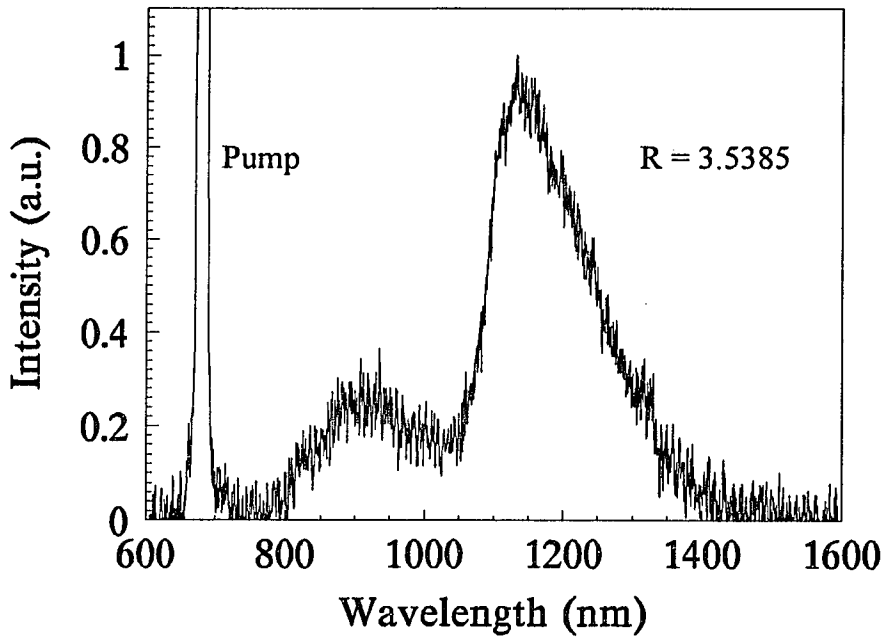

Fig. 2.2.8. Room temperature emission spectrum of Crystal 4 when excited with 670 nm radiation from a diode laser.

The emission spectrum measurements can be used to compliment absorption measurements and provide a better criterion for judging the quality of the laser crystals. We can form a ratio (R) of the maximum of the emission band centered at 1150 nm over the maximum of the emission band centered at 900 nm. This value can be used to get information on the relative concentration of Cr^{3+} and Cr^{4+} ion.

$$R \equiv \frac{I_{1150nm}}{I_{900nm}} \qquad (2.2.10)$$

This ratio will be bigger for crystals with higher concentration Cr^{4+} which is the ion responsible for laser action in forsterite and indicate that unwanted losses due to Cr^{3+} are

minimized. The results obtained so far for the quality of the Cr:forsterite crystals are summarized in table 2.2.2. Column 1 lists the number of the crystal, and Column 2 shows the absorption coefficient. Columns 3 and 4 list the figure of merit as defined by eq. 2.2.1 and the ratio R as defined by eq. 2.2.10, respectively.

Table 2.2.4. Absorption coefficient, FOM and ration R of Cr:forsterite crystals used in the mode-locking experiments.

Sample Number	α_{1064nm} (cm^{-1})	FOM	R
Crystal 1	0.5304	26	0.913
Crystal 2	0.7224	39	1
Crystal 3	0.6162	47	1.3846
Crystal 4	1.1610	58	3.5385

It is obvious by inspecting table 2.2.2 that the overall quality of the Cr:forsterite crystals is steadily improving. As it will be shown later in this thesis each time a new crystal was used with mode-locking the duration of the output pulses was reduced. It is worth mentioning that it took only five years from the first lasing experiments in 1987, to the generation of 36-fs pulses which is very close to the limit that the forsterite laser can generate (20 fs) if all emission spectrum is used. The fast development of the Cr:forsterite marks a new era lasers of rapid development and also indicates the potentials of tunable solid state lasers as reliable sources of coherent radiation.

The emission spectrum of Cr:forsterite due only to Cr^{4+} ions can be measured when 1064 nm radiation is used as the excitation source. Figure 2.2.9 shows the emission spectrum of Cr:forsterite when it was excited with 1064 nm radiation.

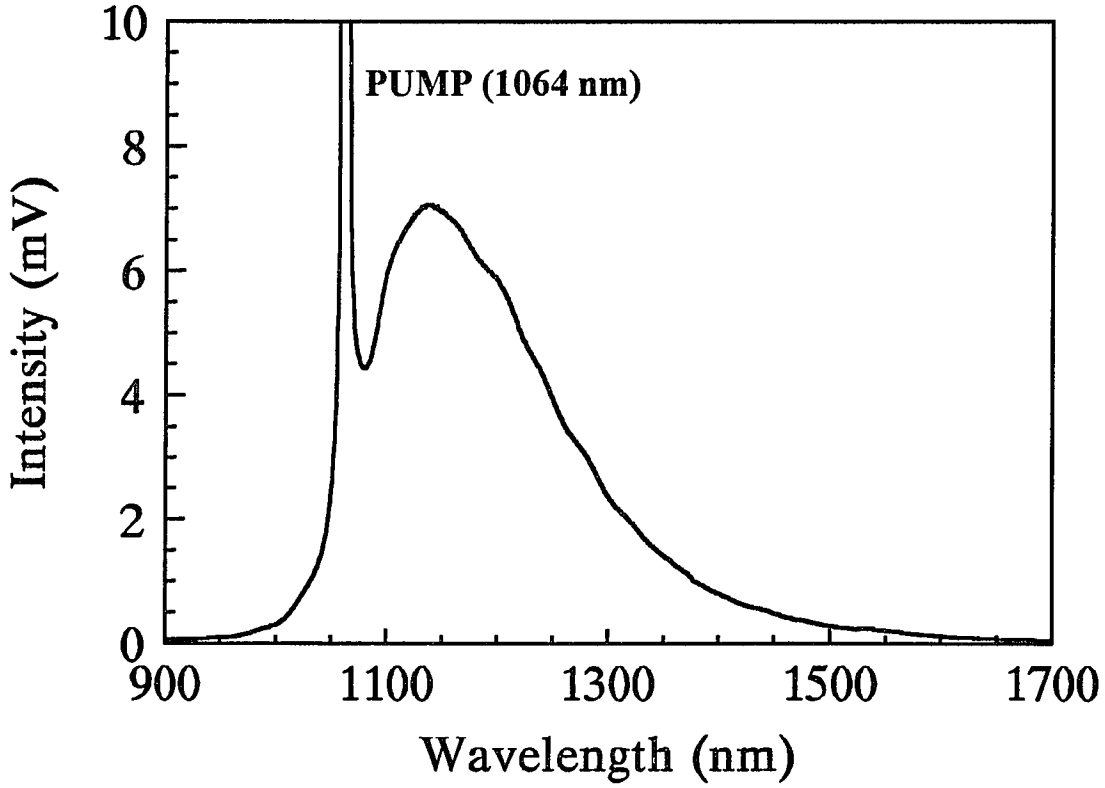

Fig. 2.2.9. Room temperature emission spectrum of Cr:Mg_2SiO_4 when excited with 1064 nm radiation from a Nd:YAG laser.

2.2.3. Simplified Energy Level

The analysis of the absorption and fluorescence spectra of chromium-doped forsterite provided conclusive evidence that the lasing ion is Cr^{4+}. The absorption in the near infrared spectral region between 850 and 1150 nm is due to transitions between the ground state and the first excited state $^3T_2$ of the Cr^{4+} ion. A simplified energy level diagram of the Cr^{4+} ion in forsterite is shown in figure 2.2.10.

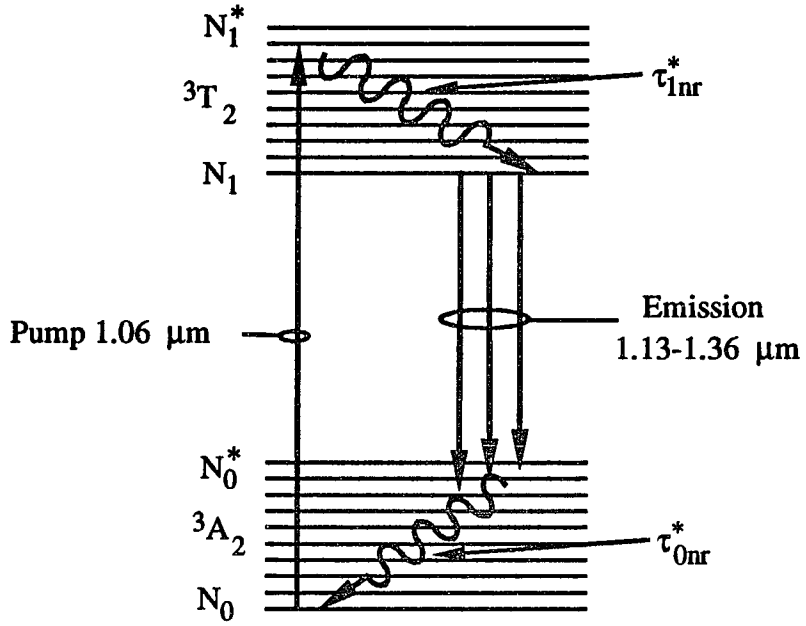

Fig. 2.2.10. Simplified energy level diagram of Cr^{4+}:Mg_2SiO_4 .

When the forsterite laser is pumped by 1064 nm radiation excited ions move from the lower lying vibrational levels of $^3A_2$ to the higher lying vibrational levels of $^3T_2$. The excited ions nonradiatively decay from the higher lying vibrational levels to the lower lying vibrational levels of $^3T_2$. The four level vibronic laser operation of Cr-doped forsterite feeds on $^3T_2$-->$^3A_2$ transition. Finally the excited ions nonradiatively decay to the lower lying vibrational levels of $^3A_2$.

Summarizing chromium-doped forsterite laser has emerged as an important tunable solid state laser in the near infrared. It is the first laser where Cr^{4+} was positively identified as the lasing ion and the only tunable solid state laser that covers the wavelength region from 1130-1367 nm. The quality of the laser crystal has been greatly improved making it a very reliable source of tunable radiation in the near infrared. The most important spectroscopic and laser properties of chromium-doped forsterite as compared with Nd:YAG laser are summarized in Table 2.2.5.

Table 2.2.5. Basic spectroscopic and laser properties of Cr:forsterite and Nd:YAG lasers.

Property	Nd:YAG	Cr:forsterite
Chemical Formula	$Nd^{3+}:Y_3Al_2O_{12}$	$Cr^{4+}:Mg_2SiO_4$
Lasing Ion	Nd^{3+} in D_2	Tetrahedral Cr^{4+}
Emission Band	1064 nm	1100 -1400 nm
Spontaneous Lifetime	230 μs	2.7 μs
Radiative Lifetime	550 μs	25 μs
Tuning Range	1064 nm	1130-1367 nm
Surface Damage	>3 GW	> 0.4 GW
Scattering Loss	0.002 cm^{-1}	0.02 cm^{-1}
Slope Efficiency		23% (Pulsed), 38% (CW)
Limiting Slope Efficiency		65% (CW)
Stimulated Emission Cross Section	$6.5x10^{-19}$ cm^2	$2x10^{-19}$ cm^2
Thermal Expansion Coefficient	0.13 (@ 300K)	0.08 (@ 300K)
Moh's Hardness	8.5	7

2.3. References

1. V. Petričević, S. K. Gayen, R. R. Alfano, K. Yamagishi, H. Anzai, and Y. Yamaguchi, "Laser action in chromium-doped forsterite", Appl. Phys. Lett. **52**, 1040 (1988).

2. V. Petričević, S. K. Gayen, and R. R. Alfano, "Laser action in Cr-activated forsterite for near infrared excitation: Is Cr4+ the lasing ion?", Appl. Phys. Lett. **53**, 2590 (1988).

3. V. Petričević, S. K. Gayen, and R. R. Alfano, "Continuous-wave operation of chromium-doped forsterite", Optics Letters, Vol. **14**, 612 (1989).

4. V. Petričević, S. K. Gayen, and R. R. Alfano, "Near infrared tunable operation of chromium doped forsterite laser", Appl. Opt. **28**, 1609 (1989).

5. V. G. Barishevskii, M. V. Korzhik, A. E. Kimaev, M. G. Livshitz, V. B. Pavlenko, M. L. Meilman, and B. I. Minkov, Zh. Prikl. Spectrosk. (Moscow) **53**, 7 (1990).

6. A. Sugimoto, Y. Segawa, Y. Yamaguchi, Y. Nobe, K. Yamagishi, P. H. Kim, and S. Namba, Japanese J. Appl. Physics, Vol. **28**, 1833, (1989).

7. V. G. Baryshevskii, V. A. Voloshin, S. A. Demidovich, A. E. Kimaev, M. V. Korzhik, M. G. Livshitz, M. L. Meil'man, B. I. Minkov, and A. P. Shkadarevich, Quantovaya Electron. (Moscow) **17**, 1389 (1990).

8. V. Petričević, A. Seas, and R. R. Alfano, "Slope efficiency measurements of a chromium-doped forsterite laser", Optics Letters, Vol. **16**, 811 (1991).

9. A. Seas, V. Petričević, and R. R. Alfano, "Continuous-wave mode-locked operation of a chromium-doped forsterite laser", Optics Letters, Vol. **16**, 1668 (1991).

10. A. Seas, V. Petričević, and R. R. Alfano, " Generation of sub-100-fs pulses from a cw mode-locked chromium-doped forsterite laser", Optics Letters, Vol. **17**, 937 (1992).

11. A. Sennaroglu, T. J. Carrig, and C. R. Pollock, "Femtosecond pulse generation by using additive-pulse mode-locked chromium-doped forsterite laser operated at 77K", Optics Letters, Vol. **17**, 1216 (1992).

12. A. Seas, V. Petričević,, R. R. Alfano, "Self-Mode-Locked Chromium-Doped Forsterite Laser Generates 50-fs Pulses", Optics Letters, Vol. **18**, pp. 891 (1993).

13. V. Petričević, S. K. Gayen, and R. R. Alfano, "Chromium-activated forsterite laser", in *Tunable Solid-State Lasers*, Vol. 5 of the OSA Proceeding Series, M. L. Shand and H. P. Jenssen, eds. (Opt. Society of America, Washington, D.C., 1989), pp. 77-84.

14. N. Nishide, Y. Segawa, P. H. Kim, S. Namba, and A. Masuyama, Reza Kagaku Kenkyu **7**, 89 (1985).

15. H. Rager and G. Weiser, Bull. Mineral. **104**, 603 (1981).

16. H. R. Verdun, L. M. Thomas, D. M. Andrauskas, T. McCollum, and A. Pinto, "Chromium-doped forsterite laser pumped by 1.06 μm radiation", Appl. Phys. Lett. **53**, 2593 (1988).

17. J. R. Smith and R. M. Hazen, Am. Mineral. **58**, 588(1973).

18. V. Devarajan and E. Funck, J. Chem. Phys. **62**, 3406 (1975).

19. Y. Yamaguchi, K. Yamagishi, A. Sugimoto, and Y. Nobe, "Optical properties and crystal growth atmosphere of forsterite", in *Advanced Solid-State Lasers*, Vol. **10** of the OSA Proceeding Series, G. Dube and L. Chase, eds. (Optical Society of America, Washington, D.C., 1991), pp. 52-56.

20. Jerry B. Marion and Mark A. Heald, "Classical Electromagnetic Radiation" , Academic Press Inc., Second Edition, pp. 162 (1980).

CHAPTER 3

GENERATION AND MEASUREMENT OF SHORT PULSES

3.1. Introduction

Ultrashort optical pulses became an extremely useful tool in almost every research laboratory in the world.[1] Time resolved techniques make use of ultrashort pulses and the physical processes of absorption, fluorescence and light scattering to measure ultrafast processes such as[2,3,4]

- Energy transfer in chemistry, biology and solids
- Primary events in biology
- Charge transfer reactions
- Rotational and vibrational relaxations
- Structural rearrangements of molecules
- High speed electronic measurements
- Characterization of semiconductor and electro-optical devices
- Optical communication
- Optical computation
- Medical processes, and
- Imaging through tissues.[5,6]

This chapter presents a brief review of mode-locking and the methods for measurements of ultrashort pulses. Section 3.2 briefly reviews the concept of modes in a

laser resonator. Next section 3.3 analyzes the basics of mode-locking and the different methods employed in the generation of ultrashort pulses from Cr:forsterite laser. In section 3.4 the method of measuring short pulses with an autocorrelator is reviewed and the design of an autocorrelator suitable for the near infrared is presented along with second harmonic generation calculations.

3.2. Modes in a Laser Resonator

The simplest form of a laser resonator consist of two mirrors and a gain medium (See figure 3.2.1). The two mirrors and the laser medium are arranged in such a way to force radiation to circulate inside the resonator. Laser oscillation occurs over the frequency band that the gain of the laser medium is higher than the losses. A field distribution circulating in the resonator reproducing itself after every round trip is termed as a mode of oscillation. Two types of modes can be identified in a laser cavity, the transverse and longitudinal modes. Transverse modes, as the name indicates, are different from each other in that their field distribution perpendicular to the resonator axis is different. The longitudinal modes differ from each other with respect to their distribution along the axis of the resonator. In general the modes in the resonator are called TEM_{qmn} modes, where q is the longitudinal mode order number and m and n are the transverse mode order number.

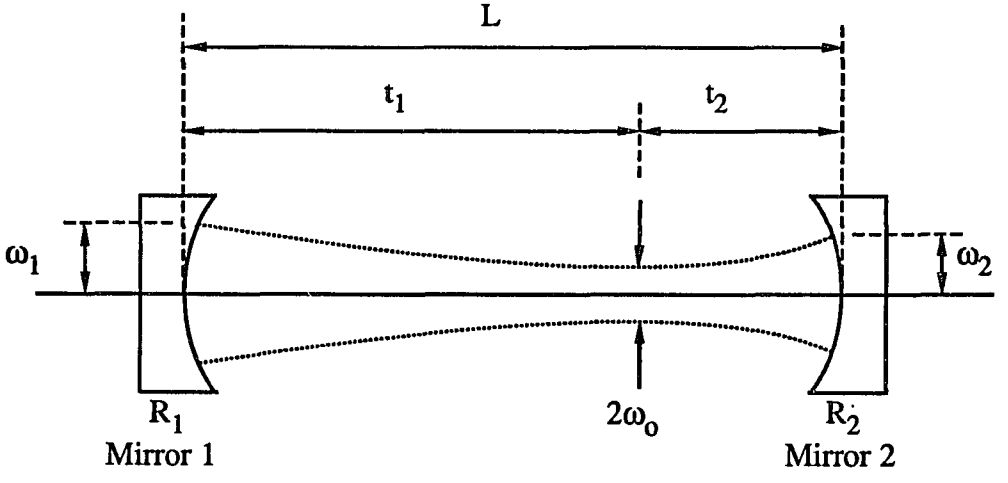

Fig. 3.2.1. Simple two mirror laser cavity.

If rectangular symmetry is assumed then the crossectional distribution E(x,y) of the transverse modes is given by the expression[7]

$$E(x,y) = E_{m,n}\left[H_m\left(\frac{\sqrt{2}x}{\omega}\right)H_n\left(\frac{\sqrt{2}y}{\omega}\right)\right]e^{-\frac{x^2+y^2}{\omega^2}} \qquad (3.2.1)$$

where x an y ate the transverse coordinates, $E_{m,n}$ is a constant amplitude factor whose value depends on the field strength of the mode, ω is the radius of the fundamental mode (m=0, n=0) at 1/e maximum amplitude , $H_a(b)$ is the ath order Hermite polynomial, and m and n are the transverse mode numbers. Figure 3.2.2 shows the x-variation of the field distribution and intensity distribution of some transverse modes. It can be seen that higher order transverse modes have their energy distribution spread along the transverse plane which allows easy control of the transverse modes by placing an aperture inside the laser resonator.

The longitudinal modes (or axial modes) are characterized by the same spatial energy distribution in the transverse plane but have different axial distributions. For a given laser resonator the allowed longitudinal modes are determined by the condition that the waves in the cavity form a standing wave-pattern. The resonant frequency for a given longitudinal mode in a two mirror laser resonator is determine by the expression[8]

$$\nu_{m,n,q} = \frac{c}{2Ln}\left[(q+1)+\frac{1+m+n}{\pi}\cos^{-1}\sqrt{\left(1-\frac{L}{R_1}\right)\left(1-\frac{L}{R_2}\right)}\right] \qquad (3.2.2)$$

where: q+1 - number of half wavelengths of light across the resonator axis (q is the number of nodes of the standing light wave pattern),

m, n - transverse mode order numbers,

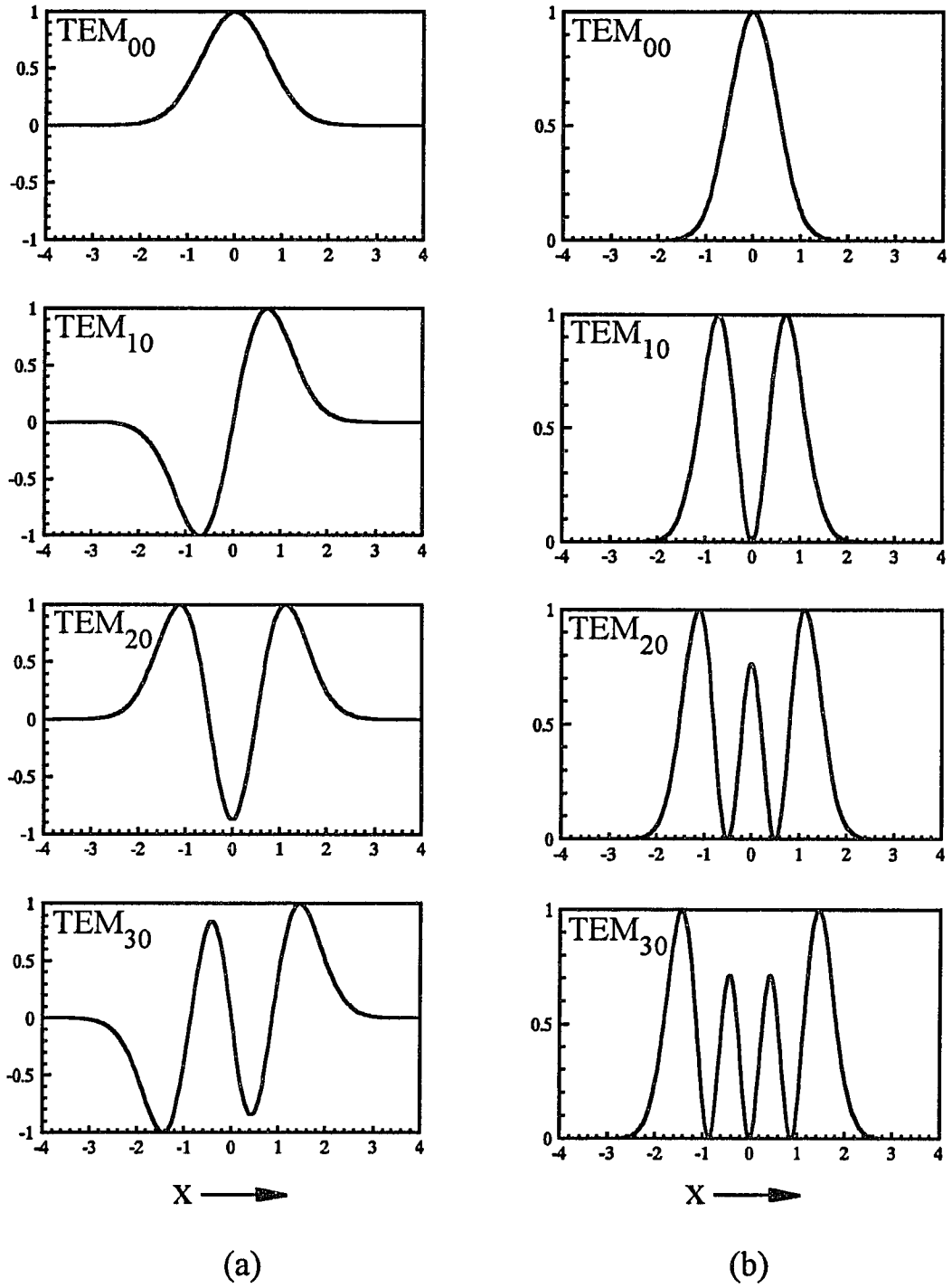

Fig. 3.2.2. Field distribution (a) and intensity distribution (b) of some low order TEM_{m0} transverse modes.

R_1, R_2 - radii of curvature of the mirrors forming the laser resonator,

c - speed of light,

L - optical length of the laser resonator,

n - the refractive index of the medium occupying the resonator.

Each transverse mode consist of regularly spaced longitudinal modes separated in frequency by c/2L. If we assume that the laser operates in a single transverse mode then the second term in the brackets of eq. 3.2.2 is a constant phase term and the frequency of the longitudinal modes can be written as

$$\nu_q = \frac{qc}{2Ln} \quad \text{or} \quad \omega_q = \frac{q\pi c}{Ln} \tag{3.2.3}$$

The difference in frequency between adjacent longitudinal modes can be estimated as

$$\Delta\omega' = \omega_{q+1} - \omega_q = \frac{\pi c}{nL} \tag{3.2.4}$$

In any real laser the number of modes which can oscillate is limited by the bandwidth $\Delta\omega$ over which the laser gain exceeds the losses. The total number of oscillating longitudinal modes, m, can be estimated by dividing $\Delta\omega$ by $\Delta\omega'$.

$$m = \frac{\Delta\omega}{\Delta\omega'} = \frac{\Delta\omega Ln}{\pi c} \tag{3.2.5}$$

Consider a 180 cm long forsterite laser cavity lasing with a bandwidth of 1 nm, centered at 1250 nm. By considering eq. 3.2.5 there should be ~ $2x10^4$ oscillating longitudinal modes in the cavity. A simplified model for the longitudinal modes in a real laser is illustrated in figure 3.2.3.

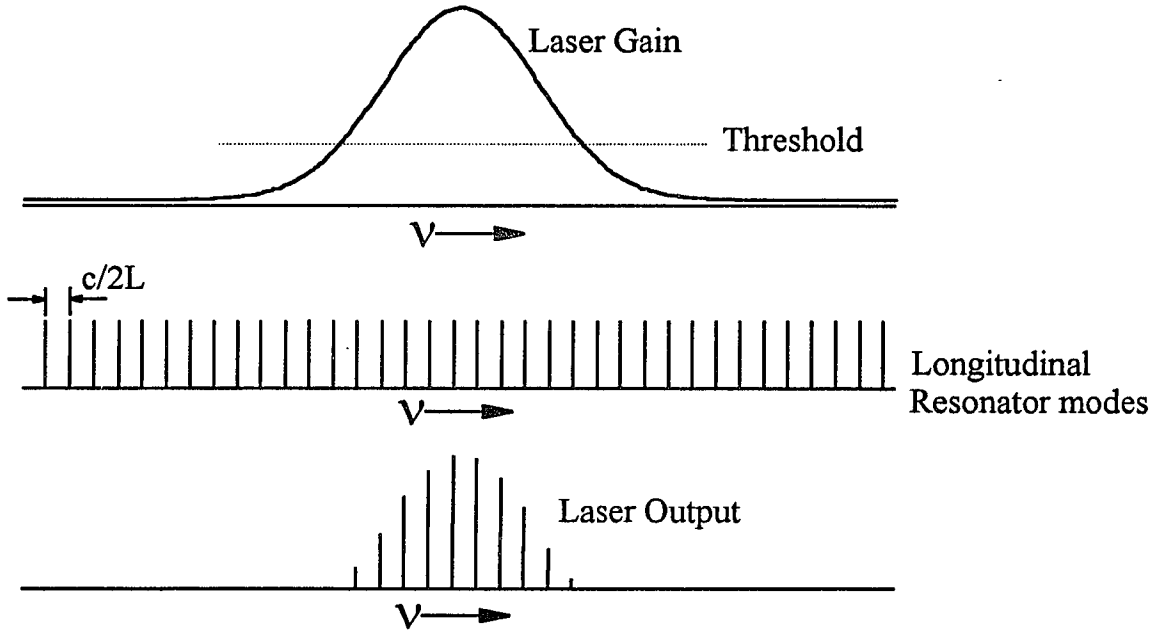

Fig. 3.2.3. Allowed longitudinal modes in a laser cavity with gain medium.

3.3. Mode-Locking: Basic Concept

Mode-locking was first demonstrated in the mid-sixties[9,10,11]. Since then it has been achieved for almost all kinds of lasers. The electromagnetic radiation field in a laser that is not mode locked consists of the sum of individual fields or modes oscillating with random phases and the output has a noise like fluctuating wave form. When the phase difference between the individual modes is fixed then the output becomes a well defined single pulse. The process of fixing the frequency and phase of the oscillating modes is defined as "mode-locking". The output of the mode-locked laser becomes a well defined periodic function of time and consists of a train of regularly spaced pulses,

characterized by high peak power since the laser energy is now concentrated in the single pulse.

The process of mode locking can be understood by considering a simplified model. Assume that there are m excited longitudinal modes in a laser cavity. The electric field of the radiation inside the cavity can be written as

$$E(t) = \sum_{m} E_m e^{i[(\omega_o + m\omega)t + \phi_m]} \tag{3.3.1}$$

where: ϕ_m - phase of the mth longitudinal mode,

E_m - amplitude of the mth longitudinal mode,

ω_o - reference frequency.

Note that the function E(t) is a periodic function with period

$$T = \frac{2\pi}{\omega} = \frac{2L}{c} \tag{3.3.2}$$

which is equivalent to the round trip transit time of the resonator. L is the length of the resonator. The phase ϕ_m varies randomly from mode to mode resulting in fluctuations in the intensity of the laser output. One way to get rid of the fluctuations is to make the laser cavity very short such that only one longitudinal mode can oscillate or somehow to force all the longitudinal modes to maintain a fixed phase. The process of fixing the phase is called mode locking. Assume that all the modes have the same amplitude $E_m = 1$ and that the phase ϕ_m=0. The electric field then is given by

$$E(t) = \sum_{k=-\frac{m-1}{2}}^{\frac{m-1}{2}} \exp\left[i(\omega_o + k\omega)t\right] \tag{3.3.3}$$

which by performing the summation yields

$$E(t) = e^{i\omega_o t} \frac{\sin\left(\frac{m\omega t}{2}\right)}{\sin\left(\frac{\omega t}{2}\right)} \tag{3.3.4}$$

The intensity is proportional to

$$I(t) = E(t)E^*(t) \propto \frac{\sin^2\left(\frac{m\omega t}{2}\right)}{\sin^2\left(\frac{\omega t}{2}\right)} \tag{3.3.5}$$

The intensity profile of the function I(t) is plotted in figure 3.3.1 for different number of modes. As it can be seen in the figure by increasing the number m corresponding to the longitudinal modes the intensity I(t) assumes a form corresponding to a train of pulses separated by a time interval T.

Some of the characteristics of the mode-locked laser output are the following:

1. The power is emitted in the form of a train of pulses. The period of the pulses is given by

$$T = \frac{2\pi}{\omega} = \frac{2L}{c} \tag{3.3.6}$$

2. The peak power is equal to m times the average power (m, number of locked modes).

3. The peak field amplitude is equal to m times the amplitude of a single mode.

4. The individual pulse width, defined as the time from the peak to the first zero is

$$\tau_0 = \frac{T}{m} \tag{3.3.7}$$

Substituting equation 3.2.5 for the number of oscillating modes m, and eq. 3.3.2 for the period T we get

$$\tau_o \sim \frac{2\pi}{\Delta\omega} = \frac{1}{\Delta\nu} \tag{3.3.8}$$

or in words the pulse width is approximately equal to the inverse of the linewidth.

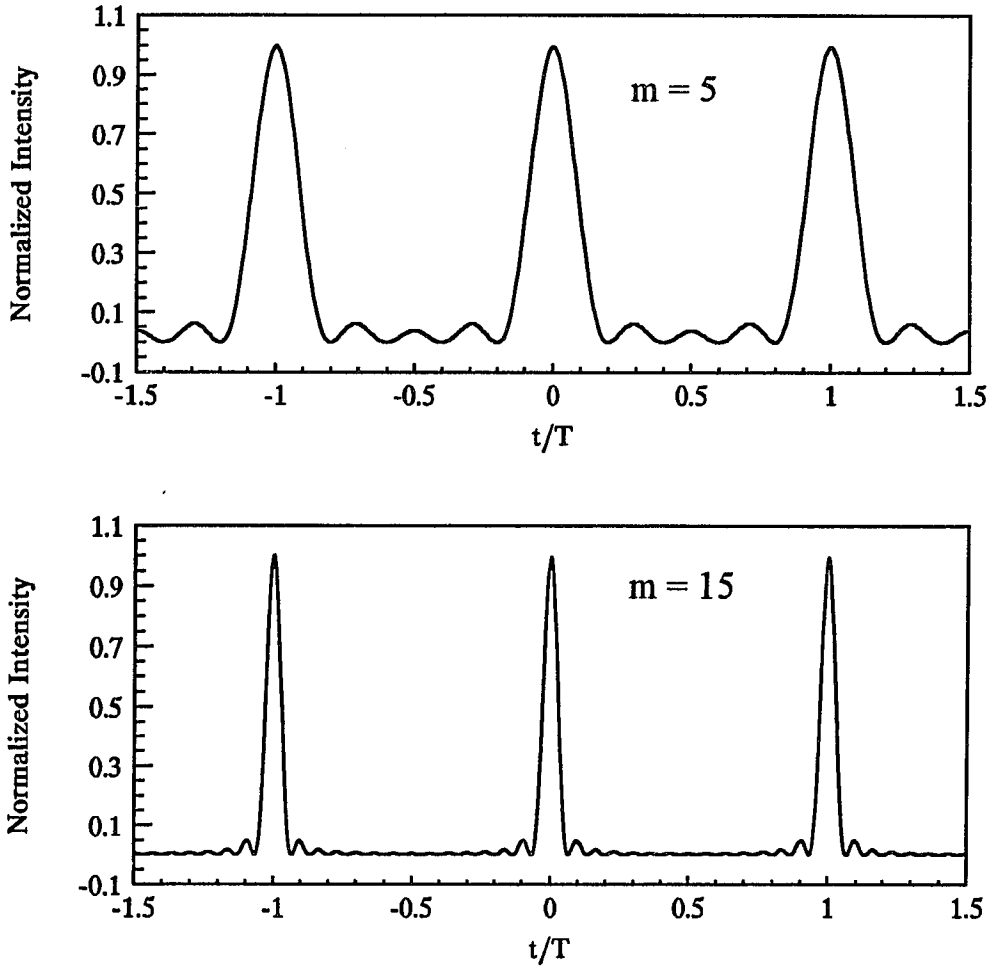

Fig. 3.3.1. Intensity profile of a) 5 locked longitudinal modes, b) 15 locked longitudinal modes.

Mode-locking can be achieved by employing one or a combination of different methods. Some of the most commonly used methods for mode-locking are:

- Active mode-locking
- Passive mode-locking
- Synchronously pumped mode-locking
- Self-mode-locking

3.3.1. Active Mode-Locking

The first experiments of active mode-locking were performed in 1965 using a He-Ne laser. Active mode-locking is the most commonly used techniques for mode-locking solid state lasers. Active mode-locking is achieved by placing a device inside the laser cavity. This device periodically modulates the losses in the cavity and it is externally driven and it is independent of the radiation inside the cavity. When the period of the loss modulation is exactly equal to the round-trip period of the cavity it results in active mode locking. Note that the field that passes through the modulator at the time of minimum loss does so at every round trip through the cavity and it is allowed to grow in intensity, while the field that passes through the modulator at the time of maximum loss dies.

Consider that the central longitudinal mode is amplitude modulated at a frequency ω_{mod}. The electric field of this mode can be written as

$$E(t) = E_o\left[1+\beta\cos(\omega_{mod})\right]e^{i(\omega_o t+\phi_o)} \qquad (3.3.9)$$

where b is the modulation depth and satisfies the condition $0 < \beta \leq 1$. Expression 3.3.9 can be rewritten as

$$E(t) = E_o e^{i(\omega_o t+\phi_o)} + \frac{\beta E_o}{2} e^{i[(\omega_o+\omega_{mod})t+\phi_o]} + \frac{\beta E_o}{2} e^{i[(\omega_o-\omega_{mod})t+\phi_o]} \quad (3.3.10)$$

where the following property of cosine was used

$$\cos(\omega_{mod}t) = \frac{e^{i\omega_{mod}t} + e^{-i\omega_{mod}t}}{2}$$

By inspection of eq. 3.3.10 it can be seen that the amplitude modulation resulted in the conversion of the frequency of the central mode ω_o into three mode locked modes with frequencies ω_o, $\omega_o + \omega_{mod}$, $\omega_o - \omega_{mod}$. If the modulation frequency is chosen to correspond to the difference between adjacent modes then the two new frequencies will coincide with the neighboring modes and the sidebands of the two neighboring modes will overlap with the central frequency. In other words, the modes will be locked with the central mode. If the summation of the electric fields corresponding to all the longitudinal modes is carried out results in a similar picture as the one shown in figure 3.3.1.

Active mode-locking has been studied by many authors[12,13,14] but analytical expressions describing the transient effects occurred during the process of mode-locking are not possible due to the multimode nature of the problem. One of the most widely used theories has been presented by Kuizenga and Siegman[13] who considered the steady state theory of active mode-locking. An outline of the steady-state theory is presented next.

A chirped gaussian optical pulse can be represented by

$$E(t) = \frac{E_o}{2} e^{-\alpha t^2} e^{i\left(\omega_p t+\beta t^2\right)} \quad (3.3.11)$$

where: ω_p - the center frequency of the optical pulse,

$i\beta t$ - linear frequency shift (chirp) during the pulse,

α - the term describing the gaussian envelope.

The full width at half maximum of the pulse is given by

$$\tau_p = \sqrt{\frac{2\ln 2}{\alpha}} \tag{3.3.12}$$

A complex constant γ can be defined as

$$\gamma = \alpha - i\beta \tag{3.3.13}$$

The gaussian pulse can be written as

$$E(t) = \frac{E_o}{2} e^{-\gamma t^2} e^{-i\omega_p t} \tag{3.3.14}$$

The frequency spectrum $E(\omega)$ associated with the pulse $E(t)$ can be evaluated by taking the Fourier transform,

$$E(\omega) = F\{E(t)\} = \frac{E_o}{2}\sqrt{\frac{\pi}{\gamma}} \exp\left[-\frac{(\omega-\omega_p)^2}{4\gamma}\right] \tag{3.3.15}$$

The function for $E(\omega)$ is also a gaussian function. The spectral width (Δf_p) defined as the frequency between half power points is given by

$$\Delta f_p = \frac{1}{\pi}\sqrt{2\ln 2\left(\frac{\alpha^2+\beta^2}{\alpha}\right)}\ \text{Hz} \tag{3.3.16}$$

A pulse can be characterized using the bandwidth-pulsewidth product. For the gaussian pulse it is given by

$$\tau_p \Delta f_p = \left(\frac{2\ln 2}{\pi}\right)\sqrt{1+\left(\frac{\beta}{\alpha}\right)^2} = 0.44\sqrt{1+\left(\frac{\beta}{\alpha}\right)^2} \qquad (3.3.17)$$

If the pulse has no chirp, $\beta = 0$, then the pulsewidth-bandwidth product has a value of 0.440.

Active Mode-Locking: Steady-State theory

In the analysis of active mode locking Kuizenga and Siegman assumed that the resulting mode locked pulse has gaussian profile and they followed the pulse through the resonator for a complete round trip. At the end of the round trip through the cavity they required that the pulse should be self consistent or in other words it should reproduce itself. This enables them to obtain expressions for the pulse width and the bandwidth of the output pulses. An outline of the steady state theory is presented next

Consider the cavity shown in figure 3.3.2. The pulse $E_1(t)$ is a gaussian pulse that enters the active medium which exhibits population inversion. The intensity of the pulse increases and when it comes out of the active medium is given by

$$E_2(t) = E_1(t)\exp\left(\frac{g_a}{2}\right) \qquad (3.3.18)$$

where $g_a(t)$ is the round trip gain coefficient. In the frequency domain $E_2(\omega)$ is given by

$$E_2(\omega) = g_a(\omega)E_1(\omega) \qquad (3.3.19)$$

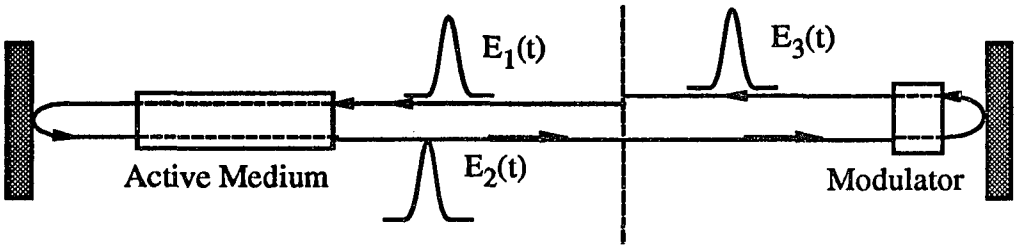

Fig. 3.3.2. Model for steady-state actively mode-locked laser.

If the bandwidth of the pulse is much smaller than the linewidth of the laser then the expression for the function $g_a(\omega)$ is given by

$$g_a(\omega) \cong G\exp\left[-2ig\left(\frac{\omega-\omega_a}{\Delta\omega}\right)-4g\left(\frac{\omega-\omega_a}{\Delta\omega}\right)^2\right] \qquad (3.3.20)$$

where $G = e^g$

g - the saturated gain through the active medium at line center (ω_a) for one round trip in the cavity

Again the line shape is a gaussian function. A gaussian pulse going through an active medium with a gaussian line shape will remain gaussian. Therefore $E_2(\omega)$ is given by

$$E_2(\omega) = \frac{E_o G}{2}\sqrt{\frac{\pi}{\gamma}}\exp\left[-2ig\left(\frac{\omega-\omega_a}{\Delta\omega}\right)-4g\left(\frac{\omega-\omega_a}{\Delta\omega}\right)^2-\frac{(\omega-\omega_p)^2}{4\gamma}\right] \qquad (3.3.21)$$

If we assume that $\omega_p = \omega_a$, i.e. the center frequency of the pulse is the same with the center frequency of the lineshape then $E_2(\omega)$ can be written as

$$E_2(\omega) = \frac{E_o G}{2}\sqrt{\frac{\pi}{\gamma}}\exp\left[-A(\omega-\omega_a)^2 - iB(\omega-\omega_a)\right] \qquad (3.3.22)$$

where $A = \frac{1}{4\gamma} + \frac{4g}{\Delta\omega^2}$

$$B = \frac{2q}{\Delta\omega}$$

Transforming $E_2(\omega)$ in the time domain we get

$$E_2(t) = \frac{E_0 G}{4\sqrt{\gamma A}} \exp\left[-\frac{(t-B)^2}{4A}\right] \exp(i\omega_a t) \qquad (3.3.23)$$

Next the beam goes through the amplitude modulator. The transmission through the active modulator can be written as

$$a(t) = \exp\left(-2\delta_1 \sin^2(\omega_m t)\right) \qquad (3.3.24)$$

where: ω_m - the modulation frequency,

δ_1 - the effective single pass amplitude modulation.

Considering that the pulse duration is much shorter that the modulation frequency ($\omega_m t << 1$) the expression for the transmission becomes

$$a(t) \approx \exp\left(2\delta_1 (\omega_m t)^2\right) \qquad (3.3.25)$$

which also is a gaussian function. If the peak of the pulse goes through the modulator at time t = B then the pulse coming out of the modulator is given by

$$E_3(t) = E_2(t) \exp\left(-2\delta_1 \omega_m^2 (t-B)^2\right) \qquad (3.3.26)$$

The round trip of the pulse around the cavity is completed by including an additional time delay

$$\frac{2L_o}{c}$$

corresponding to the round trip time in the cavity and the losses due to the effective reflectivity of the mirrors (r). The pulse after the complete round trip is given by

$$E_4(t) = rE_3\left(t - \frac{2L_o}{c}\right) \tag{3.3.27}$$

For a self consistent solution it is required that the pulse envelope go through the modulator at the same modulation phase every time or in other words the modulation frequency correspond to the total round trip time of the cavity

$$T_m = \frac{\pi}{\omega_m} \tag{3.3.28}$$

Therefore, for a self consistent solution

$$E_1(t - T_m)e^{-i\phi} = E_4(t) \tag{3.3.29}$$

where ϕ - phase angle included for possible phase shift of the optical signal with respect to the pulse envelope .

By combining eqs. 3.3.11, 3.3.23, 3.3.26, and 3.3.27 the analytical form of eq. 3.3.29 is

$$\frac{E_o}{2}\exp\left[-\gamma(t - T_m)^2\right]\exp\left[-i\omega_a(t - T_m)\right]\exp[-i\phi] = \tag{3.3.30}$$

$$\frac{rE_oG}{4\sqrt{\gamma A}}\exp\left[-\frac{t - B - \left(\frac{2L_o}{c}\right)^2}{4A}\right]\exp\left[-2\delta_1\omega_m^2\left(t - B - \left(\frac{2L_o}{c}\right)^2\right)\right]\exp\left[i\omega_a\left(t - \frac{2L_o}{c}\right)\right]$$

By comparing terms on the left and right hand side of the above equation analytical expressions describing such constants as the modulation frequency, the pulse width and bandwidth can be derived. The expression for γ is given by (g was defined in eq. 3.3.13)

$$\gamma = \frac{2\delta_l\omega_m^2}{2} + \frac{1}{2}\sqrt{\left(2\delta_l\omega_m^2\right)^2 + \frac{2\delta_l\omega_m^2\Delta\omega^2}{4g}} \qquad (3.3.31)$$

Using the condition that $\omega_m << \Delta\omega$ then

$$\frac{\Delta\omega^2}{8g\omega_m^2\delta_l} >> 1 \qquad (3.3.32)$$

and the expression for γ becomes

$$\gamma \approx \frac{\omega_m\Delta\omega}{4}\sqrt{\frac{2\delta_l}{g}} \qquad (3.3.33)$$

If we assume that the linear frequency shift is zero (b = 0) then the expressions for pulse width and bandwidth can be evaluated using

$$\tau_p = \sqrt{\frac{2\ln 2}{\gamma}} \qquad (3.3.34)$$

$$\Delta f_p = \frac{1}{\pi}\sqrt{2\gamma\ln 2} \qquad (3.3.35)$$

yielding

$$\tau_p = \frac{\sqrt{\sqrt{2}\ln 2}}{\pi}\left(\frac{g_o}{\delta_l}\right)^{1/4}\left(\frac{1}{f_m\Delta f}\right)^{1/2} \qquad (3.3.36)$$

and

$$\Delta f_p = \sqrt{2\sqrt{2}\ln 2}\left(\frac{\delta_1}{g_o}\right)^{1/4}(f_m \Delta f)^{1/2} \qquad (3.3.37)$$

where g_o is a constant and is given by

$$g_o = \frac{1}{2}\ln\left(\frac{1}{R}\right) - \frac{1}{2}\ln\left[1 - 16\ln\left(2\delta_1\left(\frac{f_m}{\Delta f_p}\right)^2\right)\right] \qquad (3.3.38)$$

which by using that $\Delta f_p << f_m$ it becomes

$$g_o \approx \frac{1}{2}\ln\left(\frac{1}{R}\right) \qquad (3.3.39)$$

where R - The effective mirror reflection and includes all losses

By inspecting eqs. 3.3.36 the pulse width of the generated pulses is proportional to the ratio of g_o over δ_1, the depth of modulation. Both of these values range between 0.1 - 1, and their ratio reduced to the one quarter power can be approximated as 1. Therefore the pulse width of the output pulses depends primarily on the second term i.e.

$$\left(\frac{1}{f_m \Delta f}\right)^{1/2}$$

The main limitation of this theory is that it assumes a gaussian pulse and any slight distortion in the shape of the pulse may considerably affect the results. Also the assumption that the bandwidth of the pulse is much smaller compared with the linewidth may not always be true.

3.3.2. Passive Mode-Locking

Probably the most widely used method of generating ultrashort pulses is passive mode-locking. This type of mode-locking is called "passive" since the phases of the longitudinal modes in the cavity are locked without the need of an external modulator. Passive mode-locking is achieved when a passive saturable absorber element or cell is placed in the cavity. The saturable absorber is dye in solvent that has an optical absorption that it is linear at low intensities, but saturates and decreases at high laser intensities.

The loss modulation in a passively mode-locked laser is produced by the mode-locked pulse which means that the modulation is in perfect synchronism with the circulating pulse. The modulation becomes stronger and faster as the pulse becomes shorter. Passive mode locking generally leads to significantly shorter pulses than active mode-locking. The first optical pulses generated with picosecond[15] and femtosecond[16] pulse duration used the passive mode-locking method.

Passively mode locked lasers can be divided into two categories: I. Pulsed passively mode-locking, used with solid state lasers such as Nd:glass, and II. Continuous wave passive mode-locking used in dye lasers.

I. Pulsed Passive Mode-Locking

The typical experimental setup used for pulsed passively mode-locked laser is shown in figure 3.3.3. The pulse evolution using the technique of passive mode locking can be explained as follows:

1. Initially when the pump is turned weak laser oscillation starts to build up. The transmission of the saturable absorber is not affected by the radiation resulting in a linear loss. The light intensity inside the resonator fluctuates due to the random phase relations between the laser modes.

2. As the pumping continues the gain increases and the noise like signal is amplified. The absorption of the saturable absorber dye becomes nonlinear because the intensity peaks of the noise like signal in the laser cavity approach values of the saturation intensity of the dye.
3. The most intense noise spike will grow to an intensity level that can saturate the dye and grows quickly in intensity. Smaller fluctuations encounter larger absorption in the dye cell and get suppressed. Under proper conditions the transmission of the dye is close to 1 and the laser oscillation is forced to build up in the form of a single very short pulse circulating inside the laser cavity.

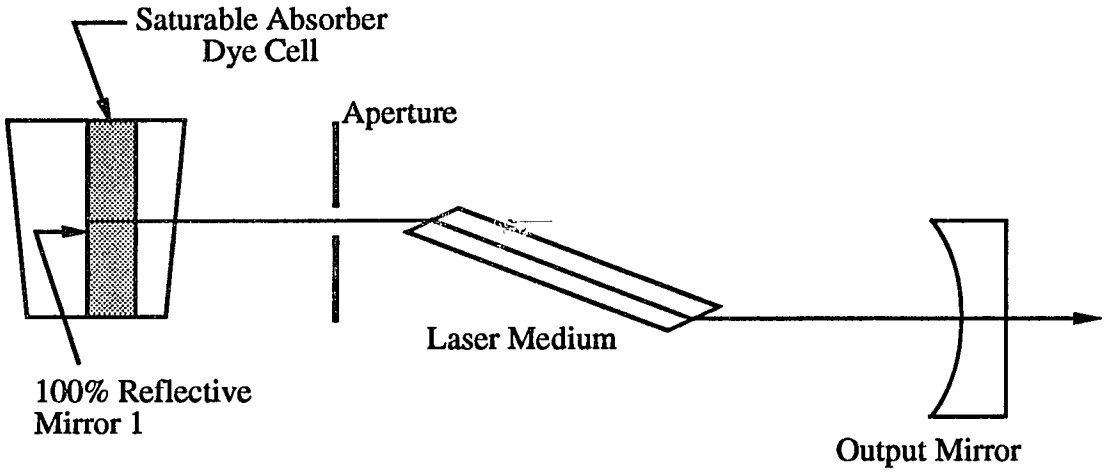

Fig. 3.3.3. Pulsed passively mode locked solid-state laser

A saturable absorber employed in pulsed passive mode-locking must have the following physical characteristics to be suitable for mode-locking:

1. The absorption curve of the saturable absorber should be centered at the laser wavelength.
2. The linewidth of the saturable absorber should be equal to or greater than the laser line width.

3. The saturable absorber should have a recovery time much shorter than the round trip time of a pulse circulating in the laser resonator. The shortest the recovery time of the saturable absorber the shorter pulses will be generated.

II. Continuous Wave Passive Mode-Locking

Continuous wave passive mode locking has been successfully employed with dye lasers. A typical setup for a cw mode-locked dye laser is shown in figure 3.3.4.

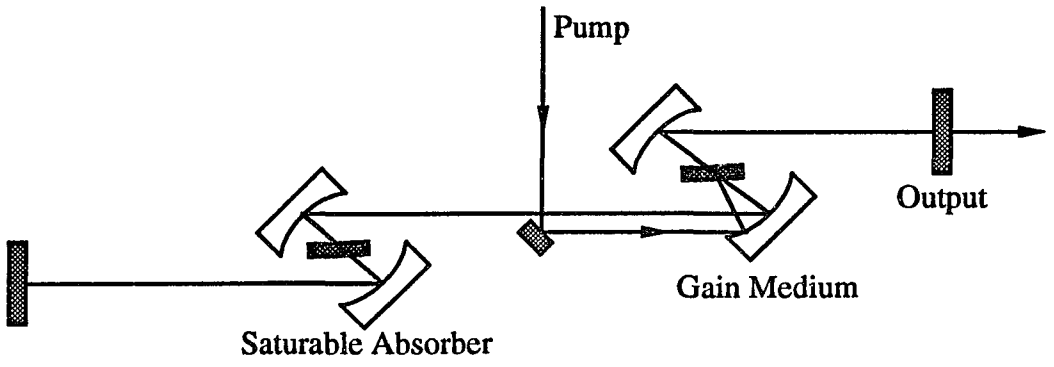

Fig. 3.3.4. Continuous wave passively mode locked dye laser.

Passive mode locking of a continuous laser can be easily understood by considering figure 3.3.5 where it is assumed that the saturable absorber and the gain are at the same plane and that the circulating pulse inside the cavity is strong enough to saturate both the gain medium and the saturable absorber. Just before the pulse enters the plane the loss due to the saturable absorber and the cavity are greater than the initial gain value and the leading edge of the pulse gets attenuated. As the pulse moves forward the absorber saturates and the losses become smaller than the gain, leading to pulse amplification. At the final stage as a result of the amplification of the pulse the gain medium saturates and the losses increase resulting in the attenuation of the back tail of

the pulse. The result of the repetitive passage of the pulse through this plane the peak of the pulse is amplified while the tails of the pulse are suppressed.

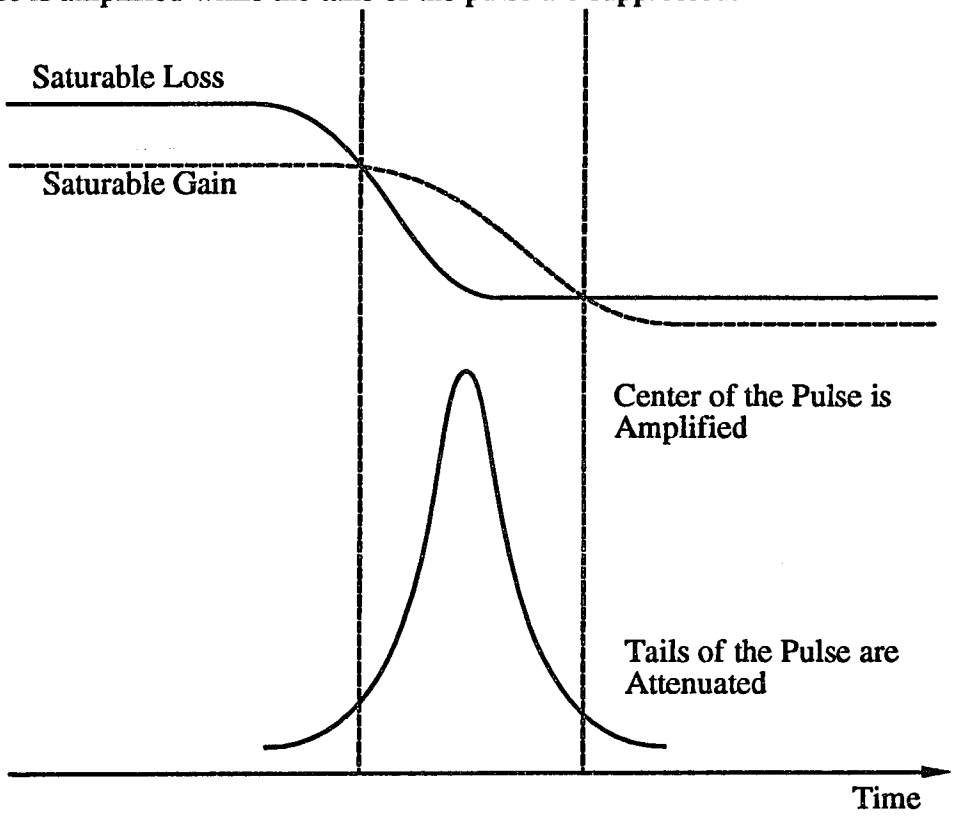

Fig. 3.3.5. Behavior of gain and absorber saturation for each pass of the mode locked pulse in a cw mode locked dye laser.

3.3.3. Synchronously Pumped Mode-Locking

Synchronously pumped mode locking is another common way of generating ultrashort pulses from lasers. The basic idea in this technique is to modulate the laser gain at a frequency that equals the cavity mode spacing, by modulating the pump power incident in the gain medium. The technique of synchronous optical pumping is illustrated in figure 3.3.6 where the pumping laser acts as the master oscillator and the optically pumped laser is the slave.

The output of the pump source is a train of pulses separated in time by 2L/c. When the lengths of the two lasers are exactly equal then the gain modulation is in phase with a pulse that circulates in the slave laser. Subsequently when the pulse in the slave

laser passes through the gain medium, stimulated emission depletes the upper lasing level population and reduces the gain to a value equal to the cavity losses.

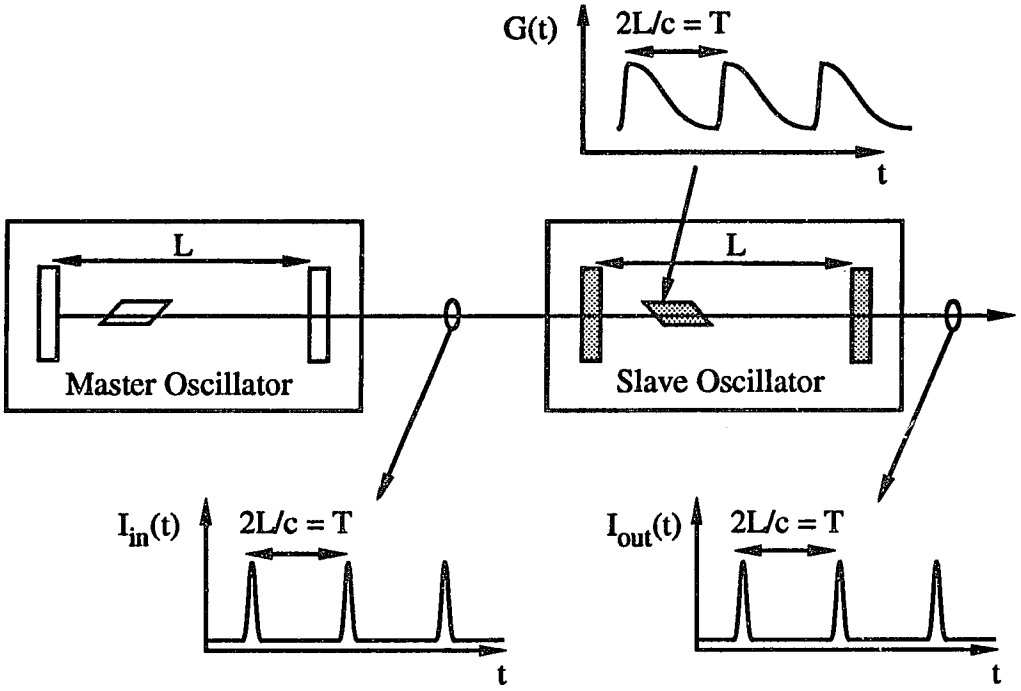

Fig. 3.3.6. Synchronously-pumped mode-locking technique.

The mechanism of formation of pulses in a synchronously pumped laser was investigated by Kovrigin et. al.[17] using a computer simulation. Figure 3.3.7 shows the time profiles of the pump pulse, the gain of the active medium, and the output pulse for different times during the growth process. The first pump pulse creates amplification in the gain medium sufficient to generate long pulses. These long pulses exist throughout the time that the gain exceed the losses (figures 3.3.7 (a) and 3.3.7 (b)). During subsequent transits the pulse is amplified and shorten since the center of the pulse corresponds to high gain while the tails of the pulse experience smaller gain. This process continues until the circulating pulse is strong enough to saturate the gain medium and the pulse becomes even shorter (figures 3.3.7 (c)). Finally, steady state is reached (figures 3.3.7 (d)) and the pulse parameters generating an output pulse train separated by the round trip time of the cavity.

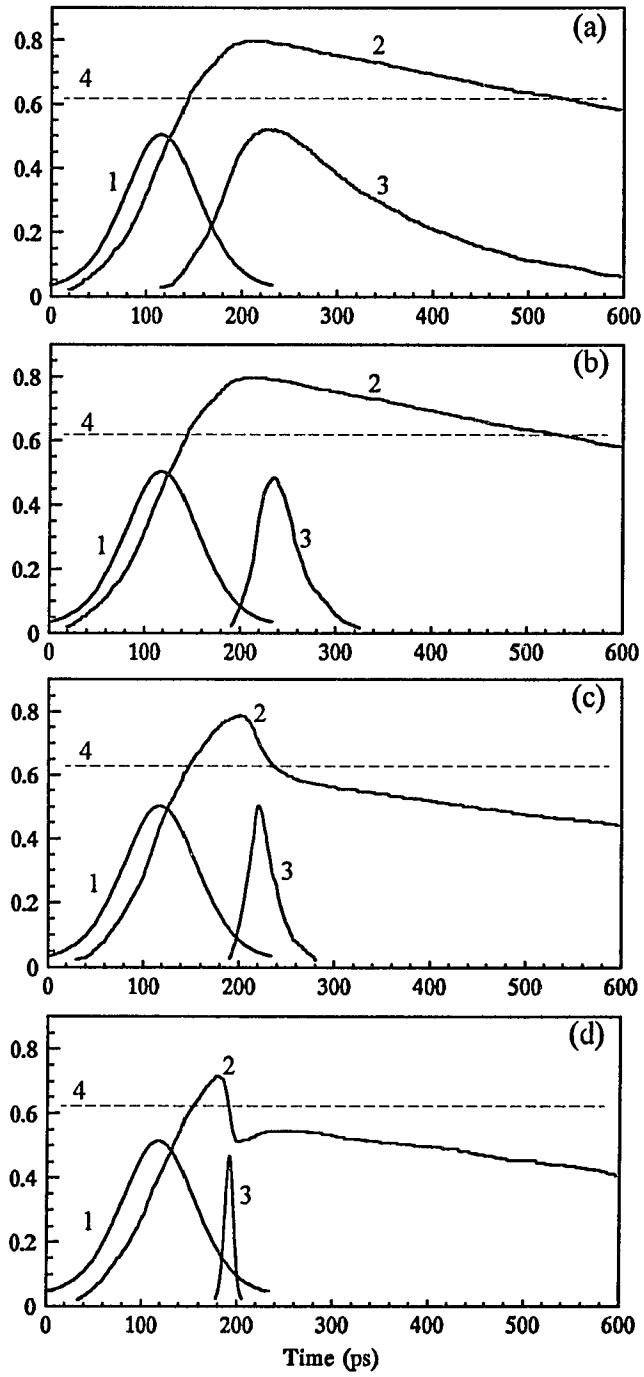

Fig. 3.3.7. Time profiles of the pump pulse, the gain of the active medium, and the output pulse for different times during the growth process: 1, pump pulse; 2, gain profile; 3, output pulse; 4, level of losses.[18]

Some essential conditions for the generation of ultrashort pulses are the following:

1. The lengths of the master and slave lasers are exactly matched .
2. The pumping rate is very stable.
3. An active medium with a low saturation energy ensures generation of ultrashort pulses even in the case of a long (compared with the characteristic pump period) lifetime of the laser active level.[19]

Synchronously pumped mode-locking has been very successfully applied to dye lasers. Synchronously pumped mode-locking of tunable solid state lasers have not been as successful as in the case of dye lasers except for the case of color center lasers. Synchronously pumped Ti:sapphire and Cr:forsterite lasers generated pulses with duration of 340 ps 260 ps, respectively. The reason for the long pulses is that the gain cross section is much smaller for solid state lasers, as compared with dye lasers, and as a result is very hard to achieve saturation.[16]

In recent years due to the exploitation of self mode-locked systems synchronous optical pumping may become very helpful since all self mode locked systems require a starting mechanism. In experiments with Cr:forsterite and Ti:sapphire lasers this technique work very effectively generating sub-100-fs pulses.

3.3.4. Self-Mode-Locking

Traditionally passive mode locking was achieved by placing a saturable absorber inside the cavity. This requires careful selection of saturable absorber to match the absorption of the laser medium. In recent years a new technique has emerged where the gain and saturable absorbing media is the same medium. Self-mode-locking or as is usually termed Kerr lens mode-locking (KLM) takes advantage of the nonlinear refractive index of the gain medium and aperturing to achieve a fast saturable absorber-

like action. Since KLM does not rely on population excitation and resonant excitation of a real saturable absorber it can be used over a wide range of wavelengths.

The technique of passive mode-locking of a laser with long relaxation time (most solid-state lasers) using a fast saturable absorber is illustrated in figure 3.3.8.[20] In this case the saturable absorber is able to create a short gain window by itself. The width of the gain window is extremely short since it relies on the non resonant Kerr-nonlinearity that has an almost instantaneous response (<10 fs).[21] Since this system is independent of the carrier frequency over a wide wavelength range, it can provide efficient pulse shaping for a wide range of lasers with long upper lasing level lifetimes.

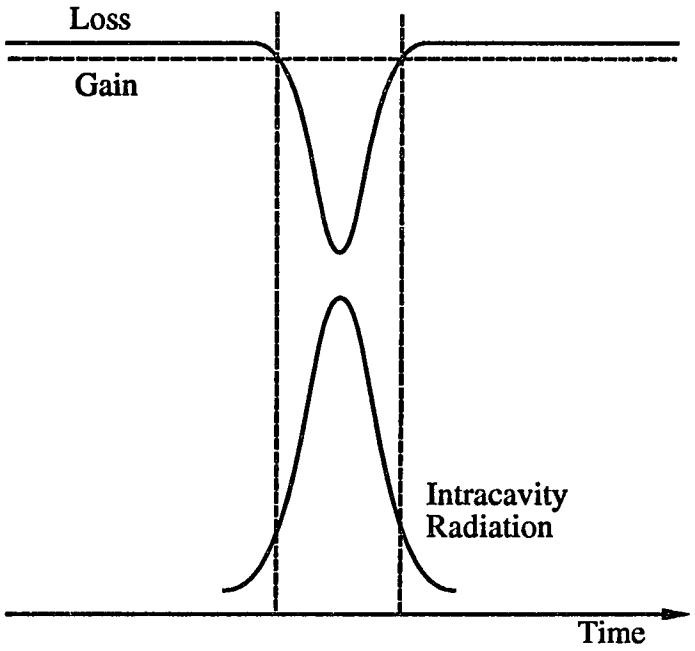

Fig. 3.3.8. Passive mode-locking using a fast saturable absorber and a gain medium with a long upper lasing level lifetime.

The basic principle of self mode-locking can be understood by considering a high intensity pulse incident in nonlinear medium in combination with an aperture. The self mode-locking technique is illustrated in figure 3.3.9. When the high intensity laser pulse enters the nonlinear medium it induces an intensity dependent lens inside the material.

The size of the aperture is such to allow all the radiation to go through. When the laser pulse is not intense then there is no self-focusing and part of the beam is cut by the aperture. Therefore in the presence of an intense laser pulses there is maximum transmission and for all other cases there is high loss through the combination of nonlinear material and aperture. The aperture after the nonlinear medium can be a real hard aperture or it can be a soft aperture provided by the spatial profile of the gain in the laser cavity.

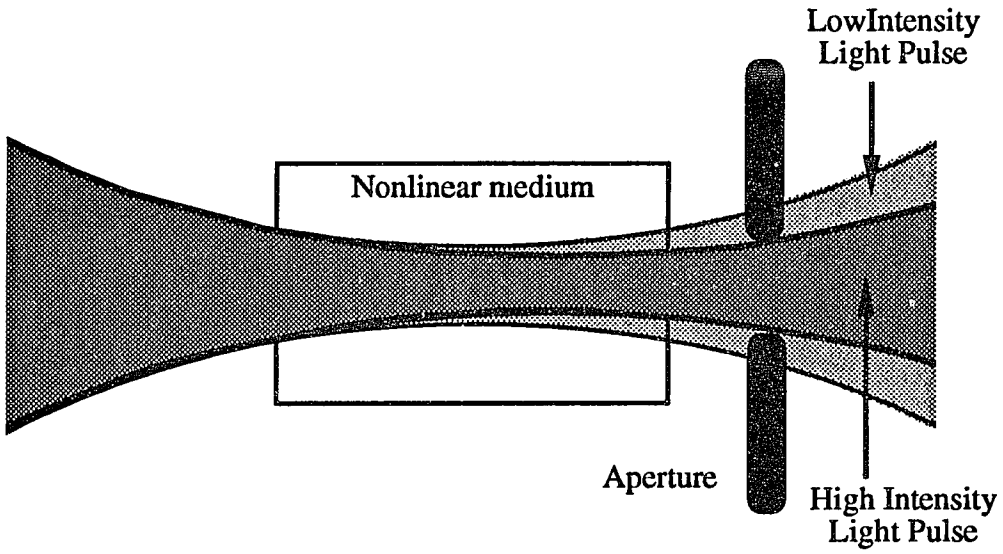

Fig. 3.3.9. Self-mode-locking using a nonlinear medium.

The typical cavity configuration for self-mode-locked solid state lasers is shown in figure 3.3.10. It is a four mirror z-fold astigmatically compensated cavity with intracavity chirp compensation. The two end mirrors are usually flat and the curved folding mirrors have radius of curvature ranging between 10-15 cm. As it will be shown in chapter 4 such cavity designs offer a very small cavity mode (< 100μm) between the two folding mirrors. The gain medium is placed between two focusing mirrors where high intensity fields induce the nonlinear response necessary for self mode locking. The

purpose of the prism pair is to provide phase distortions compensation induced by group velocity dispersion and self phase modulation in the gain medium.

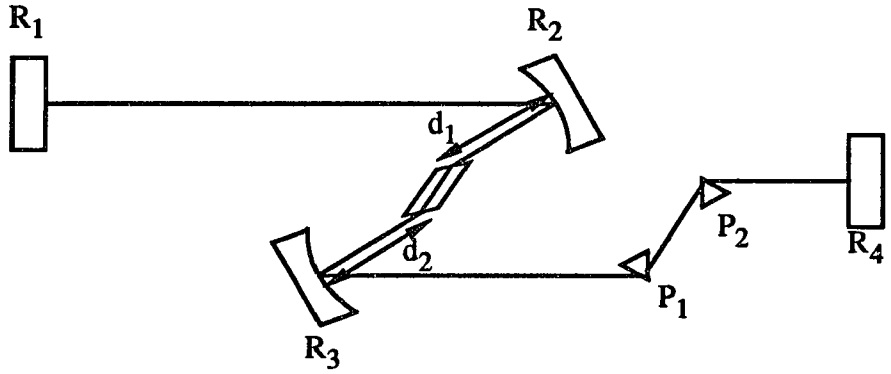

Fig. 3.3.10. Typical cavity configuration used for self-mode-locking of solid-state lasers.

Self-mode-locking and the effects of the nonlinear index of refraction was analyzed by many authors using computer simulations and the ABCD matrix formulation.[22,23,24,25] Their analysis suggests that one of the key parameters in a self-mode-locked laser is the relative position of the gain medium with respect to the two folding mirrors (d_1, d_2). Other parameters that affect self-mode-locking is the aperture size, the gain medium thickness and nonlinear index of refraction, and the beam power. The basic concept of an all optical modulator is not new,[26,27,28] but successful self-mode-locking is fairly new.[29,30] A complete analysis of self-mode-locking and determination of the design parameters are not yet available.

One of the drawbacks in self mode locking systems is that it is not self starting and there is need for a starting mechanism. Once the laser reaches a steady state, the modulation is self sustain and removal of the starting mechanism causes no change to the self mode-locking process. The problem of starting self mode locking has been overcome using a variety of methods such as [31]

- Active mode-locking,
- Synchronous optical pumping,

- Slow saturable absorber (Dye or glass) in the cavity,
- External cavity containing optical fiber or quantum well,
- Linear external cavity with a moving mirror,
- Rotating an intracavity Brewster plate,
- Sudden cavity length changes, and
- Tapping on a cavity mirror.

3.4. Measurement of Duration of Short Pulses

Pulses below few ps can not be measured using a streak camera or with fast detectors coupled to oscilloscopes. Indirect measurements have emerged with subpicosecond time resolution to measure the duration of these ultrashort pulses. A variety of optical phenomena have been used to measure short pulses, including phase conjugation[32], two photon absorption[33], and second harmonic generation (SHG).[40] The most popular method for short pulse measurements is the autocorrelator which combines a Michelson Interferometer and second harmonic generation[34].

The typical hardware implementation of an autocorrelator is presented in Figure 3.4.1.

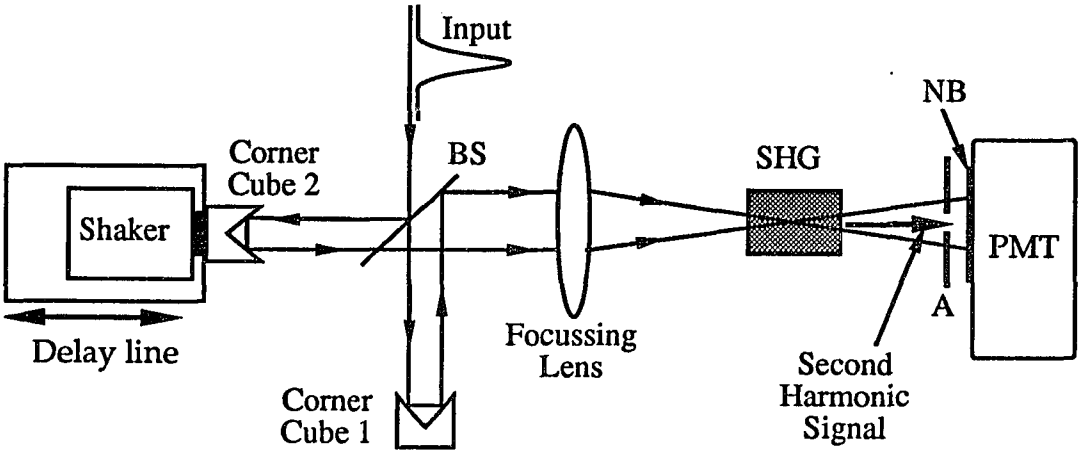

Fig. 3.4.1. Typical autocorrelator design; BS, beam splitter; A, aperture; NB, narrow band filter; SHG, second harmonic generation crystal; PMT, photomultiplier.

The optical pulse is divided into two parts which travel different paths before they recombine in a nonlinear crystal. By adjusting the time delay between the two beams, it can be arranged that no SHG is detected when the two pulses arrive at the crystal at different times, and maximum SHG when the two pulses arrive at the crystal at the same time. The arriving time of one of the pulses can be externally controlled by mechanically changing the path length (usually a corner cube is mounted on a shaker). The average power of the SHG of the recombine is recorded as a function of the time delay between the two pulses.

3.4.1. Intensity Autocorrelator

The manner in which an autocorrelator can be used to determine the width of optical pulses is described in this section. Suppose that the amplitude of the electric field of the two beams passing through the second harmonic crystal is

$$E(t) = E_1(t) = E_2(t) \tag{3.4.1}$$

where $$E(t) = E_o(t)e^{i(\omega t+\phi)}$$

The second harmonic radiation generated in the crystal is proportional to

$$E_{2\omega}(t) \propto [E(t) + E(t-\tau)]^2 \tag{3.4.2}$$

The output signal $A_d(\tau)$ generated by the detector having a slow response time (such as a photomultiplier) is then given by [35]

$$A_d(\tau) = \int_{-\infty}^{+\infty} |E_{2\omega}(t)|^2 dt = W_{2\omega}(1+2G(\tau)) \tag{3.4.3}$$

where $W_{2\omega}$ is the second harmonic pulse energy and $G(\tau)$ is the autocorrelation function of the pulse intensity which can be expressed as follows

$$W_{2\omega} = \int_{-\infty}^{+\infty} E^4(t)dt \tag{3.4.4}$$

and

$$G(\tau) = \frac{\int_{-\infty}^{+\infty} E^2(t)E^2(t-\tau)dt}{\int_{-\infty}^{+\infty} E^4(t)dt} \tag{3.4.5}$$

The recorded signal $A_d(\tau)$ can also be expressed in terms of intensity as

$$A_d(\tau) = 1+2\left[= \frac{\int_{-\infty}^{+\infty} I(t)I(t-\tau)dt}{\int_{-\infty}^{+\infty} I^2(t)dt} \right] \tag{3.4.6}$$

Note that when $\tau = 0$, $A_d(\tau) = 3$ and when τ -> infinity, $A_d(\tau) = 1$, or in other words the recorded signal has a peak to background ratio of 3 to 1. Expression 3.4.6 represents the autocorrelation signal when all of the second harmonic radiation generated is recorded by the PMT.

It is possible to design the autocorrelator in a way that only the second harmonic radiation generated by the combined action of the two beams is recorded (See figure 3.4.1). This type of autocorrelator is termed as background free and the recorded signal is proportional to

$$A_d(\tau) = \frac{\int_{-\infty}^{+\infty} I(t)I(t-\tau)dt}{\int_{-\infty}^{+\infty} I^2(t)dt} \tag{3.4.7}$$

In the case of the background free autocorrelator the recorded signal has a peak to background ratio of 1 to 0 since for $\tau = 0$, $A_d(\tau) = 1$ and when τ -> infinity, $A_d(\tau) = 0$.

The intensity autocorrelator described so far is an easy way of determining the temporal properties of the pulses but reveals no information about the coherence of the pulse.

3.4.2. Interferometric Autocorrelator

If the generated second harmonic radiation is recorded with interferometric accuracy then the recorded signal is proportional to[36]

$$A_i(\tau) = \int_{-\infty}^{+\infty} \left| \left\{ E_0(t) e^{i[\omega t + \phi(t)]} + E_0(t-\tau) e^{i[\omega(t-\tau) + \phi(t-\tau)]} \right\}^2 \right|^2 dt \qquad (3.4.8)$$

The autocorrelation reveals additional information about the measured pulses as compared to the intensity autocorrelation since it can indicate the presence of linear chirp. If the time delay is set to zero in eq. 3.4.8, the intensity is given by

$$A_i(0) = 2^4 \int E_0^4(t) dt \qquad (3.4.9)$$

The autocorrelation signal corresponds to the coherent superposition of the two electric fields and the recorded signal is maximum. If now the time delay is set at half the light period the two electric fields add destructively and the resulting signal is almost zero. As a result of the constructive and destructive addition of the two fields every half light period, the recorded signal has a spike-like behavior bounded by the pulse envelope. (See figure 3.4.2 a). In the case of chirped pulses the center of the pulse contains different frequencies than the wings of the pulse. The constructive and destructive interference between the two fields lasts as long as the time delay is smaller than the coherence time

of the pulse after which the interferometric autocorrelation merges with the intensity autocorrelation.

In order to gain more insight in to the process of interferometric autocorrelation assume a linearly chirped gaussian pulsewith unity amplitude

$$E(t) = \exp\left(-\frac{t^2}{2T^2}\right)\cos\left(\omega t + \frac{bt^2}{T^2}\right) \tag{3.4.10}$$

The interferometric autocorrelation can be written as

$$A_i(\tau) = 1 + 4\exp\left[-\frac{\left(3+4b^2\right)\tau^2}{8T^2}\right]\cos(\omega t)\cos\left(\frac{b^2\tau^2}{2T^2}\right) + \exp\left[-\frac{\left(1+4b^2\right)\tau^2}{2T^2}\right]\cos(2\omega t) + 2\exp\left(-\frac{\tau^2}{2T^2}\right) \tag{3.4.11}$$

Numerical calculations were carried out using eq. 3.4.10 assuming a gaussian pulse with FWHM of 30 fs where the corresponding spectrum is centered at 1250 nm and for different values of the chirp parameter b. Figure 3.4.2 shows the interferometric autocorrelation of a gaussian pulse for three values of the dimensionless chirp parameter b: a) b = 0, b) b = 0.974, and c) b = 2.921. The dashed line is the envelope function and is calculated by replacing $\omega\tau$ in equation 3.4.11 by 2π for the upper envelope and π for the lower envelope.

When the pulse has no chirp (b=0) all the fringes in the interferometric autocorrelation are resolved since the field is coherent throughout the pulse. As the chirp parameter increases ($b\neq 0$) the field becomes incoherent at the wings of the pulse, and no interference is possible at the wings. The signal merges with the intensity autocorrelation for time delays exceeding the coherence length of the pulse as illustrated in figure 3.4.2.

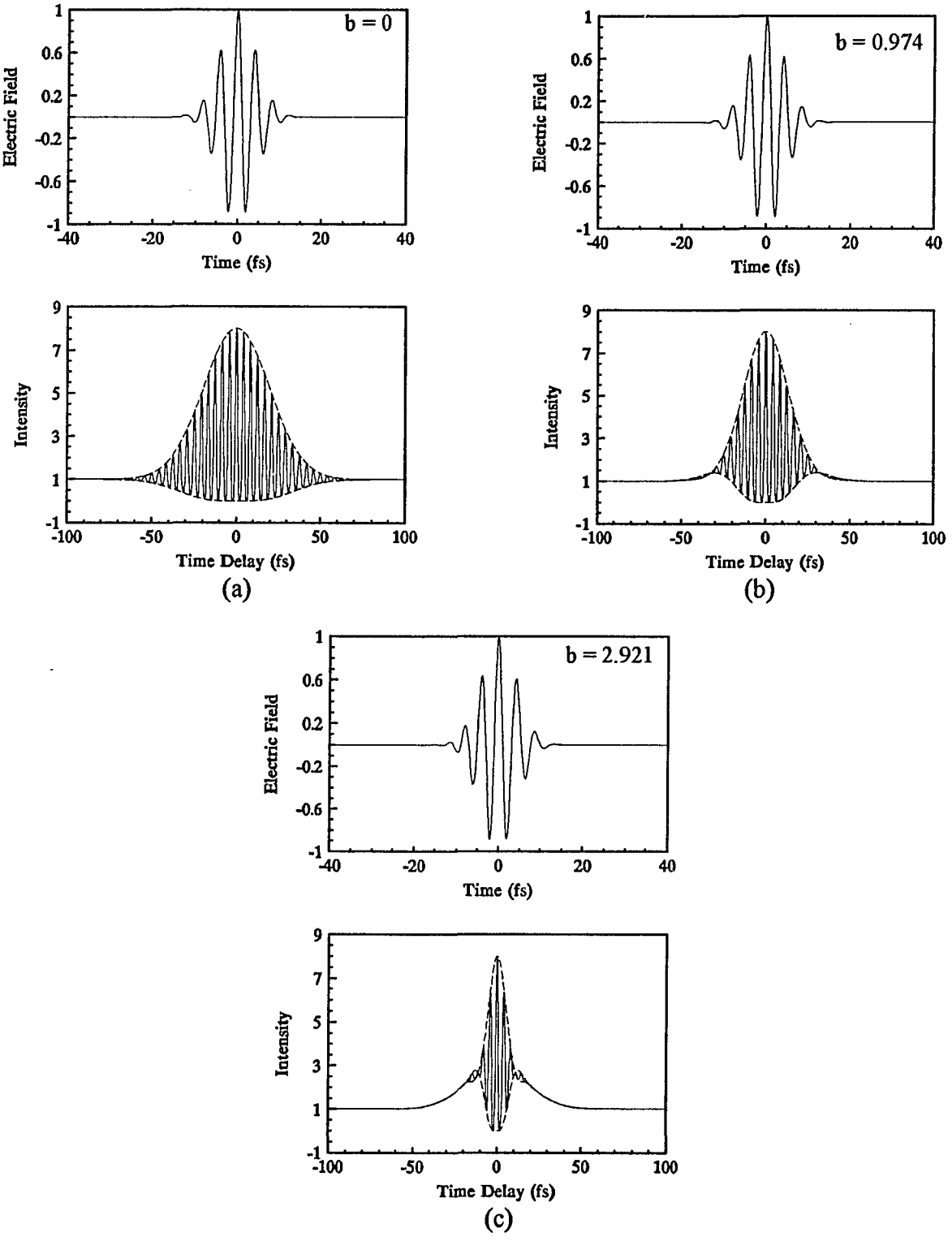

Fig. 3.4.2. Interferometric autocorrelation of gaussian pulses with FWHM of 30 fs for different values of the chirp parameter b: a) b = 0, b) b = 0.974, and c) b = 2.921.

In the calculations it was assumed that the pulse possessed linear chirp. The situation varies unpredictably if more complicate forms of phase distortions are present in the pulse. The interferometric autocorrelation provides information on the presence of chirp but gives no indication of the form of the chirp. In the case of an unchirped pulse the interferometric autocorrelation can be used to estimate the pulse width by assuming a form of pulses and fitting the upper and lower envelope of the autocorrelation.

3.4.3. Correlation Functions for Laser Pulse Shapes

Some commonly used mathematical functions describing light pulses are the gaussian function, secant hyperbolic function, lorentzian function and symmetric double sided exponential. Figure 3.4.3 shows the autocorrelation of a 30 fs pulse for the four mathematical functions. The main difference of the autocorrelations is how fast they decay to zero.

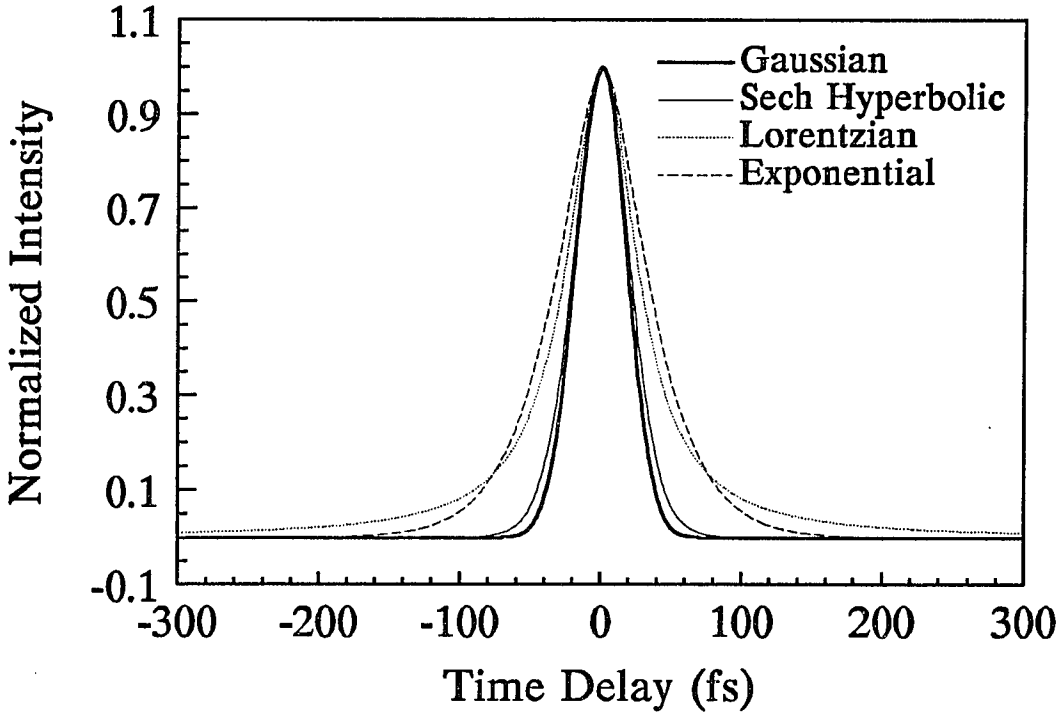

Fig. 3.4.3. Autocorrelation of some commonly used mathematical functions.

Gaussian Pulses: An optical pulse with a carrier frequency ω_0, a complex gaussian envelope and linear chirp b is written in the form

$$E(t) = E_0 e^{-at^2} e^{i(\omega_0 t + bt^2)} \tag{3.4.12}$$

The instantaneous intensity I(t) of the gaussian pulse can be written as[8]

$$I(t) = E(t)E^*(t) = |E(t)|^2 = I_0 e^{-2at^2} \tag{3.4.13}$$

Note that all the variables related to the phase of the pulse are lost. The pulse width τ_p of the intensity, defined as the full width at half maximum (FWHM), is related to the parameter a by the expression

$$\tau_p = \sqrt{\frac{2\ln 2}{a}} \tag{3.4.14}$$

The intensity autocorrelation function of gaussian pulses can be evaluated using eq. 3.4.7

$$I(\tau) = \frac{\int_{-\infty}^{+\infty} I_0 e^{-2at^2} I_0 e^{-2a(t-\tau)^2} dt}{\int_{-\infty}^{+\infty} I_0 e^{-2at^2} dt} = e^{-a\tau^2} \tag{3.4.15}$$

The autocorrelation function is also a gaussian pulse with a FWHM given by

$$\tau_{auto} = \sqrt{\frac{4\ln 2}{a}} \tag{3.4.16}$$

Comparing the relationship between the FWHM of the autocorrelation function and the FWHM (τ_p) of the intensity of the optical pulse eqs. 3.4.12 and 3.4.14 we get the relationship between the measured and the actual pulse widths

$$a = \frac{4\ln 2}{\tau_{auto}^2} = \frac{2\ln 2}{\tau_p^2} \tag{3.4.17}$$

and

$$\tau_p = \frac{\tau_{auto}}{\sqrt{2}} = \frac{\tau_{auto}}{1.4142} \tag{3.4.18}$$

The intensity autocorrelation provides information on the duration of the optical pulses but reveals no information on the presence of any phase distortions like linear chirp in the optical pulse. Some information of the phase characteristics of the pulse can be found if the pulse width measurements are accompanied with measurements of the spectrum. Mathematically the spectrum of the pulse can be found by taking the Fourier transform.

Neglecting the amplitude term in equation 3.4.12 a gaussian pulse with chirp can be written as

$$E(t) = e^{i\omega_o t-(a-ib)t^2} \tag{3.4.19}$$

The Fourier transform of E(t) is given by

$$E(\omega) = \exp\left[-\frac{(\omega-\omega_o)^2}{4(a-ib)}\right] \tag{3.4.20}$$

or

$$E(\omega) = \exp\left[-\frac{1}{4}\left(\frac{a}{a^2+b^2}\right)(\omega-\omega_o)^2 - i\frac{1}{4}\left(\frac{b}{a^2+b^2}\right)(\omega-\omega_o)^2\right]$$

Note that the Fourier transform of the optical pulse is also a gaussian function. The power spectrum is estimated by multiplying E(ω) with its complex conjugate E*(ω).

$$E(\omega)E^*(\omega) = |E(\omega)|^2 = \exp\left[-\frac{1}{2}\left(\frac{a}{a^2+b^2}\right)(\omega-\omega_0)^2\right] \qquad (3.4.21)$$

The FWHM of the spectrum is given by

$$\Delta\omega_p = \sqrt{8\ln 2}\sqrt{\frac{a^2+b^2}{a}} \qquad (3.4.22)$$

In terms of frequency eq. 3.4.22 can be written as ($\omega = 2\pi f$)

$$\Delta f_p = \frac{\sqrt{2\ln 2}}{\pi}\sqrt{\frac{a^2+b^2}{a}} \qquad (3.4.23)$$

Measurement of the FWHM of the spectrum reveals information of the chirp since the phase parameter b is present in the resulting equation. By taking the bandwidth-pulse width product we get

$$\Delta f_p \tau_p = \frac{2\ln 2}{\pi}\sqrt{1+\frac{b^2}{a^2}} = 0.441\sqrt{1+\frac{b^2}{a^2}} \qquad (3.4.24)$$

When the optical pulses are free of chirp, b = 0, then the bandwidth-pulsewidth product is 0.441. Bigger values for the bandwidth-pulsewidth product indicate the presence of chirp in the pulse but still give no information on the sign of the chirp.

Table 3.4.1 presents a list of functions used to represent optical pulses and their characteristics. Column 1 gives the general form of mathematical function. Column 2 list

the bandwidth-pulsewidth product for unchirped optical pulse; Column 3 is the relationship between the FWHM and the variables of the function; Column 4 is the expression describing the autocorrelation; Column 5 is the relationship between the FWHM of the autocorrelation and the characteristics of the optical pulse; and Column 6 lists the relationship between the pulse width of the pulse and the pulse width of the measured autocorrelation.

Table 3.4.1. Mathematical functions used to describe light pulses.[37]

1	2	3	4	5	6
I(t) $\left(x=\frac{t}{T}\right)$	$\Delta\nu\Delta t$	$\frac{\tau_p}{T}$	$A_d(\tau)$ $\left(y=\frac{\tau}{T}\right)$	$\frac{\tau_a}{T}$	$\frac{\tau_p}{\tau_a}$
Gaussian $I(t)=e^{-x^2}$	0.4413	$2\sqrt{\ln 2}$	$e^{-\frac{y^2}{2}}$	$2\sqrt{2\ln 2}$	0.7071
Hyperbolic Sech $I(t)=\mathrm{sech}^2 x$	0.3148	1.7627	$\frac{3}{\sinh^2 y}[y\coth y-1]$	2.7196	0.6482
Lorenzian $I(t)=\frac{1}{1+x^2}$	0.2206	2	$\frac{1}{1+\left(\frac{y}{2}\right)^2}$	4	0.500
Symmetric two sided exponential $I(t)=e^{-2\lvert x\rvert}$	0.1420	ln2	$(1+2\lvert y\rvert)e^{-2\lvert y\rvert}$	1.6783	0.4130

3.4.4. Second Harmonic Generation

One of the most important elements in an autocorrelator is the nonlinear crystal used for second harmonic generation (SHG). Special emphasis should be given to the choice of an appropriate nonlinear crystal that can efficiently convert the input

fundamental radiation to second harmonic radiation. One of the most commonly used nonlinear crystal is Potassium Phosphate (KH_2PO_4) or KDP whose transmission characteristics as a function of wavelength are displayed in figure (3.4.4). As is shown in the figure KDP has significant absorption over the wavelength region that Cr:forsterite laser operates (1130-1367 nm) making it unsuitable for autocorrelation measurements in the near infrared. Figure (3.4.4) also shows the transmission characteristics of deuterated KDP (KD*P).[38] The transmittance of KD*P is shifted in the infrared depending on the amount of deuteration, making it suitable for use in the near infrared. In the autocorrelator used to measure the pulse width of the pulses generated from the forsterite laser we used 99% KD*P.

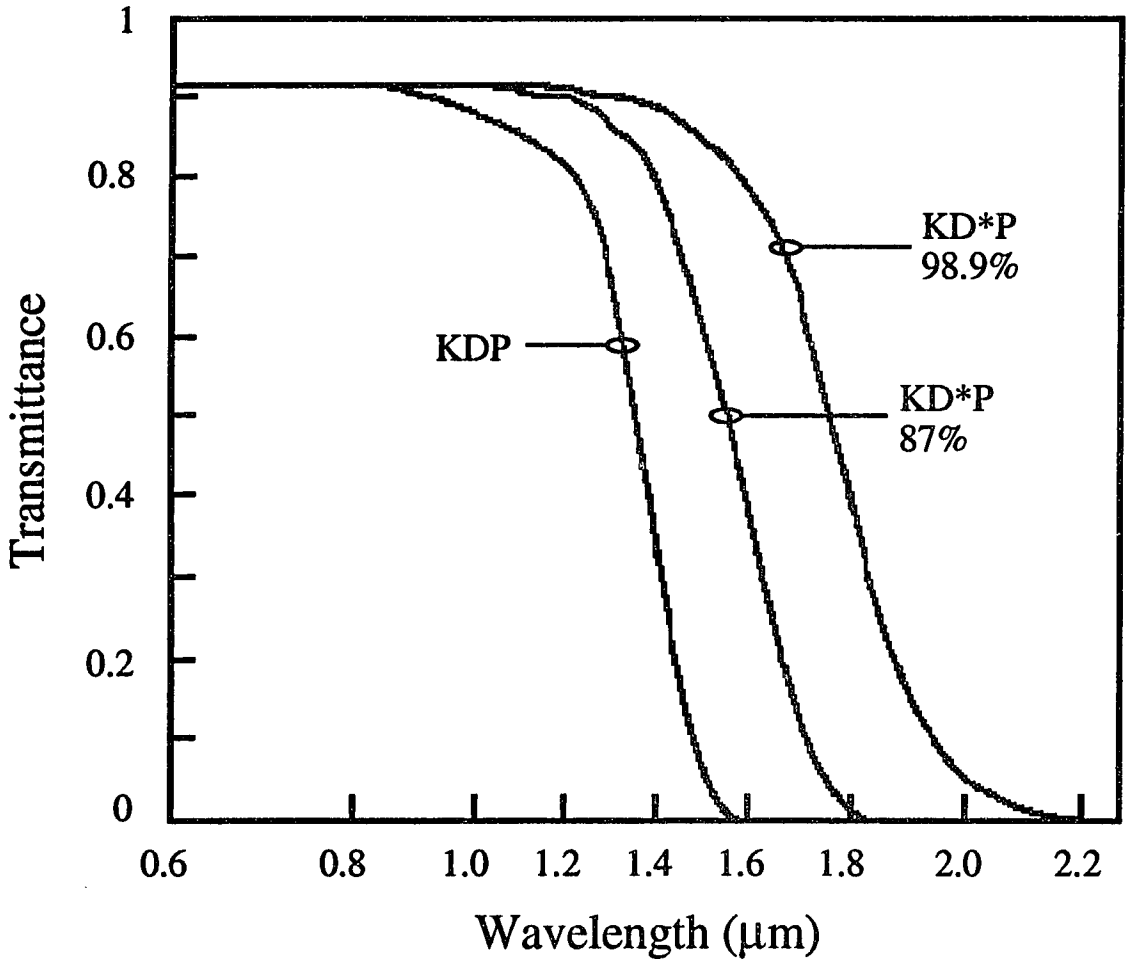

Fig. 3.4.4. Absorption characteristics of KDP and KD*P nonlinear crystals.

Second harmonic generation can be viewed as a process involving three waves with frequencies ω_1, ω_2, and ω_3 that satisfy the condition

$$\omega_1 = \omega_2 = \omega \text{ and } \omega_3 = 2\omega \tag{3.4.25}$$

Phase matching in an anisotropic crystal is accomplished by using linearly polarized waves propagating at the proper angle to insure that

$$n_{2\omega} = n_{\omega} \tag{3.4.26}$$

The indices of refraction for the case of light propagating in a uniaxial crystal such as KD*P making an angle θ with respect to the optic axis are

$$n_o = n_o \tag{3.4.27}$$

$$\frac{1}{n_e^2(\theta)} = \frac{\cos^2(\theta)}{n_o^2} + \frac{\sin^2(\theta)}{n_e^2} \tag{3.4.28}$$

There are two methods for phase-matching using birefringence depending on the polarization of the input beams.

TYPE I: The waves with frequencies ω_1 and ω_2 both have the same polarization i.e. both are e-waves or both are o-waves. The third wave at frequency ω_3 is polarized in an orthogonal direction.

TYPE II: The waves with frequencies ω_1 and ω_2 are orthogonally polarized. The third wave at frequency ω_3 is polarized parallel to either of the other waves.

The formulas for estimating the indices of refraction and the phase matching angle for a negative uniaxial crystal such as KD*P are listed in table 3.4.2.

Table 3.4.2. Expressions used for estimation of phase matching angles for a negative uniaxial crystal ($n_e < n_o$).

TYPE I:	$n_e(\omega_3) = \frac{\omega_1}{\omega_3} n_o(\omega_1) + \frac{\omega_2}{\omega_3} n_o(\omega_2)$
	$n_e^{2\omega}(\theta_m) = n_o^{\omega}$
	Phase matching angle $\sin^2\theta_m = \frac{\left(n_o^{\omega}\right)^{-2} - \left(n_o^{2\omega}\right)^{-2}}{\left(n_e^{2\omega}\right)^{-2} - \left(n_o^{2\omega}\right)^{-2}}$
TYPE II:	$n_e(\omega_3) = \frac{\omega_1}{\omega_3} n_e(\omega_1) + \frac{\omega_2}{\omega_3} n_o(\omega_2)$
	$n_e^{2\omega}(\theta_m) = \frac{1}{2}\left[n_e^{\omega}(\theta_m) + n_o^{\omega}\right]$
	Phase matching angle[39] $\left[\frac{\cos^2\theta_m}{\left(n_o^{2\omega}\right)^2} + \frac{\sin^2\theta_m}{\left(n_e^{2\omega}\right)^2}\right]^{-\frac{1}{2}} = \frac{1}{2}\left\{n_o^{\omega} + \left[\frac{\cos^2\theta_m}{\left(n_o^{\omega}\right)^2} + \frac{\sin^2\theta_m}{\left(n_e^{\omega}\right)^2}\right]^{-\frac{1}{2}}\right\}$

The indices of refraction of KD*P crystal can be estimated by using the general form of Sellmeier equation.[40]

$$n^2 = A + \frac{B}{1 - \frac{C}{\lambda^2}} + \frac{D}{1 - \frac{E}{\lambda^2}} \qquad (3.4.29)$$

where λ is the wavelength in μm.

The Sellmeier coefficients for KD*P crystal at 300K are shown in Table 3.4.3.

Table 3.4.3. Sellmeier Coefficients for KD*P Crystal

	A	B	C	D	E
Ordinary	1.661824	0.585337	0.016017	0.691221	30
Extraordinary	1.687522	0.447488	0.017039	0.596216	30

The Sellmeier coefficients are dependent on temperature.[41] Their value at different temperatures can be evaluated by fitting in the equation

$$X = mT + c \qquad (3.4.30)$$

where T is the temperature in K and m and c are shown in Table 3.4.4.

Table 3.4.4. Linear fitted constants of the temperature dependent Sellmeier coefficients for KD*P crystal.

Sellmeier Coefficients	Fitted Constants	Ordinary Axis	Extraordinary Axis
A	$mx10^3$	0.33935	0.00343
	c	1.55934	1.68647
B	$mx10^3$	-0.41655	-0.06260
	c	0.71098	0.46629
C	$mx10^5$	0.64904	0.13626
	c	0.01407	0.01663
D	$mx10^4$	0.48281	0.00241
	c	0.67671	0.59614
E		30	30

Numerical calculation were carried out to determine the phase matched angle for the KD*P crystal to be used for pulsewidth measurements in the near infrared. As a first step the ordinary and extraordinary indices of refraction were calculated using the Sellmeier equation. Figure 3.4.5 displays the dependence of index of refraction of KD*P as a function of wavelength for 300K. Next the calculated indices of refraction together with the equations listed in Table 4.4.4 are used to calculate the phase matched angles as a function of wavelength for both Type I and Type II phase matching conditions. The results of the calculations are displayed in figure 3.4.6. The phase matched angles for Type I and Type II are fairly constant in the near infrared (1.1 -1.3 μm) due to small dispersion. This is important since it indicates that the phase matched angle is not very critical in the wavelength region that the Cr:forsterite laser operates and an autocorrelator will allow pulse width measurements through out the tuning range. This makes KD*P an ideal crystal for intracavity second harmonic generation with the forsterite laser.

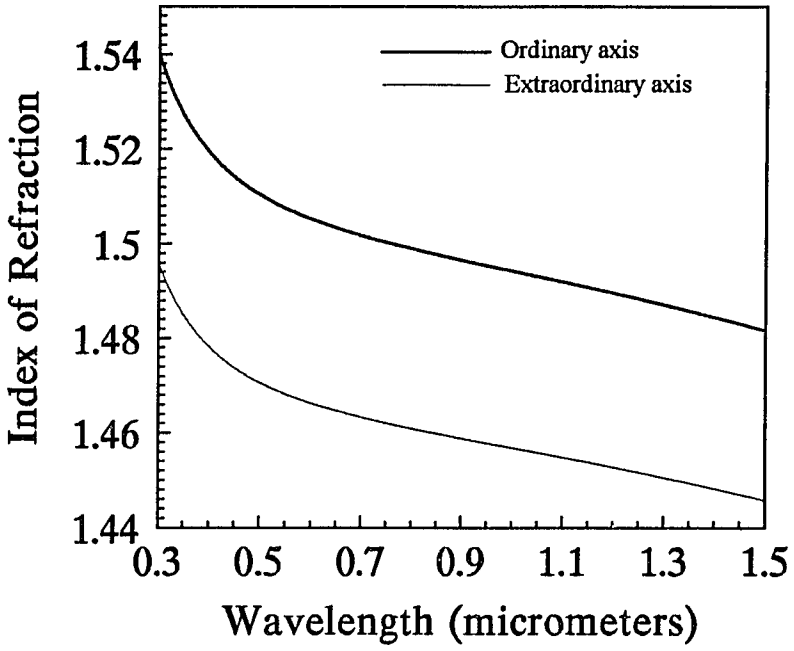

Fig. 3.4.5. Index of refraction of KD*P at 300K for ordinary and extraordinary indices vs. wavelength.

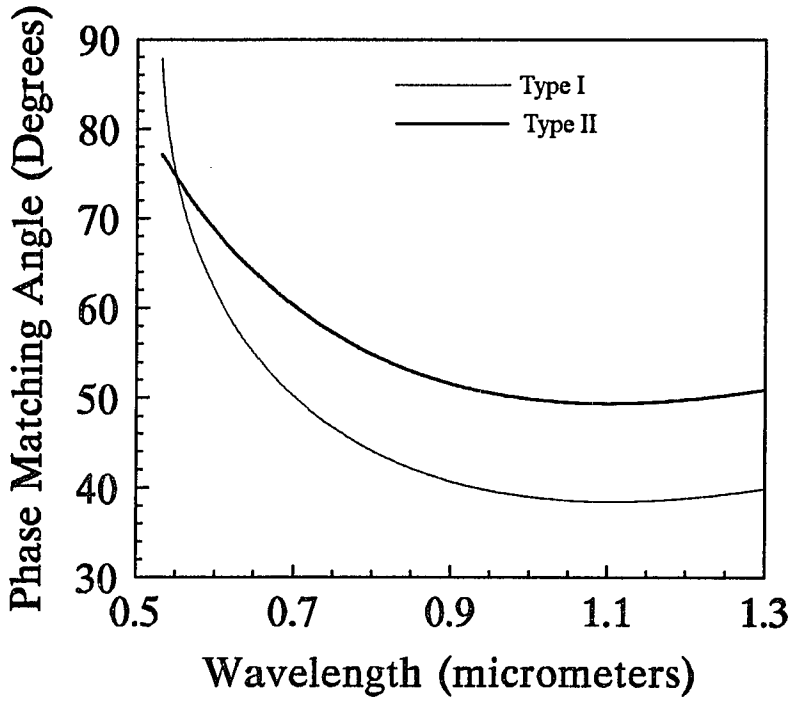

Fig. 3.4.6. Phase matching angle of KD*P at 300K for TYPE I and TYPE II conditions vs. wavelength.

Another problem that has to be considered in the design of an autocorrelator capable of measuring sub-100-fs pulses is the thickness of the nonlinear crystal. Propagation of an ultrashort pulse in a dispersive medium broadens the pulse due to group velocity dispersion. This situation can be avoid by using a very thin second harmonic crystal. The pulse duration of pulse after propagating a distance z in a dispersive medium is given by (Complete analysis of the dispersion effects is presented in Chapter 5)

$$\tau_p(z) = \tau_p(0)\sqrt{\left[1+\left(\frac{4k'' z \ln 2}{\tau_p^2(0)}\right)^2\right]} \qquad (3.4.31)$$

where $\tau_p(0)$ - Pulse duration of input pulse

$\tau_p(z)$ - Pulse duration after propagating a distance z in the medium

k" - Second derivative of propagation constant with respect to frequency

The parameter k" is related to the wavelength and the second derivative of the index of refraction with respect to wavelength by

$$k'' = \frac{\lambda^3}{2\pi c^2}\frac{\partial^2 n}{\partial \lambda^2} \qquad (3.4.32)$$

The relation between pulse width and the thickness of the KD*P crystal was determined using eq. 3.4.31. In the calculations it was assumed that the center wavelength of the pulse is 1250 nm and the thickness of the KD*P was varied between 0-3 cm. The effect is small due to the lack of high dispersion in the near infrared. The results of the calculation are shown in figure 3.4.7. The crystal thickness should be kept below 0.5 mm for best results.

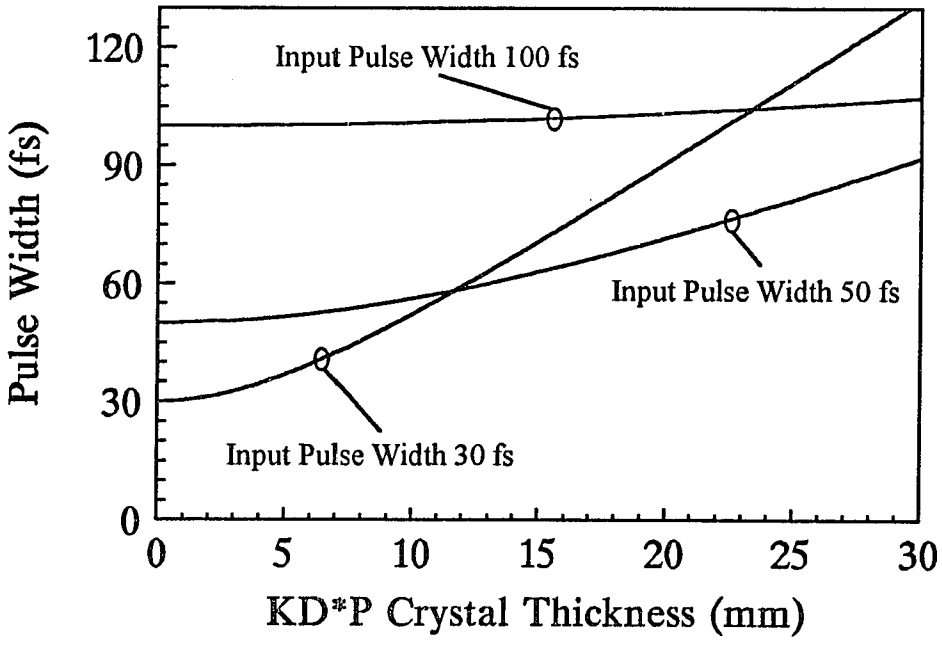

Fig. 3.4.7. Pulse broadening of a femtosecond pulse due to group velocity dispersion in a KD*P crystal for λ = 1250 nm.

When 100 fs pulses are being measured the effect of pulse broadening due to group velocity dispersion is minimum and can be neglected. When sub-50-fs pulses are measured the KD*P the effect of pulse broadening is significant and crystals thinner than 2 mm should be used.

Advantages and Disadvantages of Autocorrelators

Measurements of pulses using autocorrelators have specific advantages and disadvantages. Some of the disadvantages are:

* Correlation measurements are not particularly sensitive to low-level background signals which may be present in addition to a short intense pulse.
* SHG is insensitive to the actual pulse shape and an assumption for the pulse shape is necessary to estimate the duration of the pulses.
* A proper SHG correlation measurement requires careful alignment.

The particular advantage of SHG to lower power lasers is its relatively high nonlinear conversion efficiency under phase-matched conditions. It is important to note that phase matching in dispersive material imposes a restriction on the bandwidth over which efficient generation occurs and can limit the resolution of a correlation measurement if too thick a crystal is used.

3.5. References

1. R. R. Alfano and S. L. Shapiro, "Ultrafast Phenomena in Liquids and solids", Scientific American, 288, pp. 43 (1973).

2. A. G. Doukas, B. Buchert, and R. R. Alfano, " Picosecond Laser Techniques and Design", in "Biological Events Probed by Ultrafast Laser Spectroscopy", Academic Press, New York (1982).

3. M. S. Demokan, "Mode-Locking in Solid-State Lasers", Research Studies Press, John Wiley & Sons Ltd., pp. 215 (1982).

4. "Biological Events Probed by Ultrafast Laser Spectroscopy, Robert R. Alfano, editor, Academic Press, New York (1982).

5. F. Liu, K. M. Yoo, and R. R. Alfano, "Ultrafast pulse transmission and imaging through biological tissues", Applied Optics, Vol. **32**, pp. 554 (1993).

6. L. M. Wang, P. P. Ho, and R. R. Alfano, "Double-stage picosecond Kerr gate for ballistic time-gated optical imaging in turbid media", Applied Optics, Vol. **32**, pp. 535 (1993).

7. H. Kogelnik, and T. Li, "Laser beams and resonators", Appl. Opt., Vol. **5**, pp. 1550 (1966).

8. P. W. Smith, " Mode-locking of lasers", Proc. IEEE, Vol. **58**, pp. 1342 (1970).

9. M. DiDomenico, "Small-signal analysis of internal (Coupling-type) modulation of lasers", J. Appl. Phys., Vol. **35**, pp. 2870 (1964).

10. L.E. Hargrove, L. R. Fork, and M.A. Pollack, "Locking of He-Ne laser modes induced by synchronous intracavity modulation", Appl. Phys. Letters, Vol. **5**, pp. 4 (1964) .

11. A. Yariv, "Internal modulation of multimode laser oscillators", J. Appl. Phys., Vol. **36**, pp. 388 (1965).

12. T. W. Chong, and P. A. Lindsay, " The generation of picosecond pulses in actively mode-locked c.w. solid-state lasers", Int. J. Electronics, Vol. **45**, pp. 573 (1978).

13. D.J. Kuizenga, and A. E. Siegman, "FM and AM mode-locking of the homogeneous laser - Part I: Theory", IEEE J. Quantum Electr., **QE-6**, pp. 694 (1970).

14. A. E. Siegman, and D.J. Kuizenga, Opto-Electronics, Vol. **6**, 1, pp. 43 (1974).

15. A. J. DeMaria, D. A. Stetser, and H. Heyman, Appl. Phys. Lett. **7**, pp. 270 (1965).

16. R. L. Fork, B. I. Greene, C. V. Shank, "Generation of optical pulses shorter than 0.1 psec by colliding pulse mode locking", Appl . Phys. Lett., Vol. **38**, pp. 671 (1981).

17. A. I. Kovrigin, V. A. Nekhaenko, S. M. Pershin, and A. A. Podshivalov, "Dynamics of emission from dye lasers pumped synchronously by finite picosecond pulse trains", Sov. J. Quantum Electron., Vol. **14**, pp. 1346 (1984).

18. V. A. Nekhaenko, S. M. Pershin, and A. A. Podshivalov, "Synchronously pumped tunable picosecond lasers (review)", Sov. J. Quantum Electron., Vol. **16**, pp. 299 (1986).

19. L. F. Mollenauer, N. D. Vieira, and L. Szeto, " Mode-locking by synchronous pumping using a gain medium with microsecond decay times", Optics Letters, Vol. **9**, pp. 414 (1982).

20. F. Krausz, M. E. Fermann, T. Brabec, P. F. Curley, M. Hofer, M. H. Ober, C. Spielman, E. Wintner, and A. J. Schmidt, "Femtosecond solid-state lasers", IEEE J. Quantum Electr., **QE-28**, pp. 2097 (1992).

21. A. B. Grudinin, E. M. Dianov, D. V. Korobkin, A. M. Prokhorov, V. N. Serkin, and D. V. Khaidarov, "Decay of femtosecond pulses in single-mode optical fibers", JETP Lett., Vol. **46**, pp. 221 (1987).

22. T. Brabec, Ch. Spielmann, P. F. Curley, and F. Krausz, "Kerr lens mode locking", Optics Letters, Vol. **17**, pp. 1292 (1992).

23. F. Salin, J. Squier, and M. Piche, "Mode locking of Ti:Al2O3 lasers and self-focusing: a Gaussian approximation", Opt. Lett. Vol. 16, pp. 1674 (1991).

24. S. Chen, and J. Wang, "Self-starting issues of passive self-focusing mode locking", Optics Letters, Vol. **16**, pp. 1689 (1991).

25. D. Huang, M. Ulman, L. H. Acoli, H. A. Haus, and J. Fujimoto, "Self-focusing saturable loss for laser mode locking", Optics Letters, Vol. **17**, pp. 511 (1992).

26. J. Laussade, A. Yariv, " Analysis of mode locking and ultrashort laser pulses with a nonlinear refractive index", IEEE J. Quantum Electron., Vol. **QE-5**, pp. 435 (1969).

27. L. Dahlstrom, "Passive mode-locking and Q-switching of high power lasers by means of the optical kerr effect", Optics Comm., Vol. **5**, pp. 157 (1972).

28. K. Sala, M. C. Richardson, and N. R. Isenor, "Passive mode locking of lasers with the optical Kerr effect modulator", IEEE J. Quantum Electron., Vol. **QE-13**, pp. 915 (1977).

29. D. E. Spence, P. N. Kean, and W. Sibbett, "60 fsec generation from a self-mode-locked Ti:sapphire laser", Optics Letters, Vol. **16**, pp. 42 (1991).

30. D.K. Negus, L. Spinelli, N. Goldblatt, and G. Feuget, "Sub-100-fs pulse generation by Kerr lens modelocking in Ti:Al_2O_3", in Tech. Dig. Topic. Meet. Advan, Solid State Lasers, Washington, DC, OSA, 1991, postdeadline paper.

31. J. D. Kafka, M. L. Watts, and J. J. Pieterse, "Picosecond and femtosecond pulse generation in a regeneratively mode-locked Ti:sapphire laser", IEEE J. Quantum Electron., Vol. **QE-28**, pp. 2151 (1992) and references therein.

32. J. Buchert, R. Dorsinvile, P. Delfyett, S. Krimchansky, and R. R. Alfano "Determination of temporal correlation of ultrafast laser pulses using phase conjugation", Opt. Comm.,Vol. **52** , pp. 433 (1985).

33. J. A. Giordmaine, P. M. Rentzepis, S. L. Shapiro, and K. W. Wecht "Two photon excitation of fluorescence by picosecond light pulses." Appl. Phys. Lett., Vol. **11**, pp. 216 (1967).

34. M. Maier, W. Kaiser, J. A. Giordmaine, " Intense light bursts in the stimulated Raman effect", Phys. Rev. Lett., Vol. **17**, pp. 1275 (1966).

35. A. J. DeMaria, W. H. Glenn Jr., M. J. Brienza, and M. E. Mack, "Picosecond laser pulses", Proc. IEEE, Vol. **57**, pp. 2 (1969).

36. Jean-Claude M. Diels, J. J. Fontaine, I. C. McMichael, and F. Simoni, "Control and measurement of ultrashort pulse shapes (in amplitude and phase) with femtosecond accuracy", Applied Optics, Vol. **24**, pp 1270 (1985).

37. K. L. Sala, G. A. Kenney-Wallace, and G. E. Hall, "CW autocorrelation measurements of picosecond laser pulses", IEEE J. Quantum Electron. Vol. **QE-16**, pp. 990 (1980).

38. "Handbook of Laser Science and Technology, Volume III, Optical Materials: Part I", Marvin J. Weber, CRC Press Inc., pp. 12 (1986).

39. "Optical Waves in Crystals", A. Yariv, John Wiley & Sons, pp. 524 (1984).

40. H. P. Weber, "Method for pulsewidth measurement of ultrashort light pulses generated by phase-locked lasers using nonlinear optics", J. Appl. Phys., **38**, pp. 2231 (1967).

41. "Temperature Dispersion in ADP, KDP, and KD*P for Nonlinear Devices", G. C. Ghosh and G. C. Bhar, IEEE Journal of Quantum Electronics, Vol. **QE-18**, pp. 143 (1982).

CHAPTER 4

PICOSECOND OPERATION OF CHROMIUM-DOPED FORSTERITE LASER

4.1. Introduction

The generation of ultrashort pulses from a mode-locked chromium doped forsterite laser is of great technological importance. Many applications are possible such as imaging through tissues, second harmonic generation, semiconductor alloy research, and optical communications.[1] Forsterite laser is the only system that offers wide tunability in the near infrared from 1130-1367 nm. Mode-locked laser system demand careful design. Some of the requirements are the complete elimination of reflections from various components inside the laser resonator. Similar attention should be given to avoid back reflections in the resonator from optical elements located outside the laser cavity. Another key point is to choose a cavity design that provides an intracavity focus where the modal beam is highly concentrated to less than 100 μm. This small spot is demanded by pumping requirements for lasers with small gain coefficients and short lasing level lifetimes.

This chapter describes the different cavity designs used in the mode-locking experiments of the forsterite laser resulting in the generation of picosecond pulses. In section 4.2, the theory and numerical calculations of the most important characteristics of different cavity designs such as stability range, location and size of the beam waist are presented. Section 4.3 deals with tuning of the forsterite laser and the design of a three

stage birefringent filter suitable for tuning the forsterite laser. Synchronously pumped and active mode-locking are presented in sections 4.4 and 4.5, respectively.

4.2. Optical Resonators

Cavity designs used for mode-locking of low gain, end pumped solid state lasers must meet certain requirements for efficient, and lowest order transverse mode operation. These requirements are:

1. the gain medium should be long enough to absorb a large fraction of the pump light,[2]
2. small beam waist in the laser medium (<100 μm),
3. the radius of the pump beam must be less than or equal to the fundamental mode radius,[3,4] and
4. compensates for the astigmatic effects introduced by the use of a Brewster angled components in the laser resonator.

Resonators that satisfy the tight focusing requirement are cavities with internal lenses or focusing mirrors. Figure 4.2.1 shows a resonator with internal lenses and folded cavities with focusing mirrors which are equivalent to cavities with internal lenses and avoid the reflective losses of lenses. Another advantage of folded cavity designs is that they may be design to compensate for the astigmatic effects introduced by the use of Brewster angled elements in the cavity such as Brewster-angled gain medium or birefringent plates.

4.2.1. Analysis of Multi-Element Laser Resonators

The analysis of a complicated multielement paraxial resonator can be achieved based only on the knowledge of the round trip ABCD matrix and by requiring that the mode reproduces itself after one round trip in the resonator. The round trip matrix is the

ordered product of the 2x2 ABCD matrices corresponding to the individual optical elements in the resonator. Some examples of 2x2 matrices that will be used later are listed in table 4.2.1.

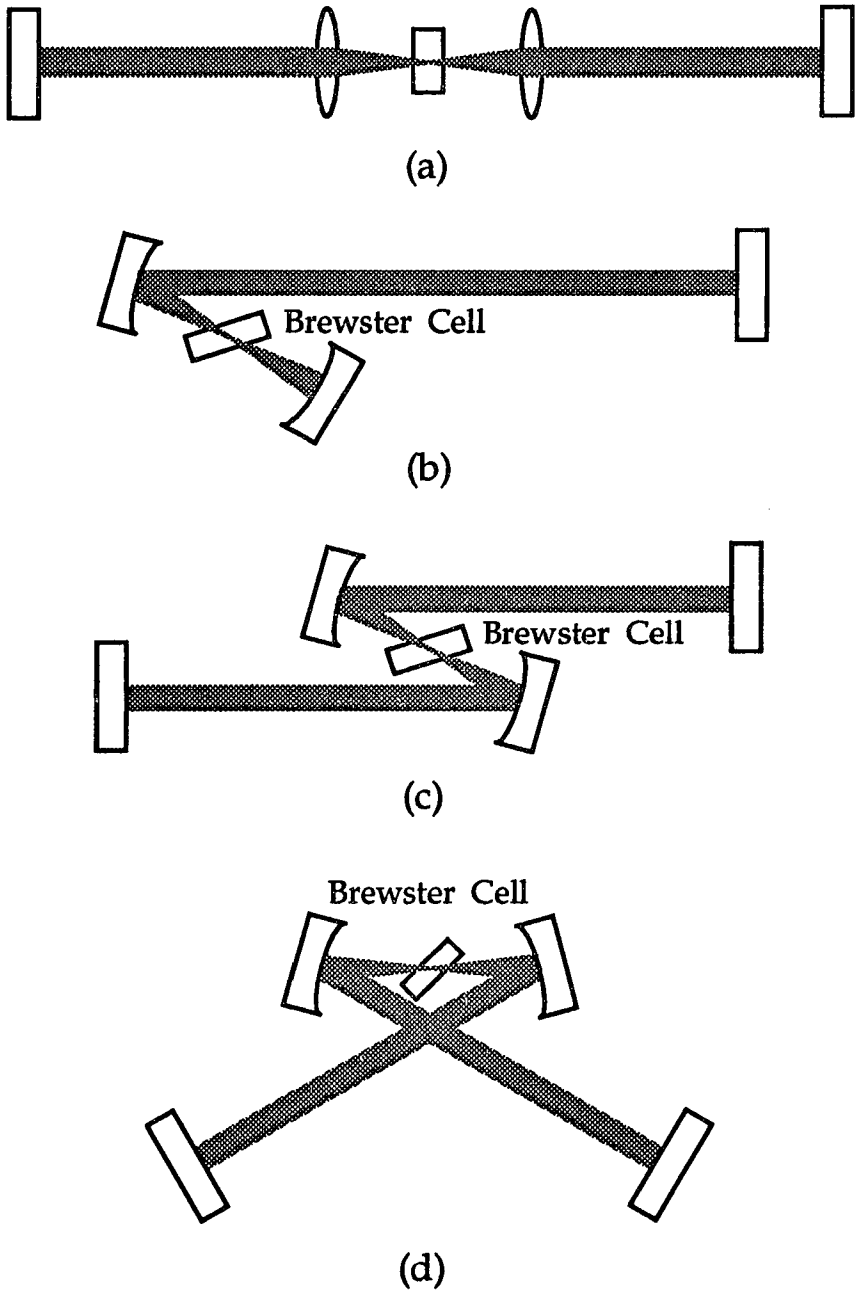

Fig. 4.2.1. Examples of cavity designs which offer tight focusing. (a) Two mirrors with internal lenses, (b) Three mirror astigmatically compensated cavity, (c) Four mirror z-fold astigmatically compensated cavity, (d) Four mirror x-fold astigmatically compensated cavity.

Table 4.2.1. ABCD matrices for various optical systems.[5,6]

"Free Space" region, index n_o, length d $\begin{bmatrix} 1 & d/n_o \\ 0 & 1 \end{bmatrix}$	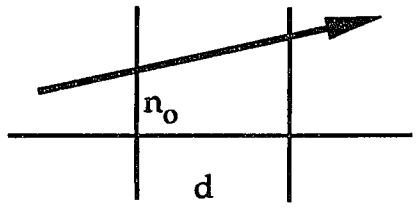
Spherical Mirror (normal incidence) : Radius of curvature R (R>0 for concave mirror) $\begin{bmatrix} 1 & 0 \\ -2/R & 1 \end{bmatrix}$	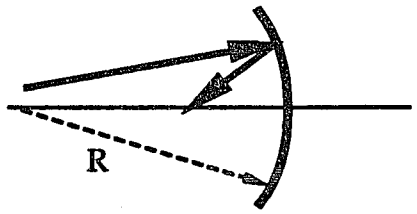
Curved Mirror, arbitrary incidence $R_e = R\cos\theta$ in the plane of incidence $R_e = R/\cos\theta$ for the plane perpendicular to the plane of incidence $\begin{bmatrix} 1 & 0 \\ -2/R_e & 1 \end{bmatrix}$	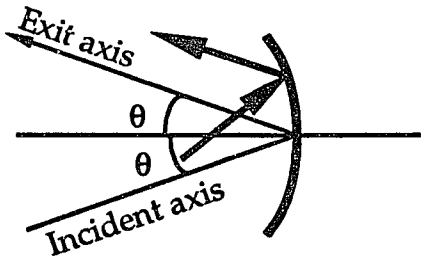
xz plane: $\begin{bmatrix} 1 & \frac{tn^2(1-\sin^2\theta_1)}{(n^2-\sin^2\theta_1)^{3/2}} \\ 0 & 1 \end{bmatrix}$ yz plane: $\begin{bmatrix} 1 & \frac{t}{(n^2-\sin^2\theta_1)^{1/2}} \\ 0 & 1 \end{bmatrix}$ If angle θ_1 is the Brewster angle xz plane: $\begin{bmatrix} 1 & \frac{t}{n^3\sin(\tan^{-1}n)} \\ 0 & 1 \end{bmatrix}$ yz plane: $\begin{bmatrix} 1 & \frac{t}{n\sin(\tan^{-1}n)} \\ 0 & 1 \end{bmatrix}$	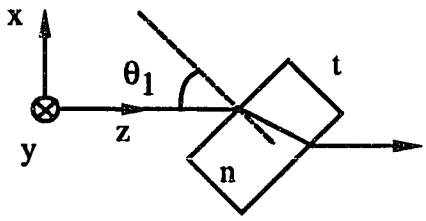 t - the plate thickness n - the plate's refractive index θ_1 - Angle of incidence

The propagation of gaussian beams can be described by defining a complex beam parameter "q" [5]

$$\frac{1}{q} \equiv \frac{1}{R} - i\frac{\lambda}{\pi\omega^2 n} \qquad (4.2.1)$$

where R is the radius of curvature of the wave front, ω is the spot size of the beam, n is the index of refraction of the medium, and λ is the wavelength. The law of propagation of gaussian beam or so called ABCD law is

$$q_2 = \frac{Aq_1 + B}{Cq_1 + D} \qquad \text{or} \qquad \frac{1}{q_2} = \frac{C + D/q_1}{A + B/q_1} \qquad (4.2.2)$$

where A, B, C, and D are the elements of the total 2x2 matrix that describes the optical system that the beam transverse.

The requirements for a physically meaningful gaussian mode in a generalized paraxial resonator are:[7]

1. The q parameter of the mode must be self consistent in one complete round trip.
2. At least one of the two self consistent solutions must be confined (have a finite spot size) in the transverse direction.
3. The confined and self consistent mode must be perturbation stable.

The self consistent condition describes the requirement that the mode must reproduce itself after every round trip in the cavity. In terms of the q parameter this can be expressed as

$$\frac{1}{q_2} = \frac{C + D/q_1}{A + B/q_1} = \frac{1}{q_1} \qquad (4.2.3)$$

The above equation can be rewritten as

$$\left(\frac{1}{q}\right)^2 + \frac{A-D}{B}\left(\frac{1}{q}\right) + \frac{1-AD}{B^2} = 0 \qquad (4.2.4)$$

by using the determinantal relationship

$$AD - BC = 1 \qquad (4.2.5)$$

The solution to the quadratic equation gives two self consistent solutions

$$\frac{1}{q_{a,b}} = \frac{D-A}{2B} \pm \frac{1}{B}\sqrt{\left(\frac{A+D}{2}\right)^2 - 1} \qquad (4.2.6)$$

The two solutions of the quadratic equation q_a and q_b are not necessarily acceptable in a real system and sometimes none of the solutions is acceptable.

The second requirement for a practical resonator is that one of the two self consistent solutions must be confined in the transverse direction. This conditions states that the beam waist in the resonator must have a finite size. By comparing the expression of two self consistent solutions to the definition of the q parameter we require that the second term is an imaginary number. This condition can be expressed as

$$-1 \le \frac{A+D}{2} \le 1 \qquad (4.2.7)$$

The third condition for a stable resonator is that the confined and self consistent mode must be perturbation stable. This is very important since all of the optical systems suffer from imperfections such as mirror coatings, misalignment, and irregularities in the gain medium and other optical components in the cavity. If it is assumed that the q

parameter at the reference plane is perturbed by a small amount δ then after a complete round trip through the resonator the beam parameter can be written as [8]

$$\frac{1}{q_1}+\delta' = \frac{C+D/q_1+\delta D}{A+B/q_1+\delta B} \tag{4.2.8}$$

where δ' is the new perturbation. If the perturbation is small compared to $1/q_1$ the above expression can be simplified to

$$\frac{\delta'}{\delta} = \left(A+\frac{B}{q_r}\right)^{-2} \tag{4.2.9}$$

If the ratio of the new perturbation to the previous perturbation is less than 1 then the disturbance will die out after multiple passes through the resonator. This in terms of the elements of the ABCD matrix can be written as

$$1 \le \left|A+\frac{B}{q_r}\right| \tag{4.2.10}$$

or by using equation (4.2.6)

$$1 \le \left|\frac{A+D}{2} \pm \sqrt{\left(\frac{A+D}{2}\right)^2 - 1}\right| \tag{4.2.11}$$

Note that the same sign should be used for equations (4.2.6) and (4.2.11).

In order to analyze a multielement laser resonator one must select a reference plane inside the resonator, and then evaluate the ABCD matrix for a complete round trip

inside the cavity. The radius of curvature of the confined solution and the beam waist at the chosen reference plane can be evaluated using the expressions[7]

$$R = \frac{2B}{D-A} \tag{4.2.12}$$

$$\omega_2^2 = \frac{|B|\lambda}{\pi}\sqrt{\frac{1}{1-m^2}} \tag{4.2.13}$$

where

$$m \equiv \frac{A+D}{2} \tag{4.2.14}$$

4.2.2. Three Mirror Astigmatically Compensated Cavity Design

The three mirror cavity shown in figure 4.2.1 (b) has been extensively used in dye lasers and it was studied by Kogelnik et. al.[9] The analysis of the three mirror cavity was done by considering the equivalent two mirror cavity with an internal lens. The two mirror cavity with an internal lens can be transformed to a two mirror cavity by using the imaging rules (See figure 4.2.2). The radius of curvature, R_2' and the position of the equivalent mirror, d_2' can be estimated by using the expressions[10]

$$d_2' = \frac{d_2 f}{d_2 - f} \tag{4.2.15}$$

$$R_2' = \frac{R_2 f^2}{(d_2 - f)(d_2 - R_2 - f)} \tag{4..2.16}$$

The stability condition for the two mirror cavity with an internal lens is the same as in the two mirror cavity

$$0 \le g_1 g_2 \le 1 \tag{4.2.17}$$

where g_1 and g_2 are given by[11]

$$g_1 = 1 - \frac{d_2}{f} - \frac{1}{R_1}\left(d_1 + d_2 - \frac{d_1 d_2}{f}\right) \qquad (4.2.18)$$

$$g_2 = 1 - \frac{d_1}{f} - \frac{1}{R_2}\left(d_1 + d_2 - \frac{d_1 d_2}{f}\right) \qquad (4..2.19)$$

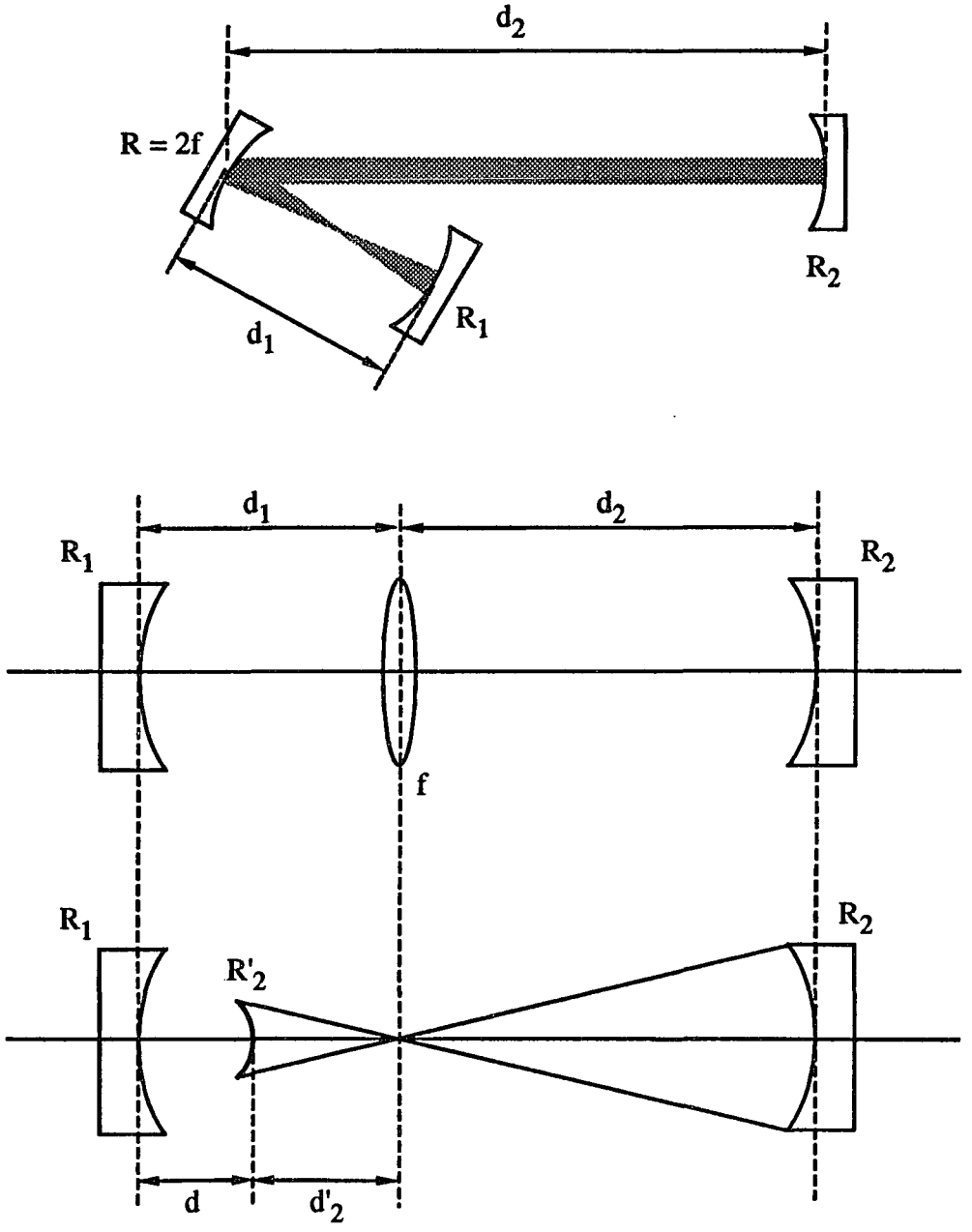

Fig. 4.2.2. Three mirror cavity and equivalent cavity designs.

The stability range of the three mirror cavity was numerically evaluated. The constants used in the calculation correspond to the cavity design used in the mode-locking experiments which are:

$R_1 = 5$ cm $\qquad\qquad$ $d_2 = 180$ cm

$R = 10$ cm ($f = 5$ cm) $\qquad\qquad$ $d_1 = 9$ - 10.7 cm

$R_2 = \infty$ (Flat mirror))

The separation between mirrors R_1 and the folding mirror R was varied from 9 to 10.7 cm. Figure 4.2.3 shows the position of the three mirror cavity in the stability diagram as the separation between the two mirrors is varied.

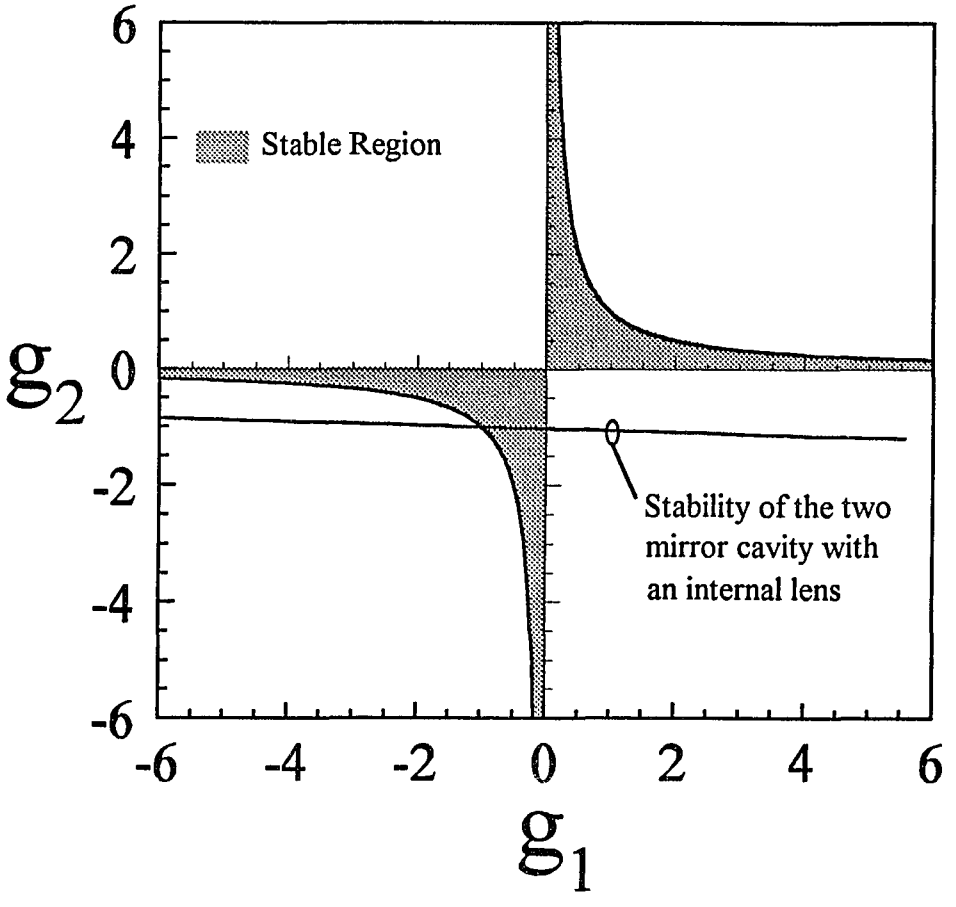

Fig. 4.2.3. Stability Diagram of a two mirror cavity with an internal lens which is equivalent to a three mirror cavity.

As it can be seen from figure 4.2.3 the cavity goes from the unstable to the stable and then back to the unstable region for only a 1.7 cm change in this separation. The three mirror cavity lies in the stable region for only ± 0.85 mm from the center of the stability range. This is indicative of the difficulty involved in the alignment of a three mirror cavity .

One of the advantages of the three mirror cavity as compared with the two mirror cavity is that the three mirror cavity can be designed to compensate for astigmatism. Astigmatism results from the use of folding mirrors or Brewster angled optical components in the cavity. As a result of astigmatism the beam has different spatial distribution in the xz and yz planes. A folded three mirror cavity contains a minimum of two astigmatic elements which are the folding mirror and the brewster cell. The basic idea in the three mirror cavity design is to offset the astigmatism introduced by the Brewster angled laser medium by selecting an appropriate angle for the folding mirror.

The astigmatism introduced by the folding mirror is given by

$$f_{xz} = \frac{f}{\cos\theta} \tag{4.2.20}$$

$$f_{yz} = f.\cos\theta \tag{4.2.21}$$

where θ is the folding angle of the mirror as indicated in figure 4.2.4. The astigmatism introduced by the Brewster cell is determined by

$$d_{xz} = \frac{t\sqrt{n^2+1}}{n^2} \tag{4.2.22}$$

$$d_{yz} = \frac{t\sqrt{n^2+1}}{n^4} \tag{4.2.23}$$

where n is the index of refraction of the laser medium and t is the thickness as shown in figure 4.2.4.

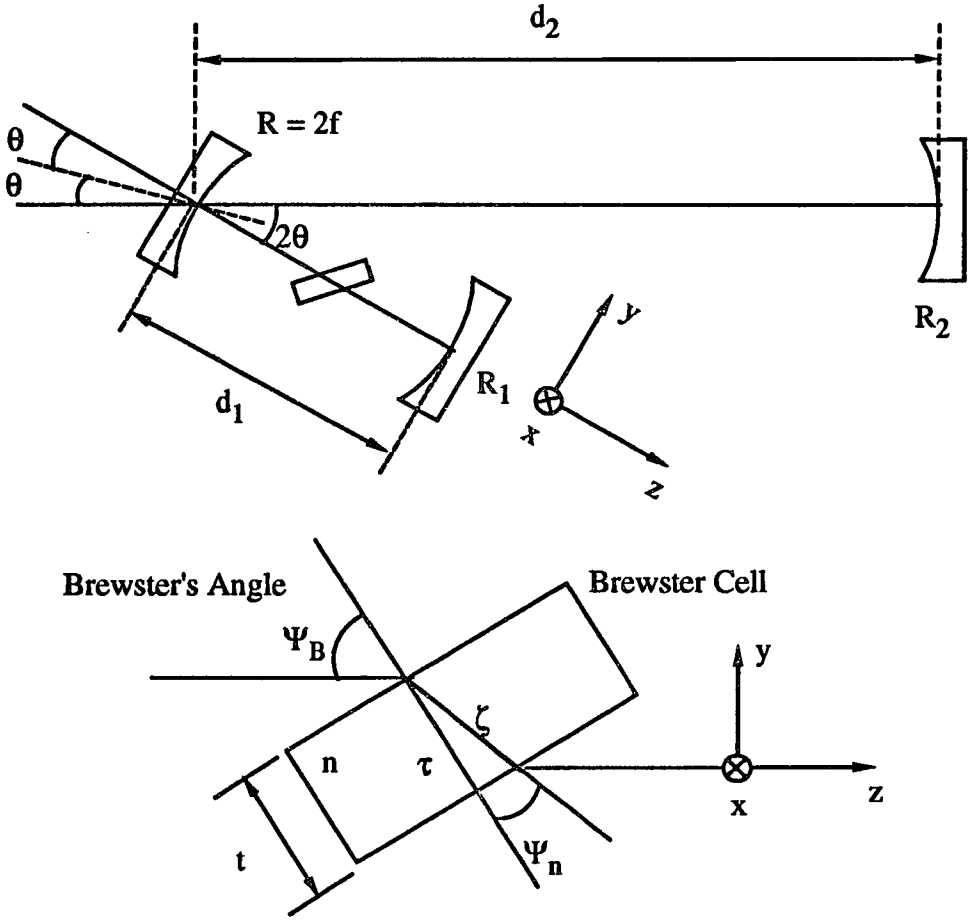

Fig. 4.2.4. Three mirror cavity design, θ is the folding angle, Ψ_B is the brewster angle for the gain medium, and t the thickness of the gain medium.

The expression relating the thickness of the Brewster laser medium to the angle of incidence in the folding mirror for astigmatic compensation is[9]

$$2t\left(\frac{\left(n^2-1\right)\sqrt{n^2+1}}{n^4}\right)=2f\sin\theta\tan\theta \qquad (4.2.24)$$

Expression 4.2.24 was used to calculate the folding angle corresponding to different thicknesses of the forsterite crystal and different radius of curvature folding mirrors. The result of this calculation is shown in figure 4.2.5 where the thickness of the crystal is plotted vs. the angle for astigmatic compensation for three different folding mirrors. The value used for the refractive index in the calculations was n=1.635 corresponding to the b crystallographic axis of Cr:forsterite. The first experiments for mode-locking the forsterite laser employed a three mirror cavity consisting of a folding mirror with radius of curvature of 10 cm and a forsterite crystal with thickness t = 0.85 cm. The angle for astigmatic compensation for this configuration was estimated to be 15.75°.

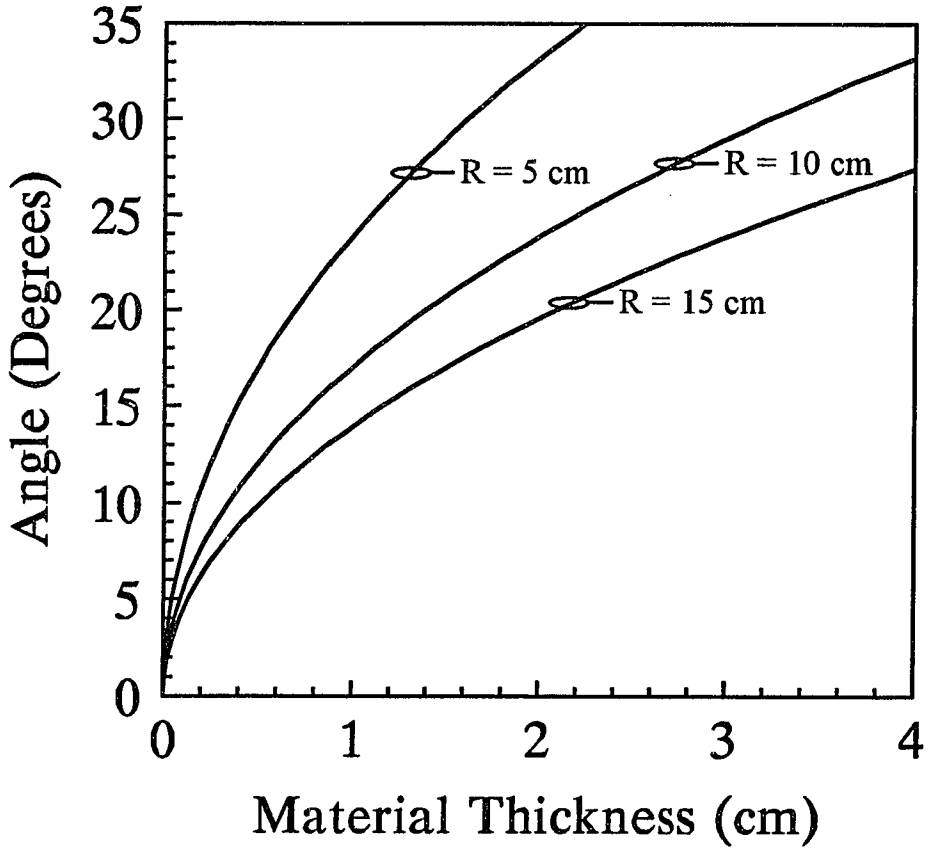

Fig. 4.2.5. Sample thickness vs. folding angle, θ, for the forsterite laser for various radius of curvature of the folding mirror.

Further analysis of the three mirror cavity should be performed separately for the xz (sagittal) and yz (tangential) planes since the resonator behaves differently in the two planes.

The size of the minimum beam waist and its location with respect to mirror R_1 can be estimated using the expressions derived in ref. 9. The minimum beam waist is given by the expression

$$\left(\frac{\pi\omega_0^2}{\lambda}\right) = \frac{d(R_1 - d)\left(R_2' - d\right)(R_1 + R_2 - d)}{(R_1 + R_2 - 2d)^2} \qquad (4.2.25)$$

and the distance of the minimum beam waist from the input mirror R_1 using

$$t_1 = \frac{d\left(R_2' - d\right)}{(R_1 + R_2 - 2d)^2} \qquad (4.2.26)$$

A computer program was written to determine the characteristics of the three mirror cavity design. In the program it was assumed that the cavity consisted of three mirrors with radii of curvature R_1 = 5 cm, R = 10 cm, and R_2 was flat (see figure 4.2.4). The folding angle was set to θ = 15.75° corresponding to astigmatic compensation of an 0.85 cm forsterite crystal. The program first calculated the equivalent mirror curvatures and equivalent distances for the xz and yz planes using eqs. 4.2.20-4.2.23. The stability range for the two planes was next determined. Finally the separation between the folding mirror and mirror R_1 was varied according to the stability ranges and the size of the beam waist and its location with respect to mirror R_1 were evaluated using eqs. 4.2.25 and 4.2.26. Note that eqs. 4.2.25 and 4.2.26 used once for the xz and once for the yz planes.

The results of the computer simulation are shown in figure 4.2.6 and 4.2.7. Figure 4.2.6 shows the position of the minimum beam waists relative to mirror R_1 as a function of the separation between mirror R_1 and the folding mirror. The positions of the minimum beam waists in the two planes are located very close to the center of mirror R_1. The problem is that for a specific mirror separation the location of the minimum beam waists is different for the xz and yz planes. The relation between the mirror separation and the size of the minimum beam waists is shown in figure 4.2.7. The size of the minimum beam waists is smaller than 20 μm but again for a specific mirror separation the size of beam waist in the xz plane is different than the one for yz planes.

The numerical calculations performed so far indicated that the position of the minimum beam waist and its size do not change significantly within the stability region of the three mirror cavity. Further analysis of the three mirror cavity is necessary to determine how the beam behaves inside the brewster angled gain medium. This is necessary in order to determine how the pump beam should be focused inside the laser medium for better match between the pump and the cavity mode. According to the results obtained so far it is assumed that the beam at the entrance of the gain medium is given by

$$\omega_{xz} \approx \omega_{yz} \approx \omega_o \tag{4.2.27}$$

$$t_{1xz} \approx t_{1yz} \approx R_1 \tag{4.2.28}$$

Just after entering the gain medium the beam radii for the xz and yz planes are given by

$$\omega_{xz} = \omega_o \quad \text{and} \quad \omega_{yz} = n\omega_o \tag{4.2.29}$$

where it was assumed that the gain medium is positioned at Brewster's angle.

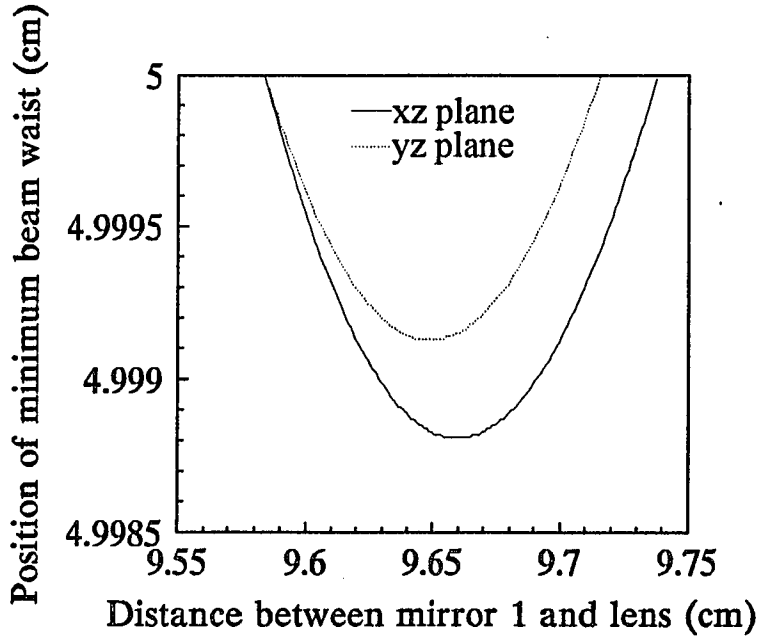

Fig. 4.2.6. Position of the beam waist versus the separation between mirrors R_1 and R_2.

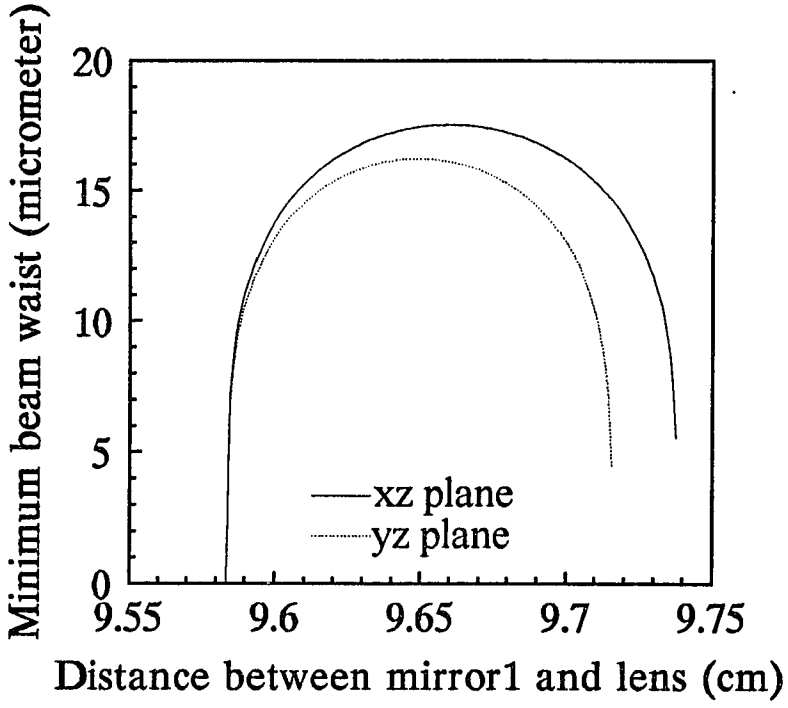

Fig. 4.2.7. Size of minimum beam waist versus the separation between mirrors R_1 and R_2.

Assuming gaussian beams and using the laws of propagation and expansion of gaussian beams, the beam waist inside the laser medium after propagating a distance ζ in the cell (See figure 4.2.4) is given by [9]

$$\omega_{xz}(\zeta) = \omega_0\sqrt{1+\left(\frac{\lambda\zeta}{\pi n\omega_0^2}\right)^2} \tag{4.2.30}$$

$$\omega_{yz}(\zeta) = \omega_0 n\sqrt{1+\left(\frac{\lambda\zeta}{\pi n^3\omega_0^2}\right)^2} \tag{4.2.31}$$

where the distance ζ is given by

$$\zeta = \frac{\tau\sqrt{n^2+1}}{n} \tag{4.2.32}$$

The beam area inside the laser medium can be approximated by

$$A(\zeta) = \pi\omega_{xz}(\zeta)\omega_{yz}(\zeta) \tag{4.2.33}$$

Equations (4.2.30), (4.2.31), and (4.2.33) were numerically evaluated for the case of a 0.85 cm thick forsterite crystal and the results are shown in figures 4.2.8 and 4.2.9. Figure 4.2.8 shows the variation of the beam size inside the laser medium as a function of the distance inside the forsterite crystal for the xz and yz planes. As it can be seen from this figure the beam has its minimum waist at different positions for the two planes. The minimum beam waist in the xz plane is formed 4.4 mm away of the position of the minimum waist in the yz plane. The result of this discrepancy is also shown in figure 4.2.9 where the beam area is plotted as a function of the position in the forsterite crystal. The irregularity of the beam area in the lasing medium is the major disadvantage of the

three mirror cavity design since it would be very hard to match the cavity mode with the pumping mode.

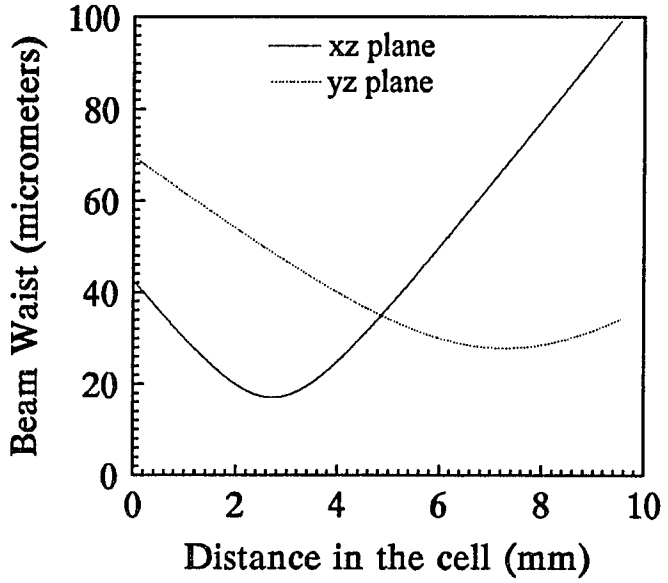

Fig. 4.2.8. Position of minimum beam waist for the xz and yz plane and in the forsterite crystal when placed in a three mirror astigmatically compensated cavity.

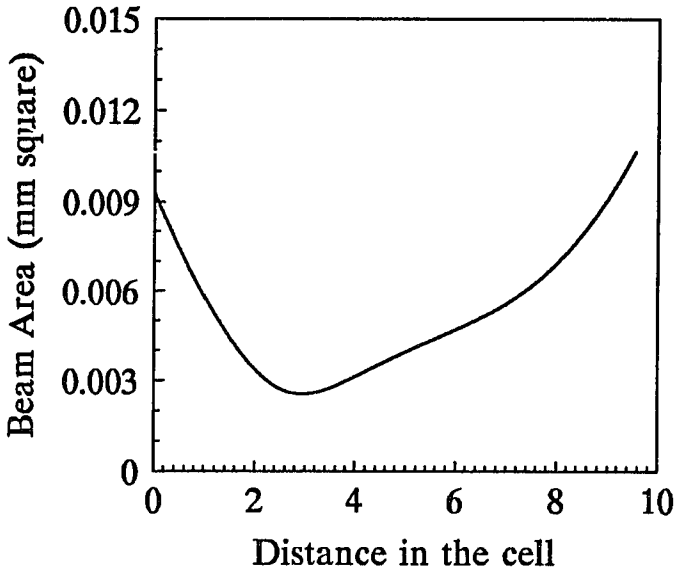

Fig. 4.2.9. Beam area in the forsterite crystal as a function of distance in the forsterite crystal.

4.2.3. Four Mirror Astigmatically Compensated Cavity Design

The major disadvantage of the three mirror cavity is that when is used with long samples the beam area inside the gain medium is not uniform. This problem can be overcome by using a four mirror z-fold astigmatically compensated cavity. The z-fold astigmatically compensated cavity design takes advantage of symmetry to force the beam size in the xz and yz planes to be simultaneously minimum at the same spatial position in the laser medium[12]. This section describes the analysis of a four mirror cavity using the method described in section 4.2.1.

The z-fold four mirror cavity design is shown in figure 4.2.10. The four mirror cavity can be thought of as a combination of two three mirror cavities as shown in figure 4.2.10. One three mirror cavity consists of mirrors R_1, R_2, and a flat mirror positioned at the image plane and the other consists of mirrors R_4, R_3 and the flat mirror at the image plane. Both cavities use half of the gain medium. The folding angles of the mirrors R_2 and R_3 that compensate for astigmatism can be estimated using eq. 4.2.24, except that in the case of the four mirror cavity half of the thickness of the laser medium should be used. Numerical calculations were performed using eq. 4.2.24 to estimate the folding angle for mirrors R_2 and R_3 to achieve astigmatic compensation in the four mirror z-fold cavity. In the calculations it was assumed that $R_2 = R_3$. Figure 4.2.11 shows the folding angle as a function of the laser crystal thickness in the case of the forsterite laser and assuming different values for the radius of curvature of the folding mirrors.

Four forsterite crystals were used during the mode-locking experiments in combination with the four mirror z-fold cavity design. The radius of curvature of the two folding mirrors was $R_2 = R_3 = 10$ cm. Table 4.2.2 lists the forsterite crystals, their dimensions and the mirror folding angle for astigmatic compensation.

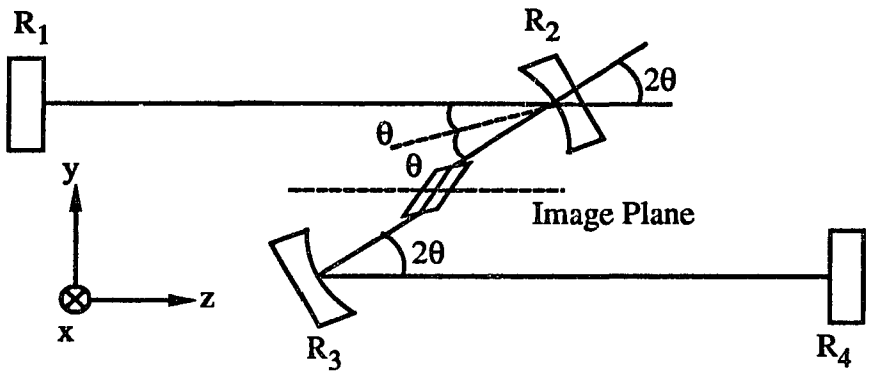

Fig. 4.2.10. Four mirror z-fold astigmatically compensated cavity design. θ is the folding angle of mirrors R_2 and R_3.

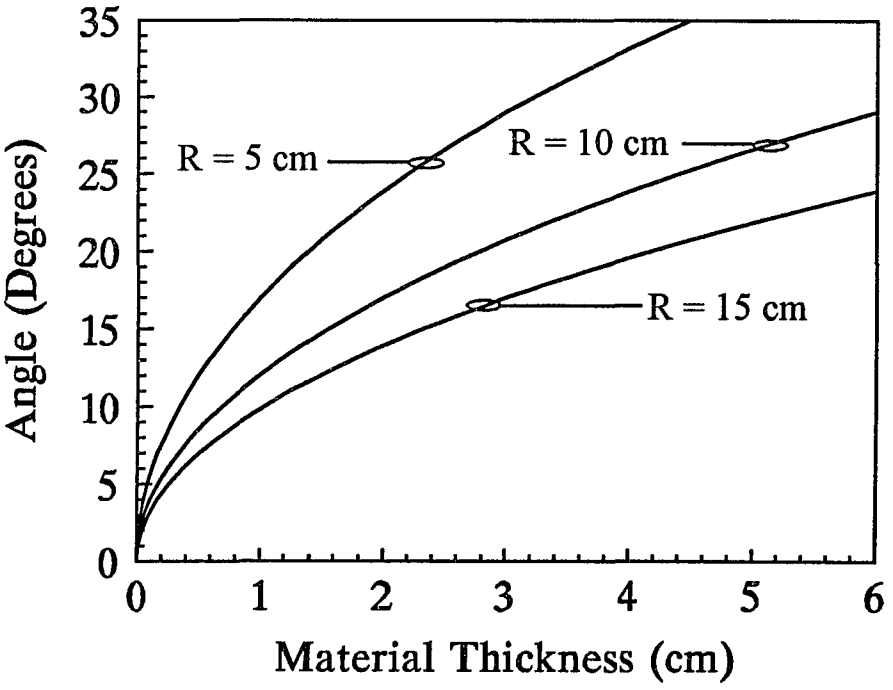

Fig. 4.2.11. Folding angle, θ, vs. forsterite crystal thickness for astigmatic compensation in a four mirror cavity.

Table 4.2.2. Forsterite crystals used in the mode-locking experiments and angles for astigmatic compensation for $R_2 = R_3 = 10$ cm (radius of curvature folding mirrors).

Forsterite Crystal	Dimensions (mm)	Thickness (mm)	Folding Angle for Astigmatic Compensation
Crystal 1	8x8x10	8.53	$\theta = 11.17°$
Crystal 2	4x4x10	8.53	$\theta = 11.17°$
Crystal 3	4x4x12	10.23	$\theta = 12.23°$
Crystal 4	5x5x14.4	12.28	$\theta = 13.39°$

The dimensions of the forsterite crystal in column 2 give the length of the crystal, L, as shown in figure 4.2.12. Column 3 lists the thickness of the crystals which is the parameter that was used in eq. 4.2.24 in order to evaluate the folding angles of mirrors R_2 and R_3. The relation between the length and the thickness of the crystal can be estimated using figure 4.2.12 and is given by

$$t = L\cos\theta_{in}$$

where θ_{in} can be estimated using Snell's law and assuming that the angle of incidence is equal to the Brewster's angle.

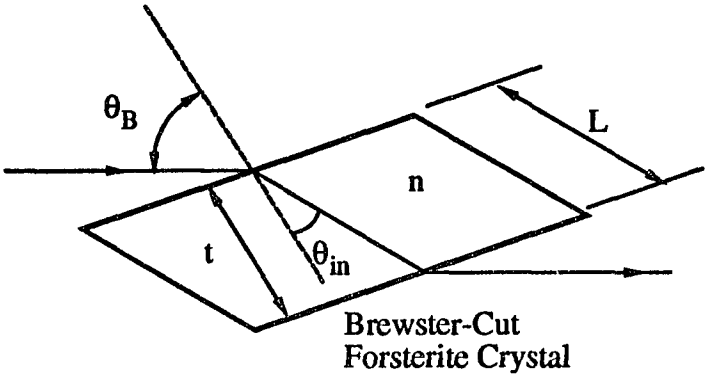

Fig. 4.2.12. Geometry of a brewster-angle gain medium.

Other characteristics of the four mirror cavity can be determined by using the theory presented in section 4.2.1. A computer program was developed to simulate the beam size in the four mirror cavity used in the mode-locking experiments. For the program it was assumed that a 1 cm long chromium-doped forsterite crystal was positioned exactly at the center of the two folding mirrors R_2 and R_3. The round trip ABCD matrix of the four mirror cavity was calculated by choosing a reference plane and following the beam for a complete round trip through the cavity (see figure 4.2.13). The ABCD matrices for various systems are listed in table 4.2.1. Note that this process was performed twice, once for the xz and once for the yz plane since the folding mirrors and the brewster-cut crystal behave differently in the two planes (see table 4.2.1)

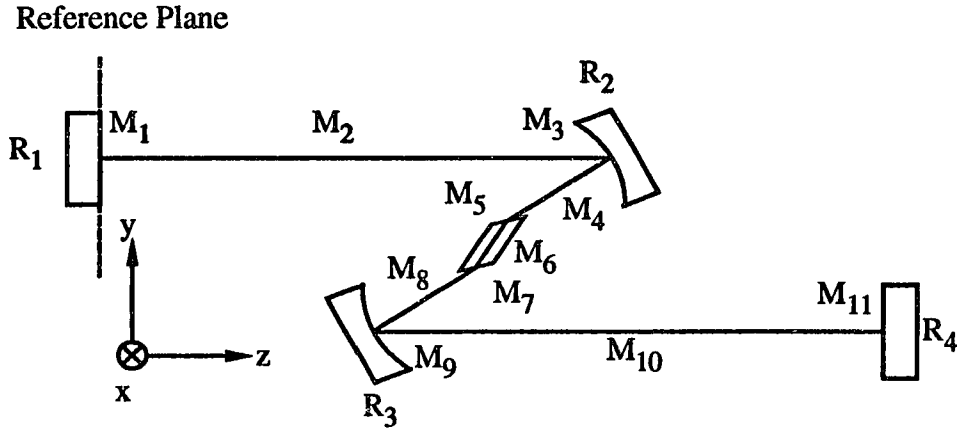

Fig. 4.2.13. Cavity configuration used in the numerical simulation.

The ABCD matrix for a complete round trip through the cavity is given by

$$M_t = M_2M_3M_4M_5M_6M_7M_8M_9M_{10}M_{11}M_{10}M_9M_8M_7M_6M_5M_4M_3M_2M_1$$

where: M_2, M_4, M_8, M_{10} - ABCD matrices for traveling a distance in free space

M_1, M_{11} - ABCD matrices for reflection from a flat mirror

M_9, M_3 - ABCD matrices for reflection from a curved mirror at an arbitrary angle of incidence (Different for the xz and yz planes)

M_5, M_7 - ABCD matrices for interface between air and forsterite crystal

M_6 - ABCD matrix for traveling in the forsterite crystal (Different for the xz and yz planes)

The stability range of the four mirror z-fold cavity design was determined next. This was done by determining the separation between mirrors R_2 and R_3 for which the self consistent and perturbation stable requirements, eqs. 4.2.7 and 4.2.11 were satisfied. The four mirror cavity is stable for ~± 1 mm from optimum separation between mirrors R_2 and R_3 which is similar to the three mirror cavity design .

When the stability range was determined, the distance between the folding mirrors was chosen around the center of the stability range and another program was written to calculate the size of the beam waist at any point inside the resonator. This was done by moving the reference plane through out the cavity and calculating the total ABCD matrix for the new reference plane. Then the beam waist at the reference plane was estimated using eq. 4.2.13.

The results of the calculations are shown in figures 4.2.14 and 4.2.15. Figure 4.2.14 shows the size of the beam waist as a function of the position in the cavity while figure 4.2.15 is a magnified version of figure 4.2.14 showing the behavior of the beam inside the forsterite crystal. Considering figure 4.2.14 the beam waist at zero or at mirror R_1 has a value of about 600 μm and is the same for the xz and yz planes. This fact can serve as an indication when aligning the four mirror cavity. A nice round output beam is indicative of astigmatic compensation while an elliptical beam at the output indicates that the folding angle is off the optimum value. The beam waist increases from 600 μm to 800

μm as it moves 85 cm from mirror R_1 to the folding mirror R_2. Still at mirror R_2 there is good agreement in the size in the xz and yz planes. Mirror R_2 has a radius of curvature of 10 cm, forcing the beam to focus 5 cm away from the mirror inside the forsterite crystal. As it can be seen from figure 4.2.15 the beams inside the forsterite laser have their minimum waist at exactly the same spot. The beam in the yz plane gets distorted when enter the forsterite crystal as indicated in eq. 4.2.29. Once the beam comes out of the forsterite crystal expands rapidly up to mirror R_3 which collimates the beam. Finally the beam moves from mirror R_3 to R_4 where it gets reflected and the same transformations are repeated.

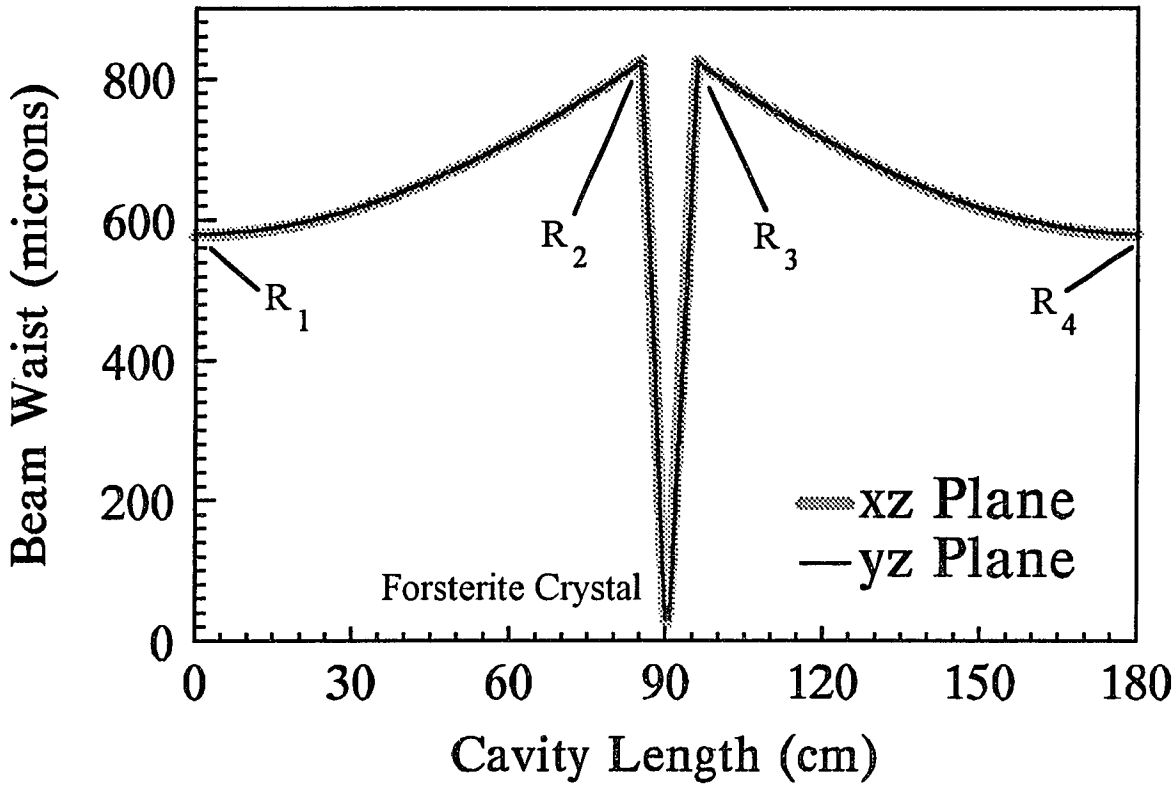

Fig. 4.2.14. Beam waist vs. position in the four mirror, z-fold, astigmatically cavity design.

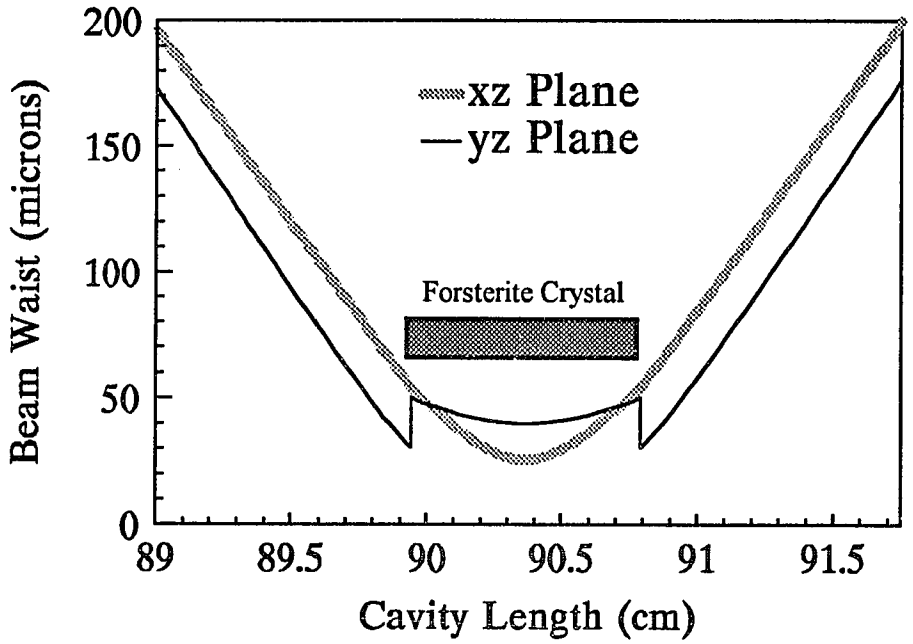

Fig. 4.2.15. Beam waist vs. position in the forsterite crystal for the four mirror, z-fold, astigmatically cavity design.

In order to be able to compare the results obtained from the analysis of the four mirror cavity design with the three mirror cavity the same computer program was modified to correspond to the three mirror cavity. For this program a 1 cm long brewster-cut forsterite crystal was placed in a three mirror cavity with R_1 = 5 cm, R = 10 cm, R_2 = flat (see figure 4.2.4) and the same procedure as with the four mirror cavity was repeated. The results of this simulation are shown in figures 4.2.16 and 4.2.17. Figure 4.2.16 shows the size of the beam waist as a function of the position in the cavity while figure 4.2.17 is a magnified version of figure 4.2.16 showing the behavior of the beam inside the forsterite crystal.

By comparing figures 4.2.15 with 4.2.17 it is clear that a four mirror z-fold cavity design has better mode characteristics as compared to the three mirror cavity. The four mirror cavity compensates for the astigmatic effects introduced by the brewster forsterite crystal and also offers a uniform mode area in the forsterite crystal. The cavity mode can be easily matched with the pump mode. In the three mirror cavity design the minimum

beam waists for the two planes are formed at different positions in the forsterite crystal resulting in a non uniform mode area making hard to match pump and cavity modes. Sub-100-μm beam size is achieved using either cavity configuration.

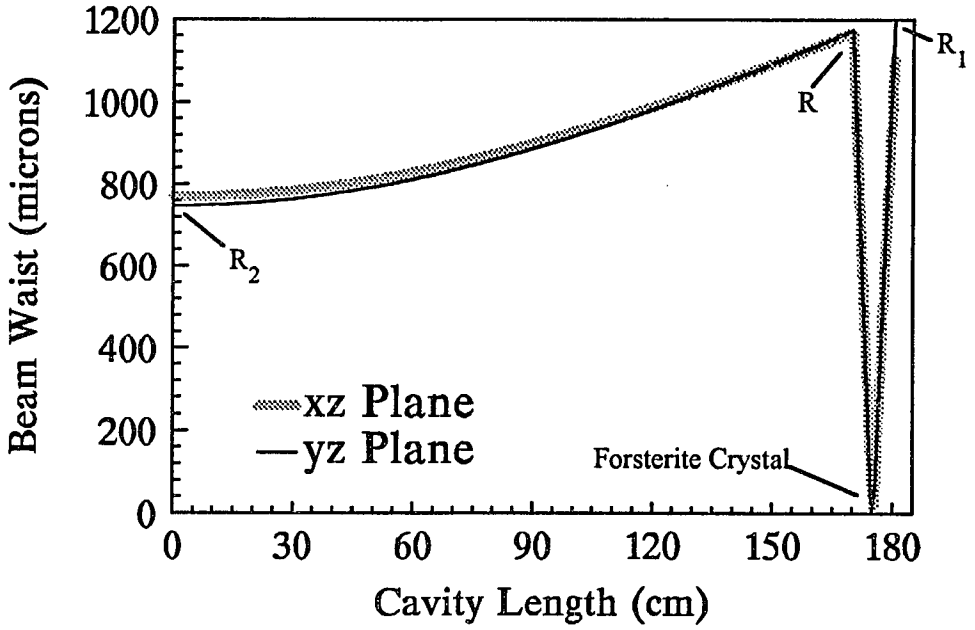

Fig. 4.2.16.Beam waist vs. position in the three mirror astigmatically compensated cavity design.

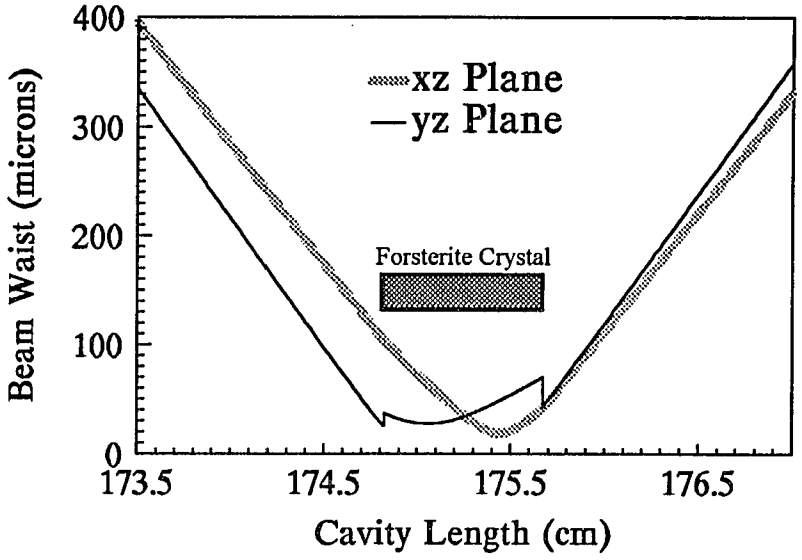

Fig. 4.2.17Beam behavior inside the forsterite crystal in the three mirror astigmatically compensated cavity design.

4.3. Tuning Using a Birefringent Crystal

Wavelength selection in the Cr:forsterite laser can be accomplished by using a birefringent filter or a prism inside the laser cavity as shown in figure 4.3.1. The reported tuning range of the Cr:forsterite laser extends from 1130 to 1367 nm. This section reviews the theory of tuning using a birefringent filter and presents results from numerical evaluations of specific birefringent filter design suitable for the Cr:forsterite laser.

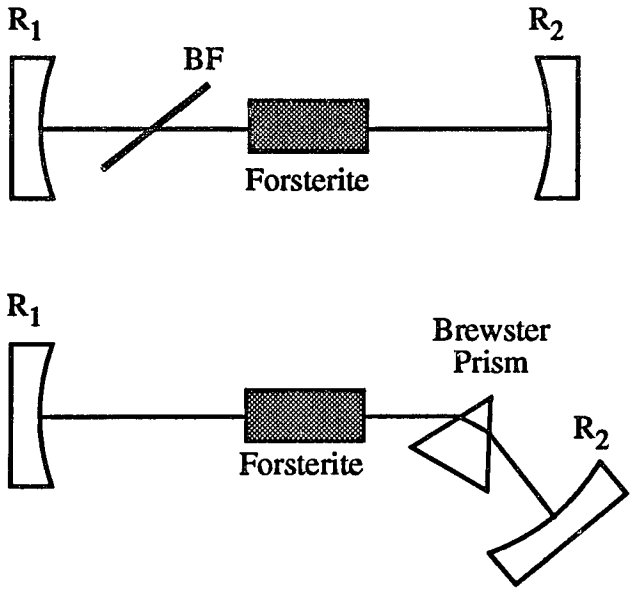

Fig. 4.3.1. Different methods for tuning the Cr:forsterite laser.

Tuning using a birefringent filter is taking advantage of the fact that a laser can operate only with the polarization that is transverse magnetic (TM) with respect to any intracavity elements oriented at Brewster's angle. Incident radiation on a single birefringent crystal that is polarized TM is transformed into some elliptical polarization composed of both TM and TE linear polarization components. As a result the TE polarized component stops lasing when it encounters the brewster cells in the cavity.

The way that a single birefringent plate can be used to tune a laser is illustrated in Figure 4.3.2. In figure 4.3.2(a) the plate is perpendicular to the ray axis and the optic axis

is aligned with the x-axis. With this plate orientation, light linearly polarized in the x direction will experience a refractive index n_e, and light polarized in the y direction will experience a refractive index n_o. The effect of the plate in this orientation is only to retard the phases of the x and y linearly polarized components. The intensities of these two components are unchanged. In figure 4.3.2 (b) the plate is rotated about the y axis by an angle (90°- Θ), so that the optic axis makes an angle Θ with the ray axis (z). Again at this orientation the plate serves only to retard the two polarized components.

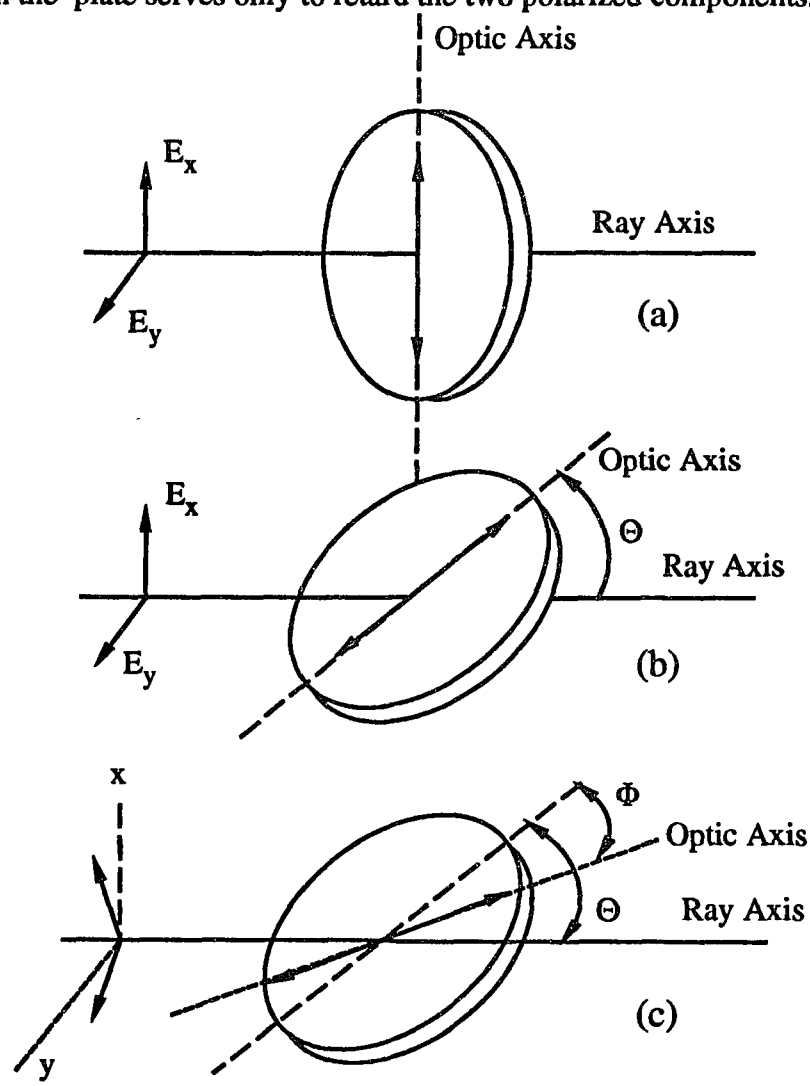

Fig. 4.3.2. Plate tilted by Θ degrees and rotated by Φ degrees.

A further rotation by an angle Φ about an axis perpendicular to the surface of the plate as shown in figure 4.3.2 (c) changes the polarizations of the x and y linear components. Using Jones matrix representation for the polarized fields and following the changes of the plate described so far, the Jones matrix for the final orientation is given by[13]

$$M(\Theta,\Phi) = \left[n_o^2 - \cos^2\Phi\cos^2\Theta\right]^{-1}$$

$$\begin{bmatrix} \exp(i\delta_e)\left(n_o^2 - \cos^2\Theta\right)\cos^2\Phi + \exp(i\delta_o)n_o^2\sin^2\Phi & \\ \left(\exp(i\delta_e) - \exp(i\delta_o)\right)n_o\sin\Phi\cos\Phi\left(n_o^2\cos^2\Theta\right)^{0.5} & \\ \left(\exp(i\delta_e) - \exp(i\delta_o)\right)n_o\sin\Phi\cos\Phi\left(n_o^2\cos^2\Theta\right)^{0.5} & \\ \exp(i\delta_e)n_o^2\sin^2\Phi + \exp(i\delta_o)\left(n_o^2 - \cos^2\Theta\right)\cos^2\Phi & \end{bmatrix} \qquad (4.3.1)$$

where

$$\delta_e(\Theta,\Phi) = \frac{2\pi n_e t}{\lambda}\frac{\left[1 + \dfrac{\cos^2\Phi\cos^2\Theta}{n_e^2} - \dfrac{\cos^2\Theta\cos^2\Phi}{n_o^2}\right]}{\left[1 - \dfrac{\cos^2\Theta\sin^2\Phi}{n_e^2} - \dfrac{\cos^2\Theta\cos^2\Phi}{n_o^2}\right]} \qquad (4.3.2)$$

$$\delta_o(\Theta,\Phi) = \frac{2\pi n_o t}{\lambda}\left[1 - \frac{\cos^2\Theta}{n_o^2}\right]^{0.5} \qquad (4.3.3)$$

When a TM linearly polarized electric field is incident on the birefringent filter as shown in figure 4.3.2 (c) then the electric field that reaches the exit surface of the plate can be described by the relation

$$\begin{bmatrix} E_{TE} \\ E_{TM} \end{bmatrix} = M(\Theta,\Phi)\begin{bmatrix} 0 \\ 1 \end{bmatrix} \qquad (4.3.4)$$

The amplitude of the emerging TM-polarized component of the electric field is given by

$$E_{TM} = \frac{1}{n_o^2 - \cos^2\Phi\cos^2\Theta}\left[\exp(i\delta_e)n_o^2\sin^2\Phi + \exp(i\delta_o)(n_o^2 - \cos^2\Theta)\cos^2\Phi\right] \quad (4.3.5)$$

The intensity of the emerging field is

$$I_{TM} = E_{TM}E_{TM}^{*} \quad (4.3.6)$$

$$= 1 - \sin^2(2\Phi)\frac{n_o^4 - n_o^2\cos^2\Theta}{\left(n_o^2 - \cos^2\Phi\cos^2\Theta\right)^2}$$

$$\sin^2\left(\left(\frac{\pi t}{\lambda}\right)\frac{n_e\left[1 + \frac{\cos^2\Phi\cos^2\Theta}{n_e^2} - \frac{\cos^2\Theta\cos^2\Phi}{n_o^2}\right]}{\left[1 - \frac{\cos^2\Theta\sin^2\Phi}{n_e^2} - \frac{\cos^2\Theta\cos^2\Phi}{n_o^2}\right]^{0.5}} - \left(\frac{\pi t}{\lambda}\right)\frac{n_o}{\left[1 - \frac{\cos^2\Theta}{n_o^2}\right]^{0.5}}\right)$$

By inspecting the above relation the birefringent plate will neither altered nor attenuated the incident TM-polarized rays if one of two conditions is satisfied

$$\Phi = \frac{m}{2\pi} \quad (4.3.7)$$

$$\frac{t}{\lambda}\left(\frac{n_e\left[1 + \frac{\cos^2\Phi\cos^2\Theta}{n_e^2} - \frac{\cos^2\Theta\cos^2\Phi}{n_o^2}\right]}{\left[1 - \frac{\cos^2\Theta\sin^2\Phi}{n_e^2} - \frac{\cos^2\Theta\cos^2\Phi}{n_o^2}\right]^{0.5}} - \frac{n_o}{\left[1 - \frac{\cos^2\Theta}{n_o^2}\right]^{0.5}}\right) = m \quad (4.3.8)$$

where m is an integer. The first condition leads to an I_{TM} of unity for all wavelengths and does not give rise to any frequency selectivity. The second condition is a function of wavelength and the position of the plate and therefore allows control of the frequency.

During the tuning experiments performed with the Cr:forsterite laser a single plate quartz birefringent filter was used. The plate was 0.51342 mm thick and it was made of crystalline quartz which is a positive uniaxial birefringent crystal (the quartz crystal has a single optic axis, and the refractive index for an ordinary ray is smaller than that for an extraordinary ray). The refractive indices for the two axis 1307 nm are[14]

$$n_e = 1.53951 \qquad \text{and} \qquad n_o = 1.53090$$

The tuning characteristics of this birefringent plate were evaluated by solving eq. 4.3.8 Angle Θ was set to

$$\Theta = \frac{\pi}{2} - \Theta_B = 33.006^\circ \qquad (4.3.9)$$

corresponding to a ray incident at Brewster's angle. The results of the numerical calculations are shown in figure 4.3.3 where angle Φ is plotted versus wavelength for which for which there is no loss in the polarized rays by passing through the birefringent plate. As is shown in figure 4.3.3 a single plate filter made of quartz can tune through the whole tuning range of the forsterite laser. The transmission of the birefringent filter for a specific setting can be estimated by using equation 4.3.6. Figure 4.3.4 shows the intensity transmission of the filter for $\Theta = 33.006^\circ$ and $\Phi = 45^\circ$. Assuming that wavelengths that suffer 1% loss keep lasing the output of the forsterite laser will have a bandwidth of about 40 nm.

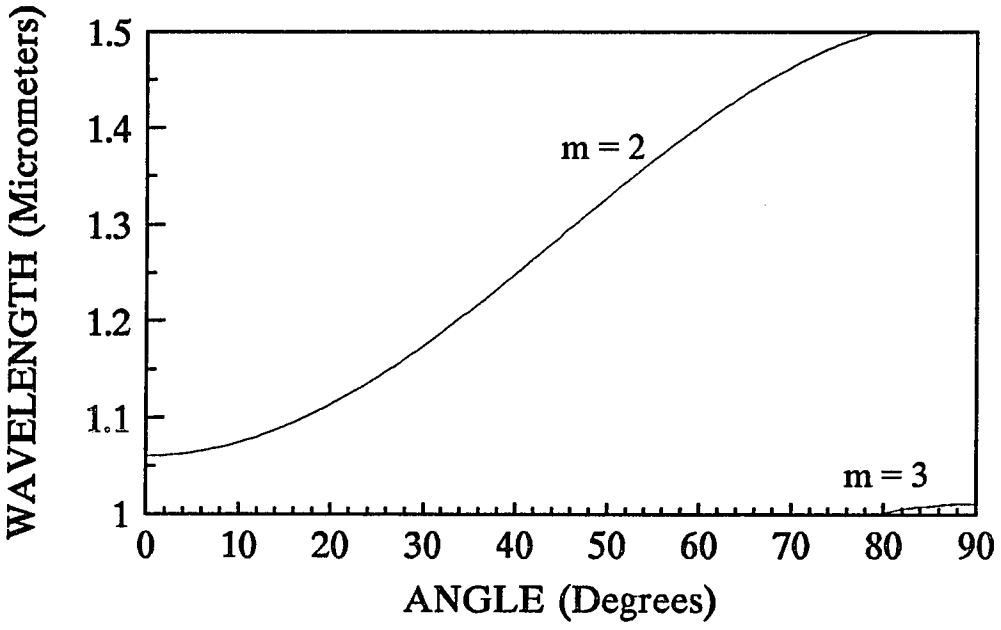

Fig. 4.3.3. Wavelengths that suffer no loss when passing through a single stage quartz birefringent filter as a function of angle Φ, t = 0.5134 mm, and $\Theta = 33.006°$.

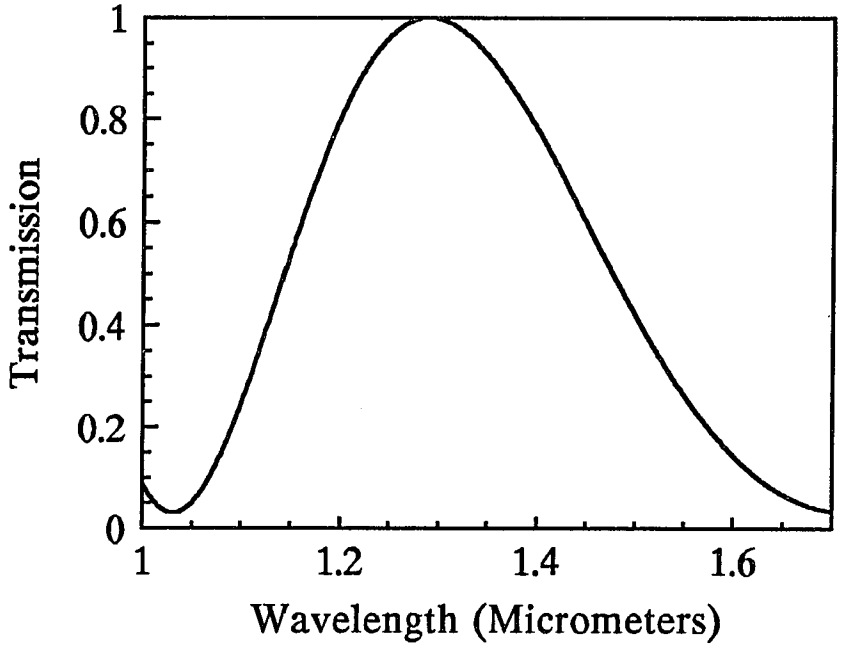

Fig. 4.3.4. Transmission of a single stage birefringent filter assuming t = 0.5134 mm, $\Theta = 33.006°$, and $\Phi = 45°$.

In many applications there is a need for very narrow spectrum. A single stage birefringent filter is not appropriate for such applications since it allows broad bandwidth to be emitted from the laser. Better wavelength control can be achieved by using a three stage birefringent filter made of three plates with different thickness. To compliment the analysis of tuning of the forsterite laser the performance of a three stage birefringent filter was numerically evaluated. The thickness of the plates are chosen to be in a whole number ratio 1:2:15 corresponding to an accepted design for a multiple stage Lyot filter.[15] The thickness of the plates are 0.5134 mm, 1.0268 mm, and 7.7013 mm. Figures 4.3.5 displays the relation between the angle and wavelength for no loss through the birefringent plates with thickness t = 1.0268 mm and t = 7.7013 mm. Note that for the thicker plates more than one wavelength suffer no loss at a specific angle.

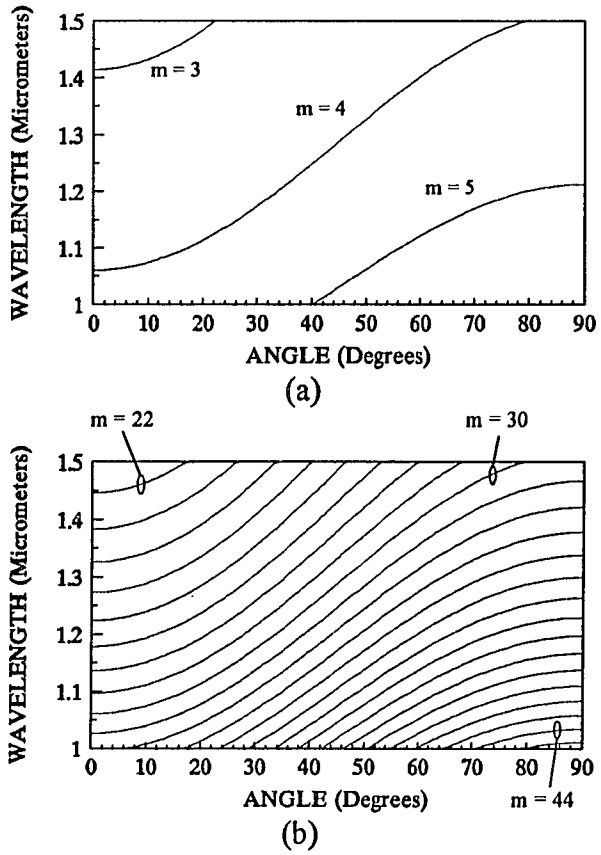

Fig. 4.3.5. Wavelengths that suffer no loss when passing through a single stage birefringent filter a s a function of angle Φ for a) t = 1.0268 mm and b) t = 7.7013 mm ($\Theta = 33.006°$).

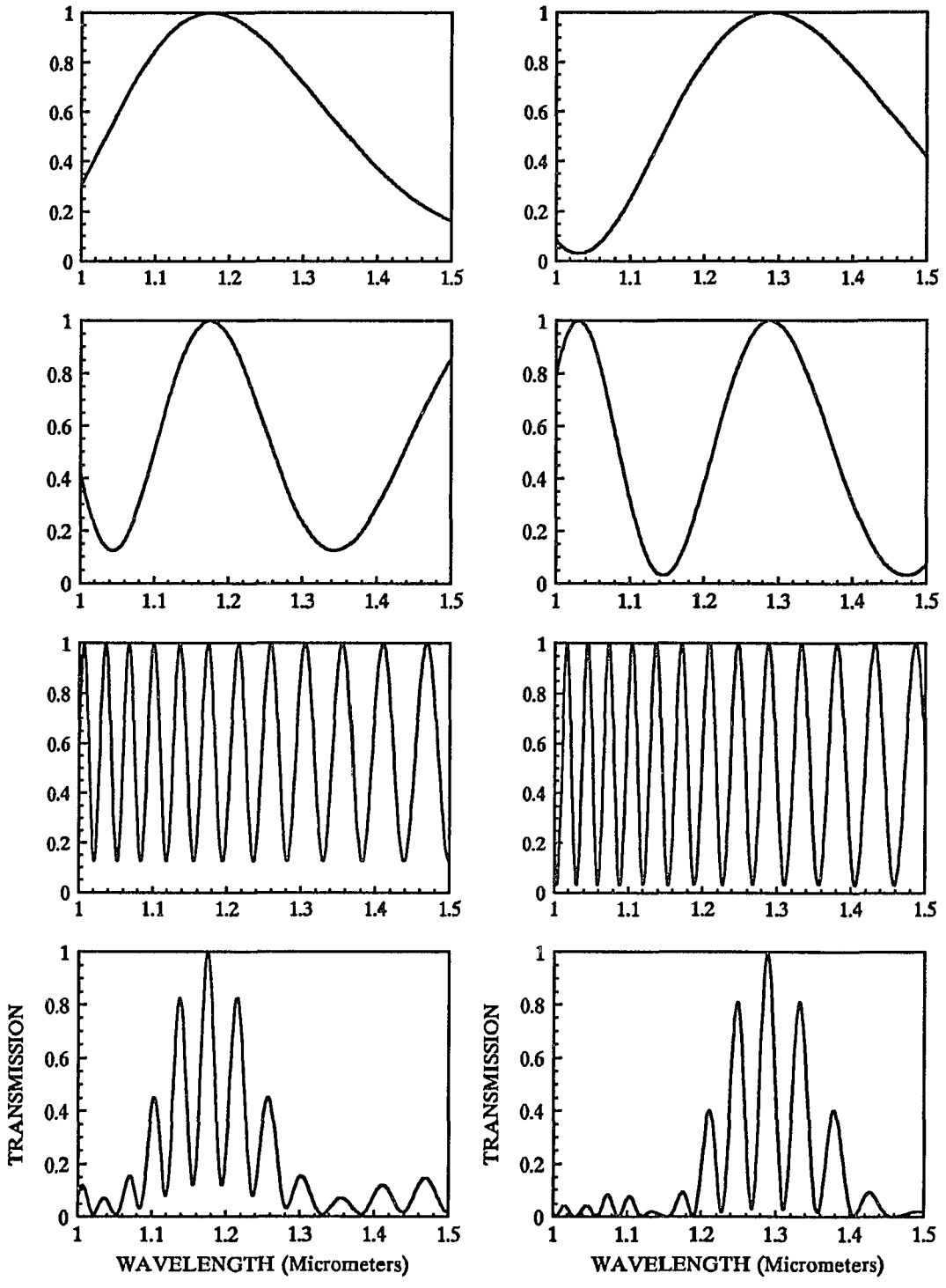

Fig. 4.3.6. Intensity transmission through a three stage birefringent filter (a) $\Phi = 30^\circ$ and $\Theta = 33.006^\circ$; and (b) $\Phi = 45^\circ$ and $\Theta = 33.006^\circ$.

The complete picture of the behavior of the three stage birefringent filter is shown in figure 4.3.6. In the first three graphs the transmission of each plate is calculated using eq. 4.3.6. The fourth graph shows the transmission of the combined action of the three plates. A much narrower spectrum is allowed to lase as compare with the single stage birefringent filter.

The intensity transmission through a three stage birefringent filter is a function of its orientation. The thickness of the plates used to construct the birefringent filter are chosen so that there is only one frequency within the gain curve of the gain medium for which the polarization will not suffer any loss. This frequency is allowed to lase while other frequencies within the gain curve suffer loss and are prohibited to lase. Different frequencies are selected by changing the orientation of the filter.

In the tuning experiments of the forsterite laser a single plate quartz birefringent filter was used. The thickness of the plate was 0.5134 mm.

4.4. Synchronously Pumped Mode-Locked Cr:Forsterite Laser

The simplest way to achieve mode-locking is by synchronous optical pumping. In this technique, the gain of the active medium is modulated at a frequency which equals the round trip time of the cavity resonator as well as the frequency of the mode locked pump source. The experimental arrangement for synchronously-pumped mode-locking is shown in figure 4.4.1. The Brewster-cut forsterite crystal was placed in a three mirror astigmatically compensated cavity and was end-pumped by a cw mode locked Nd:YAG laser. The chromium-doped forsterite crystal was grown by Mitsui Mining & Smelting Company, Japan (Crystal 1). The length of the sample was 1 cm and the absorption coefficient at pump wavelength (1064 nm) was $\alpha = 0.53\ cm^{-1}$. To eliminate the need to chop the pump beam, the laser crystal was mounted in a copper block and was cooled by a single-stage thermoelectric cooler. The crystal and the copper block were purged by nitrogen to prevent moisture condensation. The combination of mirrors used was a 5-cm

radius back mirror, a 10-cm radius folding mirror, and a flat output coupler. The transmission of the output coupler was 5% at the lasing wavelength and the back and the folding mirrors had reflectivity R=99.9% for the 1200-1300 nm range. The transmission characteristics of the mirrors used are shown in the Appendix A. L in Fig. 4.4.1 denotes the focusing lens, F_1 a 1064 nm cutoff filter, and BF a single plate quartz birefringent filter (thickness t = 0.5134 mm). The output of the forsterite laser was monitored with a fast germanium detector and the pulsewidth was measured using a Hamamatsu streak camera with S-1 response and 5-ps resolution.

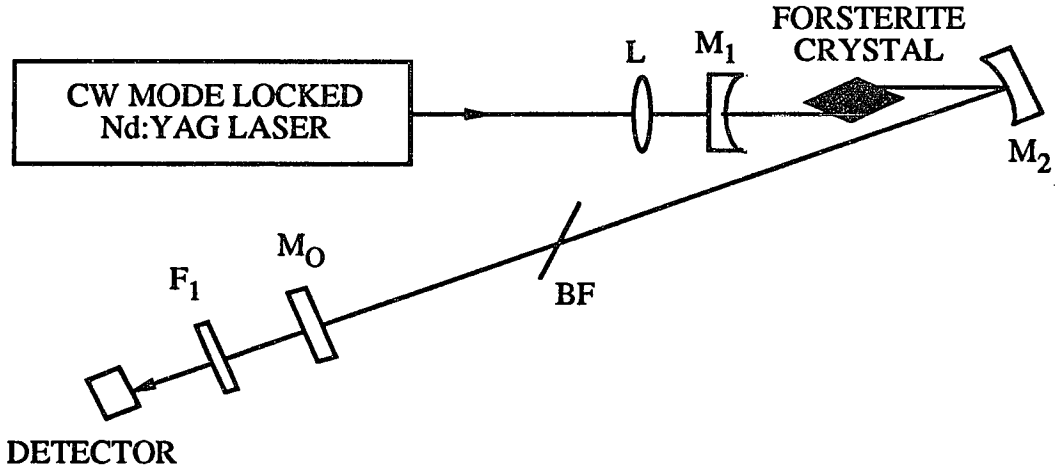

Fig. 4.4.1. Synchronously pumped mode-locked Cr:forsterite laser.

To obtain mode-locked operation by synchronous pumping, the length of the forsterite laser cavity was matched with sub micron accuracy to the length of the pump CW mode-locked Nd:YAG laser cavity of L ≈ 1.8 m, corresponding to 82 MHz repetition rate. Figure 4.3.2 shows an oscilloscope picture of the pulse train and figure 4.3.3 shows the pulsewidth of 260 ± 20 ps FWHM measured when the length of the forsterite laser was exactly matched to the length of the Nd:YAG laser.

The pulsewidth of synchronously pumped lasers broadens when the length of the cavity is not exactly matched to the length of the pump laser cavity. Figure 4.4.4 shows the dependence of the pulsewidth of the synchronously pumped Cr:forsterite laser as a

function of the mismatch of the cavity length. Pulses of duration less than 300 ps were obtained for ± 5 μm mismatch from the optimum position.

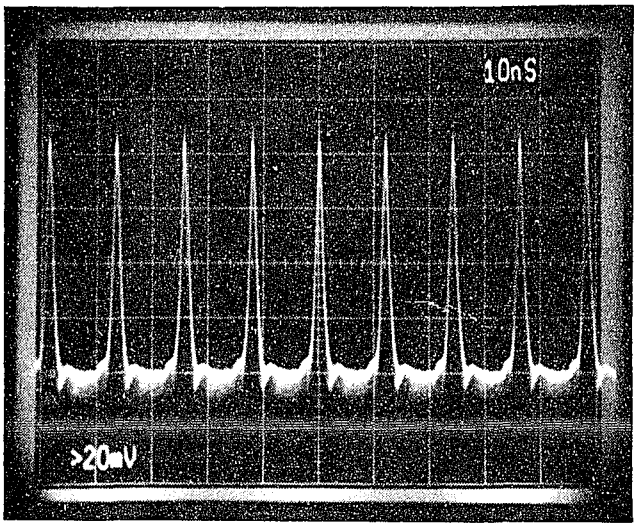

Fig. 4.4.2. Oscilloscope picture of the train of output pulses from the synchronously pumped Cr:forsterite laser.

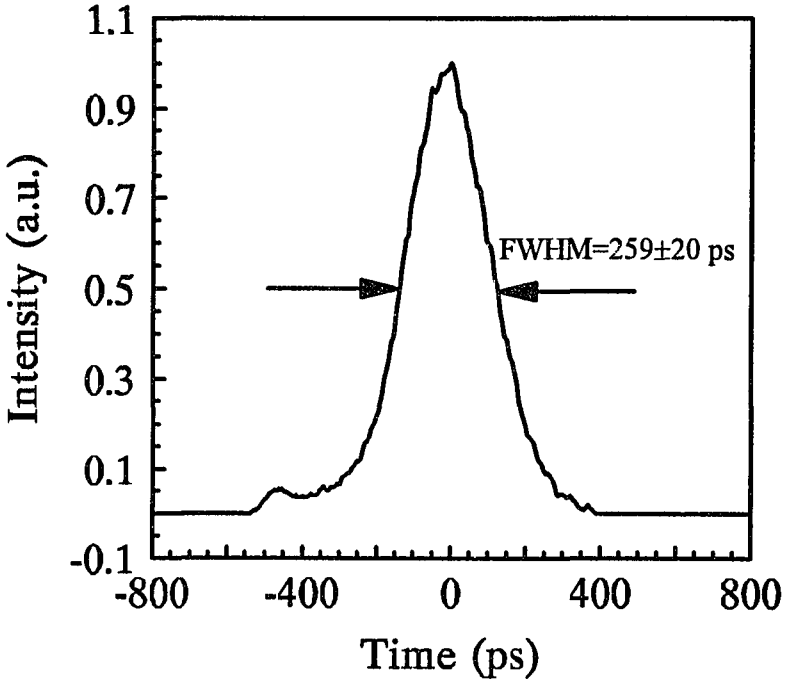

Fig. 4.4.3. Pulsewidth of the output pulses from the synchronously-pumped Cr:forsterite laser.

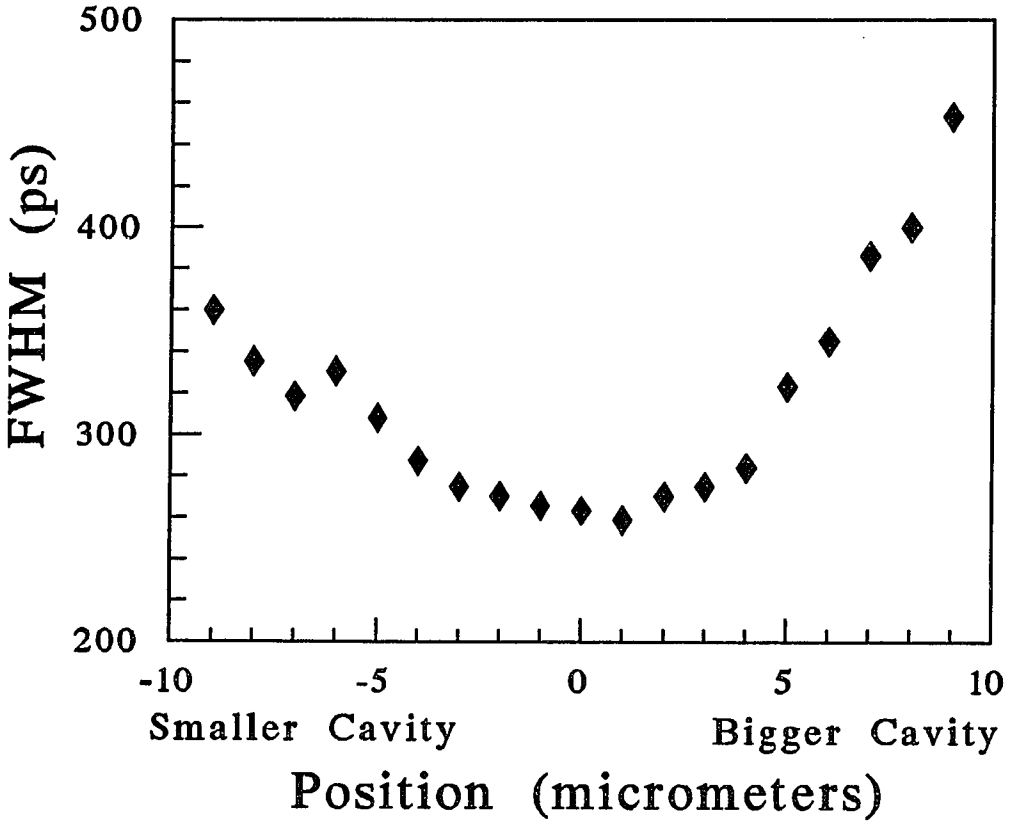

Fig. 4.4.4. Detuning curve of the synchronously-pumped Cr:forsterite laser.

The pulse widths measured in the synchronously pumped mode-locked forsterite laser are much longer than the sub picosecond pulses that may be expected, given the bandwidth of $Cr:Mg_2SiO_4$. However, the results presented are not surprising, considering the small depth of modulation that can be obtained by synchronous pumping of a medium with long luminescence decay times[16,17] such as 2.7 μs for the $^3T_2$ upper lasing level of the Cr^{4+} ion in forsterite. Using a higher output power cw mode-locked Nd:YAG laser as a pump in combination with an improved cavity design may significantly shorten the pulsewidth.

Tuning of the synchronously mode-locked forsterite laser was achieved by inserting a single-crystal quartz birefringent plate (thickness t = 0.5134 mm) in the cavity as shown in figure 4.4.1. The wavelength was determined using a lead sulfide (PbS)

detector coupled to a 0.25 m SPEX monochromator. With only one combination of laser mirrors continuous tuning was achieved between 1195 - 1295 nm. The tuning range was limited by spectral characteristics of the mirrors used. Figure 4.4.5 shows the tuning range of the synchronously pumped mode-locked forsterite laser.

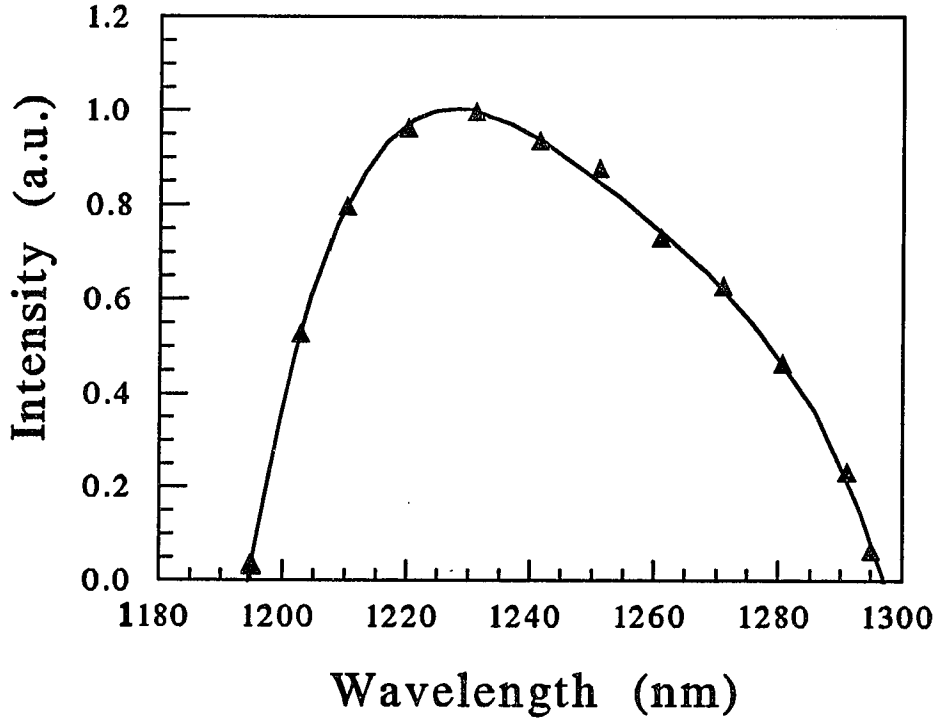

Fig. 4.4.5. Tuning of the synchronously-pumped Cr:forsterite laser.

Maximum power output of 175 mW was measured at 1232 nm, for 2.4 W of absorbed pump power. Slope efficiency was determined by controlling the pump power with the combination of a half wave plate and a polarizer for the 1064 nm pump radiation. The slope efficiency of the synchronously pumped forsterite laser was determined to be 12.5% with a threshold of 0.7 W of absorbed pump power. Figure 4.4.6 shows the slope efficiency curve of the synchronously pumped forsterite laser. Using the results from the slope efficiency measurements the losses in the cavity can be estimated using[18]

$$\eta = \frac{\lambda_P}{\lambda_L}\left(\frac{T}{L+T}\right) \qquad (4.4.1)$$

where: T - the total transmission of the cavity mirrors,

L - the internal loss,

λ_P - wavelength of the pump beam,

λ_L - lasing wavelength.

Using eq. 4.4.1 the losses of the cavity are estimated to be 29.6%. Moderate power output, as well as relatively long pulsewidth are indication of high losses in the cavity, which are most likely due to reflection, absorption and scattering losses and mismatch of the pump beam and cavity mode in the crystal.

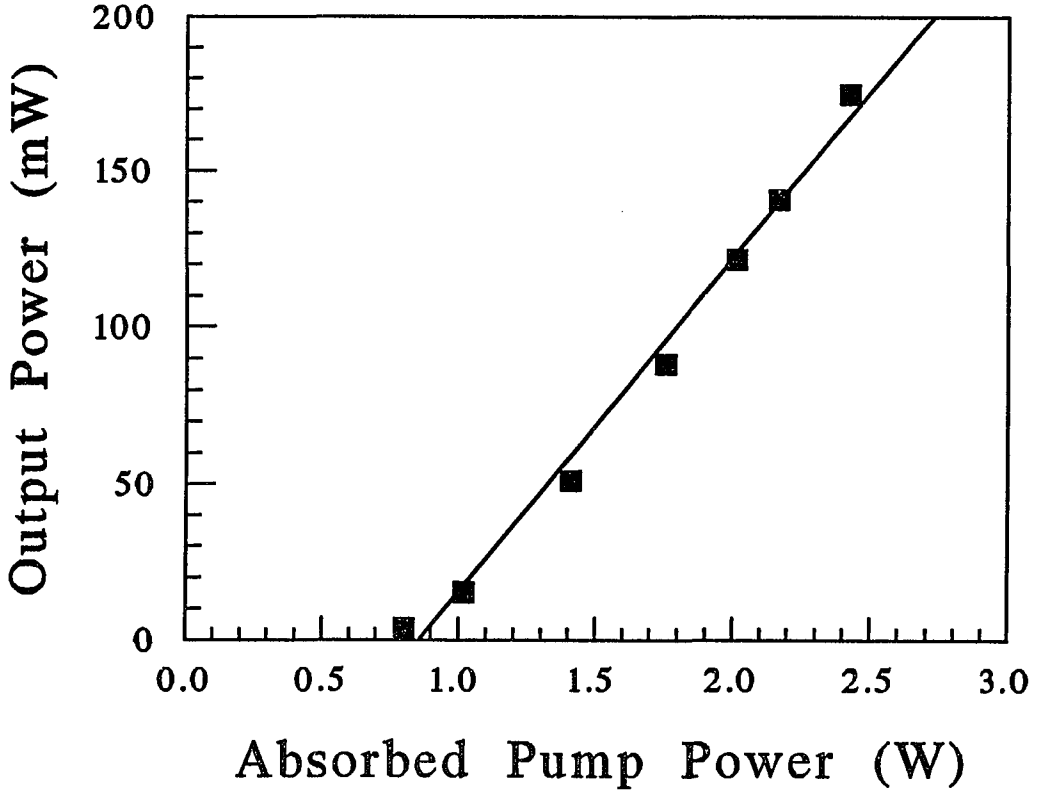

Fig. 4.4.6. Slope efficiency of the synchronously-pumped forsterite laser.

4.5. Active Mode-Locked Cr:Forsterite Laser

Actively mode-locked operation of the forsterite laser was achieved using the same cavity configuration as for synchronously pumped forsterite laser with the addition of an acousto-optic modulator ML in the cavity. The experimental set-up used for active mode-locking is shown figure 4.5.1.

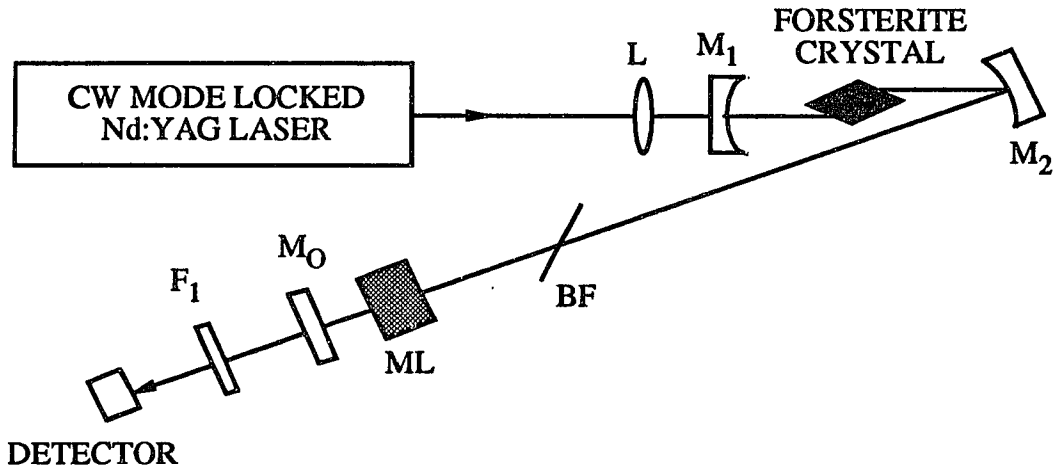

Fig. 4.5.1. Experimental set-up used for active mode-locking of the forsterite laser.

The Brewster acousto-optic modulator Model S/N F-BW-3 and mode-locker driver Model 7600 used in the experiment were provided by Coherent Laser Products Group of Coherent, Inc. The modulation frequency of the mode-locker was 76 MHz. Mode-locking was observed when the length of the three-mirror cavity was adjusted to the length corresponding to the frequency of the acousto-optic modulator (~1.97 m). A stable train of ~ 50-ps pulses was obtained. Figure 4.5.2 shows an oscilloscope trace of the pulse train and figure 4.5.3 shows the intensity profile of the output pulses as it was measured using the streak camera.

When the cavity was slightly misaligned pulses became shorter (~20 ps), but satellite pulses were observed. The separation between the satellite pulses suggests that these pulses may be due to feedback effects from one of the cavity mirrors since the

mirrors used were not wedged. Figure 4.5.4 shows the intensity profile of the 20 ps pulses with satellites.

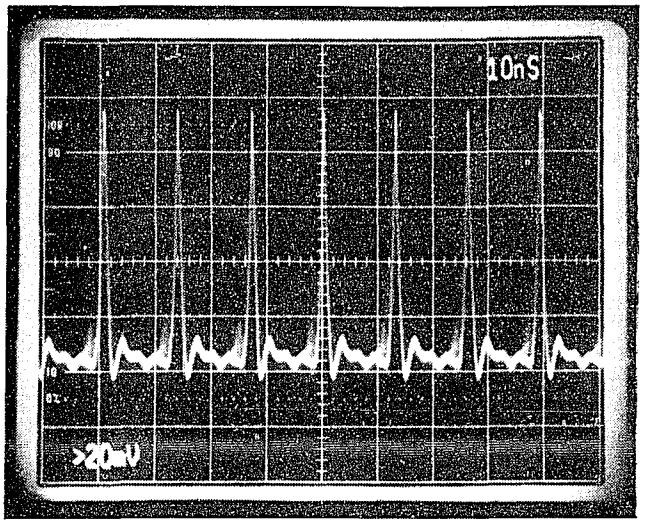

Fig. 4.5.2. Oscilloscope picture of the pulse train output of the active mode-locked Cr:forsterite laser.

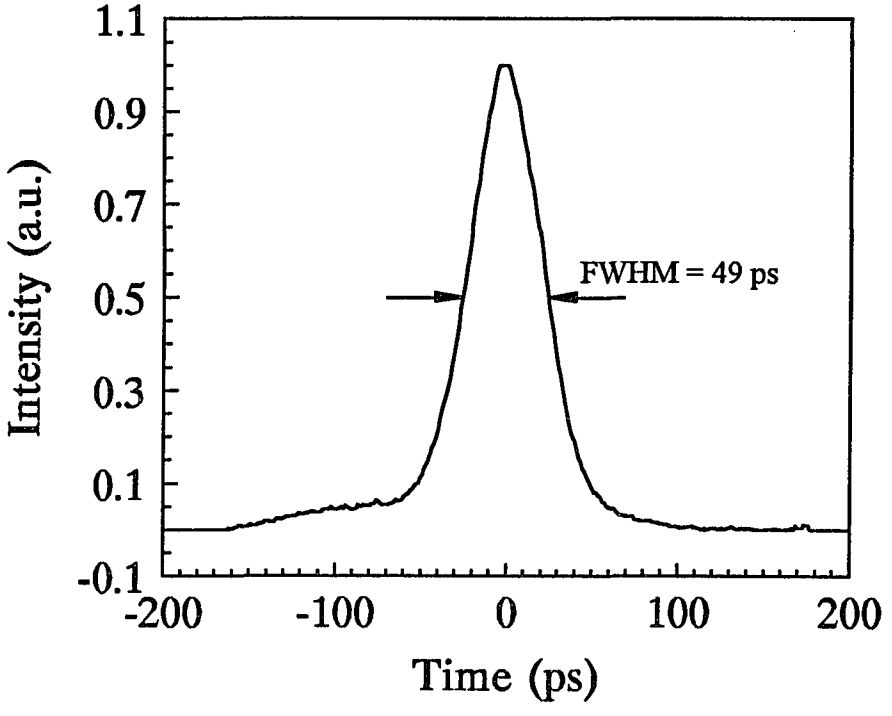

Fig. 4.5.3. Intensity profile of the output pulses of the active mode-locked Cr:forsterite laser.

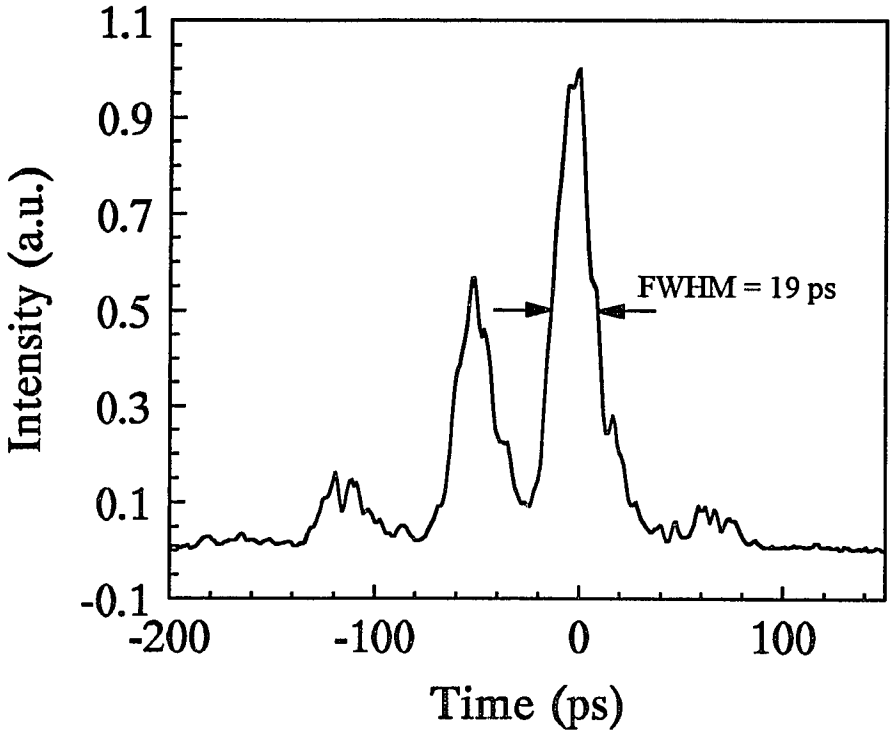

Fig. 4.5.4. Intensity profile of the 20 ps pulses with satellites.

The actively mode-locked forsterite laser was tuned by inserting a single-crystal quartz birefringent plate into the three mirror cavity as shown in figure 4.5.1. With only one combination of laser mirrors the laser output was continuously tuned between 1204 - 1277 nm. The tuning range of the actively mode-locked forsterite laser versus output intensity is shown in figure 4.5.5. The power output of 120 mW was measured at 1227 nm, for 2.4 W of absorbed pump power. The slope efficiency of the actively mode-locked forsterite laser was determined to be 9.1% with a threshold of 0.9W of absorbed pump power. Using eq 4.4.1 we can estimate the losses of the forsterite laser to be 42.44%. Lower power output than in the case of synchronous pumping is a consequence of additional losses introduced by inserting the acousto-optic modulator in the laser cavity.

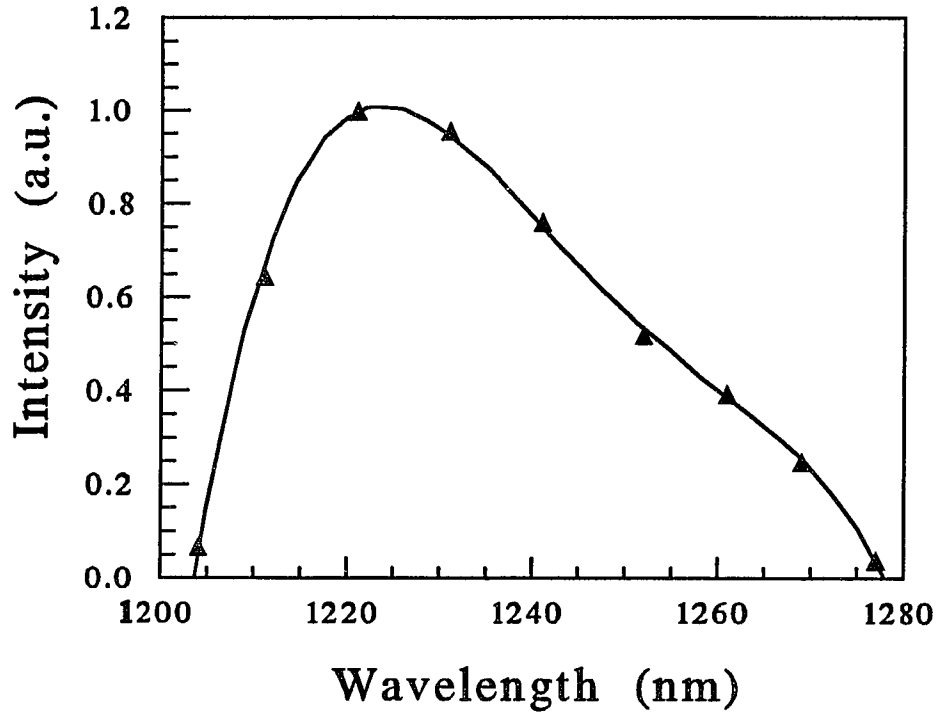

Fig. 4.5.5. Tuning range of the active mode-locked Cr:forsterite laser.

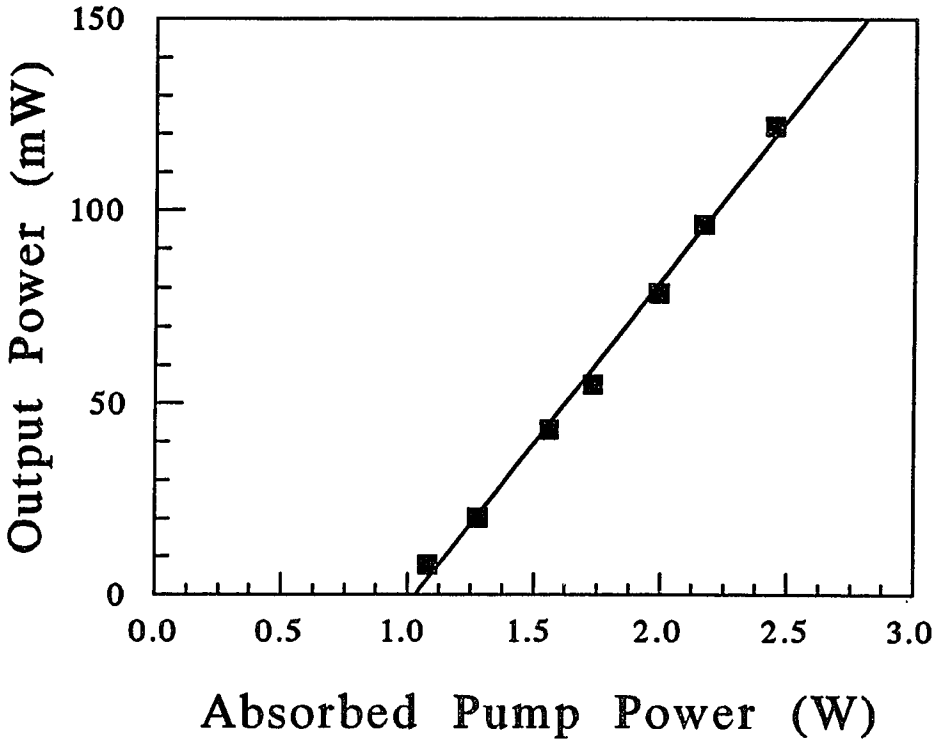

Fig. 4.5.6. Slope efficiency of the active mode-locked Cr:forsterite laser.

The results obtained so far were very encouraging since they demonstrated the ability of the Cr:forsterite laser to generate ultrashort pulses. The main objective after the first demonstration of mode locking was to take advantage of the broad emission spectrum of Cr:forsterite and generate femtosecond pulses.

The analysis presented in section 4.2 indicated that a four mirror cavity offers better mode characteristics in the laser medium. To take advantage of the better mode characteristics the same Brewster cut forsterite crystal (Crystal 1) was placed in a four mirror z-fold astigmatically compensated cavity. The experimental arrangement is shown in figure 4.5.8. The combination of mirrors used was flat for the two end mirrors and 10 cm radius of curvature for the two folding mirrors. Active mode locking was achieved when the length of the four mirror cavity was matched to the frequency of the acousto-optic modulator. The pulsewidth of the output pulses was reduced from 49 ps down to 31 ps. The temporal profile of the 31 ps pulses is shown in figure 4.5.9.

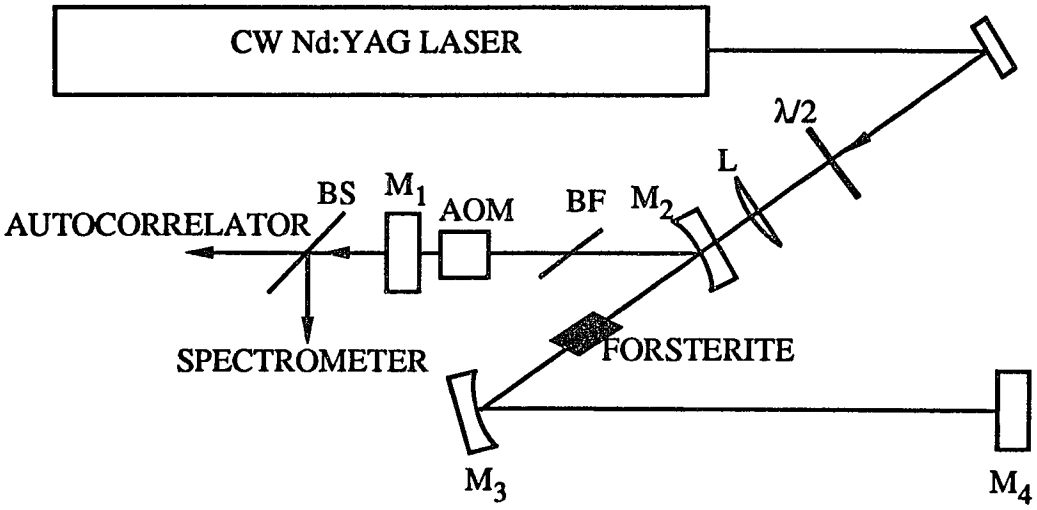

Fig. 4.5.8. Four mirror astigmatically compensated forsterite laser.

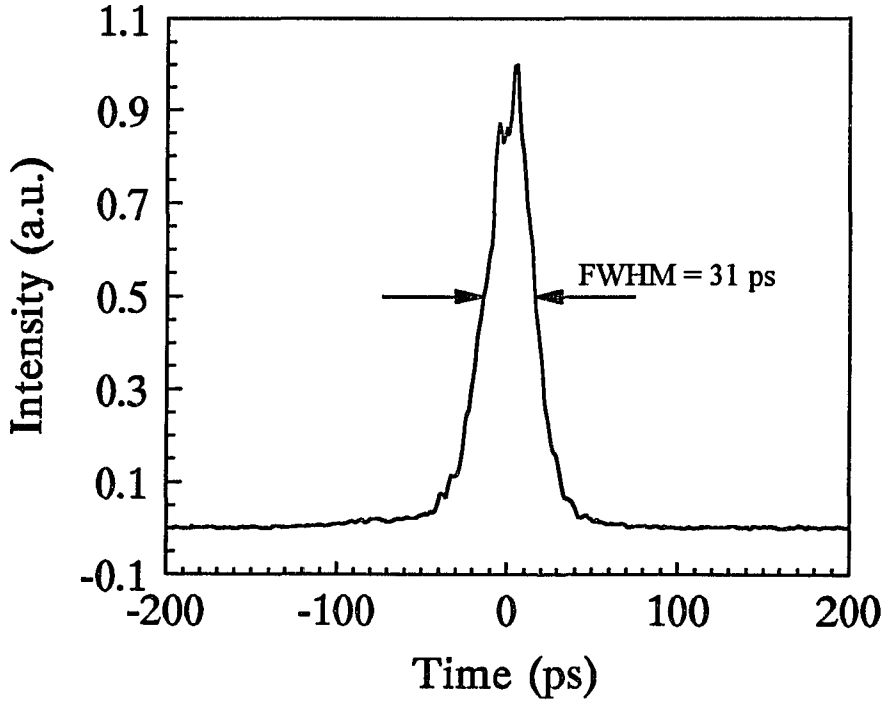

Fig. 4.5.9. Intensity profile of 31 ps pulses generated from the four mirror cavity design.

Further improvement of the pulsewidth of the actively mode-locked forsterite laser was achieved by replacing the forsterite crystal (Crystal 1) with a newer forsterite crystal (Crystal 2). Crystal 2 has a higher absorption coefficient at 1064 nm and a better figure of merit as compared with Crystal 1 (See table 2.2.1). In order to reduce the losses of the laser cavity the 5% output coupler was replaced with a 1% output coupler. Better thermal contact between the crystal and the copper block was achieved by wrapping the crystal in 1 mm thick indium foil.

Pulsewidth measurements were carried out using a background free real time autocorrelator since it was expected that the pulses will be shorter than the 10 ps limit of the streak camera (5 ps rise time). The bandwidth of the mode-locked forsterite laser was

measured using a PbS detector coupled to a 50-cm Jarrel Ash monochromator, equipped with 10-μm slits.

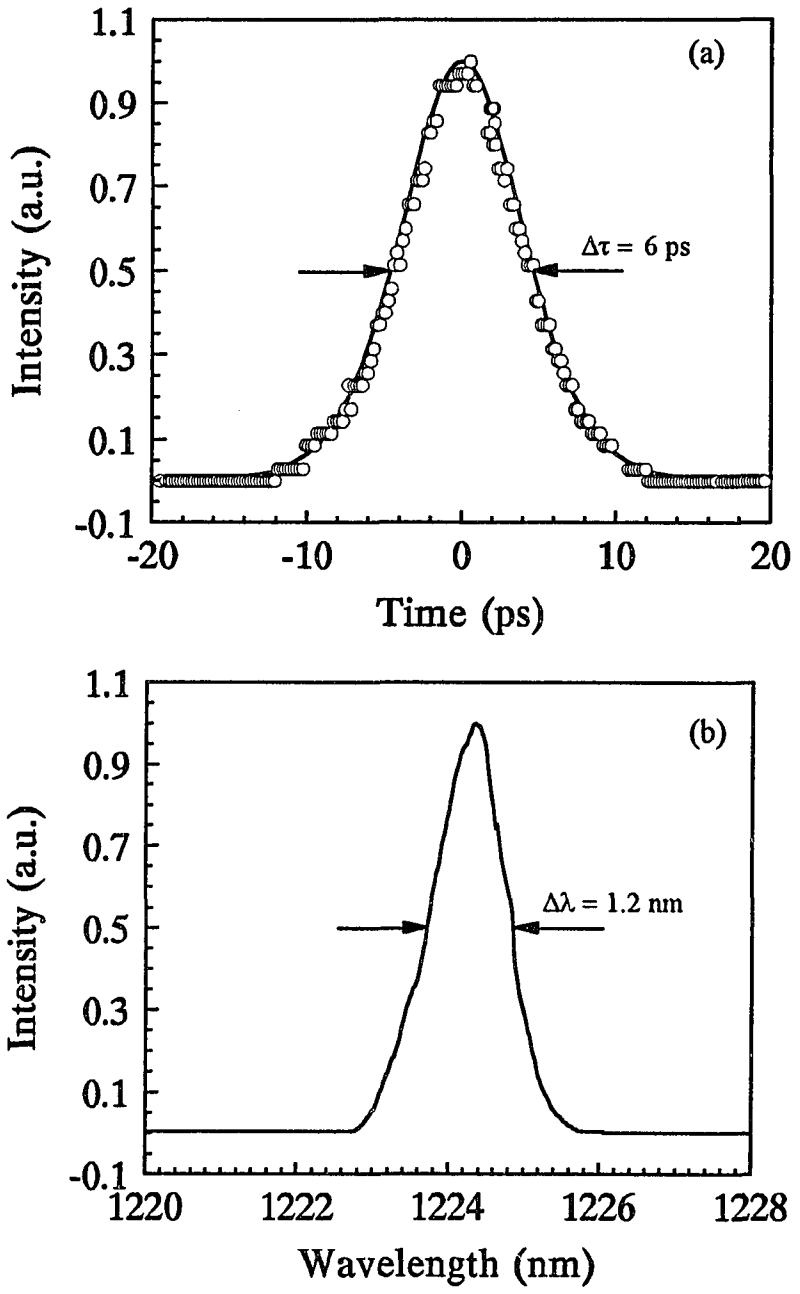

Fig. 4.5.10. An autocorrelation trace (a) and spectrum (b) of the 6-ps pulses. Circles represent experimental data and the solid line is the best fit. $sech^2$ pulse shape was assumed for fitting. The pulsewidth-bandwidth product is $\Delta\tau_p\Delta\nu = 1.34$.

The autocorrelation trace of the pulse and the corresponding spectrum of the output pulses from the active mode-locked Cr:forsterite laser are shown in figure 4.5.10 (a) and (b), respectively. Circles represent the experimental data from the autocorrelator and the solid line is the best fit assuming $sech^2$ pulse shape with FWHM of 6 ps. The FWHM of the bandwidth was measured to be 1.2 nm.

The pulsewidth-bandwidth product $\Delta\tau_p\Delta\nu = 1.34$ which is about 4 times the transform limit, indicating that the pulses from the mode-locked forsterite laser were chirped. The source of chirp is mainly group-velocity dispersion and self-phase modulation in the forsterite crystal.

4.6. Conclusion

In conclusion, mode-locked operation of chromium-doped forsterite laser was achieved using two methods: synchronous optical pumping and active mode-locking. Pulsewidth measurements yielded pulses of 260 ps for synchronous pumping, and 31 ps for active mode-locking. In both cases the tuning range was of the order of 100 nm, limited only by the coating of the mirrors used and the cavity losses.

Improvements in the cavity design resulted in the generation of 31 ps and by using a laser crystal with better characteristics the pulsewidth was reduced to 6 ps. Pulsewidth-bandwidth measurements indicated that the output pulses are 4 times the transform limit when secant hyperbolic pulses are assumed.

4.7. References

1. V. Petričević, A. Seas, and R. R. Alfano, "Forsterite Laser Tunes in Near IR", Laser Focus World **26** (11), pp. 109 (1990).

2. T. Y. Fan, and A. Sanchez, "Pump Source Requirements for End-Pumped Lasers", IEEE J. Quantum Electronics, Vol. **QE 26**, pp. 311 (1990).

3. P. F. Moulton, "An investigation of the Co:MgF_2 laser system", IEEE J. Quantum Electron., Vol. **QE-21**, pp. 1582 (1985).

4. D. G. Hall, R. J. Smith, and R. R. Rice, "Pump-size effects in Nd:YAG lasers", Appl. Opt., Vol. **19**, pp. 1041 (1980).

5. H. Kogelnik, and T. Li, "Laser beams and resonators", Appl. Opt., Vol. **5**, pp. 1550 (1966).

6. D. C. Hanna, "Astigmatic gaussian beams produced by axially asymmetric laser cavities", IEEE J. Quantunm Electron., Vol. **QE-10**, pp. 483 (1974).

7. A. E. Siegman, "Lasers", University Science Books, Mill Valey, California, chapter 21 (1986).

8. L. W. Casperson, "Mode stability of lasers and periodic optical systems", IEEE J. Quantum Electron., Vol. **QE-10**, pp. 629 (1974).

9. H. Kogelnik, E. P. Ippen, A. Dienes, and C. V. Shank, "Astigmatically compensated cavities for CW dye lasers", IEEE J. Quantum Electron., Vol. QE-8, pp. 373 (1972).

10. H. Kogelnik, "Imaging of optical modes-resonators with internal lenses", Bell Syst. Tech. J., Vol. **44**, pp. 455 (1965).

11. L. V. Tarasov, "Laser Physics", MIR Publishers, Moscow, chapter 2.6 (1983).

12. W. D. Johnston, P. K. Runge, "An improved Astigmatically Compensated Resonator for CW Dye Lasers", IEEE J. Quantum Electron., Correspondence, pp. 724 (1972).

13. D. R. Preuss, and J.L. Gole, " Three-stage birefringent filter tuning smoothly over the visible region: theoretical treatment and experimental design", Applied Optics, Vol. **19**, pp. 702 (1980).

14. D. E. Gray, ed., "American Institute of Physics Handbook", 3rd ed. (McGraw-Hill, New York, 1972, pp. 6-29.

15. G. Holtom, and O. Teschke, "Design of a Birefringent filter for high-power dye lasers", IEEE J. Quantum Electronics, Vol. **QE-10**, pp. 577 (1974).

16. J. T. Darrow, and R. K. Jain, in *Digest of Meeting on Tunable Solid State Lasers*, Optical Society of America, D.C., paper PD-2 (1987).

17. L. F. Mollenauer, N. D. Vieira, and L. Szeto, "Mode locking by synchronous pumping using a gain medium with microsecond delay times", Optics Letters, Vol. **7**, pp. 414 (1982).

18. H. G. Damielmeyer, in "Lasers", A. K. Levine and A. DeMaria, eds. (Dekker, New York, 1975), Vol. IV.

CHAPTER 5

FEMTOSECOND OPERATION OF CHROMIUM-DOPED FORSTERITE LASER

5.1. Introduction

Generation of femtosecond pulses during the decade of 1980-1990 was dominated by dye lasers.[1] Recently tunable solid state lasers have emerged as new gain media for the generation and amplification of ultrashort pulses.[2] As it was discussed in previous chapters the Cr:forsterite laser can generate femtosecond laser due to its wide emission Spectrum. The best result obtained so far were pulses with FWHM of 6 ps using active mode-locking.

The generation of femtosecond pulses depends on the elimination or compensation of group velocity dispersion and other sources of phase distortions in the generated pulses either inside or outside of the laser cavity. Over the past years several techniques were successfully used for controlling the phase in a laser pulse. Some of the most popular methods have been the use of diffraction gratings,[3] pair of prisms,[4,5] and Gire-Tounois interferometer. [6,7]

In this chapter the focus is on the generation of femtosecond pulses by eliminating the chirp from the output of the forsterite laser. The basic theory of propagation of a gaussian pulse through a dispersive medium and such effects as pulse broadening and pulse compression are discussed. Group velocity dispersion compensation using a pair of prisms is presented, and numerical calculations are carried out for different types of glass to determine material appropriate for chirp compensation in the near infrared. Section 5.4

shows the experimental setup and the generation of 105 fs pulses from the self-mode-locked Cr:forsterite laser. Cubic phase distortion compensation is considered in section 5.5 and the generation of pulses with FWHM of 36 fs was demonstrated by using prisms that corrected quadratic phase and introduced minimum cubic phase distortions.

5.2. Propagation of Gaussian Pulses in a Dispersive Medium

In many applications there is need for pulsed laser operation where the light energy is concentrated in very small periods of time. The finite duration of the laser pulses indicates that there is also a finite distribution of frequencies. The propagation of a light pulse in a dispersive medium gives rise to interesting phenomena such as pulse broadening or pulse compression.

A dispersive medium is a material whose optical properties are functions of frequency. Propagation of a group of frequencies through a dispersion medium results to dispersion, since each frequency travels at a different speed and experiences different propagation characteristics. The goal in this section is to determine the effects of a dispersive medium on a light pulse and methods to minimize or compensate for these effects.

The propagation of a gaussian light pulse in a dispersive medium is consider next. A very good analysis of the described phenomena can be found in references 8 and 9.

Consider a gaussian pulse entering a dispersive medium at z = 0. The pulse can be represented by[8,9]

$$E_0(0,t) = e^{-a_0 t^2} e^{i\omega_0 t + ib_0 t^2} = \exp\left(-\Gamma_0 t^2 + i\omega_0 t\right) \qquad (5.2.1)$$

where

$$\Gamma_0 \equiv a_0 - ib_0 \qquad (5.2.2)$$

The pulse is described by a fast oscillating function, $\exp(i\omega_0 t)$, and a slow varying envelope function, $\exp(-a_0 t^2 + ib_0 t^2)$. The frequency distribution of the gaussian pulse is the Fourier transform of $E(0,t)$ and is given by

$$\tilde{E}_0(0,\omega) = \exp\left(-\frac{(\omega-\omega_0)^2}{4\Gamma_0}\right) \qquad (5.2.3)$$

After propagating a distance z inside the dispersive medium the pulse's spectrum is given by

$$\tilde{E}(z,\omega) = \tilde{E}(0,\omega)\exp(-ik(\omega)z) \qquad (5.2.4)$$

where $k(\omega)$ is the propagation constant of the light in the medium, which is a function of frequency.

A medium is called "dispersive" when its propagation constant, k, is a function of frequency. Using the Taylor series expansion around the central frequency ω_0 the propagation constant can be written as

$$k(\omega) = k(\omega_0) + \left.\frac{dk}{d\omega}\right|_{\omega_0}(\omega-\omega_0) + \frac{1}{2}\left.\frac{d^2k}{d\omega^2}\right|_{\omega_0}(\omega-\omega_0)^2 + \frac{1}{6}\left.\frac{d^3k}{d\omega^3}\right|_{\omega_0}(\omega-\omega_0)^3 + \ldots \qquad (5.2.5)$$

For a specific frequency the propagation constant in the dispersive medium is given by

$$k(\omega_0) = \frac{\omega_0 n(\omega_0)}{c} \qquad (5.2.6)$$

where $n(\omega_0)$ is the refractive index of the medium for frequency ω_0 and c is the speed of light in free space. The derivatives of the propagation constant with respect to frequency

can be expressed in terms of the index of refraction and its derivatives with respect to wavelength. Using eq. 5.2.6 the first, second, and third derivatives are written as

$$\frac{\partial k}{\partial \omega} = \frac{n}{c} + \frac{\omega}{c}\frac{\partial n}{\partial \omega} \tag{5.2.7}$$

$$\frac{\partial^2 k}{\partial \omega^2} = \frac{2}{c}\frac{\partial n}{\partial \omega} + \frac{\omega}{c}\frac{\partial^2 n}{\partial \omega^2} \tag{5.2.8}$$

$$\frac{\partial^3 k}{\partial \omega^3} = \frac{3}{c}\frac{\partial^2 n}{\partial \omega^2} + \frac{\omega}{c}\frac{\partial^3 n}{\partial \omega^3} \tag{5.2.9}$$

The derivatives of the refractive index with respect to frequency can be changed to derivatives of the refractive index with respect to wavelength by using the relation

$$\omega = \frac{2\pi c}{\lambda} \tag{5.2.10}$$

Therefore,

$$\frac{\partial n}{\partial \omega} = -\frac{\lambda^2}{2\pi c}\frac{\partial n}{\partial \lambda} \tag{5.2.11}$$

$$\frac{\partial^2 n}{\partial \omega^2} = \frac{\lambda^3}{2\pi c^2}\frac{\partial n}{\partial \lambda} + \frac{\lambda^4}{2\pi^2 c^2}\frac{\partial^2 n}{\partial \lambda^2} \tag{5.2.12}$$

$$\frac{\partial^2 n}{\partial \omega^2} = -\frac{3\lambda^4}{4\pi^3 c^3}\frac{\partial n}{\partial \lambda} - \frac{3\lambda^5}{2\pi^3 c^3}\frac{\partial^2 n}{\partial \lambda^2} - \frac{\lambda^6}{8\pi^3 c^3}\frac{\partial^3 n}{\partial \lambda^3} \tag{5.2.13}$$

Substituting eqs. 5.2.11-5.2.13 in eqs. 5.2.7-5.2.9 then the derivatives of the propagation constant with respect to frequency are given by

$$\frac{\partial k}{\partial \omega} = \frac{n}{c} - \frac{\lambda}{c}\frac{\partial n}{\partial \lambda} \tag{5.2.14}$$

$$\frac{\partial^2 k}{\partial \omega^2} = \frac{\lambda^3}{2\pi c^2}\frac{\partial^2 n}{\partial \lambda^2} \tag{5.2.15}$$

$$\frac{\partial^3 k}{\partial \omega^3} = -\frac{\lambda^5}{4\pi^2 c^3}\frac{\partial^3 n}{\partial \lambda^3} \tag{5.2.16}$$

By substituting the expression for $k(\omega)$ in the equation of $\tilde{E}(z,\omega)$ neglecting the term for the third derivative results to

$$\tilde{E}(z,\omega) = \tilde{E}(0,\omega)\exp\left\{-iz\left[k(\omega_o) + \left.\frac{dk}{d\omega}\right|_{\omega_o}(\omega-\omega_o) + \frac{1}{2}\left.\frac{d^2k}{d\omega^2}\right|_{\omega_o}(\omega-\omega_o)^2\right]\right\} \tag{5.2.17}$$

The notation in eq. 5.2.17 can be simplified by setting

$$k = k(\omega_o) \tag{5.2.18}$$

$$k' = \left.\frac{dk}{d\omega}\right|_{\omega_o} \tag{5.2.19}$$

$$k'' = \left.\frac{d^2k}{d\omega^2}\right|_{\omega_o} \tag{5.2.20}$$

Eq. 5.2.17 takes the form

$$\tilde{E}(z,\omega) = \tilde{E}(0,\omega)\exp\left\{-iz\left[k + k'(\omega-\omega_o) + \frac{k''}{2}(\omega-\omega_o)^2\right]\right\} \tag{5.2.21}$$

By substituting for $\tilde{E}(0,\omega)$, $\tilde{E}(z,\omega)$ is given by

$$\tilde{E}(z,\omega) = \exp\left\{-\left[ikz + ik'z(\omega-\omega_0) + \frac{1}{4\gamma(z)}(\omega-\omega_0)^2\right]\right\} \qquad (5.2.22)$$

where

$$\frac{1}{4\gamma(z)} = \frac{1}{4\Gamma_0} + i\frac{k''z}{2} \quad \text{or} \quad \frac{1}{\gamma(z)} = \frac{1}{\Gamma_0} + i2k''z \qquad (5.2.23)$$

The pulse in the time domain can be estimated by taking the Fourier transform of $\tilde{E}(z,\omega)$

$$E(z,t) = \int_{-\infty}^{\infty} \tilde{E}(z,\omega)e^{i\omega t}d\omega \qquad (5.2.24)$$

$$E(z,t) = \int_{-\infty}^{\infty} \exp\left\{-\left[ikz + ik'z(\omega-\omega_0) + \frac{1}{\gamma(z)}(\omega-\omega_0)^2 - \omega t\right]\right\}d\omega \qquad (5.2.25)$$

which by changing the variable to $(\omega - \omega_0)$

$$E(z,t) = \exp[i(\omega_0 t - kz)]\int_{-\infty}^{\infty} \exp\left\{-\frac{(\omega-\omega_0)^2}{4\gamma(z)} + i(\omega-\omega_0)(t-k'z)\right\}d(\omega-\omega_0) \qquad (5.2.26)$$

Finally by solving the integral the resulting pulse is given by

$$E(z,t) = \sqrt{4\pi\gamma(z)}\exp[i(\omega_0 t - kz)]\exp\left[-\gamma(z)(t-k'z)^2\right] \qquad (5.2.27)$$

$$E(z,t) = \sqrt{4\pi\gamma(z)}\exp\left[i\omega_0\left(t-\frac{z}{v_p}\right)\right]\exp\left[-\gamma(z)\left(t-\frac{z}{v_g}\right)^2\right] \qquad (5.2.28)$$

The resulting equation of the gaussian pulse after traveling a distance z in the dispersive medium is still gaussian and is similar to the input pulse. It is characterized by a fast oscillating function which is delayed by a phase given by

$$\frac{k(\omega_0)}{\omega_0}z \qquad (5.2.29)$$

The central frequency ω_0 is seen to travel at a phase velocity given by

$$v_p(\omega_0) = \frac{\omega_0}{k(\omega_0)} \quad \text{(Phase Velocity)} \qquad (5.2.30)$$

Phase velocity is the velocity that somebody has to travel with in order to keep up with a maximum of the fast oscillating field.

The slower envelope function is also delayed by an amount of k'z. The envelope of the pulse seems to move at a group velocity given by

$$v_g(\omega_0) = \frac{1}{k'} = \frac{1}{dk/d\omega\big|_{\omega_0}} = \text{(Group Velocity)} \qquad (5.2.31)$$

Group velocity is the velocity that the pulse propagates in the dispersive medium. Group velocity can be considered as the speed that the energy of the pulse propagates.

The envelope function is also affected by the complex variable $\gamma(z)$ given by eq. 5.2.23. If k" = 0 then for a narrow band pulse the envelope moves forward at a group velocity v_g and the individual optical cycles move forward at a phase velocity v_p. If k" is

non zero then there will be a variation of the group velocity as a function of frequency which is the so called Group Velocity Dispersion (GVD). Group velocity dispersion gives rise to phenomena such as pulse broadening, pulse compression and pulse reshaping. Group velocity dispersion is related to group velocity by

$$k'' = \left.\frac{d^2k}{d\omega^2}\right|_{\omega_o} = \left.\frac{d(1/v_g)}{d\omega}\right|_{\omega_o} \quad \text{(GVD)} \tag{5.2.32}$$

The pulsewidth before entering the dispersive medium is given by

$$\tau_p(0) = \sqrt{\frac{2\ln 2}{a_o}} \tag{5.2.33}$$

Similarly the pulsewidth at z is given by

$$\tau_p(z) = \sqrt{\frac{2\ln 2}{a(z)}} \tag{5.2.34}$$

The function a(z) can be estimated from eq. 5.2.23

$$\frac{1}{\gamma(z)} = \frac{1}{a(z) - ib(z)} = \frac{1}{\Gamma_o} + i2k''z \tag{5.2.35}$$

By solving equation 5.3.35 the expressions for the functions a(z) and b(z) can be estimated as

$$a(z) = \frac{a_o}{\left(1 + 2k''zb_o\right)^2 + \left(2k''za_o\right)^2} \tag{5.2.36}$$

$$b(z) = \frac{b_o\left(1+2k''zb_o\right)+2k''za_o^2}{\left(1+2k''zb_o\right)^2+\left(2k''za_o\right)^2} \qquad (5.2.37)$$

If the input pulse has no chirp ($b_o = 0$) then the pulsewidth of the output pulse at z is

$$\tau_p(z) = \sqrt{\frac{2\ln 2}{a(z)}} = \sqrt{\frac{2\ln 2}{a_o}\left[1+\left(2k''a_o\right)^2\right]} \qquad (5.2.38)$$

or by substituting for a_o from eq. 5.2.33

$$\tau_p(z) = \tau_p(0)\sqrt{\left[1+\left(\frac{4k''z\ln 2}{\tau_p^2(0)}\right)^2\right]} \qquad (5.2.39)$$

As is shown from eq. 5.2.39 the pulsewidth of the output pulse depends on the GVD (k"), the distance traveled (z), and the pulsewidth of the input pulse.

If the input pulse is chirped then one can determine the distance after which the pulse will shorten and the chirp will be removed from the pulse. Considering eq. 5.2.38 the pulsewidth is inversely dependent on a(z) and the pulsewidth will be minimum when a(z) is maximum. Another condition that will make the pulsewidth minimum is when b(z) = 0. Using either of these conditions the distance that will make the pulsewidth minimum is given by

$$z_{b(z)=0} = \frac{-b_o}{2k''\left(a_o^2+b_o^2\right)} = \frac{-b_o}{2k''\left[\left(\frac{2\ln 2}{\tau_p^2(0)}\right)^2+b_o^2\right]} \qquad (5.2.40)$$

Consider an unchirped pulse, b = 0, going into a dispersive medium. After a distance z the width of the pulse is given by

$$\tau_p^2(z) = \tau_p^2(0) + \left(\frac{4k'' z \ln 2}{\tau_p^2(0)}\right)^2 = \tau_p^2(0)\left[1 + \left(\frac{z}{z_D}\right)^2\right] \qquad (5.2.41)$$

The dispersion length, z_D, is called the "Rayleigh length" and is defined as the distance traveled in the dispersive medium after which the pulsewidth will increase by a factor $\sqrt{2}$ and is given by

$$z_D = \frac{\tau_p^2(0)}{4k'' \ln 2} \qquad (5.2.42)$$

Another way of discussing pulse dispersion in a nonlinear medium is by using the group velocity dispersion constant D. The constant D is defined as

$$D \equiv \frac{1}{L}\frac{dT}{d\lambda} \qquad (5.2.43)$$

where T is the pulse transmission time through a dispersive material of length L. The constant D measures the variation in the time it takes for a pulse to transmit through a dispersive material as a function of the different frequencies (wavelengths). The units of D are picoseconds or femtoseconds of delay per nanometer of bandwidth per centimeter of distance traveled in the dispersive medium. The dispersion constant is related to the second derivative of the propagation constant by the relation[10]

$$D = -\frac{2\pi c}{\lambda^2}\frac{d^2k}{d\omega^2} \qquad (5.2.44)$$

Substituting eq. 5.2.44 in the expression for pulse duration after the pulse had traveled a distance z in a dispersive medium, eq. 5.2.39 relates the pulsewidth to the group velocity dispersion constant by

$$\tau_p(z) = \tau_p(0)\sqrt{1+\left(\frac{2\ln 2}{\pi c}\frac{Dz\lambda^2}{\tau_p^2(0)}\right)^2} \qquad (5.2.45)$$

To gain some insight in the process of pulse propagation in a dispersive medium the effect of different optical materials were numerically evaluated. Initially the index of refraction and its derivatives with respect to wavelength are evaluated. The dispersion constant is next calculated as a function of wavelength, and finally the effect of propagation of a 30 through the dispersive material is consider. The spectrum of the 30-fs pulse is centered at 1250 nm corresponding to a light pulse generated from a Cr:forsterite laser.

The dependence of the index of refraction with respect to wavelength for some commonly used optical glasses is shown in figure 5.2.1. As is the case with all optical glasses the index of refraction is bigger, and is more wavelength dependent in the visible region as compared with the infrared. This indicates that light pulses with spectrum centered in the near infrared are less affected by propagation through a dispersive medium that pulses in the visible. This can also be realized by evaluating the dispersion constant as a function of wavelength. The dispersion constant was calculated using eq. 5.2.44. Figure 5.2.2 shows the dependence of the dispersion constant as a function of wavelength. Considering eq. 5.2.45 the pulsewidth of a light pulse after propagation through a dispersive medium is proportional to the dispersion constant. The bigger the dispersion constant the broader the pulse will become after propagation through the material. Again the dispersion constant is bigger and more wavelength dependent in the visible than what it is in the near infrared.

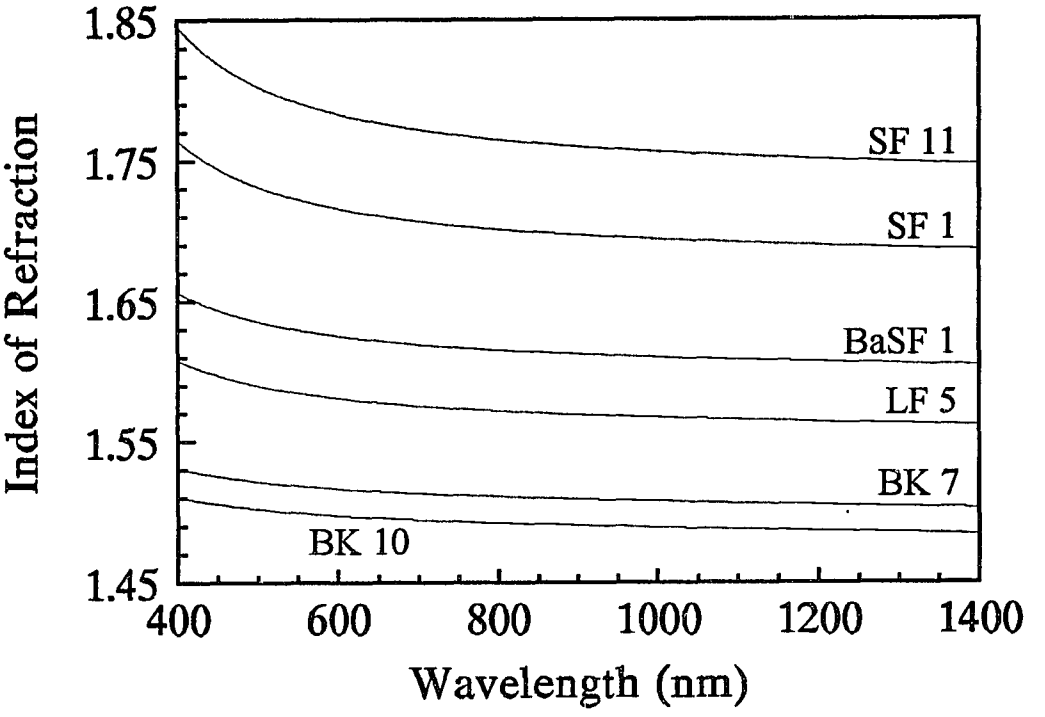

Fig. 5.2.1. Index of refraction vs. wavelength for a variety of optical glasses.

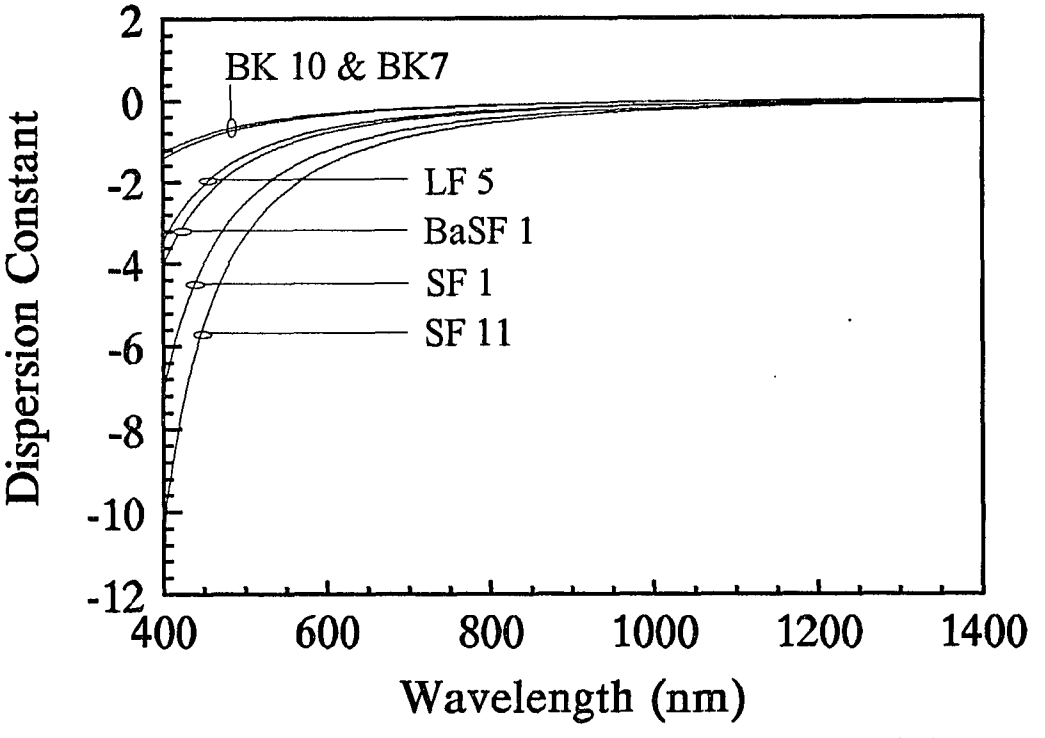

Fig. 5.2.2. Dispersion constant vs. wavelength for a variety of optical glasses.

The duration of a light pulse after propagating a distance z in the dispersive medium is given by eq. 5.2.45, and was numerically evaluated for a 30-fs pulse, and an 8-fs pulse. The pulse broadening as a function of the thickness of the dispersive medium is shown in figure 5.2.3. Propagation of the femtosecond pulses through the optical glass with the smaller index of refraction and dispersion constant results in minimum pulse broadening, while the higher index glasses change the pulse significantly.

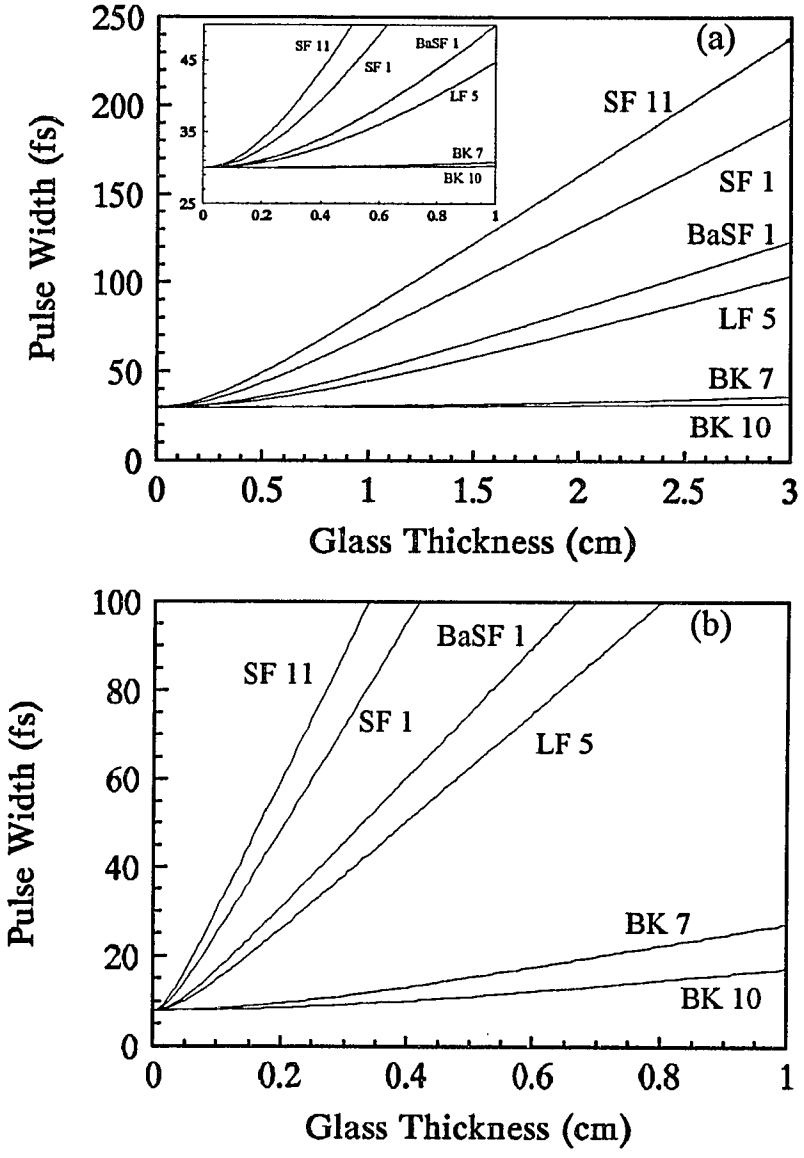

Fig. 5.2.3. Pulsewidth vs. distance traveled in a dispersive medium (a) for a 30-fs, and (b) for an 8-fs light pulse centered at 1250 nm.

Discussions on pulse propagation are usually carried out using the total phase of a light pulse. The equivalent expression to eq. 5.2.1 describing a gaussian light pulse before entering a dispersive medium (z = 0) can be written as

$$E(0,t) = E_0 e^{at^2} e^{i\Phi(t)} \tag{5.2.46}$$

Using the same procedure that resulted in eq. 5.2.4, the expression describing the pulse after propagating a distance z in the dispersive medium is given by

$$\tilde{E}(z,\omega) = \tilde{E}(0,\omega) e^{i\Phi(\omega)} \tag{5.2.47}$$

The phase shift suffered by a light pulse after propagation through an optical system is a function of the frequency and is denoted as $\Phi(\omega)$. The phase $\Phi(\omega)$ can be expressed as a series using the Taylor series expansion around the center frequency of the pulse ω_0 as

$$\Phi(\omega) = \Phi(\omega_0) + \left.\frac{d\Phi}{d\omega}\right|_{\omega_0} (\omega - \omega_0) + \frac{1}{2}\left.\frac{d^2\Phi}{d\omega^2}\right|_{\omega_0} (\omega - \omega_0)^2 + \frac{1}{6}\left.\frac{d^3\Phi}{d\omega^3}\right|_{\omega_0} (\omega - \omega_0)^3 + \ldots \tag{5.2.48}$$

where $\Phi(\omega) = \Phi_0$ - A constant phase shift

$\left.\frac{d\Phi}{d\omega}\right|_{\omega_0} = \tau_0$ - The system's delay for the carrier frequency ω_0 i.e. the time it takes for frequency ω_0 to transverse the dispersive system

$\left.\frac{d^2\Phi}{d\omega^2}\right|_{\omega_o}$ - Quadratic phase of the delay line. (Associated with the group velocity dispersion of the delay line)

$\left.\frac{d^3\Phi}{d\omega^3}\right|_{\omega_o}$ - Cubic phase of the delay line

In his paper "Optical Pulse Compression with Diffraction Gratings" Treacy[3] showed that the relation between the phase, Φ, and the optical path, P, traveled by the pulse is given by

$$\Phi(\omega) = \frac{\omega P}{c} \tag{5.2.49}$$

The derivatives of phase with respect to frequency in eq. 5.2.48 can be written as functions of the optical path.

$$\tau_o = \frac{d\Phi}{d\omega} = \frac{d\left(\frac{\omega P}{c}\right)}{d\omega} = \frac{1}{c}\left(\omega\frac{dP}{d\omega} + P\right) \tag{5.2.50}$$

$$\frac{d^2\Phi}{d\omega^2} = \frac{2}{c}\frac{dP}{d\omega} + \frac{\omega}{c}\frac{d^2P}{d\omega^2} \tag{5.2.51}$$

$$\frac{d^3\Phi}{d\omega^3} = \frac{3}{c}\frac{d^2P}{d\omega^2} + \frac{\omega}{c}\frac{d^3P}{d\omega^3} \tag{5.2.52}$$

Eq. 5.2.50 - 5.2.52 can be written as derivatives of the optical path, P, with respect to wavelength, λ. This is very useful since most of the times the phase is given as a

function of wavelength. The relation between the frequency and wavelength as stated in eq. 5.2.10 is

$$\omega = \frac{2\pi c}{\lambda} \tag{5.2.53}$$

Using eq. 5.2.53 then eqs. 5.2.49 - 5.2.52 can be expressed in terms of derivatives of the optical path with respect to wavelength. The equivalent expressions for eq. 5.2.49 and 5.2.50 are

$$\Phi = \frac{2\pi P}{\lambda} \tag{5.2.54}$$

$$\frac{d\Phi}{d\omega} = \frac{P}{c} - \frac{\lambda}{c}\frac{dP}{d\lambda} \tag{5.2.55}$$

In order to modify eq. 5.2.51 it requires few steps, and the procedure is presented next. First using the chain rule for the second derivative of phase with respect to frequency we can write

$$\frac{d^2\Phi}{d\omega^2} = \frac{d^2\lambda}{d\omega^2}\frac{d\Phi}{d\lambda} + \left(\frac{d\lambda}{d\omega}\right)^2 \frac{d^2\Phi}{d\lambda^2} \tag{5.2.56}$$

The derivatives of phase with respect to wavelength can be written as

$$\frac{d\Phi}{d\lambda} = \frac{d\left(\omega P/c\right)}{d\lambda} = -\frac{2\pi}{\lambda^2}P + \frac{2\pi}{\lambda}\frac{dP}{d\lambda} \tag{5.2.57}$$

$$\frac{d^2\Phi}{d\lambda^2} = \frac{4\pi}{\lambda^3}P - \frac{4\pi}{\lambda^2}\frac{dP}{d\lambda} + \frac{4\pi}{\lambda}\frac{d^2P}{d\lambda^2} \tag{5.2.58}$$

Using eq. 5.2.53 the derivatives of wavelength with respect to frequency can be expressed as

$$\frac{d\lambda}{d\omega} = -\frac{\lambda^2}{2\pi c} \tag{5.2.59}$$

and

$$\frac{d^2\lambda}{d\omega^2} = \frac{\lambda^3}{2\pi^2 c^2} \tag{5.2.60}$$

Substituting eqs. 5.2.57 - 5.2.60 in eq. 5.2.56 results to

$$\frac{d^2\Phi}{d\omega^2} = \frac{\lambda^3}{2\pi^2 c^2}\left(-\frac{2\pi}{\lambda^2}P + \frac{2\pi}{\lambda}\frac{dP}{d\lambda}\right) + \frac{\lambda^3}{2\pi^2 c^2}\left(\frac{4\pi}{\lambda^3}P - \frac{4\pi}{\lambda^2}\frac{dP}{d\lambda} + \frac{4\pi}{\lambda}\frac{d^2P}{d\lambda^2}\right) \tag{5.2.61}$$

which after the algebra is performed can be written as

$$\frac{d^2\Phi}{d\omega^2} = \frac{\lambda^3}{2\pi c^2}\frac{d^2P}{d\lambda^2} \tag{5.2.62}$$

Therefore the problem of estimating the quadratic phase of a system has been simplified to one of determining the optical path of the system and its dependence to the wavelength.

The cubic phase term can be evaluate in a similar fashion. The chain rule for the third derivative is

$$\frac{d^3\Phi}{d\omega^3} = \frac{d^3\Phi}{d\lambda^3}\left(\frac{d\lambda}{d\omega}\right)^3 + 3\frac{d^2\Phi}{d\lambda^2}\frac{d\lambda}{d\omega}\frac{d^2\lambda}{d\omega^2} + \frac{d\Phi}{d\lambda}\frac{d^3\lambda}{d\omega^3} \tag{5.2.63}$$

Following the same procedure as outlined above the cubic phase can be written as

$$\frac{d^3\Phi}{d\omega^3} = -\frac{\lambda^4}{4\pi^2 c^3}\left[3\frac{d^2P}{d\lambda^2} + \lambda\frac{d^3P}{d\lambda^3}\right] \qquad (5.2.64)$$

The dispersion constant, D, can also be expressed in terms of the optical path, P, using the following analysis. Treacy also showed that the time it takes a light pulse to transverse an optical system is related to the phase by

$$T = \frac{\partial\Phi(\omega)}{\partial\omega} \qquad (5.2.65)$$

where $\Phi(\omega)$ is the phase function and is given by

$$\Phi(\omega) = \frac{\omega P}{c} \qquad (5.2.66)$$

Substituting eq. 5.2.66 in eq. 5.2.65 the time T is given by

$$T = \frac{d\left(\frac{\omega P}{c}\right)}{d\omega} = \frac{1}{c}\left(\omega\frac{dP}{d\omega} + P\right) \qquad (5.2.67)$$

Using

$$\lambda = \frac{2\pi c}{\omega} \quad \text{and} \quad d\omega = -\frac{2\pi c}{\lambda^2}d\lambda \qquad (5.2.68)$$

eq. 5.2.67 can be written as a function of wavelength

$$T = \frac{1}{c}\left(P - \lambda\frac{dP}{d\lambda}\right) \qquad (5.2.69)$$

$$\frac{dT}{d\lambda} = \frac{1}{c}\left(\frac{dP}{d\lambda} - \frac{dP}{d\lambda} - \lambda\frac{d^2P}{d\lambda^2}\right) = -\frac{\lambda}{c}\frac{d^2P}{d\lambda^2} \qquad (5.2.70)$$

Substituting the expression for T in the definition of the group velocity dispersion constant as defined in eq. 5.2.43

$$D \equiv \frac{1}{L}\frac{dT}{d\lambda} \qquad (5.2.71)$$

results in the following expression

$$D = -\frac{\lambda}{Lc}\frac{d^2P}{d\lambda^2} \qquad (5.2.72)$$

Next consider a light pulse crossing a dispersive medium of thickness l_m. The optical path of this system is

$$P = l_m n_m \qquad (5.2.73)$$

where n_m is the index of refraction of the dispersive medium. The second derivative of P with respect to wavelength is

$$\frac{d^2P}{d\lambda^2} = l_m\frac{d^2n_m}{d\lambda^2} \qquad (5.2.74)$$

Substituting eq. 5.2.74 in eq. 5.2.62 the quadratic phase induced on the light pulse is given by

$$\frac{d^2\Phi_m}{d\omega^2} = \frac{\lambda^3 l_m}{2\pi c^2}\frac{d^2 n_m}{d\lambda^2} \qquad (5.2.75)$$

Using the same procedure the cubic phase induced on the pulse as a result of propagating through the dispersive medium is written as

$$\frac{d^3\Phi_m}{d\omega^3} = \frac{-\lambda^4}{4\pi^2 c^3}\left[3\frac{d^2 n_m}{d\lambda^2} + \lambda\frac{d^3 n_m}{d\lambda^3}\right] \qquad (5.2.76)$$

The analysis presented so far provides the base for discussion of phase distortion compensation in the Cr:forsterite laser. In the following section the problem of chirp compensation using a pair of prisms is considered.

5.3. Pulse Compression Using a Pair of Prisms

Propagation through an optical glass results into positive chirp. A positively chirped pulse has the low frequencies at the leading edge while the high frequencies are in the trailing edge. In other words the pulse is blue in the rear and red at the front. Optical systems such as a pair of gratings or suitably positioned prisms can act as negative dispersive elements. A negative dispersive element forces the lower frequencies (red) to travel a longer optical path than the higher frequencies (Blue). As a result the higher frequencies of the trailing edge of the pulse catch up with the leading edge resulting in a compressed pulse.

Prism pairs is the most popular method of controlling group velocity dispersion in a laser cavity. Prisms arranged as shown in figure 5.3.1 can introduce group-velocity dispersion that is both low loss and can be easily adjusted from negative to positive values.[4] A ray incident on the first prism gets refracted and as a result different frequencies are leaving the prism at different angles. Each frequency travels different

path length before reaching prism 2. The second prism causes an additional path deviation to be inflicted on the beam and also serves to collimate the beam. The beam it then goes through another prism pair, either by using another prism pair or by using a mirror and reflecting the beam back. Depending on the prism material, the amount of glass the beam passed through, and the prism separation the output beam has either positive or negative group velocity dispersion. This section presents the theory of chirp compensation using a pair of prisms and numerical calculation to determine type of glass to be used for prisms suitable for the near infrared. In the analysis cubic phase distortions are neglected and their effect will be consider in section 5.6.

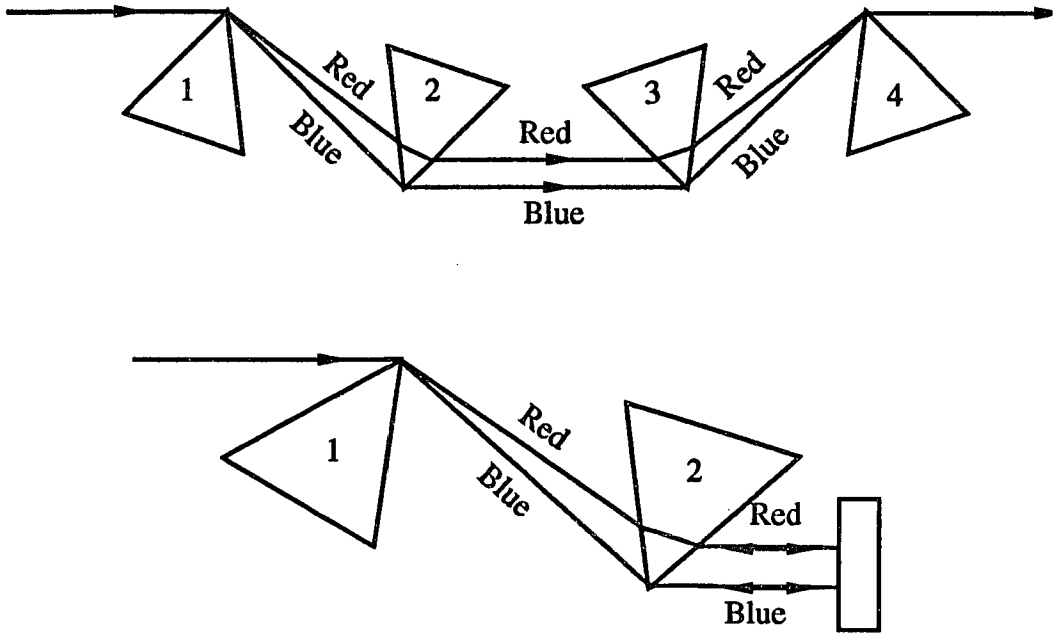

Fig. 5.3.1. Prisms configurations used for group velocity dispersion compensation.

As it was shown in the previous section the quadratic phase induced on a pulse after propagating through an optical system can be evaluated using the eq. 5.2.62 and the dispersion constant of the system using eq. 5.2.72

$$\frac{d^2\Phi}{d\omega^2} = \frac{\lambda^3}{2\pi c^2}\frac{d^2P}{d\lambda^2} \tag{5.3.1}$$

$$D = -\frac{\lambda}{Lc}\frac{d^2P}{d\lambda^2} \tag{5.3.2}$$

The following paragraphs describe the process of evaluating the optical path, P, for a prism pair and its derivatives with respect to wavelength.

In order to find P consider the prism configuration shown in figure 5.3.2.

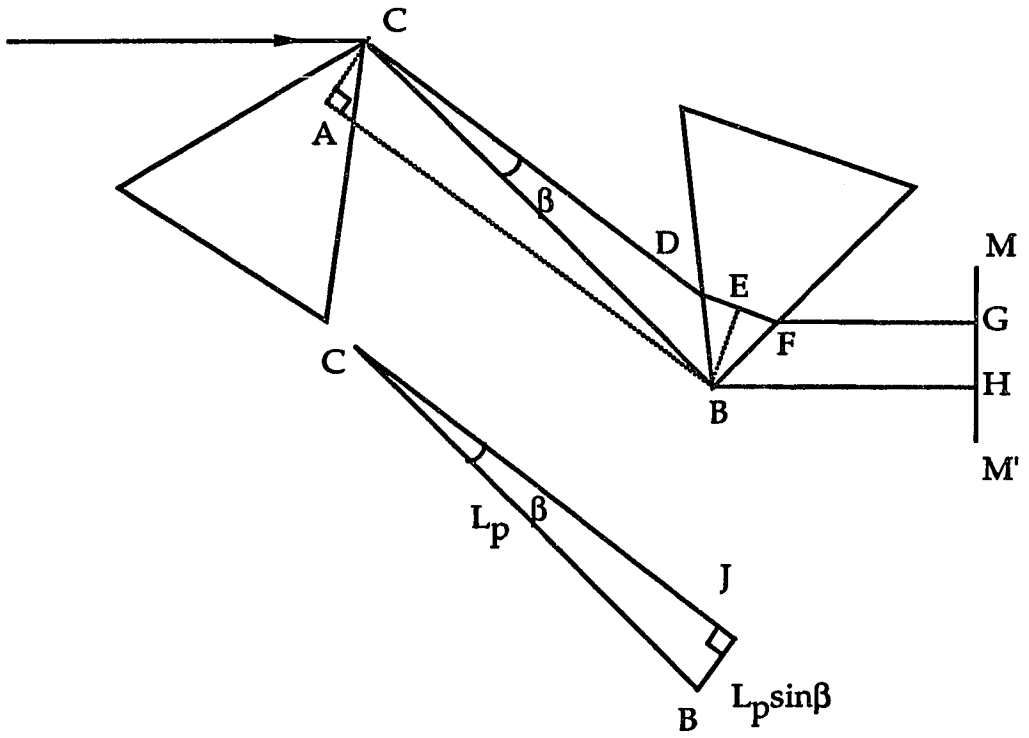

Fig. 5.3.2. Effect of a pair of prisms to the input rays.

$$AB = CDE \tag{5.3.3}$$

because AC and DE are possible wave fronts. Also by construction

$$CJ = AB \tag{5.3.4}$$

Therefore using eqs. 5.3.3 and 5.3.4

$$CDE = CJ$$

$$CJ = CB\cos\beta = L\cos\beta \qquad (5.3.5)$$

Another relationship is

$$EFG = BH \qquad (5.3.6)$$

because BE and GH are both possible wave fronts.

The rays FG and BH are parallel to the incident ray and hence to each other because the initial prism pair is equivalent in its effect on the ray direction to a slab having plane-parallel faces.

By symmetry, the second pair of prisms or a mirror directing the beams backwards introduces the same amount of dispersion as the first prism pair but reverses the transverse displacement of the rays. The final rays are therefore collinear with each other and collinear with the path of the incident rays. The total optical path that contributes to the dispersion is then

$$P = 2L_p\cos\beta \qquad (5.3.7)$$

The derivatives of P with respect to angle β are given by

$$\frac{dP}{d\beta} = -2L_p\sin\beta \qquad (5.3.8)$$

$$\frac{d^2P}{d\beta^2} = -2L_p\cos\beta \qquad (5.3.9)$$

The dispersion constant, D, in eq. 5.3.2 is a function of the second derivative of P with respect to λ. The variable β can change to λ in eq. 5.3.9 by noticing that the angle β is a function of the prism index n, which is in turn a function of the wavelength λ. Since n is a function of λ, we can express the derivatives of P with respect to λ in terms of derivatives of P with respect to n by

$$\frac{dP}{d\lambda} = \frac{dn}{d\lambda}\frac{dP}{dn} \tag{5.3.10}$$

$$\frac{d^2P}{d\lambda^2} = \frac{d^2n}{d\lambda^2}\frac{dP}{dn} + \left(\frac{dn}{d\lambda}\right)^2 \frac{d^2P}{dn^2} \tag{5.3.11}$$

Since β is a function of n, the derivatives with respect to n can be expressed as derivatives with respect to β, yielding [4]

$$\frac{d^2P}{d\lambda^2} = \left(\frac{d^2n}{d\lambda^2}\frac{d\beta}{dn} + \left(\frac{dn}{d\lambda}\right)^2 \frac{d^2\beta}{dn^2}\right)\frac{dP}{d\beta} + \left(\frac{dn}{d\lambda}\right)^2\left(\frac{d\beta}{dn}\right)^2 \frac{d^2P}{d\beta^2} \tag{5.3.12}$$

Now consider the schematic shown in figure 5.3.3. The angle of incidence of the beam at prism 1, Φ_1 is taken as fixed and the angle that the transmitted beam makes with the normal to the prism face Φ_2 is allowed to vary. Let the respective interior angles be Φ'_1 and Φ'_2 . Using Snell's law

$$n\sin\Phi'_1 = \sin\Phi_1 \tag{5.3.13}$$

$$n\sin\Phi'_2 = \sin\Phi_2 \tag{5.3.14}$$

By taking the derivatives of eqs. 5.3.13 and 5.3.14 with respect to n then

$$\sin\Phi'_1 + n\cos\Phi'_1\frac{d\Phi'_1}{dn} = 0 \tag{5.3.15}$$

$$\sin\Phi'_2 + n\cos\Phi'_2\frac{d\Phi'_2}{dn} = \cos\Phi_2\frac{d\Phi_2}{dn} \tag{5.3.16}$$

The relation between the prism's apex angle and angles Φ_1' and Φ_2' is given by this relationship

$$\alpha = \Phi_1' + \Phi_2' \tag{5.3.17}$$

and therefore

$$\frac{d\Phi_2'}{dn} = -\frac{d\Phi_1'}{dn} \tag{5.3.18}$$

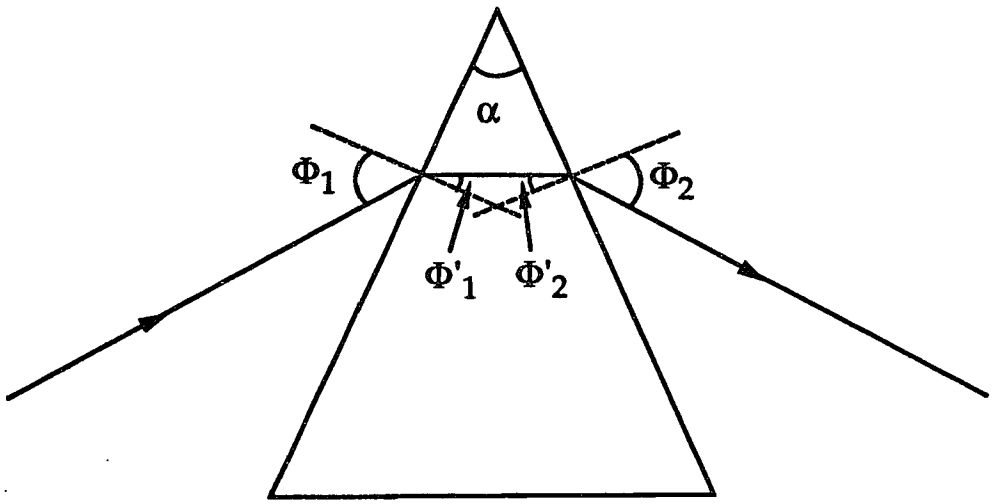

Fig. 5.3.3. Ray tracing through the prism.

Using eqs. 5.3.13 - 5.3.18 the derivatives of the angles Φ_1 and Φ_2 with respect to the index of refraction can be written

$$\frac{d\Phi_2}{dn} = \frac{1}{\cos\Phi_2}\left(\sin\Phi_2' + \cos\Phi_2' \tan\Phi_1'\right) \tag{5.3.19}$$

$$\frac{d^2\Phi_2}{dn^2} = \tan\Phi_2\left(\frac{d\Phi_2}{dn}\right)^2 - \frac{\tan^2\Phi_1'}{n}\left(\frac{d\Phi_2}{dn}\right) \tag{5.3.20}$$

For minimum deviation and Brewster's angle incidence then

$$\Phi_1' = \Phi_2' \tag{5.3.21}$$

$$\tan\Phi_2 = n \tag{5.3.22}$$

The change in angle β due to the index of refraction n is equal to the change in angle Φ_2 due to n. Therefore by inspection

$$\frac{d\beta}{dn} = -\frac{d\Phi_2}{dn} \tag{5.3.23}$$

$$\frac{d^2\beta}{dn^2} = -\frac{d^2\Phi_2}{dn^2} \tag{5.3.24}$$

which yields

$$\frac{d\beta}{dn} = -2 \tag{5.3.25}$$

$$\frac{d^2\beta}{dn^2} = -4n + \frac{2}{n^3} \tag{5.3.26}$$

Inserting the results obtained so far in eq. 5.3.12 the expression for the second derivative of P is given by [4]

$$\frac{d^2P}{d\lambda^2} = 4L_p\left\{\left[\frac{d^2n}{d\lambda^2} + \left(2n - \frac{1}{n^3}\right)\left(\frac{dn}{d\lambda}\right)^2\right]\sin\beta - 2\left(\frac{dn}{d\lambda}\right)^2\cos\beta\right\} \tag{5.3.27}$$

or

$$\frac{d^2P}{d\lambda^2} = 4\left[\frac{d^2n}{d\lambda^2} + \left(2n - \frac{1}{n^3}\right)\left(\frac{dn}{d\lambda}\right)^2\right]L_p\sin\beta - 8\left(\frac{dn}{d\lambda}\right)^2 L_p\cos\beta \tag{5.3.28}$$

The first term in eq. 5.3.31 can be either positive or negative depending on the physical properties of the prism's material, and the second term is always negative. Considering figure 5.3.2 angle β is of the order of the angular deviation of the ray bundle and therefore is small. Therefore the sine and cosine of angle β can be approximated by

$$\sin\beta << \cos\beta \qquad \text{and} \qquad \cos\beta \sim 1 \tag{5.3.29}$$

Also from figure 5.3.2 the term $L_p\sin\beta$ is of the order of twice the spot size

$$L_p\sin\beta \sim 2mm = \text{Constant} \tag{5.3.30}$$

Considering eqs. 5.3.29 and 5.3.30 then eq. 5.3.28 can be written as

$$\frac{d^2P}{d\lambda^2} = A - BL_p \tag{5.3.31}$$

where A and B are constants that depend on the physical properties of the prism's material.

$$A = 8\left[\frac{d^2n}{d\lambda^2} + \left(2n - \frac{1}{n^3}\right)\left(\frac{dn}{d\lambda}\right)^2\right] \tag{5.3.32}$$

$$B = 8\left(\frac{dn}{d\lambda}\right)^2 \tag{5.3.33}$$

Using a similar analysis the third derivative of the optical path P with respect to wavelength can be evaluated as [4]

$$\frac{d^3P}{d\lambda^3} = 4\frac{d^3n}{d\lambda^3}l_p\sin\beta - 24\frac{dn}{d\lambda}\frac{d^2n}{d\lambda^2}l_p\cos\beta \tag{5.3.34}$$

This will be used later in section 5.6 when cubic phase distortion compensation will be considered.

Bandwidth-pulsewidth measurements with the active mode-locked forsterite laser indicated the presence of GVD in the output pulses. Since there are no reports of the dispersion of the forsterite crystal numerical calculations were carried out to determine the type of glass to be used for prisms that can selectively add negative or positive GVD. To do this one needs the index of refraction, n, and its derivatives with respect to wavelength as indicated by eq. 5.3.28.

The numerical calculations were carried out using eq. 5.3.28 for prisms made of different types of glass. The material characteristics

$$n, \quad \frac{dn}{d\lambda}, \quad \frac{d^2n}{d\lambda^2}$$

were evaluated using the dispersion formula.[11]

$$n(\lambda) = \sqrt{A_o + A_1\lambda^2 + \frac{A_2}{\lambda^2} + \frac{A_3}{\lambda^4} + \frac{A_4}{\lambda^6} + \frac{A_5}{\lambda^8}} \qquad (5.3.35)$$

The calculations indicated that prisms made of SF 14 prism can add either positive or negative group velocity dispersion. The coefficients in the dispersion formula for SF 14 optical glass are shown in table 5.3.1 and the calculated index of refraction and its derivatives are shown in figure 5.3.4.

By substituting the calculated values of the index of refraction and its derivatives in equation 5.3.28 the constants A and B in eq. 5.3.31 are estimated. Table 5.3.2 lists the calculated values for A and B at different wavelengths. As an example consider that λ = 1250 nm and that the beam passes through the tip of the two prisms so there is no significant GVD due to the material. Figure 5.3.5 shows the variation of $d^2P/d\lambda^2$ as a function of the prism separation L_p.

Table 5.3.1. Constants of dispersion formula for SF 14 optical glass.

A_o	2.9826955
A_1	$-1.1720091 \times 10^{-2}$
A_2	3.5994978×10^{-2}
A_3	2.9250972×10^{-3}
A_4	$-2.1913665 \times 10^{-4}$
A_5	2.6700784×10^{-5}

Table 5.3.2. Calculated values for constants A and B of eq. 5.3.31 for SF 14 optical glass at different wavelengths.

λ (nm)	A	B
1210	0.22757	0.00358
1230	0.20879	0.00341
1250	0.19158	0.00326
1270	0.17578	0.00312
1290	0.16126	0.00299

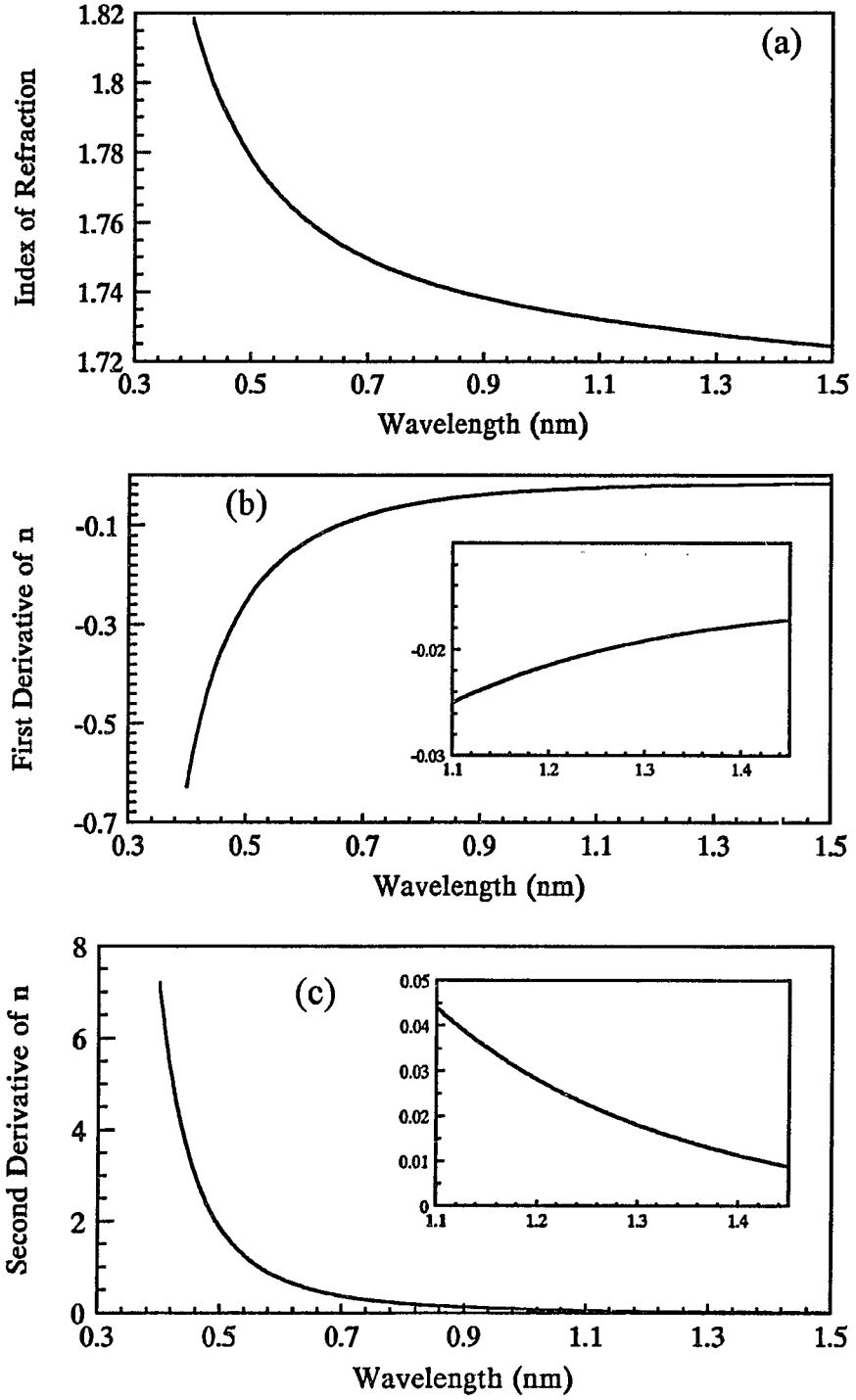

Fig. 5.3.4. Index of refraction and its derivatives with respect to wavelength for SF 14 optical glass a) Index of refraction vs. wavelength b) First derivative of index of refraction with respect to wavelength vs. wavelength c) Second derivative of index of refraction with respect to wavelength vs. wavelength.

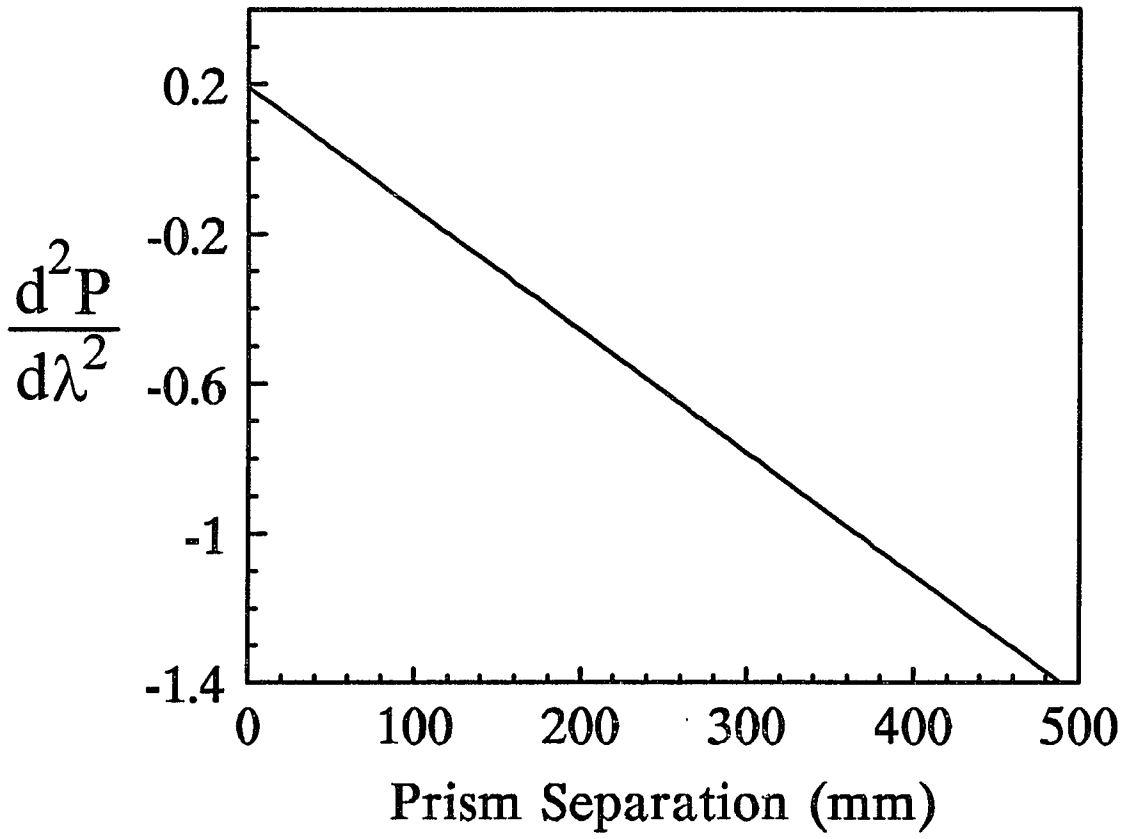

Fig. 5.3.5. Second derivative of P with respect to wavelength for a double pass prism pair as a function of prism separation.

By inspecting Fig. 5.3.5 a pair of SF 14 prisms can introduce either positive or negative GVD. For $L_p > 60$ mm at 1250 nm the prism pair introduces negative GVD, and for $L_p < 60$ mm the prism pair introduces positive GVD. GVD can be varied either by controlling the amount of prism material the beam goes through (more prism => more positive GVD, less prism => less positive GVD), or by controlling the prism separation L_p (larger prism separation => more negative GVD , smaller prism separation => less negative GVD).

5.4. Femtosecond Operation of Active Mode-Locked Cr:Forsterite Laser

The generation of femtosecond pulses from a continuous-wave mode-locked chromium-doped forsterite (Cr^{4+}:Mg_2SiO_4) laser is presented in this section. The forsterite laser was actively mode-locked using an acousto-optic modulator operating at 76 MHz with two Brewster high-dispersion glass prisms for intra-cavity chirp compensation. Transform-limited sub-100-fs pulses were routinely generated in the TEM_{00} mode tunable over 1230-1280 nm. The shortest pulses of 60-fs pulsewidth were measured and the for the first time the forsterite laser operated in the self-mode-locked mode.

The experimental arrangement is shown in Fig. 5.4.1 which is the same four mirror z-fold cavity used before with the addition of two SF 14 prisms. The details of the experimental setup are presented again since the same setup will be used for the rest of the experiments with only minor changes. The Brewster-angle-cut forsterite crystal was placed in a four-mirror, z-fold astigmatically compensated cavity which is widely used for Ti:sapphire lasers.[12,13] The combination of mirrors used was: a flat back mirror, two 10-cm-radius folding mirrors, and a flat output coupler. The transmission of the output coupler was 1% at the lasing wavelength, while the folding mirrors and the back mirror had reflectivity R=99.9% for the 1200-1300 nm range. The transmission characteristics of the mirrors used in the four mirror cavity are shown in Appendix B. The Cr:forsterite crystal used in this study was grown by the Mitsui Mining & Smelting Company, Japan (Crystal 2). The length of the sample was 1 cm and the absorption coefficient at the pump wavelength of 1064 nm was $\alpha = 0.7224\ cm^{-1}$. To eliminate the need to chop the pump beam, the laser crystal was mounted in a copper block and was cooled by a single-stage thermoelectric cooler. Better thermal contact between the crystal and the copper block was achieved by wrapping the crystal in an indium foil. The crystal and the copper block were purged by nitrogen to prevent moisture condensation. The Cr:forsterite crystal was pumped by a continuous-wave Nd:YAG laser. The pump beam was focused by a 7.5-cm

lens through the 10-cm-radius folding mirror into the crystal. The 1064-nm pump power incident on the forsterite crystal was 4.7 W. The output of the forsterite laser was monitored with a fast germanium detector and an oscilloscope, and the pulsewidth was measured with a real-time autocorrelator. The bandwidth of the mode-locked forsterite laser was measured using a lead sulfide (PbS) detector coupled to a 50-cm Jarrel Ash monochromator, equipped with 10-μm slits.

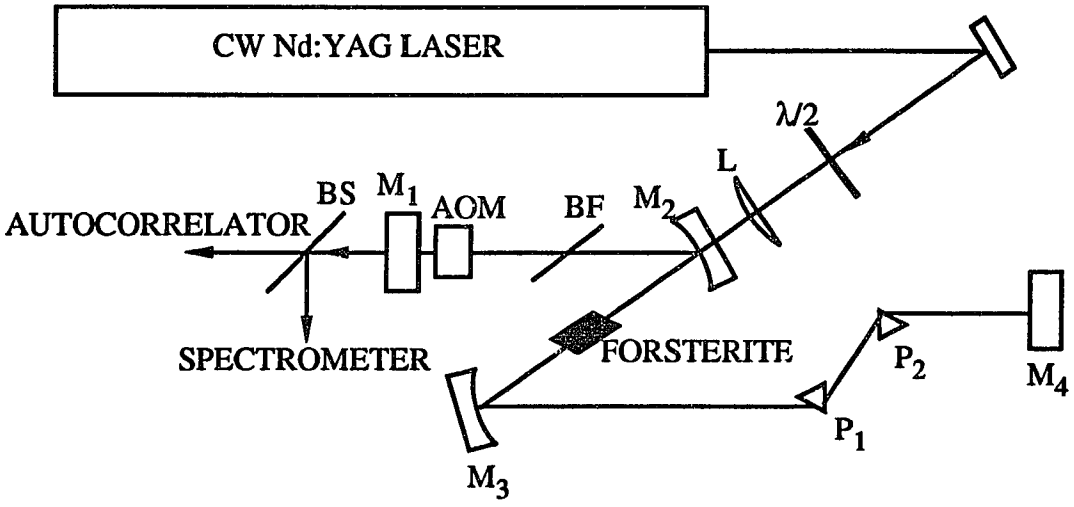

Fig. 5.4.1. Schematic diagram of the experimental arrangement for the actively mode-locked operation of the Cr:forsterite laser: λ/2, half-wave plate for 1064 nm; L, focusing lens; M_1, output mirror, M_2, M_3, 10-cm-radius folding mirrors; M_4, back mirror; AOM, acousto-optic modulator; BF, birefringent tuning plate; BS, beam splitter; P_1 and P_2, Schott SF 14 glass prisms.

Actively mode-locked operation of the forsterite laser was achieved when the acousto-optic modulator was inserted in the cavity. Mode-locking was observed when the length of the cavity was adjusted to a length of ~1.97 m corresponding to the frequency of the acousto-optic modulator (76 MHz). When the prisms are not part of the cavity a

stable train of 6-ps pulses was obtained as described in section 4.5 with a bandwidth-pulsewidth product of 1.34 indicating that the pulses were chirped.

To compensate for the dispersion, a pair of high-dispersion Schott SF 14 glass Brewster prisms were inserted in the cavity. A pair of prisms was expected to introduce negative group-velocity dispersion, without increasing the cavity loss. The distance between the prisms was varied until the shortest pulse width were measured, while maintaining the total length of the cavity constant.

The insertion of the pair of SF 14 prisms in the cavity resulted in a significant reduction of pulsewidth. We observed two distinct regimes where the forsterite laser would produce femtosecond pulses. In the first regime we had compensation of GVD introduced by the forsterite crystal. The shortest pulses measured in this case had duration of 900 fs FWHM and spectral width of 1.9 nm FWHM. Figure 5.4.2 (a) shows the autocorrelation trace of the pulsewidth and figure 5.4.2 (b) shows the corresponding spectrum for the 900 fs pulses. Circles represent experimental data and the solid line is the best fit sech^2 pulse shape was assumed for fitting. The pulsewidth-bandwidth product $\Delta\tau_p\Delta\nu = 0.33$, indicated nearly transform limited pulses.

Further optimization of the cavity (optimize the position of the forsterite crystal with respect to the two folding mirrors and the distance between the two folding mirrors) resulted in a significant reduction of pulsewidth, to less than 100 fs, with a spectral width of the order of 20 nm. An autocorrelation trace and the corresponding spectrum of a typical pulse are shown in figure 5.4.3 (a) and (b). The pulsewidth shown is 90 fs and the bandwidth is 19 nm. The pulsewidth-bandwidth product $\Delta\tau_p\Delta\nu = 0.32$, indicating transform-limited pulses for a sech^2 pulse. The optimum distance between the two prisms when stable 90-fs pulses were obtained, was determined to be 35 cm. Shorter pulses were observed after long hours of cavity optimization and only for brief times. The autocorrelation trace presented in Fig. 5.4.4 shows a pulse of less than 60 fs FWHM.

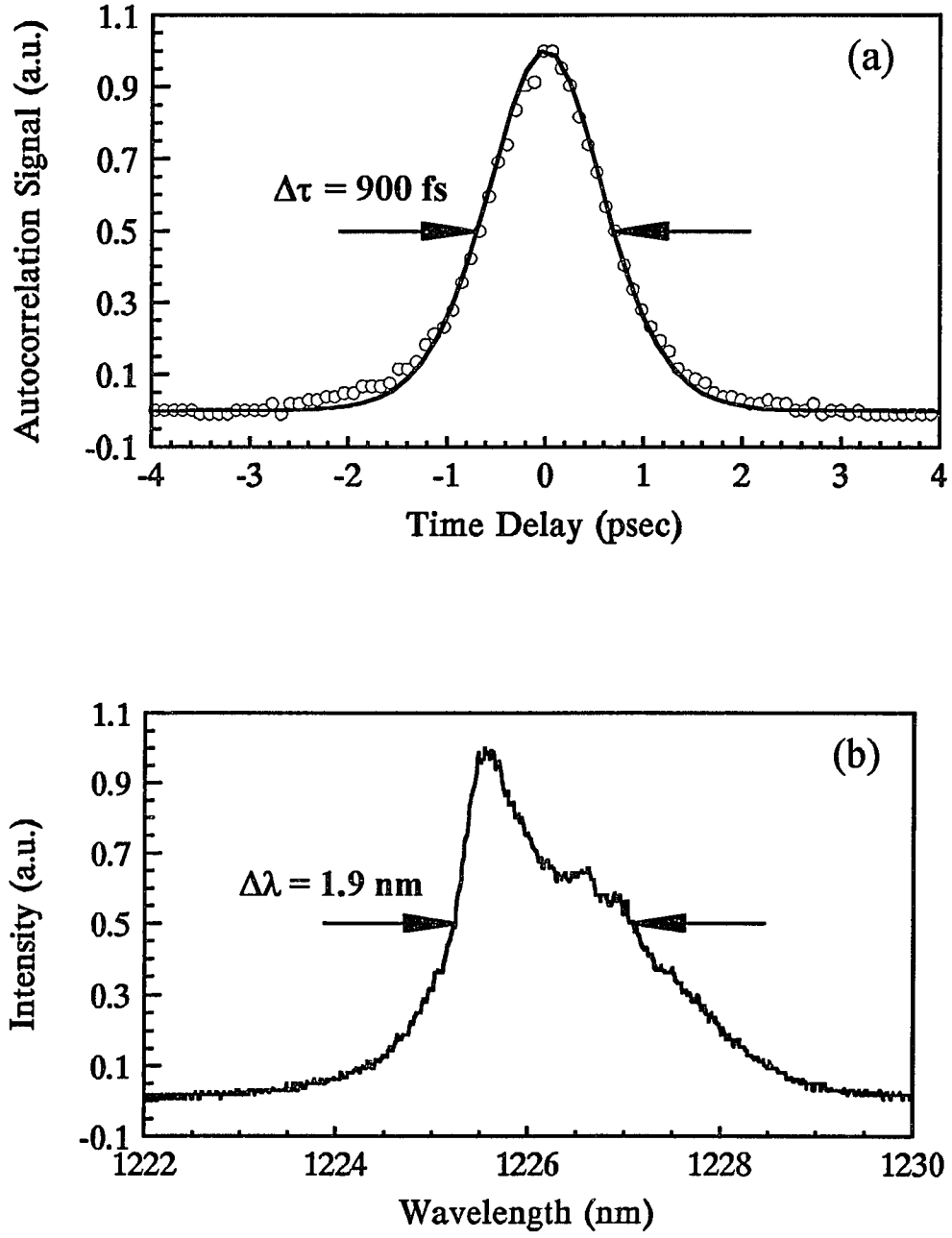

Fig. 5.4.2. An autocorrelation trace (a) and spectrum (b) of the 900 fs pulses. Circles represent experimental data and the solid line is the best fit. $sech^2$ pulse shape was assumed for fitting. The pulsewidth-bandwidth product is $\Delta\tau_p\Delta\nu = 0.33$.

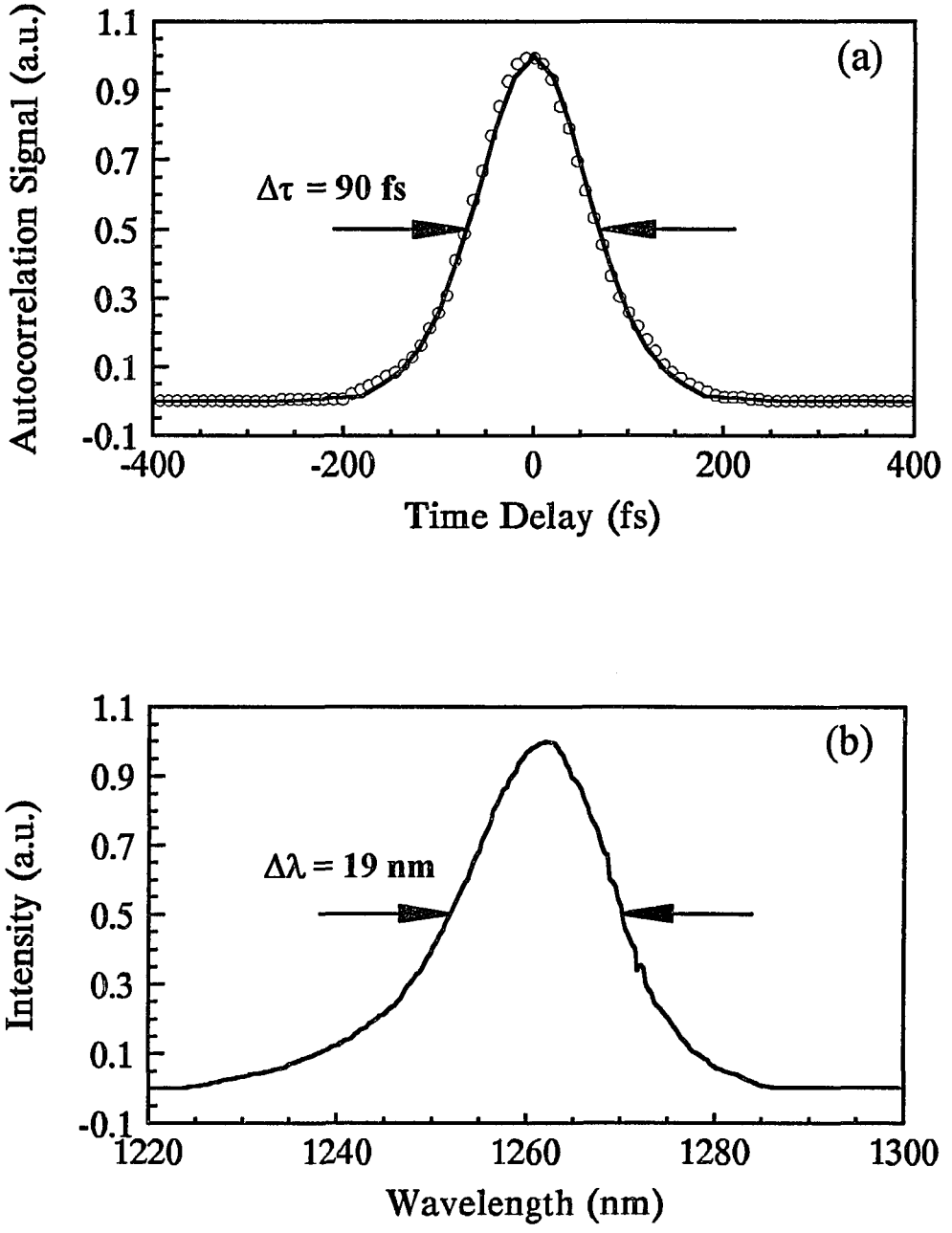

Fig. 5.4.3. An autocorrelation trace (a) and spectrum (b) of 90-fs pulses. Circles represent experimental data and the solid line is the best fit. $sech^2$ pulse shape was assumed for fitting. The pulsewidth-bandwidth product $\Delta\tau_p\Delta\nu = 0.32$.

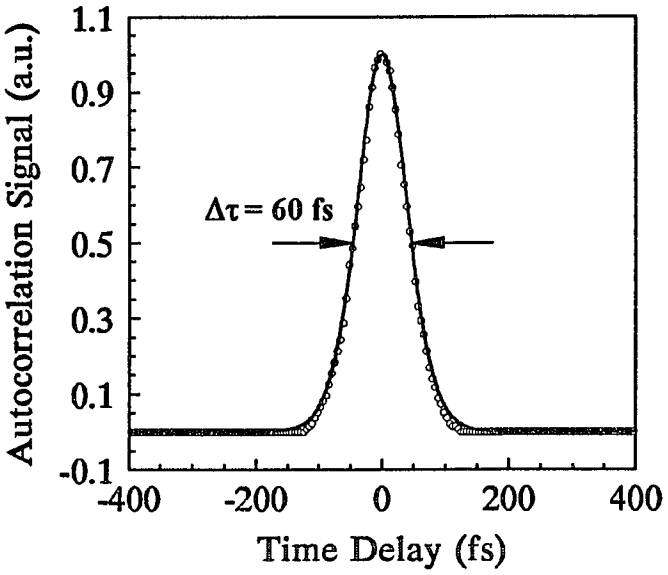

Fig. 5.4.4. An autocorrelation trace of 60-fs pulses (assuming $sech^2$ pulse shape). Circles represent experimental data and the solid line is the best fit.

The reduction of the pulsewidth from 900 fs to 90 fs indicated that another mechanism besides active modulation is responsible for the shortening of the pulses. It was suspected that the self mode-locking mechanism was responsible for the generation of the 90 fs pulses. To investigate this possibility the RF power from the acousto-optic modulator was disconnected while stable sub-100-fs pulses were monitored. Within the first 30 seconds no change in the output was observed, i. e. stable sub-100-fs pulses were generated without any external modulation. The mode-locked operation usually ceased after this initial period, most likely due to some mechanical disturbances (Self mode-locking will be discussed in subsequent sections). This is an indication that the Cr:forsterite laser actually operated, similar to Ti:sapphire lasers[14,15] in a self-mode locked regime, where active mode-locking only sets the conditions necessary for self-mode-locked operation by producing intense optical fields in the cavity. Intensity-induced Kerr nonlinearities in the gain medium, combined with negative group velocity dispersion introduced by the prisms are responsible for production of the shortest pulses.

The actively mode-locked forsterite laser was tuned using an intracavity single-crystal quartz birefringent plate as shown in figure 5.3.1. With only one combination of laser mirrors the laser output was continuously tuned between 1230 - 1280 nm. The power output of 50 mW was measured, for 1.9 W of absorbed pump power. The pulsewidth and output power did not change significantly over the tuning range.

The dependence of the pulsewidth on the pump power was measured. As described above, when pumped by the maximum available power of 4.7 W incident on the crystal, stable sub-100-fs pulses were generated. As the pump power was lowered, the pulsewidth increased to above 1 ps at 3.9 W pump power incident on the forsterite crystal. The tendency of pulse shortening with increasing power suggests that, if more pump power were available, even shorter pulses may be obtained.

5.5. Self-Mode-Locked Cr:Forsterite Laser

The observed mechanism of generation of femtosecond pulses from the active-mode locked forsterite laser suggests that femtosecond pulses can be generated from chromium doped forsterite laser without the need of active modulation. In order to achieve pure self mode locked operation we design the laser shown in figure 5.5.1. The cavity is the same four mirror astigmatically compensated cavity used before but now pumping is provided by a CW mode-locked Nd:YAG laser. We removed the acousto-optic modulator and the birefringent plate, and we inserted an aperture between the second prism and the end mirror M_4 for tuning purposes. The forsterite crystal, Crystal 2, was replaced by a new forsterite crystal, Crystal 3 (See chapter 2 for crystal characteristics). Crystal 3 has similar absorption characteristics as Crystal 2 at the pump wavelength but less absorption in the lasing wavelength region yielding a higher FOM (47 as compared to 39 for Crystal 2).

The main idea behind this experiment is that picosecond pulses will be generated by adjusting the length of the forsterite laser to match the frequency of the pumping CW

mode-locked Nd:YAG laser (synchronously-pumped mode-locking). These picosecond pulses in turn will generate the passive modulation and provide the starting mechanism for self mode-locking.

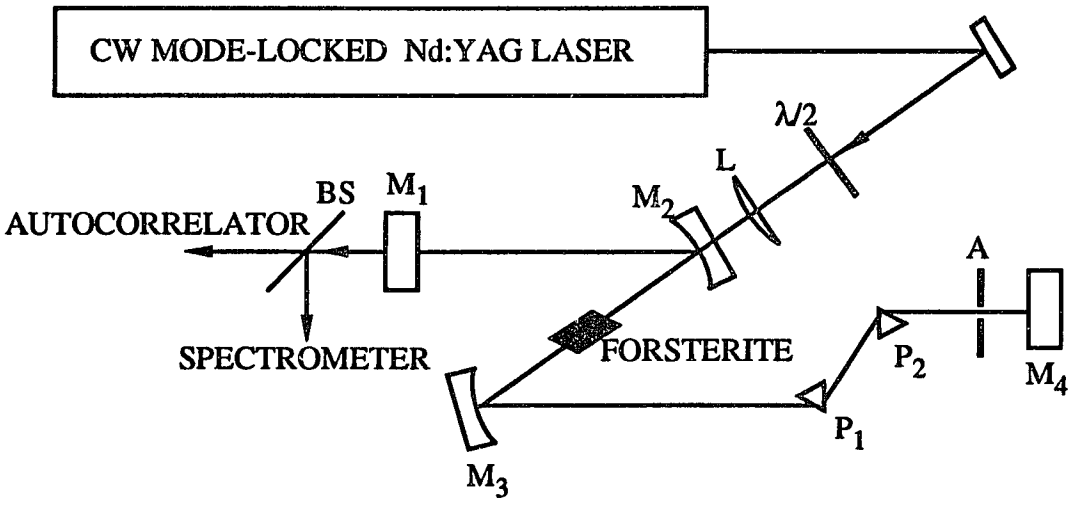

Fig. 5.5.1. Synchronously pumped forsterite laser design engineered for the generation of femtosecond pulses and self-mode-locking.

Synchronously pumped mode locking was observed when the length of the forsterite laser cavity was matched to the length of the Nd:YAG laser. The output pulses of the synchronously pumped forsterite laser had duration of the order of 200-300 ps. By careful optimization of the cavity by adjusting the position of the laser crystal with respect to the two folding mirrors, the forsterite laser was self mode-locked and the pulsewidth was reduced to 105 fs with a spectral width of the order of 15 nm. In order to confirm that self mode-locking was achieved the cavity length was increased while monitoring the pulsewidth and the pulse train on the oscilloscope. The forsterite laser continued to generate femtosecond pulses even when the length of the cavity was changed by few centimeters. This clearly indicated that the forsterite laser was self mode-locked and that synchronously pumped mode-locking acted as the starting mechanism for

self mode-locking. The output power of the forsterite laser when femtosecond pulses were generated was 60 mW.

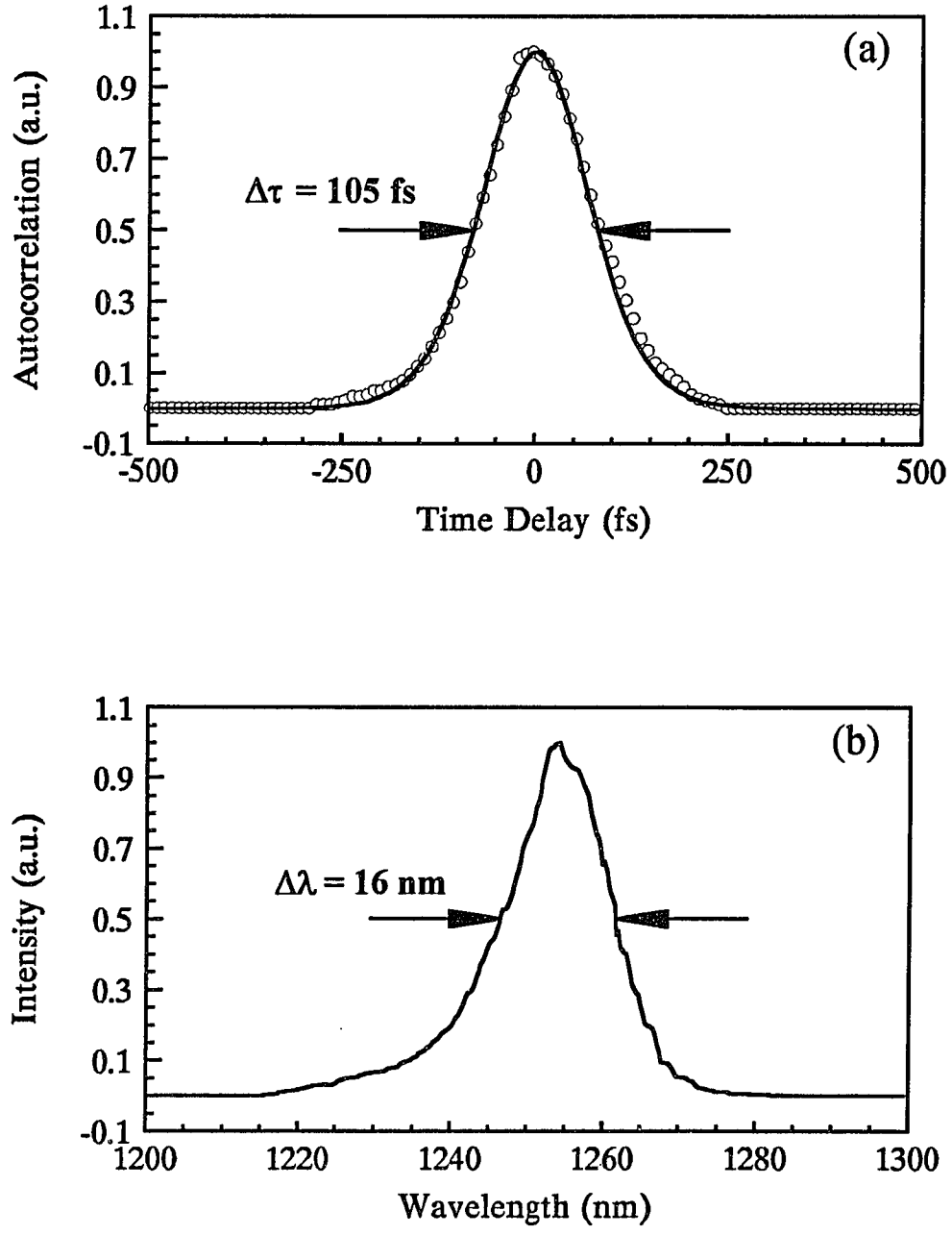

Fig. 5.5.2. An autocorrelation trace (a) and spectrum (b) of 105-fs pulses obtained from a z-fold cavity with SF 14 prisms for chirp compensation. Circles represent experimental data and the solid line is the best fit for $sech^2$ pulse shape.

An intensity autocorrelation trace and the corresponding spectrum of a typical pulse are shown in figure 5.5.2 (a) and (b). The pulsewidth shown is 105 fs and the bandwidth is 16 nm. The pulsewidth-bandwidth product $\Delta\tau_p\Delta\nu = 0.32$, indicating transform-limited pulses assuming $sech^2$ pulses.

Figure 5.5.3 shows an oscilloscope photograph of the interferometric autocorrelation trace of the output pulses. Since there is good visibility of the fringes at the wings of the pulse it is evident that the pair of prisms compensated for the chirp introduced by the forsterite crystal. The self mode-locked forsterite laser was tuned using an aperture mounted on a translation stage between prism P_2 and mirror M_4. Continuous tuning of the laser was achieved between 1240 and 1270 nm limited only by the dielectric coating of the mirrors. The duration of pulses did not vary throughout the whole tuning range.

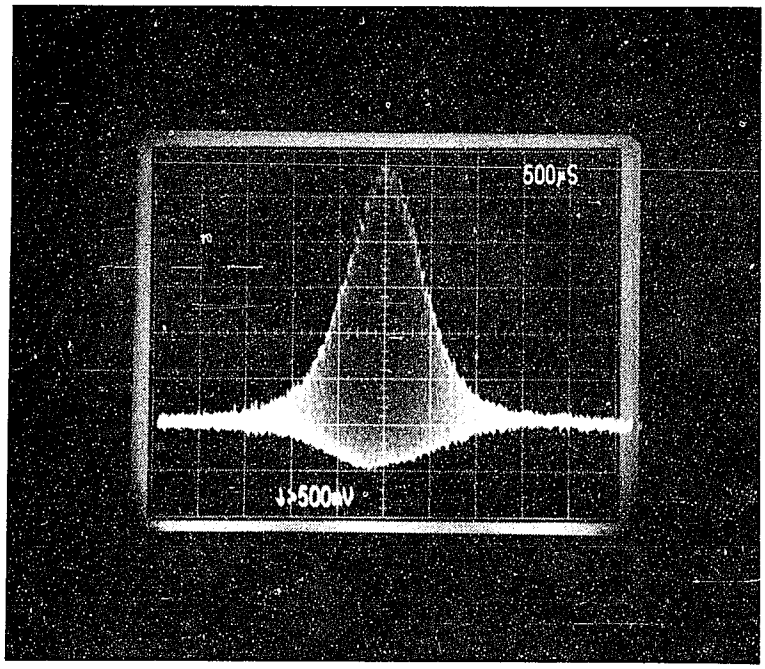

Fig. 5.5.3. Interferometric autocorrelation of the output pulses of the forsterite laser.

The stability of the self mode-locked forsterite laser was greatly improved as compared with the previous experiment where the acousto-optic modulator was part of the cavity.[10] The forsterite laser was operating in a self mode-locked mode for up to one hour without significant change in the output pulse characteristics. We believe that the improvement was mainly due to the absence of the losses and phase distortions due to the mode locker and the birefringent filter.

5.6. Elimination of Cubic Phase Distortions

The calculations performed in section 5.3 emphasize the elimination of the quadratic phase in the pulses generated by the Cr:forsterite Crystal while the effects of the cubic phase were neglected. The observation of self mode-locking from the Cr:forsterite laser suggests that as in the case of Ti:sapphire shortest pulses can be generated by careful selection of prism material.

The calculation performed so far and experimental results indicated that a pair of SF 14 prism can compensate for group velocity dispersion in the forsterite laser. The optical characteristics of SF 14 optical glass for 1250 nm are n = 1.729, $dn/d\lambda$ = -0.02017 μm^{-1}, $d^2n/d\lambda^2$= 0.02262 μm^{-2}, and $d^3n/d\lambda^3$= -0.0999 μm^{-3}. The optimum distance between the two prisms was determined to be 35 cm when stable 105-fs pulses were obtained. Carrying out the calculation for the phase derivatives with respect to frequency we obtained $\partial^2\phi/\partial\omega^2$= -3273 $fsec^2$ and $\partial^3\phi/\partial\omega^3$= -2170 $fsec^3$ (for a round trip). This calculation indicates that SF 14 may not the most appropriate glass for pulse shortening in this wavelength region since it introduces a large cubic phase term. Shorted pulses may be generated by using material which will introduce less cubic phase as is the case with Ti:sapphire.[16,17,18]

Calculations of higher order phase order terms introduced by a pair of prisms in the cavity were performed to determine optical glass that can compensate for GVD and

introduce minimum cubic phase term. Table 5.6.1 lists the expressions used for the numerical evaluation of the dispersion characteristics of different optical materials.[19] Using these expressions the dispersion formula for the second and third order phase terms are evaluated and then the distance that these prism should be placed in order to introduce an equal amount of quadratic phase term as SF 14 prisms is determined. Then the amount of cubic phase by using the specific optical material is calculated.

Table 5.6.1. Second and third order derivatives of phase with respect to frequency for a double pair prism and material.

PRISM	MATERIAL
$\frac{d^2\Phi_p}{d\omega^2} = \frac{\lambda^3}{2\pi c^2}\frac{d^2P}{d\lambda^2}$	$\frac{d^2\Phi_m}{d\omega^2} = \frac{\lambda^3 l_m}{2\pi c^2}\frac{d^2n_m}{d\lambda^2}$
$\frac{d^3\Phi_p}{d\omega^3} = \frac{-\lambda^4}{4\pi^2 c^3}\left[3\frac{d^2P}{d\lambda^2} + \lambda\frac{d^3P}{d\lambda^3}\right]$	$\frac{d^3\Phi_m}{d\omega^3} = \frac{-\lambda^4}{4\pi^2 c^3}\left[3\frac{d^2n_m}{d\lambda^2} + \lambda\frac{d^3n_m}{d\lambda^3}\right]$

Where

$$\frac{d^2P}{d\lambda^2} = 4\left[\frac{d^2n}{d\lambda^2} + \left(2n + \frac{1}{n^3}\right)\left(\frac{dn}{d\lambda}\right)^2\right] l_p \sin\beta - 8\left(\frac{dn}{d\lambda}\right)^2 l_p \cos\beta$$

and

$$\frac{d^3P}{d\lambda^3} = 4\frac{d^3n}{d\lambda^3} l_p \sin\beta - 24\frac{dn}{d\lambda}\frac{d^2n}{d\lambda^2} l_p \cos\beta$$

Phase calculations were carried out for prism pairs for all the types of optical glasses listed in Schott catalogue. Table 5.6.2 lists the numerical results for some types of glass that can compensate for chirp in this wavelength region and introduce less cubic phase term. Column 1 lists the glass type. Columns 2 and 3 list the second and third derivative of the phase with respect to frequency for material dispersion, respectively and indicate the amount of quadratic and cubic phase that will be introduced to the pulse when it transverses length l_m of the specified material. Columns 4 and 5 list the second and third derivative of the phase with respect to frequency introduced by a pair of prism with separation l_p, respectively. They indicate the amount of quadratic and cubic phase that will be introduced to the pulse when it passes through a pair of prism with separation l_p, assuming minimum glass pathway in the prisms. Column 6 shows the prism separation that will introduce the same quadratic phase term as SF 14 glass prisms, and the last column shows the cubic phase which will be introduced by using the specified type of glass for a prism separation which compensates for the quadratic phase. The values of phase derivatives shown for the pair of prisms are for round trip, l_p is measured in mm and the calculations were performed for λ=1250 nm.

Figure 5.6.1 shows the cubic phase for different types of prisms vs. wavelength assuming that the prism separation is set to compensate for the quadratic phase in the forsterite laser cavity, and minimum glass pathway in the prisms. As is indicated SF 14 prisms introduce a large cubic phase at 1250 nm but will be more appropriate to be used for chirp compensation when the forsterite laser operates beyond 1300 nm. In figure 5.6.1 we also show other types of prisms that can be used for chirp compensation in the tuning range of chromium doped forsterite.

Table 5.6.2 Dispersion characteristics for different optical glasses at 1250 nm

1	2	3	4	5	6	7
Glass Type	$\frac{d^2\Phi_m}{d\omega^2}$ (fsec^2)	$\frac{d^3\Phi_m}{d\omega^3}$ (fsec^3)	$\frac{d^2\Phi_p}{d\omega^2}$ (fsec^2)	$\frac{d^3\Phi_p}{d\omega^3}$ (fsec^3)	l_p (mm)	$\frac{d^3\Phi_p}{d\omega^3}$ (fsec^3)
SF 14	78 l_m	130 l_m	662 - 11.2 l_p	974 - 9.0 l_p	350	-2170
SF 15	63 l_m	110 l_m	532 - 8.5 l_p	827 - 5.2 l_p	451	-1504
SF 2	52 l_m	93 l_m	436 - 56.5 l_p	706 - 3 l_p	573	-1008
SFN 64	61 l_m	115 l_m	516 - 9.9 l_p	859 - 3.2 l_p	384	-359
F 2	45 l_m	87 l_m	376 - 5.8 l_p	662 - 1.4 l_p	629	-214
BaSF 1	43 l_m	81 l_m	361 - 5.2 l_p	621 - 1.5 l_p	698	-394
LaF 13	54 l_m	107 l_m	461 - 9 l_p	794 - 1.5 l_p	417	+171
LaFN 7	53 l_m	115 l_m	460 - 10.3 l_p	853 - 0.02 l_p	364	+848

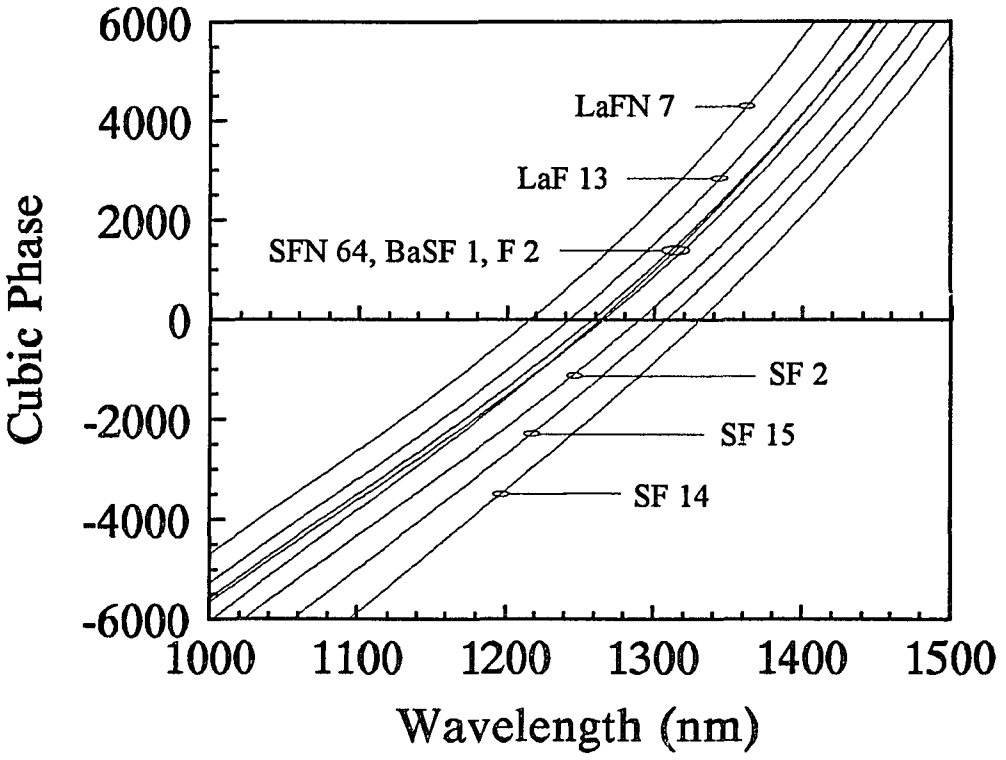

Fig. 5.6.1. Round-trip cubic phase of various Brewster prism pairs. Zero round-trip cavity quadratic phase and minimum glass pathway in the prism are assumed.

5.6. Improved Self-Mode-Locked Cr:Forsterite Laser

The results of the calculations shown in table 5.6.2 and in figure 5.6.1 suggest that for 1250 nm other types of glass can compensate for group velocity dispersion and will introduce a smaller cubic phase term as compared with SF 14 prisms. We chose to use prisms made of SFN 64 glass because the prism separation was very close to the one for SF 14 prisms and our cavity design would required minimum changes.

The experimental arrangement used for the following experiments is exactly the same as the one described in section 5.5 except that the SF 14 prisms were replaced with

SFN 64 prisms. As before synchronously pumped mode locking was observed when the length of the forsterite laser cavity was matched to the length of the Nd:YAG laser, generating pulses with FWHM of 200-300 ps. By further optimization of the laser cavity the forsterite laser was self mode-locked generating sub-100-fs pulses. The stability of the self mode-locked forsterite laser and the ease of starting self mode-locking was improved as compared when SF 14 prisms were used. The prism separation for optimum operation was measured to be ~42 cm which is good agreement with 38.4 cm calculated. An intensity autocorrelation trace and the corresponding spectrum of a typical pulse are shown in Fig. 5.7.1 (a) and (b). The pulsewidth shown is 50 fs and the bandwidth is 33 nm. The pulsewidth-bandwidth product $\Delta\tau_p\Delta\nu = 0.32$ indicates transform-limited $sech^2$ pulses.

Further improvement in the pulsewidth of the output pulses from the self-mode-locked forsterite laser was achieved when the forsterite crystal, Crystal 3, was replaced with Crystal 4. Crystal 4 has a FOM of 58 which is the highest FOM measured for any crystals tested so far. The shortest pulses were recorded when Crystal 4 was used. An intensity autocorrelation trace and the corresponding spectrum of a typical pulse are shown in Fig. 5.7.2 (a) and (b). The pulsewidth shown is 36 fs and the bandwidth is 52.5 nm. The pulsewidth-bandwidth product $\Delta\tau_p\Delta\nu = 0.368$ indicating nearly transform-limited $sech^2$ pulses. The pulses are not totally transform-limited probably due to phase distortions introduced by the 0.5 inch thick output coupler and the 300 μm thick beam splitter in the autocorrelator.

The stability of the self-mode-locked Cr:forsterite laser was improved when Crystal 4 was used in the cavity. The laser was operating in a self mode-locked mode of operation for as long as required without degradation in the quality of the output pulses. As seen from the bandwidth measurements the corresponding spectrum of the 36-fs pulses nearly covers the whole emission spectrum of forsterite (1170 - 1310 nm).

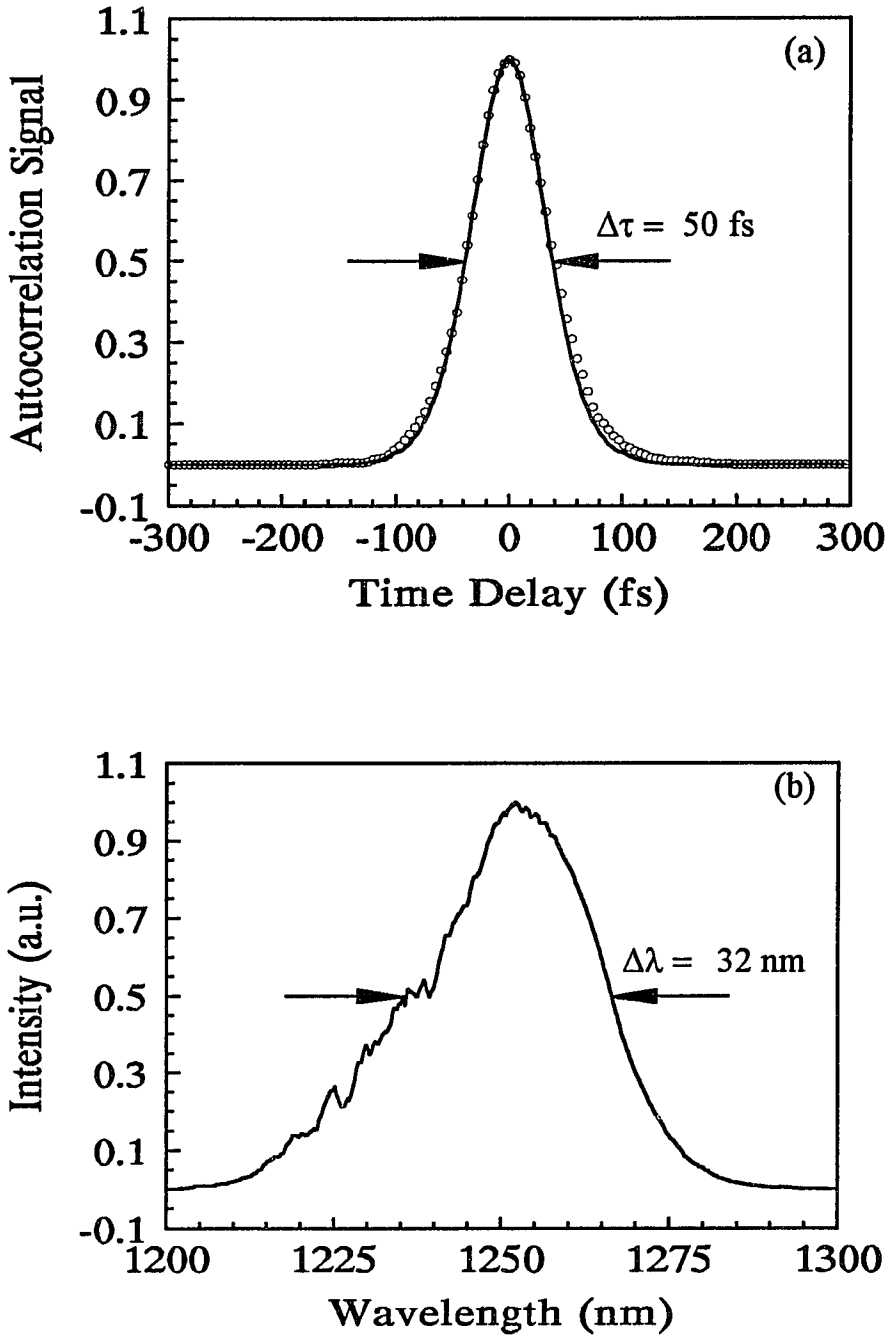

Fig. 5.7.1. An autocorrelation trace (a) and spectrum (b) of 50-fs pulses obtained from a z-cavity with SFN 64 prisms for chirp compensation. Circles represent experimental data and the solid line is the best fit for $sech^2$ pulse shape.

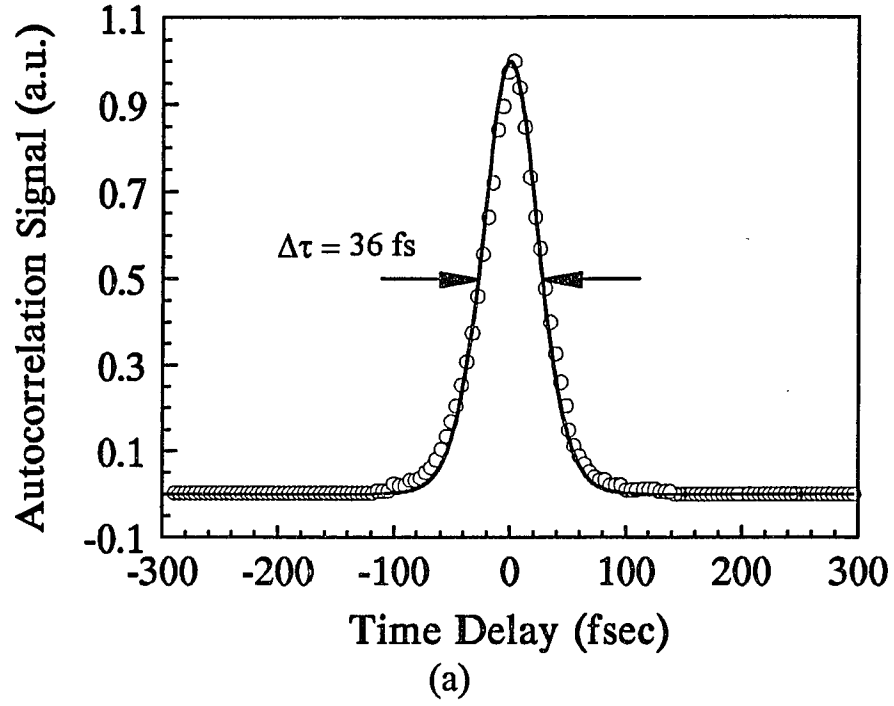

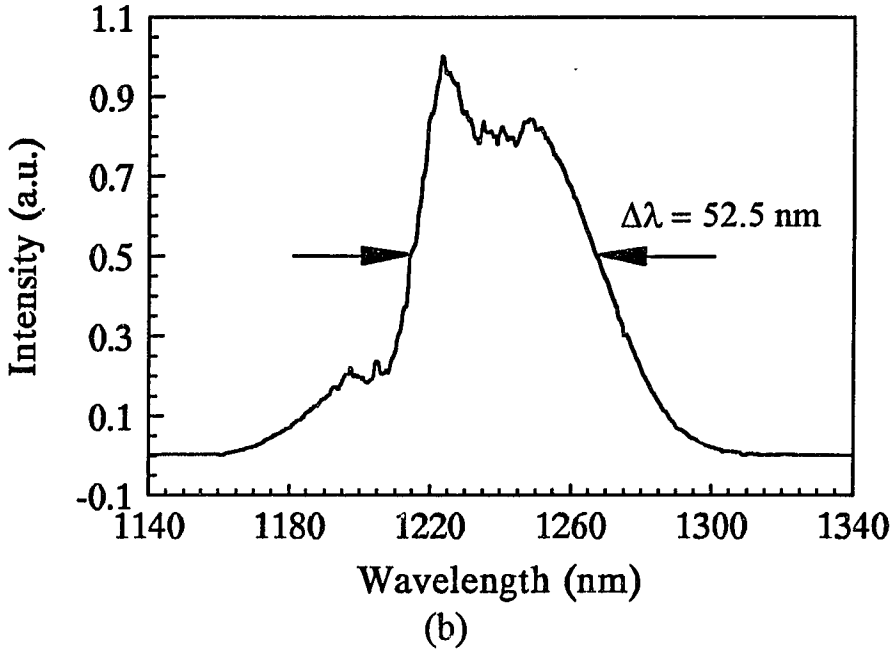

Fig. 5.7.2. An autocorrelation trace (a) and spectrum (b) of 36-fs pulses obtained from a z-fold cavity with SFN 64 prisms for chirp compensation. Circles represent experimental data and the solid line is the best fit for $sech^2$ pulse shape.

The 36-fs pulses generated by the self-mode-locked forsterite laser are longer that the pulses that will be generated if all of the emission spectrum is used. Figure 5.7.3 the dielectric coatings of the mirrors used, the emission spectrum of the forsterite crystal and the corresponding bandwidth of the 36-fs pulses are plotted using the same axis. The bandwidth of the 36-fs pulses correspond to all the spectrum that the dielectric coatings would support. Mirrors with appropriate coatings will definitely generated shorter pulses where the whole emission spectrum of the Cr:forsterite laser is used.

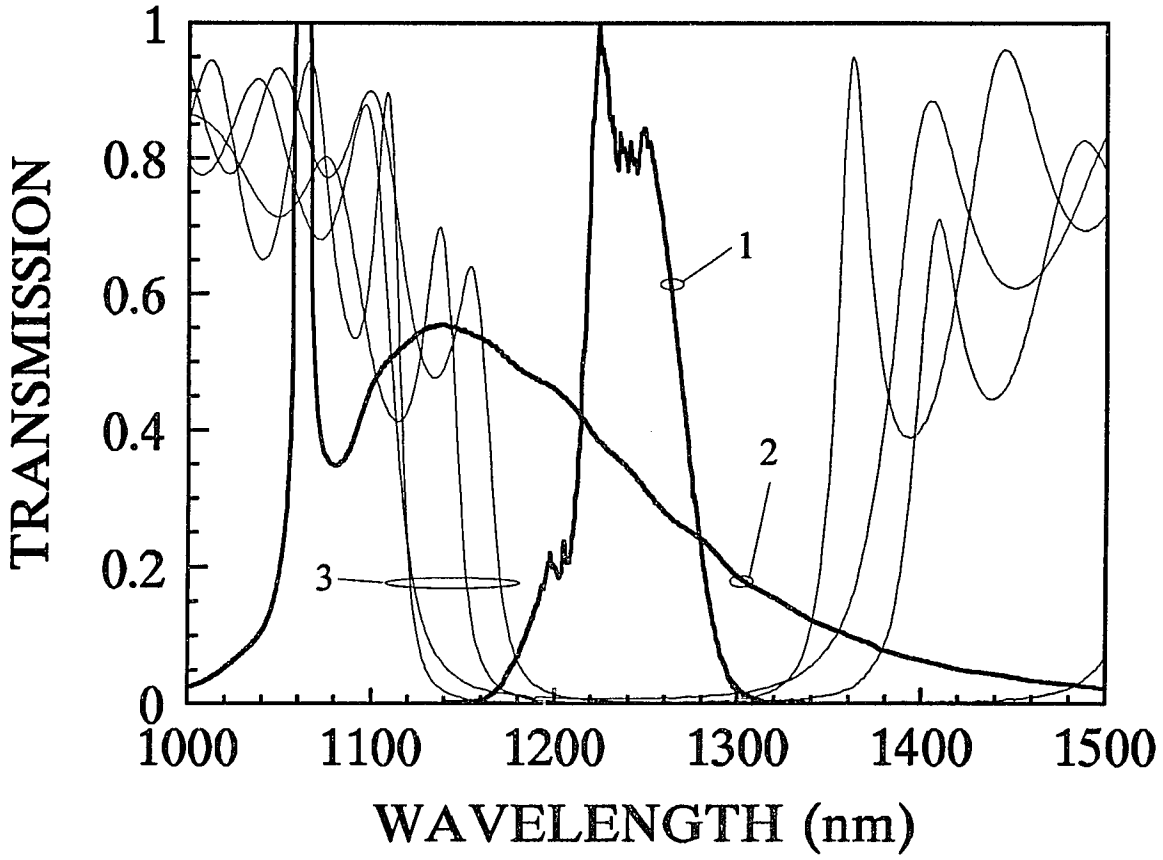

Fig. 5.7.3. Transmission of the mirror coatings forming the four mirror cavity, emission spectrum of Cr:forsterite when excited with 1064 nm radiation, and corresponding spectrum of the 36-fs pulses.

5.8. Conclusion

The observed behavior of the forsterite laser suggest the following mechanism for generating short pulses. First in the case of the cavity without any chirp compensation we generate picosecond pulse due to the modulation introduced by the acousto-optic modulator. The presence of high peak power pulses in the cavity induces chirping due to nonlinear effects in the forsterite crystal. The addition of the two prisms compensates for the chirp resulting in 900 femtosecond pulses. In presence of the 900 fs pulses the peak power inside the cavity increases even more generating higher nonlinear effects which coupled with the stability conditions of the cavity mode result in a passive modulation. This passive modulation has the same frequency and is in phase with the frequency of the acousto-optic modulator. Therefore since now we have stronger modulation inside the cavity we observe the shortening of the pulses down to 90 fs. The passive modulation continuous even when the acousto-optic modulator is disconnected until there is a mechanical disturbance that destroys the modulation and the laser goes back to the CW mode of operation.

Pure self-mode-locked operation of the Cr:forsterite laser was demonstrated. The Cr:forsterite laser was initially synchronously pumped by a CW mode-locked Nd:YAG laser generating picosecond pulses, which provided the starting mechanism for self-mode-locking generating transform limited 105-fs pulses.

The pulsewidth of the pulses from a self-mode-locked Cr:forsterite laser was reduced to 50 fs by choosing prism material which compensates for group velocity dispersion and introduces minimum cubic phase term. Even shorter pulses were obtained when a forsterite crystal was used that had a FOM of 58, the highest FOM measured for forsterite. The shortest pulses generated were 36 fs and they almost used the whole emission spectrum of forsterite.

5.9. References

1. C. V. Shank, "Generation of ultrashort optical pulses", in Ultrashort Laser Pulses and Applications, W. Kaiser, Ed. New York: Springer Verlag, 1988, chapter 2.

2. F. Krausz, M. E. Ferman, T. Brabec, P. F. Curley, M. Hofer, M. H. Ober, C. Spielmann, E. Wintner, and A. J. Schmidt, "Femtosecond Solid-State Lasers", IEEE J. Quantum Electron., Vol. **QE-28**, pp. 2097 (1992).

3. E. B. Treacy, "Optical pulse compression with diffraction gratings", IEEE J. Quantum Electron., Vol. **QE-5**, pp. 454 (1969).

4. R. L. Fork, O. E. Martinez, and J. P. Gordon, "Negative dispersion using pairs of prisms", Optics Letters, Vol. **9**, pp. 150 (1984).

5. J. P. Gordon, and R. L. Fork, "Optical (ring) resonator with negative dispersion", Optics Letters, Vol. **9**, pp. 153 (1984).

6. F. Gires, and P. Tournois, "Interferometre utilisable pour la compression d'impulsions lumineuses modulees en frequence", C. R. Acad. Sci. Paris, Vol. 258, pp. 6112 (1964).

7. J. D. Kafka, M. L. Watts, and J. J. Pieterse, "Picosecond and Femtosecond Pulse Generation in a Regeneratively Mode-Locked Ti:Sapphire Laser", IEEE J. Quantum Electron., Vol. **QE-28**, pp. 2151 (1992).

8. A. E. Siegman, "Lasers", University Science Books, Mill Valey, California, chapter 9 (1986).

9. R. R. Alfano, Ultrafast Optics Notes (1992).

10. A. Yariv, and P. Yeh, "Optical Waves in Crystals", Wiley-Interscience, John Wiley & Sons Inc., New York, Chapter 2 (1984).

11. "Optical Glass", Schott Catalog, Shchott Glass Technologies Inc., Duryea, Pensylvania.

12. D. E. Spence, P. N. Kean, and W. Sibbet, "60-fs pulse generation from a self-mode-locked Ti:sapphire laser", Optics Letters, Vol. **16**, pp. 42 (1991).

13. D. K. Negus, L. Spinelli. N. Goldblatt, and G. Feugnet, *OSA Proceedings on Advanced Solid-State Lasers,* G. Dube and L. Chase, eds. (Optical Society of America, Washington, D.C., 1991), Vol. **10**, pp. 120-124.

14. N. H. Rizvi, P. M. W. French, and J. R. Taylor, "Continuously self-mode-locked Ti:sapphire laser that produces sub-50-fs pulses", Optics Letters, Vol. **17**, pp. 279 (1992).

15. C. P. Huang, H. C. Kapteyn, J. W. McIntosh, and M. M. Murnane, "Generation of transform-limited 32-fs pulses from a self-mode-locked Ti:sapphire laser", Optics Letters, Vol. **17**, pp. 139 (1992).

16. C. P. Huang, M. T. Asaki, S. Backus, M. M. Murnane, H. C. Kapteyn, and H. Nathel, "17-fs pulses from a self-mode-locked Ti:sapphire laser", Optics Letters, Vol. 17, pp. 1289 (1992).

17. B. Proctor, and F. Wise, "Quartz prism sequence for reduction of cubic phase in a mode-locked Ti:Al_2O_3 laser", Optics Letters, Vol. 17, pp. 1295 (1992).

18. J. M. Jacobson, K. Naganuma, H. A. Haus, J. G. Fujimoto, A. G. Jacobson, "Femtosecond pulse generation in a Ti:Al_2O_3 laser using second- and third-order intracavity dispersion", Optics Letters, Vol. 17, pp. 1608 (1992).

19. R. L. Fork, C. H. Brito Cruz, P. C. Becker, and C. V. Shank, " Compression of optical pulses to six femtoseconds by using cubic phase compensation", Optics Letters, Vol. 12, pp. 483 (1987).

CHAPTER 6

SUMMARY AND FUTURE DIRECTIONS

6.1. Summary

The research efforts presented in this thesis pioneered the generation of ultrashort pulses using the chromium-doped forsterite laser. As a result Cr:forsterite laser has been established as a reliable source of femtosecond pulses tunable in the near infrared. Various mode-locking techniques were successfully engineered and implemented leading to the generation of 36 fs pulses from a self-mode locked Cr:forsterite laser. A summary of the research is presented next.

Synchronously-Pumped Cr:Forsterite Laser

Synchronously pumped mode-locking using a three mirror cavity astigmatically compensated cavity design and a forsterite crystal with a figure of merit of 26 (FOM=$\alpha_{1064nm}/\alpha_{1250nm}$) generated pulses with FWHW 260 ps.[1,2] The tuning range of the mode-locked forsterite laser was determined to be 100 nm limited only by the dielectric coatings of the mirrors used in the cavity. The slope efficiency was 12.5% and detuning measurements indicated that the synchronously-pumped Cr:forsterite laser can generate pulses with FWHM of less than 300 ps for ± 5μm from optimum position.

Actively Mode-Locked Cr:Forsterite Laser

Active mode locking was achieved using the same cavity configuration as the synchronously pumped forsterite laser with the addition of an acousto-optic modulator.[1,2]

The pulses generated from the active mode-locked forsterite laser had FWHM of 49 fs. Tuning extended from 1204 to 1277 nm, and the slope efficiency was 9.1%. The same Cr:forsterite crystal in a four mirror astigmatically compensated cavity generated pulses with FWHM of 31 ps. The pulsewidth was further reduced to 6 ps by replacing the forsterite crystal (Crystal 1) in the four mirror cavity with a new forsterite crystal (Crystal 2) with a higher figure of merit (FOM=39).[3] Pulsewidth-bandwidth measurements resulted to $\Delta\nu\Delta\tau = 1.34$, indicating the presence of chirp in the output pulses. Numerical calculation of the phase characteristics of various optical materials showed that a pair of prisms made of SF 14 optical glass can be used in the cavity to compensate for chirp. The insertion of the prisms in the cavity resulted in a reduction of the pulsewidth from 6 ps down to 900 fs. Careful optimization of the laser cavity resulted in the generation of stable 90-fs pulses, and the forsterite laser was shown to operate in the self-mode-locked mode of operation for the first time.[3,4,5]

Self-Mode-Locked Cr:Forsterite Laser

Pure self-mode-locking was achieved using the four mirror cavity and a new forsterite crystal (Crystal 3, FOM = 47). Synchronous pumping was used to mode locked the forsterite laser resulting in picosecond pulses, which in turn provided the starting mechanism for self-mode-locking. The pulses generated had a FWHM of 105 fs and were tunable between 1230 - 1270 nm.[6]

Cubic Phase Distortion and Improved Performance of the Self-Mode-Locked Cr:Forsterite Laser

Numerical calculations indicated that the pair of SF 14 prisms used in the cavity compensated for quadratic phase but introduced a large cubic phase term. Further calculations of other optical glasses indicated that a pair of SFN 64 prisms can introduce the same amount of quadratic phase as SF 14 prisms but introduce a smaller cubic phase.

When the SF 14 prisms were replaced by SFN 64 prisms the pulsewidth was reduced to 50 fs. Great improvement was observed in the stability of the self mode-locked forsterite laser and in the ease of achieving mode-locking. Using the same experimental arrangement and a new forsterite crystal (Crystal 4) with improved FOM the pulse width was reduced to 36 fs.[7]

6.2. Future Directions

6.2.1. Intracavity Second Harmonic Generation

An important application of the forsterite laser can be found in the medical field. The second harmonic radiation (620 nm) of the forsterite laser can be used in the photodynamic therapy. The presence of very large power densities inside the self mode-locked forsterite laser suggest that it would be possible to include a second harmonic crystal inside the cavity.

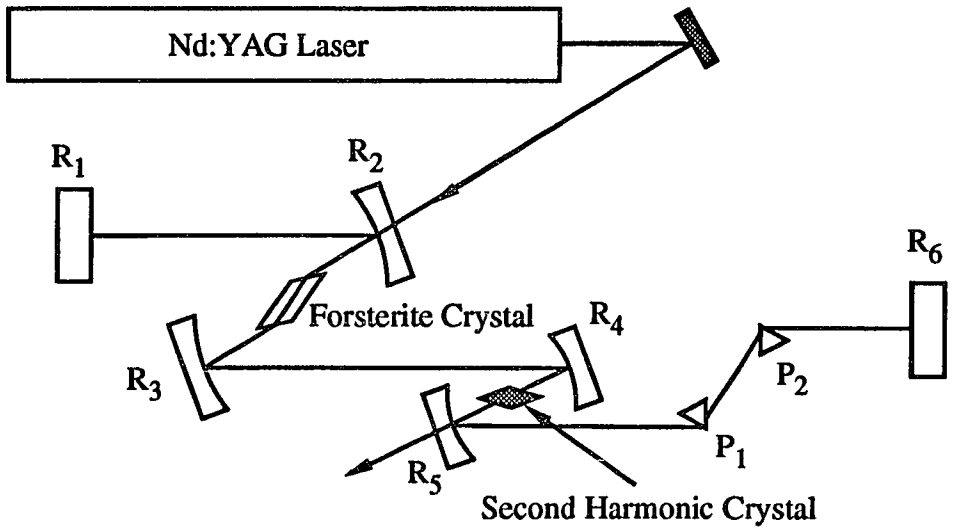

Fig. 6.2.1. Cavity configuration for intracavity second harmonic generation using the self-mode-locked Cr:forsterite laser.

A cavity suitable for intacavity second harmonic generation with the forsterite laser is shown in figure 6.2.1. It is a modified four mirror astigmatically compensated cavity with intracavity chirp compensation, and an additional branch for the second harmonic crystal. This cavity design offers two positions of tight focusing, one for the forsterite crystal and one for the second harmonic crystal.

The conversion of radiation from ω to 2ω can be considered as a loss mechanism for the oscillation of the laser frequency ω. The conversion efficiency from ω to 2ω per pass is given by the expression[8]

$$\frac{P_{2\omega}}{P_{\omega}} = 2\left(\frac{\mu_o}{\varepsilon_o}\right)^{3/2} \frac{\omega^2 d^2 l^2}{n^3} \left[\frac{\sin^2\left(\frac{\Delta kl}{2}\right)}{\left(\frac{\Delta kl}{2}\right)^2}\right] \frac{P_{\omega}}{A} \qquad (6.2.1)$$

where ω - frequency of the laser

d - the crystal nonlinear coefficient

l - length of nonlinear crystal

A - cross-sectional area of the beam

Δk - the wave vector mismatch

P_{ω} - one way traveling power inside the cavity

$P_{2\omega}$ - one way generated second harmonic radiation

Two commonly used nonlinear crystals for the generation of second harmonic are KD*P (Deuterated Potassium Dihydrogen Phosphate, KH_2PO_4), and KTP (Potassium Titanyl Phosphate, $KTiOPO_4$). As it was shown in Chapter 3 the index of refraction for the KD*P crystal changes very little in the near infrared (1100 - 1400 nm wavelength

region) resulting in a phase matching angle that does not change significantly with wavelength. The same is expected to be true for other nonlinear crystals.

The femtosecond operation of the forsterite laser is based on the minimization of phase distortions in the laser cavity. Inserting a second harmonic crystal in the self-mode-locked Cr:forsterite laser complicates phase compensation since second harmonic crystals have different indices of refraction for different axis of propagation. Next the effect of propagation of ultrashort pulses through KD*P and KTP crystals is considered. KD*P is a uniaxial crystal and the calculations are performed separately for propagation along the ordinary or extraordinary axis, while KTP is a biaxial crystal and the propagation along all three axis is considered. In the calculations the index of refraction and its derivatives with respect to wavelength are evaluated using the Sellmeier coefficients for KD*P[9] and KTP[10]. The dispersion constant is evaluated for the wavelength region that the emission spectrum of Cr:forsterite covers. Finally pulse broadening of a 30 fs pulse centered at 1250 nm as a function of the crystal thickness is evaluated.

Figures 6.2.2 (a) and (b) shows the dispersion constant as a function of wavelength for KD*P and KTP, respectively. As it can be seen the dispersion constant of KD*P crystal is much smaller as compare to that of KTP. As a result an ultrashort pulse will be less affected by propagation in KD*P as compared with propagation through an equivalent thickness KTP crystal.

Figures 6.2.3 shows the effect of pulse broadening of a 30-fs pulses centered at 1250 nm, as a function of the crystal thickness for KD*P and KTP. Pulse broadening in a KD*P crystal is smaller than KTP making KD*P more suitable for intracavity second harmonic generation using the Cr:forsterite laser. A KD*P crystal of up to 3 mm thickness can be used without significant pulse broadening.

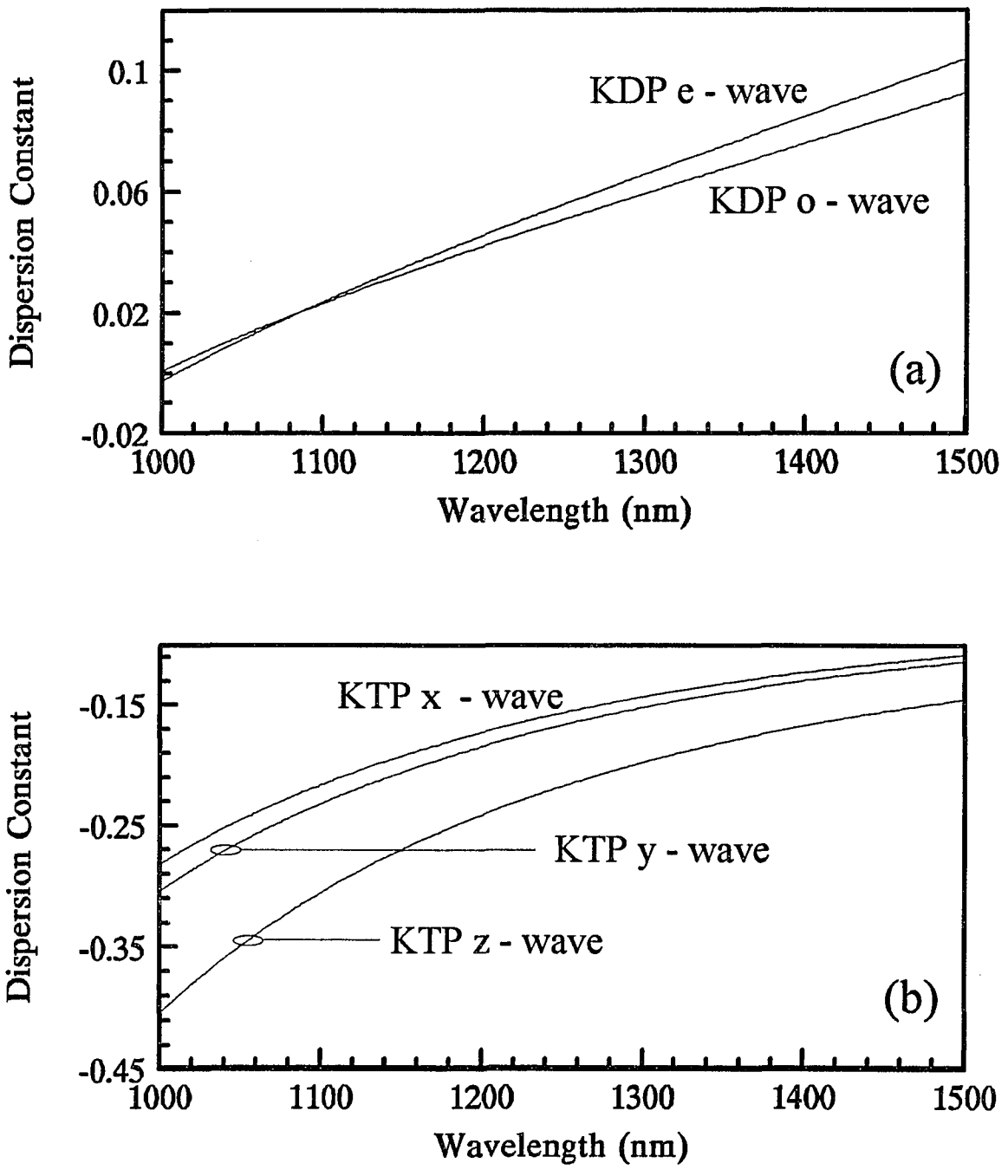

Figure 6.2.2.(a) Dispersion constant of KD*P crystal for an ordinary and extraordinary ray as a function of wavelength, (b) Dispersion constant of KTP crystal for propagation along the x, y, and z axis.

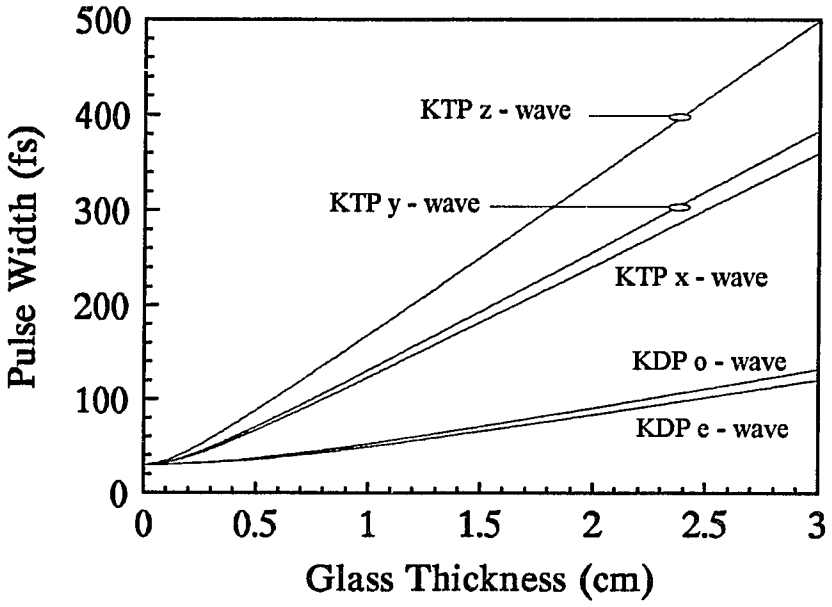

Fig. 6.2.3. Pulse broadening of a 30-fs pulse centered at 1250 nm as a function of the crystal thickness for KD*P and KTP nonlinear crystals.

6.2.2. Diode-Pumped Cr:Forsterite Laser

Semiconductor diode pumping is well recognized as a way for producing compact, high-efficiency, high-stability, and low-threshold solid-state laser devices. Benefited from the availability of GaAs lasers, the technology of diode pumping of Nd-doped crystals has been well developed. Recent advances in the semiconductor diode engineering have greatly extended the operation wavelength region of semiconductor lasers. High power diode arrays operating at 780 nm are ideal for pumping the $^3T_1$ absorption band, while diodes operating around 950 nm are suitable for pumping the $^3T_2$ band of the tetravalent chromium (Cr^{4+})-doped crystals such as Cr:forsterite. Table 6.2.1 shows the absorption coefficient and FOM for selected wavelength, corresponding to chromium-doped forsterite (Crystal 4). The FOM listed is the absorption coefficient at the designated wavelength over the absorption at 1250 nm.

Table 6.2.1. Absorption coefficient and FOM for selected pump wavelengths using the Cr:forsterite crystal.

λ (nm)	α (cm^{-1})	FOM
785	1.196	60.398
800	1.150	58.105
940	0.786	39.707
970	0.930	46.983
980	0.978	49.292
1064	1.161	58.387

A typical experimental arrangement for diode pumping the Cr:forsterite laser is shown in Fig. 6.2.4. A 10-W continuous-wave or quasi-continuous diode laser emitting at 787-nm or 950-nm is used to pump Cr:forsterite crystal. One side of the forsterite crystal provides the back mirror and is coated for high transmission at the pump wavelength and high reflection at the lasing wavelength. The other side of the forsterite crystal is antirelfection coated for the lasing wavelength in order to minimize losses. The diode pumped forsterite crystal is expected to generate tunable radiation over the 1150-1350-nm spectral region .

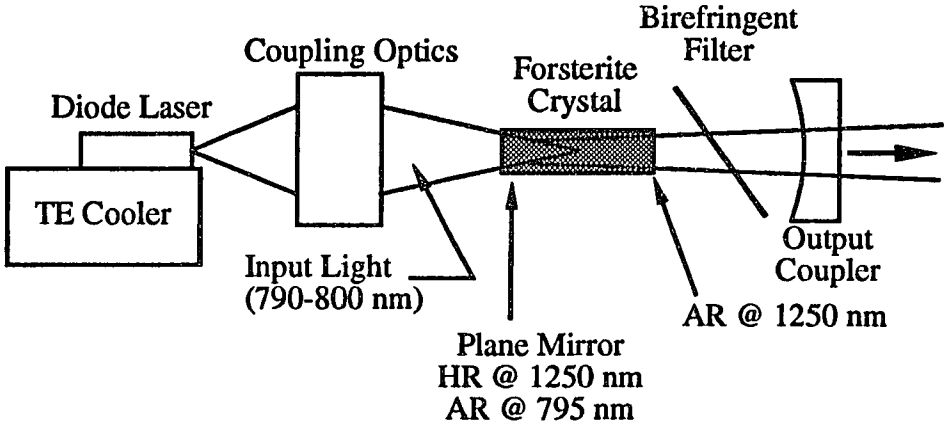

Fig. 6.2.4. Diode-pumped Cr:forsterite laser.

For high-power systems, diode-array side-pumped (or transversely-pumped) systems can be used. Since most high power diode arrays come as 1-cm long bars or stacks, simple cylinder lenses can be used to focus the pump beams into the laser rod and create nearly circular gain profile. Such a system is expected to produce multiwatt of tunable laser radiation in the near infrared. An example[11] of a side-pumped high-power forsterite laser is shown in Fig. 6.2.5.

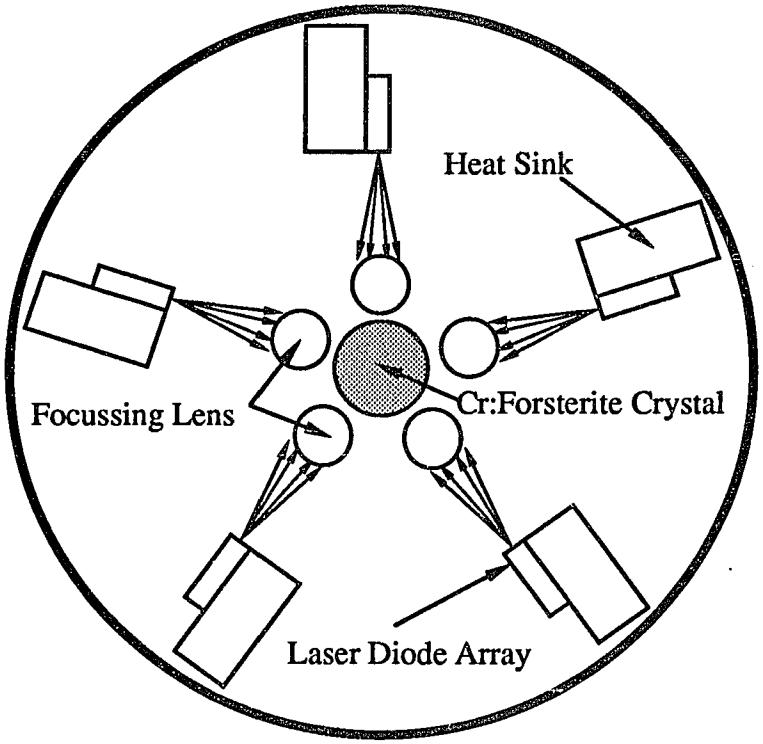

Fig. 6.2.5. High power, diode pumped Cr:forsterite laser.

6.2.3. High Power Cr:Forsterite Laser

Chromium-doped forsterite laser has been established as a reliable source of femtosecond pulses in the near infrared. The experiments presented so far were concentrated on the generation of the shortest possible pulses from the Cr:forsterite laser. The output levels generated were in the order of 50 mW mainly due to limited pump

power. It was reported that up to 700 mW can be generated directly from a self mode locked forsterite laser.[12]

The next step in the development of femtosecond Cr:forsterite laser is the amplification of the femtosecond pulses to multiwatts levels. Pumping of forsterite can be provided from Nd:YAG lasers, the most widely used laser, and Nd:YLF. This fact makes amplification of the femtosecond pulses very easy from the stand point of pump power requirements. As it was shown in section 6.2.2 the forsterite laser can also be pumped by high power diode lasers enabling the construction of a compact amplifier.

Figure 6.2.6 shows a possible design for high power operation of the forsterite laser. Sub-100-fs pulses can be generated from a self-mode-locked Cr:forsterite laser using a four mirror astigmatically compensated cavity with intracavity chirp compensation. Starting mechanism for self-mode-locking can be provided by synchronous pumping.

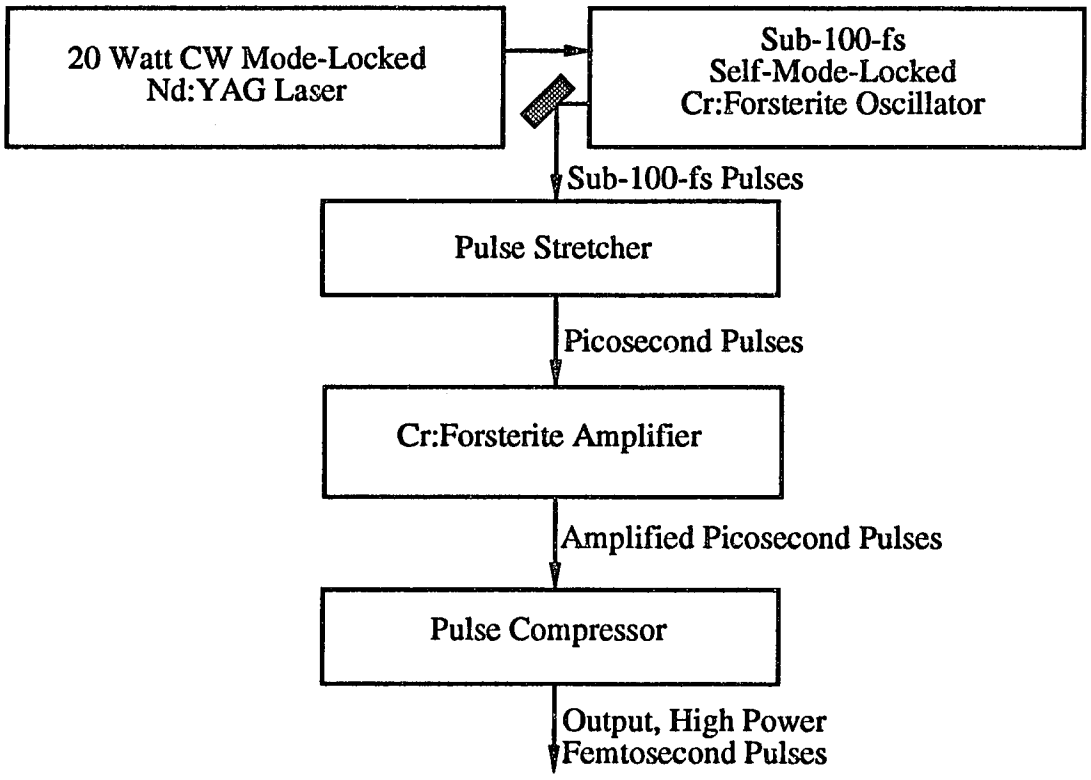

Fig. 6.2.6. Design of high power Cr:forsterite laser.

The femtosecond pulses produced by the forsterite oscillator can be amplified using a regenerative amplifier. Regenerative amplification is based on multiple passes of a weak pulse through an inverted (pumped) gain medium. Once the gain is saturated, the amplified pulse is switched (dumped) out of the resonator cavity. Gains of several orders of magnitude can be achieved. One possible design[13] of a regenerative amplifier is shown in Fig. 6.2.7. The femtosecond seed pulse is first expanded to a few hundred ps duration in a pulse stretcher to avoid damage to the Pockels cell and the gain medium. A single seed pulse to be amplified is then injected into the amplifier cavity using two thin film polarizers and an intracavity $\lambda/2$ Pockels cell, which also serves as a cavity dumper. The gain medium of the amplifier can be pumped by a 30Hz - 500Hz Q-switched Nd:YAG or 1KHz - 5KHz Nd:YLF laser readily available in the market. The amplified output is finally compressed to femtosecond duration in a pulse compressor.

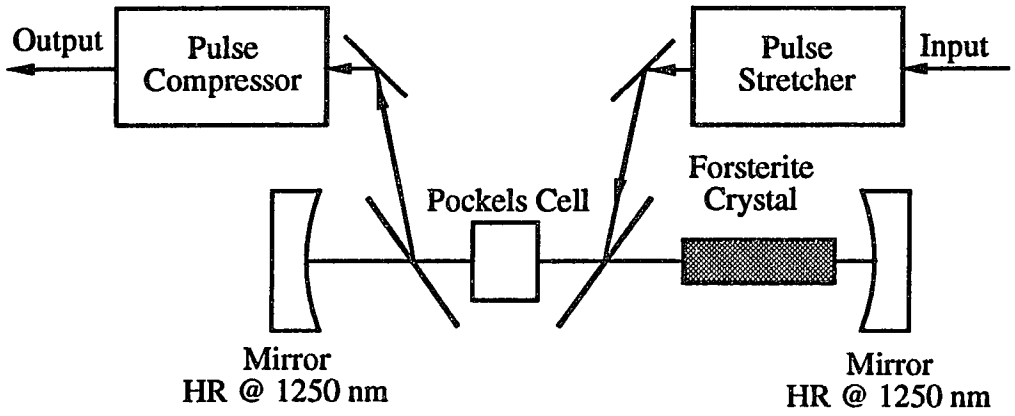

Fig. 6.2.7. Regenerative amplifier design to be used with Cr:forsterite laser.

6.3. References

1. A. Seas, V. Petričević, and R. R. Alfano, "CW Mode-Locked Operation of Chromium-Doped Forsterite Laser", *OSA Proceedings on Advanced Solid-State Lasers,* G. Dube and L. Chase, eds. (Optical Society of America, Washington, D.C., 1991), Vol. **10**, pp. 69-71.

2. A. Seas, V. Petričević, and R. R. Alfano, "Continuous-Wave Mode-Locked Operation of Chromium-Doped Forsterite Laser", Optics Letters, Vol. **16**, pp. 1668 (1991).

3. A. Seas, V. Petričević, and R. R. Alfano, "Generation of Sub-100-fs Pulses From a Continuous-Wave Mode-Locked Chromium-Doped Forsterite Laser", Optics Letters, Vol. **17**, pp. 937 (1992).

4. A. Seas, V. Petričević, and R. R. Alfano, "Generation of sub-100-fs Pulses from a Continuous-Wave Mode-Locked Chromium-Doped Forsterite Laser", Post-deadline paper, presented at the Conference on Lasers and Electro-Optics (CLEO), Anaheim, California, May 11-15, 1992.

5. A. Seas, V. Petričević, R. R. Alfano, "60-fs Chromium-Doped Forsterite (Cr^{4+}:Mg_2SiO_4) Laser", Ultrafast Phenomena VIII, J. L. Martin, A. Migus, G. A. Mourou, and A. H. Zewail, eds., Springer Series in Chemical Physics, Vol. **55**, pp. 174 (1993).

6. A. Seas, V. Petričević, and R. R. Alfano, "Femtosecond Pulses Generated From a Synchronously Pumped Chromium-Doped Forsterite Laser", To be published in the Proceedings at the Topical Meeting on Advanced Solid-State Lasers, New Orleans, Louisiana, February 1-3, 1992.

7. A. Seas, V. Petričević, and R. R. Alfano, "Self Mode-Locked Chromium-Doped Forsterite Laser Generates 50-fs Pulses", Optics Letters, Vol. **18**, pp. 891 (1993).

8. A. Yariv, "Optical Electronics", fourth edition, Sanders College Publishing, Holt Rinehart and Winston Inc., pp. 282 (1991).

9. G. C. Ghosh, and G. C. Bhar, "Temperature dispersion in ADP, KDP, and KD*P for nonlinear devices", IEEE J. Quantum Electron., Vol. **QE-18**, pp.143 (1982).

10. Catalogue from Litton-Airtron, "KTP, Potasium Titanyl Phosphate", Synthetic Crystals and Optical Products, Charlotte, NC 28273.

11. A. D. Hays, L. R. Marshall, and R. Burnham, "High powered CW diode-array-pumped Nd:YAG laser", in Tunable Solid-State Lasers, Vol. 10 of the OSA Proceeding Series, G. Dube and L. Chase, eds. (Optical Society of America, Washington, D.C., 1991), pp. 255-256.

12. Y. Pang, V. Yanovsky, F. Wise, and B. I. Minkov, "Self-mode-locked Cr:forsterite laser", to be published in Optics Letters (1993).

13. J. D. Kmetec, J. J. Macklin, and J. F. Young, "0.5-TW, 125-fs Ti:sapphire laser", Optics Letters, Vol. **16**, pp. 1001 (1991).

APPENDIX

Appendix A: Mirror Coatings of Three-Mirror Cavity Design

The mirror coatings of the three mirrors used to engineer the three mirror astigmatically compensated cavity are shown in figures A.2 - A.4. Their assignments correspond to figure A.1.

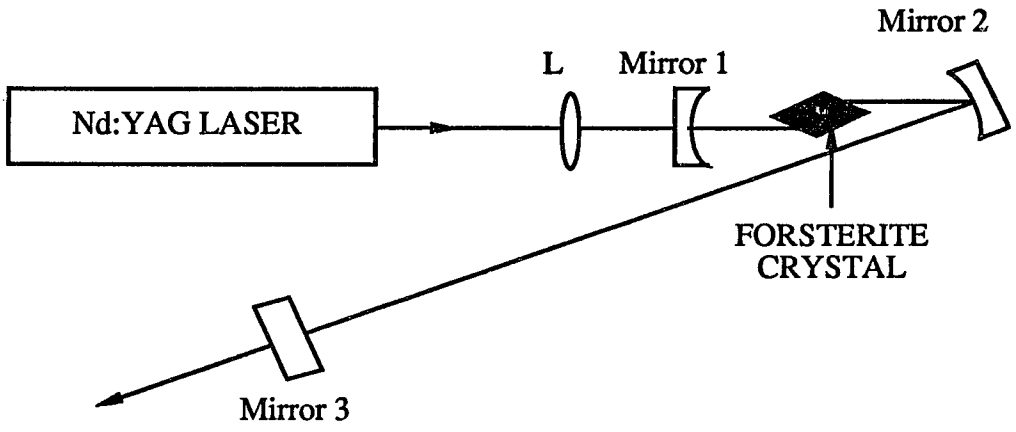

Fig. A.1. Three mirror astigmatically compensated cavity used in the mode-locking experiments.

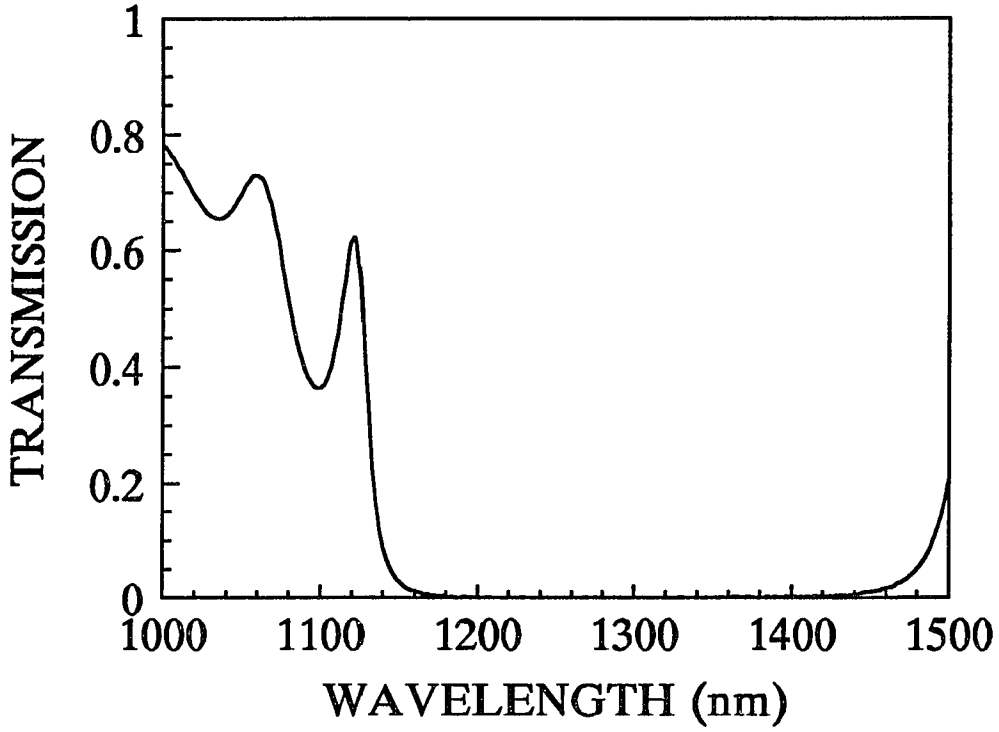

Fig. A.2. Transmission of dielectric coating on Mirror 1 vs. wavelength.

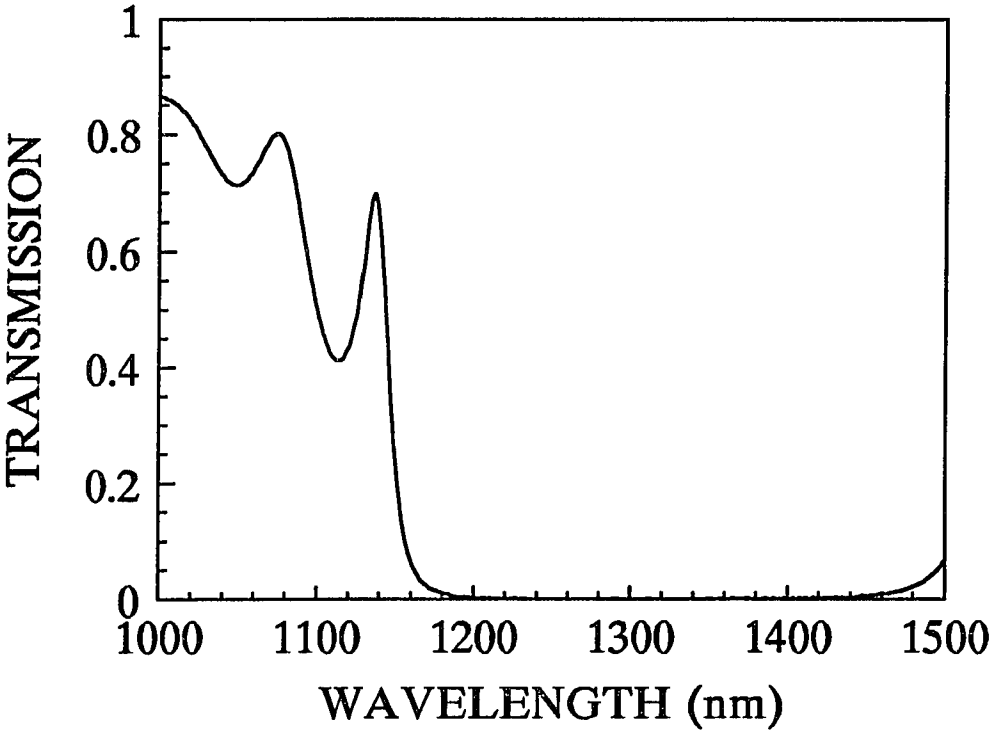

Fig. A.3. Transmission of dielectric coating on Mirror 2 vs. wavelength.

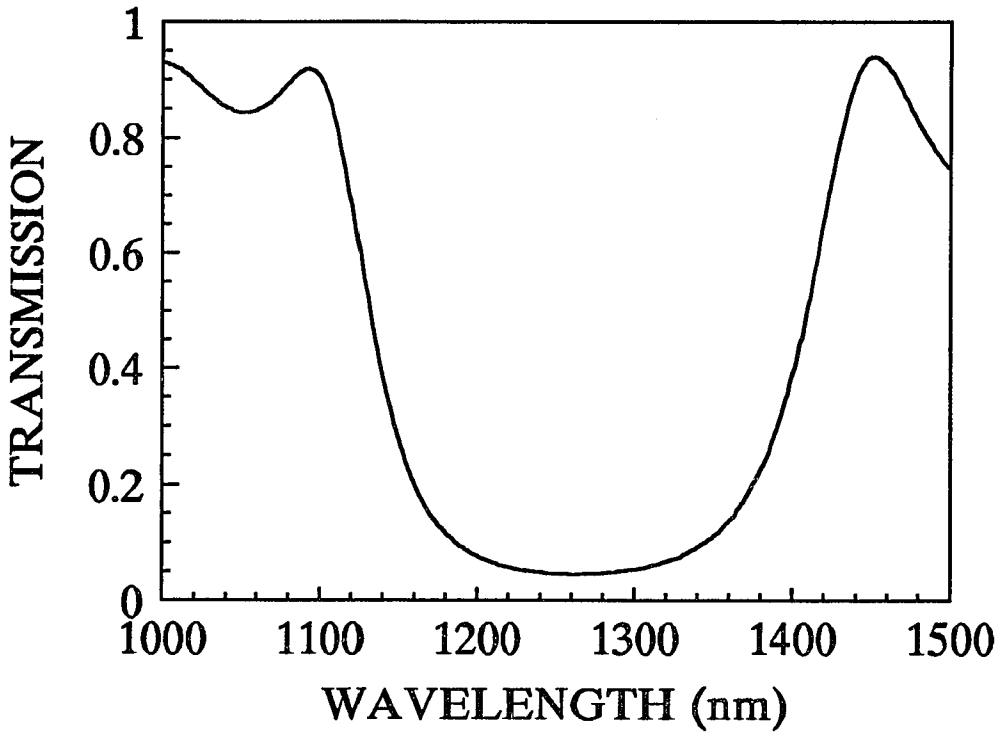

Fig. A.4. Transmission of dielectric coating on Mirror 3 vs. wavelength.

Appendix B: Mirror Coatings of Four-Mirror Cavity Design

The mirror coatings of the four mirrors used to engineer the four mirror z-fold astigmatically compensated cavity are shown in figures B.2 - B.5. Their assignments correspond to figure B.1.

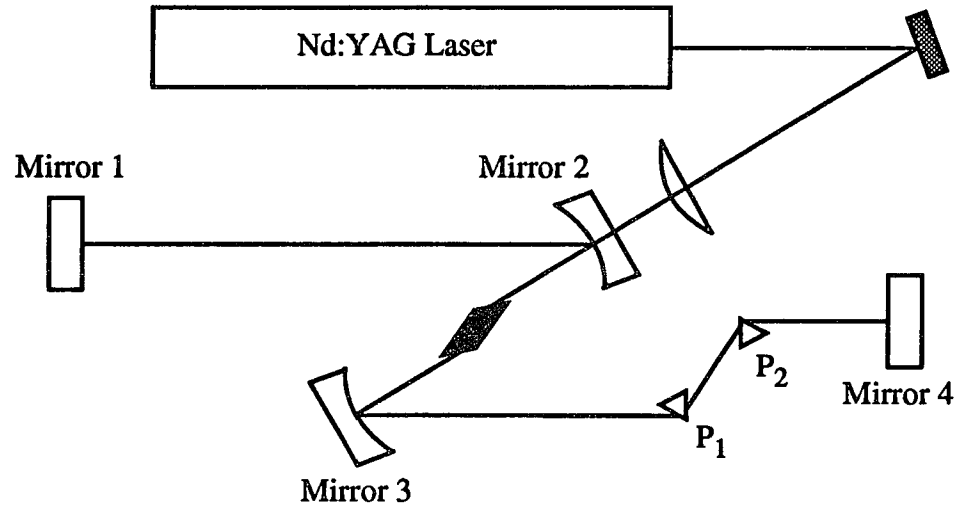

Fig. B.1. Four mirror z-fold astigmatically compensated cavity used in the self-mode-locking experiments.

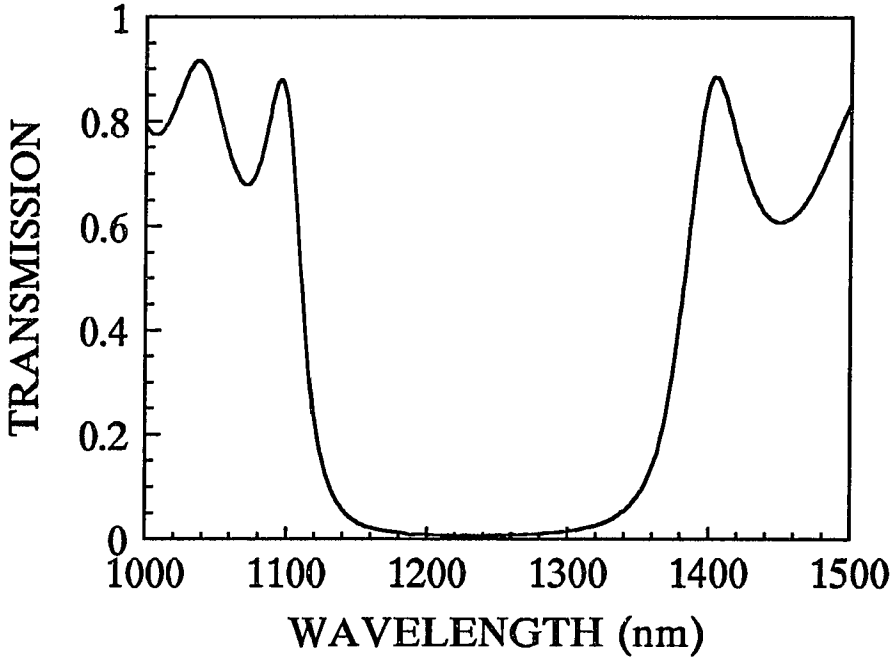

Fig. B.2. Transmission of dielectric coating on Mirror 1 vs. wavelength.

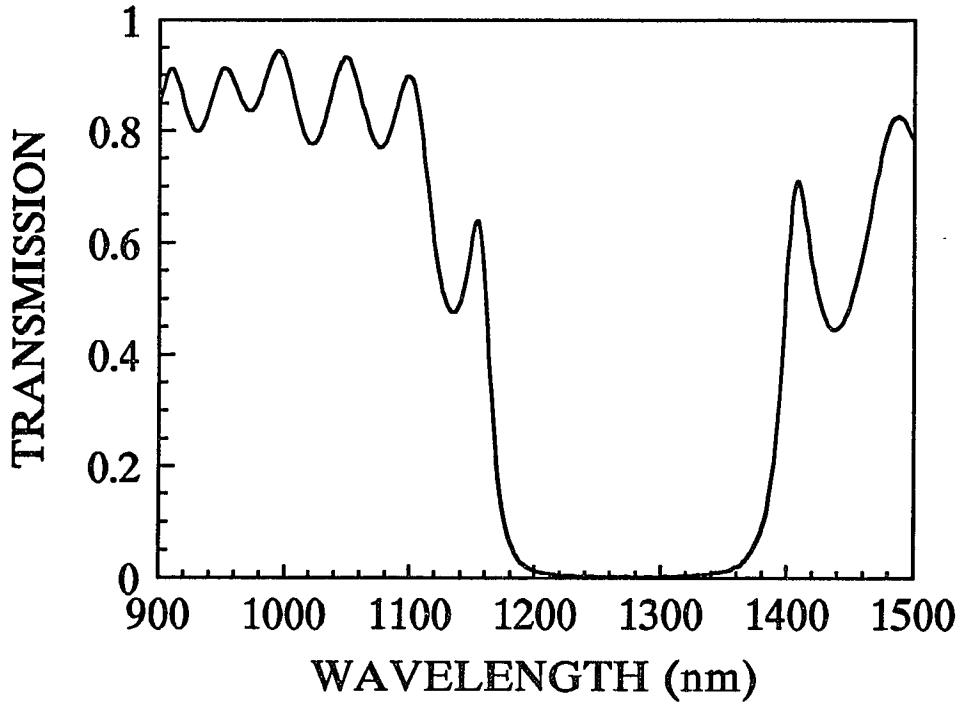

Fig. B.3. Transmission of dielectric coating on Mirror 2 vs. wavelength.

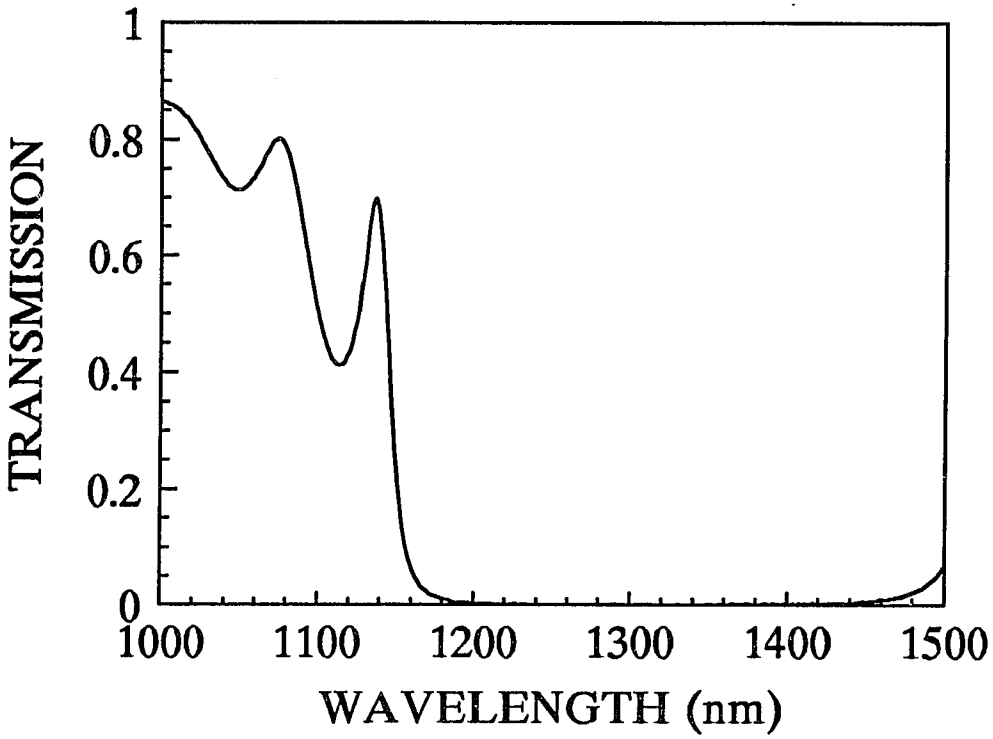

Fig. B.4. Transmission of dielectric coating on Mirror 3 vs. wavelength.

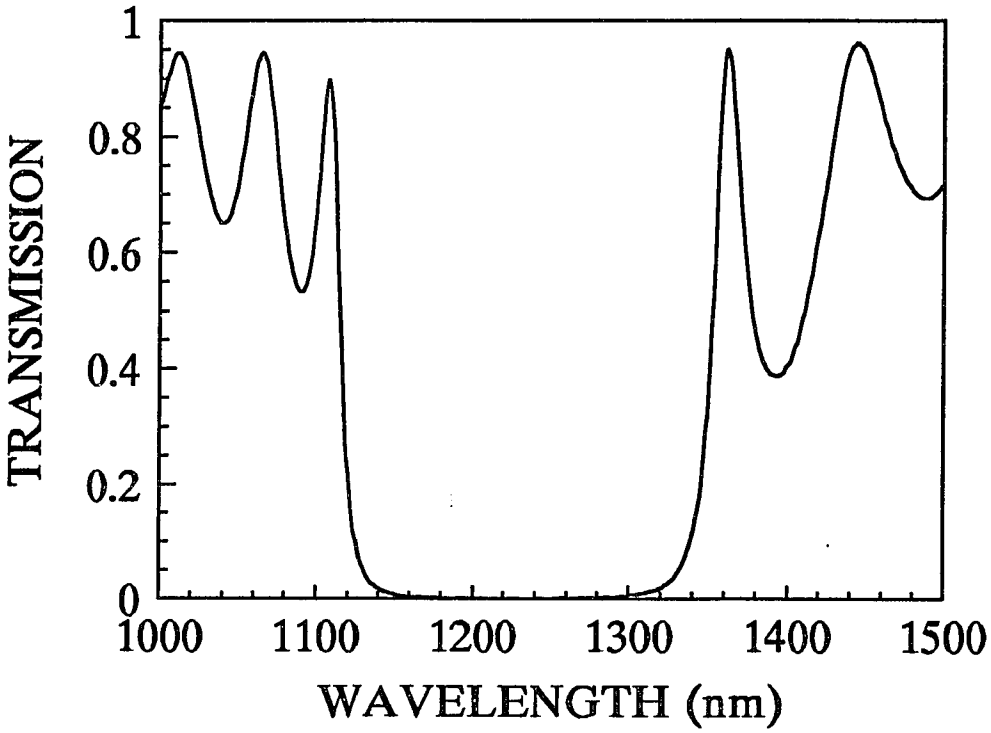

Fig. B.5. Transmission of dielectric coating on Mirror 4 vs. wavelength.

BIBLIOGRAPHY

CHAPTER 1

1. P. F. Moulton, "Tunable Paramagnetic-Ion Lasers", in: *Laser Handbook*, edited by M. Bass and M. L. Stitch, Elseviers Science Publishers B. V., (1985) and references therein.

2. P. F. Moulton, " Spectroscopic and laser characteristics of Ti:Al_2O_3", J. Opt. Soc. Am. **B3**, 125 (1986).

3. S. A. Payne, L. L. Chase, L. K. Smith, L. Kway, and H. W. Newkirk, " Laser performance of $LiSrAlF_6:Cr^{3+}$", J. Appl. Phys. **66**, 1051 (1989).

4. V. Petričević, S. K. Gayen, R. R. Alfano, K. Yamagishi, H. Anzai, and Y. Yamaguchi, "Laser action in chromium-doped forsterite", Appl. Phys. Lett. **52**, 1040 (1988).

5. V. Petričević, S. K. Gayen, and R. R. Alfano, "Laser action in Cr-activated forsterite for near infrared excitation: Is Cr^{4+} the lasing ion?", Appl. Phys. Lett. **53**, 2590 (1988).

6. R. R. Alfano and V. Petričević, "Tetravalent chromium (Cr4+) as a laser-active ion for tunable solid-state lasers", U.S. Patent# 4,987,575 (January 22, 1991).

7. V. Petričević, S. K. Gayen, and R. R. Alfano, "Near infrared tunable operation of chromium doped forsterite laser", Appl. Opt. **28**, 1609 (1989).

8. V. G. Baryshevskii, M. V. Korzhik, A. E. Kimaev, M. G. Livshitz, V. B. Pavlenko, M. L. Meil'man, and B. I. Minkov, Zh. Prikl. Spectrosk. **53**, 7 (1990).

9. V. Petričević, A. Seas, and R. R. Alfano, "Effective gain measurements in chromium-doped forsterite", *OSA Proceedings of the Advanced Solid-State Lasers Conference*, March 5-7, 1990, Salt Lake City, Utah, Vol. **6** of the OSA Proceedings Series, H. P. Jenssen and G. Dube, eds. (Optical Society of America, Washington, D.C., 1991) pp. 73-78.

10. D. E. Spence, P. N. Kean, and W. Sibbett, "60-fs pulse generation from a self-mode-locked Ti:sapphire laser", Optics Letters, Vol. **16**, 42 (1991).

11. F. Krausz, M. E. Fermann, T. Brabec, P. F. Curley, M. Hofer, M. H. Ober, C. Spielmann, E. Wintner, and A. J. Schmidt, "Femtosecond solid-state lasers" IEEE Journal of Quantum Electronics, **QE-28**, 2097 (1992).

12. H. A. Hauss, J. G. Fujimoto, and E. P. Ippen, "Analytic theory of additive pulse and Kerr lens mode-locking", IEEE Journal of Quantum Electronics, **QE-28**, 2086 (1992).

13. T. Brabec, Ch. Spielmann, P. F. Curley, and F. Krausz, "Kerr lens mode locking", Optics Letters, Vol. **17**, 1292 (1992).

14. J. G. Fujimoto, "New technologies for ultrashort pulse generation in solid-state lasers", Optics & Photonics News, pp 9, March 1991.

15. A. Seas, V. Petričević,, R. R. Alfano, " Continuous-Wave Mode-Locked Operation of Chromium-Doped Forsterite Laser", Optics Letters, Vol. **16**, pp.1668 (1991).

16. A. Seas, V. Petričević,, R. R. Alfano, "CW Mode-Locked Operation of Chromium-Doped Forsterite Laser", *Proceedings on Advanced Solid-State Lasers,* G. Dube and L. Chase, eds., Optical Society of America, Washington DC, Vol. **10**, pp. 69-71 (1991).

17. A. Seas, V. Petričević,, R. R. Alfano, "Generation of Sub-100-fs Pulses from a Continuous-Wave Mode-Locked Chromium-Doped Forsterite Laser", Optics Letters, Vol. **17**, pp. 937 (1992).

18. A. Seas, V. Petričević, R. R. Alfano, "60-fs Chromium-Doped Forsterite (Cr^{4+}:Mg_2SiO_4) Laser", Ultrafast Phenomena VIII, J. L. Martin, A. Migus, G. A. Mourou, and A. H. Zewail, eds., Springer Series in Chemical Physics, Vol. **55**, pp. 174 (1993).

19. A. Seas, V. Petričević,, R. R. Alfano, "Femtosecond Pulses Generated From a Synchronously Pumped Chromium-Doped Forsterite Laser", to be published in the Proceedings of the Topical Meeting on Advanced Solid-State Lasers, New Orleans, Louisiana, February 1-3, 1993.

20. A. Seas, V. Petričević,, R. R. Alfano, "Self-Mode-Locked Chromium-Doped Forsterite Laser Generates 50-fs Pulses", Optics Letters, Vol. **18**, pp. 891 (1993).

21. H. R. Verdun, L. M. Thomas, D. M. Andrauskas, T. McCollum, and A. Pinto, "Chromium-doped forsterite laser pumped by 1.06 μm radiation", Appl. Phys. Lett. **53**, 2593 (1988).

22. V. Petričević, S. K. Gayen, and R. R. Alfano, "Chromium-activated forsterite laser", in *Tunable Solid-State Lasers*, Vol. **5** of the OSA Proceeding Series, M. L. Shand and H. P. Jenssen, eds. (Optical Society of America, Washington, D.C., 1989), pp. 77-84.

23 H. R. Verdun, L. M. Thomas, and D. M. Andrauskas, "Laser performance of chromium-aluminum-doped forsterite", in *Tunable Solid-State Lasers*, Vol. **5** of the OSA Proceeding Series, M. L. Shand and H. P. Jenssen, eds. (Optical Society of America, Washington, D.C., 1989), pp. 85-92.

24. R. Moncorge, D. J. Simkin, G. Cormier, and J. A. Capobianco, "Spectroscopic properties and fluorescence dynamics in chromium-doped forsterite", in *Tunable Solid-State Lasers*, Vol. **5** of the OSA Proceeding Series, M. L. Shand and H. P. Jenssen, eds. (Optical Society of America, Washington, D.C., 1989), pp. 93-97.

25. Y. Yamaguchi, K. Yamagishi, A. Sugimoto, and Y. Nobe, " Optical properties and crystal growth atmosphere of forsterite", in *Advanced Solid-State Lasers*, Vol. **10** of the OSA Proceeding Series, G. Dube and L. Chase, eds. (Optical Society of America, Washington, D.C., 1991), pp. 52-56.

CHAPTER 2

1. V. Petričević, S. K. Gayen, R. R. Alfano, K. Yamagishi, H. Anzai, and Y. Yamaguchi, "Laser action in chromium-doped forsterite", Appl. Phys. Lett. **52**, 1040 (1988).

2. V. Petričević, S. K. Gayen, and R. R. Alfano, "Laser action in Cr-activated forsterite for near infrared excitation: Is Cr4+ the lasing ion?", Appl. Phys. Lett. **53**, 2590 (1988).

3. V. Petričević, S. K. Gayen, and R. R. Alfano, "Continuous-wave operation of chromium-doped forsterite", Optics Letters, Vol. **14**, 612 (1989).

4. V. Petričević, S. K. Gayen, and R. R. Alfano, "Near infrared tunable operation of chromium doped forsterite laser", Appl. Opt. **28**, 1609 (1989).

5. V. G. Barishevskii, M. V. Korzhik, A. E. Kimaev, M. G. Livshitz, V. B. Pavlenko, M. L. Meilman, and B. I. Minkov, Zh. Prikl. Spectrosk. (Moscow) **53**, 7 (1990).

6. A. Sugimoto, Y. Segawa, Y. Yamaguchi, Y. Nobe, K. Yamagishi, P. H. Kim, and S. Namba, Japanese J. Appl. Physics, Vol. **28**, 1833, (1989).

7. V. G. Baryshevskii, V. A. Voloshin, S. A. Demidovich, A. E. Kimaev, M. V. Korzhik, M. G. Livshitz, M. L. Meil'man, B. I. Minkov, and A. P. Shkadarevich, Quantovaya Electron. (Moscow) **17**, 1389 (1990).

8. V. Petričević, A. Seas, and R. R. Alfano, "Slope efficiency measurements of a chromium-doped forsterite laser", Optics Letters, Vol. **16**, 811 (1991).

9. A. Seas, V. Petričević, and R. R. Alfano, "Continuous-wave mode-locked operation of a chromium-doped forsterite laser", Optics Letters, Vol. **16**, 1668 (1991).

10. A. Seas, V. Petričević, and R. R. Alfano, " Generation of sub-100-fs pulses from a cw mode-locked chromium-doped forsterite laser", Optics Letters, Vol. **17**, 937 (1992).

11. A. Sennaroglu, T. J. Carrig, and C. R. Pollock, "Femtosecond pulse generation by using additive-pulse mode-locked chromium-doped forsterite laser operated at 77K", Optics Letters, Vol. **17**, 1216 (1992).

12. A. Seas, V. Petričević,, R. R. Alfano, "Self-Mode-Locked Chromium-Doped Forsterite Laser Generates 50-fs Pulses", Optics Letters, Vol. **18**, pp. 891 (1993).

13. V. Petričević, S. K. Gayen, and R. R. Alfano, "Chromium-activated forsterite laser", in *Tunable Solid-State Lasers*, Vol. 5 of the OSA Proceeding Series, M. L. Shand and H. P. Jenssen, eds. (Opt. Society of America, Washington, D.C., 1989), pp. 77-84.

14. N. Nishide, Y. Segawa, P. H. Kim, S. Namba, and A. Masuyama, Reza Kagaku Kenkyu **7**, 89 (1985).

15. H. Rager and G. Weiser, Bull. Mineral. **104**, 603 (1981).

16. H. R. Verdun, L. M. Thomas, D. M. Andrauskas, T. McCollum, and A. Pinto, "Chromium-doped forsterite laser pumped by 1.06 μm radiation", Appl. Phys. Lett. **53**, 2593 (1988).

17. J. R. Smith and R. M. Hazen, Am. Mineral. **58**, 588(1973).

18. V. Devarajan and E. Funck, J. Chem. Phys. **62**, 3406 (1975).

19. Y. Yamaguchi, K. Yamagishi, A. Sugimoto, and Y. Nobe, "Optical properties and crystal growth atmosphere of forsterite", in *Advanced Solid-State Lasers*, Vol. **10** of the OSA Proceeding Series, G. Dube and L. Chase, eds. (Optical Society of America, Washington, D.C., 1991), pp. 52-56.

20. Jerry B. Marion and Mark A. Heald, "Classical Electromagnetic Radiation" , Academic Press Inc., Second Edition, pp. 162 (1980).

CHAPTER 3

1. R. R. Alfano and S. L. Shapiro, "Ultrafast Phenomena in Liquids and solids", Scientific American, 288, pp. 43 (1973).

2. A. G. Doukas, B. Buchert, and R. R. Alfano, " Picosecond Laser Techniques and Design", in "Biological Events Probed by Ultrafast Laser Spectroscopy", Academic Press, New York (1982).

3. M. S. Demokan, "Mode-Locking in Solid-State Lasers", Research Studies Press, John Wiley & Sons Ltd., pp. 215 (1982).

4. "Biological Events Probed by Ultrafast Laser Spectroscopy, Robert R. Alfano, editor, Academic Press, New York (1982).

5. F. Liu, K. M. Yoo, and R. R. Alfano, "Ultrafast pulse transmission and imaging through biological tissues", Applied Optics, Vol. **32**, pp. 554 (1993).

6. L. M. Wang, P. P. Ho, and R. R. Alfano, "Double-stage picosecond Kerr gate for ballistic time-gated optical imaging in turbid media", Applied Optics, Vol. **32**, pp. 535 (1993).

7. H. Kogelnik, and T. Li, "Laser beams and resonators", Appl. Opt., Vol. **5**, pp. 1550 (1966).

8. P. W. Smith, " Mode-locking of lasers", Proc. IEEE, Vol. **58**, pp. 1342 (1970).

9. M. DiDomenico, "Small-signal analysis of internal (Coupling-type) modulation of lasers", J. Appl. Phys., Vol. **35**, pp. 2870 (1964).

10. L.E. Hargrove, L. R. Fork, and M.A. Pollack, "Locking of He-Ne laser modes induced by synchronous intracavity modulation", Appl. Phys. Letters, Vol. 5, pp. 4 (1964) .

11. A. Yariv, "Internal modulation of multimode laser oscillators", J. Appl. Phys., Vol. 36, pp. 388 (1965).

12. T. W. Chong, and P. A. Lindsay, " The generation of picosecond pulses in actively mode-locked c.w. solid-state lasers", Int. J. Electronics, Vol. 45, pp. 573 (1978).

13. D.J. Kuizenga, and A. E. Siegman, "FM and AM mode-locking of the homogeneous laser - Part I: Theory", IEEE J. Quantum Electr., QE-6, pp. 694 (1970).

14. A. E. Siegman, and D.J. Kuizenga, Opto-Electronics, Vol. 6, 1, pp. 43 (1974).

15. A. J. DeMaria, D. A. Stetser, and H. Heyman, Appl. Phys. Lett. 7, pp. 270 (1965).

16. R. L. Fork, B. I. Greene, C. V. Shank, "Generation of optical pulses shorter than 0.1 psec by colliding pulse mode locking", Appl . Phys. Lett., Vol. 38, pp. 671 (1981).

17. A. I. Kovrigin, V. A. Nekhaenko, S. M. Pershin, and A. A. Podshivalov, "Dynamics of emission from dye lasers pumped synchronously by finite picosecond pulse trains", Sov. J. Quantum Electron., Vol. 14, pp. 1346 (1984).

18. V. A. Nekhaenko, S. M. Pershin, and A. A. Podshivalov, "Synchronously pumped tunable picosecond lasers (review)", Sov. J. Quantum Electron., Vol. 16, pp. 299 (1986).

19. L. F. Mollenauer, N. D. Vieira, and L. Szeto, " Mode-locking by synchronous pumping using a gain medium with microsecond decay times", Optics Letters, Vol. 9, pp. 414 (1982).

20. F. Krausz, M. E. Fermann, T. Brabec, P. F. Curley, M. Hofer, M. H. Ober, C. Spielman, E. Wintner, and A. J. Schmidt, "Femtosecond solid-state lasers", IEEE J. Quantum Electr., QE-28, pp. 2097 (1992).

21. A. B. Grudinin, E. M. Dianov, D. V. Korobkin, A. M. Prokhorov, V. N. Serkin, and D. V. Khaidarov, "Decay of femtosecond pulses in single-mode optical fibers", JETP Lett., Vol. 46, pp. 221 (1987).

22. T. Brabec, Ch. Spielmann, P. F. Curley, and F. Krausz, "Kerr lens mode locking", Optics Letters, Vol. 17, pp. 1292 (1992).

23. F. Salin, J. Squier, and M. Piche, "Mode locking of Ti:Al2O3 lasers and self-focusing: a Gaussian approximation", Opt. Lett. Vol. 16, pp. 1674 (1991).

24. S. Chen, and J. Wang, "Self-starting issues of passive self-focusing mode locking", Optics Letters, Vol. 16, pp. 1689 (1991).

25. D. Huang, M. Ulman, L. H. Acoli, H. A. Haus, and J. Fujimoto, "Self-focusing saturable loss for laser mode locking", Optics Letters, Vol. 17, pp. 511 (1992).

26. J. Laussade, A. Yariv, " Analysis of mode locking and ultrashort laser pulses with a nonlinear refractive index", IEEE J. Quantum Electron., Vol. QE-5, pp. 435 (1969).

27. L. Dahlstrom, "Passive mode-locking and Q-switching of high power lasers by means of the optical kerr effect", Optics Comm., Vol. **5**, pp. 157 (1972).

28. K. Sala, M. C. Richardson, and N. R. Isenor, "Passive mode locking of lasers with the optical Kerr effect modulator", IEEE J. Quantum Electron., Vol. **QE-13**, pp. 915 (1977).

29. D. E. Spence, P. N. Kean, and W. Sibbett, "60 fsec generation from a self-mode-locked Ti:sapphire laser", Optics Letters, Vol. **16**, pp. 42 (1991).

30. D.K. Negus, L. Spinelli, N. Goldblatt, and G. Feuget, "Sub-100-fs pulse generation by Kerr lens modelocking in Ti:Al_2O_3", in Tech. Dig. Topic. Meet. Advan, Solid State Lasers, Washington, DC, OSA, 1991, postdeadline paper.

31. J. D. Kafka, M. L. Watts, and J. J. Pieterse, "Picosecond and femtosecond pulse generation in a regeneratively mode-locked Ti:sapphire laser", IEEE J. Quantum Electron., Vol. **QE-28**, pp. 2151 (1992) and references therein.

32. J. Buchert, R. Dorsinvile, P. Delfyett, S. Krimchansky, and R. R. Alfano "Determination of temporal correlation of ultrafast laser pulses using phase conjugation", Opt. Comm.,Vol. **52** , pp. 433 (1985).

33. J. A. Giordmaine, P. M. Rentzepis, S. L. Shapiro, and K. W. Wecht "Two photon excitation of fluorescence by picosecond light pulses." Appl. Phys. Lett., Vol. **11**, pp. 216 (1967).

34. M. Maier, W. Kaiser, J. A. Giordmaine, " Intense light bursts in the stimulated Raman effect", Phys. Rev. Lett., Vol. **17**, pp. 1275 (1966).

35. A. J. DeMaria, W. H. Glenn Jr., M. J. Brienza, and M. E. Mack, "Picosecond laser pulses", Proc. IEEE, Vol. **57**, pp. 2 (1969).

36. Jean-Claude M. Diels, J. J. Fontaine, I. C. McMichael, and F. Simoni, "Control and measurement of ultrashort pulse shapes (in amplitude and phase) with femtosecond accuracy", Applied Optics, Vol. **24**, pp 1270 (1985).

37. K. L. Sala, G. A. Kenney-Wallace, and G. E. Hall, "CW autocorrelation measurements of picosecond laser pulses", IEEE J. Quantum Electron. Vol. **QE-16**, pp. 990 (1980).

38. "Handbook of Laser Science and Technology, Volume III, Optical Materials: Part I", Marvin J. Weber, CRC Press Inc., pp. 12 (1986).

39. "Optical Waves in Crystals", A. Yariv, John Wiley & Sons, pp. 524 (1984).

40. H. P. Weber, "Method for pulsewidth measurement of ultrashort light pulses generated by phase-locked lasers using nonlinear optics", J. Appl. Phys., **38**, pp. 2231 (1967).

41. "Temperature Dispersion in ADP, KDP, and KD*P for Nonlinear Devices", G. C. Ghosh and G. C. Bhar, IEEE Journal of Quantum Electronics, Vol. **QE-18**, pp. 143 (1982).

CHAPTER 4

1. V. Petričević, A. Seas, and R. R. Alfano, "Forsterite Laser Tunes in Near IR", Laser Focus World **26** (11), pp. 109 (1990).

2. T. Y. Fan, and A. Sanchez, "Pump Source Requirements for End-Pumped Lasers", IEEE J. Quantum Electronics, Vol. **QE 26**, pp. 311 (1990).

3. P. F. Moulton, "An investigation of the Co:MgF_2 laser system", IEEE J. Quantum Electron., Vol. **QE-21**, pp. 1582 (1985).

4. D. G. Hall, R. J. Smith, and R. R. Rice, "Pump-size effects in Nd:YAG lasers", Appl. Opt., Vol. **19**, pp. 1041 (1980).

5. H. Kogelnik, and T. Li, "Laser beams and resonators", Appl. Opt., Vol. **5**, pp. 1550 (1966).

6. D. C. Hanna, "Astigmatic gaussian beams produced by axially asymmetric laser cavities", IEEE J. Quantunm Electron., Vol. **QE-10**, pp. 483 (1974).

7. A. E. Siegman, "Lasers", University Science Books, Mill Valey, California, chapter 21 (1986).

8. L. W. Casperson, "Mode stability of lasers and periodic optical systems", IEEE J. Quantum Electron., Vol. **QE-10**, pp. 629 (1974).

9. H. Kogelnik, E. P. Ippen, A. Dienes, and C. V. Shank, "Astigmatically compensated cavities for CW dye lasers", IEEE J. Quantum Electron., Vol. QE-8, pp. 373 (1972).

10. H. Kogelnik, "Imaging of optical modes-resonators with internal lenses", Bell Syst. Tech. J., Vol. **44**, pp. 455 (1965).

11. L. V. Tarasov, "Laser Physics", MIR Publishers, Moscow, chapter 2.6 (1983).

12. W. D. Johnston, P. K. Runge, "An improved Astigmatically Compensated Resonator for CW Dye Lasers", IEEE J. Quantum Electron., Correspondence, pp. 724 (1972).

13. D. R. Preuss, and J.L. Gole, " Three-stage birefringent filter tuning smoothly over the visible region: theoretical treatment and experimental design", Applied Optics, Vol. **19**, pp. 702 (1980).

14. D. E. Gray, ed., "American Institute of Physics Handbook", 3rd ed. (McGraw-Hill, New York, 1972, pp. 6-29.

15. G. Holtom, and O. Teschke, "Design of a Birefringent filter for high-power dye lasers", IEEE J. Quantum Electronics, Vol. **QE-10**, pp. 577 (1974).

16. J. T. Darrow, and R. K. Jain, in *Digest of Meeting on Tunable Solid State Lasers*, Optical Society of America, D.C., paper PD-2 (1987).

17. L. F. Mollenauer, N. D. Vieira, and L. Szeto, "Mode locking by synchronous

pumping using a gain medium with microsecond delay times", Optics Letters, Vol. **7**, pp. 414 (1982).

18. H. G. Damielmeyer, in "Lasers", A. K. Levine and A. DeMaria, eds. (Dekker, New York, 1975), Vol. IV.

CHAPTER 5

1. C. V. Shank, "Generation of ultrashort optical pulses", in Ultrashort Laser Pulses and Applications, W. Kaiser, Ed. New York: Springer Verlag, 1988, chapter 2.

2. F. Krausz, M. E. Ferman, T. Brabec, P. F. Curley, M. Hofer, M. H. Ober, C. Spielmann, E. Wintner, and A. J. Schmidt, "Femtosecond Solid-State Lasers", IEEE J. Quantum Electron., Vol. **QE-28**, pp. 2097 (1992).

3. E. B. Treacy, "Optical pulse compression with diffraction gratings", IEEE J. Quantum Electron., Vol. **QE-5**, pp. 454 (1969).

4. R. L. Fork, O. E. Martinez, and J. P. Gordon, "Negative dispersion using pairs of prisms", Optics Letters, Vol. **9**, pp. 150 (1984).

5. J. P. Gordon, and R. L. Fork, "Optical (ring) resonator with negative dispersion", Optics Letters, Vol. **9**, pp. 153 (1984).

6. F. Gires, and P. Tournois, "Interferometre utilisable pour la compression d'impulsions lumineuses modulees en frequence", C. R. Acad. Sci. Paris, Vol. 258, pp. 6112 (1964).

7. J. D. Kafka, M. L. Watts, and J. J. Pieterse, "Picosecond and Femtosecond Pulse Generation in a Regeneratively Mode-Locked Ti:Sapphire Laser", IEEE J. Quantum Electron., Vol. **QE-28**, pp. 2151 (1992).

8. A. E. Siegman, "Lasers", University Science Books, Mill Valey, California, chapter 9 (1986).

9. R. R. Alfano, Ultrafast Optics Notes (1992).

10. A. Yariv, and P. Yeh, "Optical Waves in Crystals", Wiley-Interscience, John Wiley & Sons Inc., New York, Chapter 2 (1984).

11. "Optical Glass", Schott Catalog, Shchott Glass Technologies Inc., Duryea, Pensylvania.

12. D. E. Spence, P. N. Kean, and W. Sibbet, "60-fs pulse generation from a self-mode-locked Ti:sapphire laser", Optics Letters, Vol. **16**, pp. 42 (1991).

13. D. K. Negus, L. Spinelli. N. Goldblatt, and G. Feugnet, *OSA Proceedings on Advanced Solid-State Lasers,* G. Dube and L. Chase, eds. (Optical Society of America, Washington, D.C., 1991), Vol. **10**, pp. 120-124.

14. N. H. Rizvi, P. M. W. French, and J. R. Taylor, "Continuously self-mode-locked

Ti:sapphire laser that produces sub-50-fs pulses", Optics Letters, Vol. **17**, pp. 279 (1992).

15. C. P. Huang, H. C. Kapteyn, J. W. McIntosh, and M. M. Murnane, "Generation of transform-limited 32-fs pulses from a self-mode-locked Ti:sapphire laser", Optics Letters, Vol. **17**, pp. 139 (1992).

16. C. P. Huang, M. T. Asaki, S. Backus, M. M. Murnane, H. C. Kapteyn, and H. Nathel, "17-fs pulses from a self-mode-locked Ti:sapphire laser", Optics Letters, Vol. 17, pp. 1289 (1992).

17. B. Proctor, and F. Wise, "Quartz prism sequence for reduction of cubic phase in a mode-locked Ti:Al_2O_3 laser", Optics Letters, Vol. **17**, pp. 1295 (1992).

18. J. M. Jacobson, K. Naganuma, H. A. Haus, J. G. Fujimoto, A. G. Jacobson, "Femtosecond pulse generation in a Ti:Al_2O_3 laser using second- and third-order intracavity dispersion", Optics Letters, Vol. **17**, pp. 1608 (1992).

19. R. L. Fork, C. H. Brito Cruz, P. C. Becker, and C. V. Shank, " Compression of optical pulses to six femtoseconds by using cubic phase compensation", Optics Letters, Vol. **12**, pp. 483 (1987).

CHAPTER 6

1. A. Seas, V. Petričević, and R. R. Alfano, "CW Mode-Locked Operation of Chromium-Doped Forsterite Laser", *OSA Proceedings on Advanced Solid-State Lasers,* G. Dube and L. Chase, eds. (Optical Society of America, Washington, D.C., 1991), Vol. **10**, pp. 69-71.

2. A. Seas, V. Petričević, and R. R. Alfano, "Continuous-Wave Mode-Locked Operation of Chromium-Doped Forsterite Laser", Optics Letters, Vol. **16**, pp. 1668 (1991).

3. A. Seas, V. Petričević, and R. R. Alfano, "Generation of Sub-100-fs Pulses From a Continuous-Wave Mode-Locked Chromium-Doped Forsterite Laser", Optics Letters, Vol. **17**, pp. 937 (1992).

4. A. Seas, V. Petričević, and R. R. Alfano, "Generation of sub-100-fs Pulses from a Continuous-Wave Mode-Locked Chromium-Doped Forsterite Laser", Post-deadline paper, presented at the Conference on Lasers and Electro-Optics (CLEO), Anaheim, California, May 11-15, 1992.

5. A. Seas, V. Petričević, R. R. Alfano, "60-fs Chromium-Doped Forsterite (Cr^{4+}:Mg_2SiO_4) Laser", Ultrafast Phenomena VIII, J. L. Martin, A. Migus, G. A. Mourou, and A. H. Zewail, eds., Springer Series in Chemical Physics, Vol. **55**, pp. 174 (1993).

6. A. Seas, V. Petričević, and R. R. Alfano, "Femtosecond Pulses Generated From a Synchronously Pumped Chromium-Doped Forsterite Laser", To be published in the Proceedings at the Topical Meeting on Advanced Solid-State Lasers New Orleans, Louisiana, February 1-3, 1992.

7. A. Seas, V. Petričević, and R. R. Alfano, "Self Mode-Locked Chromium-Doped Forsterite Laser Generates 50-fs Pulses", Optics Letters, Vol. **18**, pp. 891 (1993).

8. A. Yariv, "Optical Electronics", fourth edition, Sanders College Publishing, Holt Rinehart and Winston Inc., pp. 282 (1991).

9. G. C. Ghosh, and G. C. Bhar, "Temperature dispersion in ADP, KDP, and KD*P for nonlinear devices", IEEE J. Quantum Electron., Vol. **QE-18**, pp.143 (1982).

10. Catalogue from Litton-Airtron, "KTP, Potasium Titanyl Phosphate", Synthetic Crystals and Optical Products, Charlotte, NC 28273.

11. A. D. Hays, L. R. Marshall, and R. Burnham, "High powered CW diode-array-pumped Nd:YAG laser", in Tunable Solid-State Lasers, Vol. 10 of the OSA Proceeding Series, G. Dube and L. Chase, eds. (Optical Society of America, Washington, D.C., 1991), pp. 255-256.

12. Y. Pang, V. Yanovsky, F. Wise, and B. I. Minkov, "Self-mode-locked Cr:forsterite laser", to be published in Optics Letters (1993).

13. J. D. Kmetec, J. J. Macklin, and J. F. Young, "0.5-TW, 125-fs Ti:sapphire laser", Optics Letters, Vol. **16**, pp. 1001 (1991).